The 3-D structure and earthquake locations at Rabaul Caldera, Papua New Guinea

Ima ITIKARAI

B.Sc, University of Papua New Guinea, Port Moresby; **PGD in Seismology**, International Institute of Seismology and Earthquake Engineering, Tsukuba, Japan

A THESIS SUBMITTED FOR THE DEGREE OF
MASTER OF PHILOSOPHY
OF
THE AUSTRALIAN NATIONAL UNIVERSITY

Research School of Earth Sciences

31 October 2008

STATEMENT

All the results and conclusions presented in this thesis are the author's own, except where otherwise stated. All sources of information used in this thesis have been acknowledged.

I certify that this thesis contains no information that has been accepted for the award of any other degree or qualification at any other university or institution.

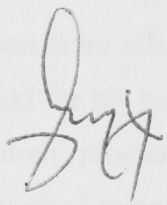

Ima ITIKARAI

31 October 2008

ACKNOWLEDGEMENTS

This study was conducted at the Research School of Earth Sciences, The Australian National University, Canberra, Australia, between February 2006 and May 2008. Financial support was provided by the Australian International Aid Agency (AusAID) in the form of an Australian Development Scholarship Award.

For the actual work, I am greatly indebted to my supervisor Professor Brian Kennett for his enduring assistance, guidance and encouragement during the entire course of my research program. I received great support and guidance from him on a lot of the work presented in Chapter 5.

I also received invaluable support from other people at the RSES. I acknowledge the assistance of Dr Cvetan Sinadinovski for his guidance in some aspects of the work in Chapter 4 and tutoring on my Fortran programming, Dr Nicholas Rawlinson for introducing me to the Fast Marching Method tomography algorithm which I used for the work in Chapter 4 and his continued support on its usage, Armando Arcidiaco for assisting me with appropriate Unix scripts to conduct some of my data processing, and lastly Ray Martin for seeking his assistance every time I had difficulties with my Unix-driven Sun computer.

I would like to acknowledge my work colleague F Taranu and his two counterparts J Kuduon and J Sukua for responding to my requests for additional data. Other colleagues including C O McKee, H Patia, K Mulina, S Saunders and cousin P Puri also assisted unselfishly in many of my personal requests on matters relating to our eldest daughter Elma who stayed back in Papua New Guinea during the period of my study.

My release from work by granting study leave was made possible by the then Department of Mining Training Committee. I acknowledge the contributions of the then Acting Secretary of the Department, Director of Human Resources Division, the Senior Staff Development Officer and the Director of Geological Survey Division. The then Department of Mining provided further support in the form of return airline tickets and allowances for my family.

I would like to extend my personal gratitude to Shane Nancarrow and Family and Doug Finlayson and Family for their kind assistance during our stay in Canberra.

Lastly I say thank you to my wife Helen and children Ima Jr, Gao and Elly for the good and challenging times we had during our stay in Canberra. I dedicate my Master of Philosophy to my parents but in particular my father, Iti Puri.

CONTENTS

ACRONYMS

AusAID - Australian Aid for International Development
BOI - Boisen seismic station
BP - Before Present
BBRF - Blanche Bay Ring Fault
BMA - Burma Hill seismic station
BVAS - Bismarck Volcanic Arc System
CDMR - Caldera Deep Magma Reservoir
CSMR - Caldera Shallow Magma Reservoir
DAV - Davaon seismic station
DOY - Duke of York seismic station
FMM - Fast Marching Method
GMT - Generic Mapping Tools
GPS - Global Positioning System
HF - High frequency
JBH - John Brown seismic station
JICA - Japanese International Co-operation Agency
KAL - Kalamalagunan seismic station
KOR - Korere seismic station
KPT - Kaputin Point Seismic station
LF - Low frequency
LTA - Long-term average
MAK - Makada seismic station
MAL - Malaguna seismic station
MPT - Matupit seismic station
MRF - Matupit Ring Fault
NA - Neighbourhood Algorithm
NEEqs - Northeast earthquakes
OBS - Ocean Bottom Seismometer
RAL - Rabalanakaia seismic station
RELACS - Rabaul Earthquake Locations and Caldera Structure
RHSN - Rabaul Harbour Seismic Network
RMR - Rabuana Magma Reservoir
RPT - Raluana Point seismic station
RSAM - Real-time Seismic Amplitude
RSES - Research School of Earth Sciences
RVO - Rabaul Volcanological Observatory
SDA - Seismic station on Matupit Island located at the SDA Church
STA - Short-term average
SVD - Singular value decomposition
TAL - Talvat seismic station
TAV - Tavurvur seismic station
TJ - Triple junction
TKA - Tanaka seismic station
TUN - Tunnel Hill seismic station
TVL - Tavuiliu seismic station
USGS - United States Geological Survey

VAZ - Varzin seismic station
VDAP - Volcano Disaster Assistance Program
VIS - Vulcan Island seismic station
V_p - P-wave velocity
VPE - Vunapope seismic station
V_s - S-wave velocity
VT - Volcano-tectonic
VUL - Vulcan seismic station
VZN - relocated Varzin seismic station
WAN - Wanlis seismic station
WTM - Watom seismic station
WWII - World War II

ABSTRACT

Rabaul Caldera is an active volcanic complex located on the eastern end of the New Britain Island. It is part of the Bismarck Volcanic Arc System (BVAS). It is nearly elliptical in shape and measures about 14 km x 9 km. The major axis of the caldera is slightly east from the north. Much of the caldera is filled by seawater from a 5km breach on the east-southeastern wall.

The caldera has a very colourful eruptive history, having produced both caldera-forming eruptions and a number of smaller eruptions in recent historical times. The last caldera-forming eruption is dated about 1400 yrs BP. The very recent historical eruptions date back only about 250 years from accounts of early European explorers.

A main feature of the recent historical eruptions is the twin eruptions from Tavurvur and Vulcan located on opposites of the harbour. The last twin eruptions occurred in September 1994 and completely destroyed about two-thirds of Rabaul Town. Rabaul Town is located on the northern end of the caldera.

Some studies have been conducted by various people in an effort to gain better understanding of the caldera system. The main outcomes of some of these studies include:

- The seismicity that has been recorded inside the caldera defines an outward dipping elliptical ring-fault. However further manipulation of the seismic data in the mid-1990's exposed possibly two ring-faults instead of one.

- The presence of a shallow magma reservoir at about 4-6 km depth beneath the central part of the caldera. Two other magma bodies have been mapped. The first is located slightly deeper beneath the Rabaul Caldera, and the second is located north-northeast of the Rabaul caldera.

- The eruptions at Rabaul Caldera have involved magma mixing and it has led to the proposition that this process has a strong influence for triggering eruptions at this active caldera.

In this study I have re-visited the original RVO earthquake solutions and conducted some studies on the spatial distribution of the earthquakes. The results reveal two ring

structures instead of one as initially proposed by Mori and McKee (1987). This outcome is consistent with Jones and Stewart (1997).

This study has also assessed the post-1994 eruption seismicity at the Rabaul Caldera and the ongoing eruptions at Tavurvur between 1995 and 2005. There has been a clear lack of seismicity inside the caldera during the period concerned. The lack of seismicity inside the caldera could be best explained by release of the caldera-wide stress during the eruption. On the other hand some anomalous seismicity northeast of the Rabaul Caldera (NEEqs) has prevailed during the same period. About ten years of simultaneous observations on the ongoing eruptions at Tavurvur and the NEEqs have produced a strong correlation between the two. The correlation is the NEEqs have always been followed by increased eruptive activity or renewed eruptions.

P- and S-wave travel time tomography has been conducted in this study. The FMM (Rawlinson and Sambridge, 2003) solved the forward problem and the subspace inversion method (Kennett et al., 1988) solved the inverse problem. The tomography has been done in two parts; the regional and local model. The data used in the tomography include near and distant regional earthquakes recorded by the RHSN between 1997 and 2004, a subset of the pre-1994 eruption Rabaul Caldera earthquakes, the post-1994 Rabaul Caldera earthquakes and the RELACS shots. Some of the regional earthquakes recorded by the RHSN coincided with the RELACS project, and so were recorded by the RELACS stations as well. The results from the tomography are fairly consistent with the outcomes of previous similar studies (Finlayson et al., 2003; Bai and Greenhalgh, 2005). The three studies have mapped the shallow magma body beneath Rabaul Caldera fairly convincingly. This study located the shallow body between 3 and 6 km depth. Bai and Greenhalgh (2005) and this study have also mapped two other anomalies. The first is located beneath the Rabaul Caldera and this study has located it between 9 and 14 km depth. The second body is located in a north-northeast direction from the Rabaul caldera at comparable dept to the shallow body beneath the Rabaul Caldera. Besides mapping the magma bodies another outcome of the travel time tomography has been the derivation of a 3-D velocity model for the Rabaul Caldera which has been used to relocate the pre- and post eruption earthquakes.

A newly developed 3-D earthquake location program, *Shak3_na*, has been used to re-locate a subset of the pre-1994 eruption Rabaul Caldera earthquakes, some of the post-1994 eruption earthquakes and a selected number of near-regional earthquakes. The 3-D velocity model for the Rabaul Caldera derived from the P- and S-wave travel time

tomography has been used. Generally the re-located epicenters for the pre-1994 eruption Rabaul Caldera earthquakes have reproduced the elliptical ring-fault extremely well. On the other hand the depth sections have differed. The general west-east cross-section has conveyed the outward dip of the ring-fault observed by Mori and McKee (1987) quite well. However, the north-south cross-sections have been completely different. Instead of the double ring-fault structure, the re-located solutions have exposed only a single structure dipping gently to the south. It is possible the two ring-faults are still present but they are pinned together. The disjointed view of the two ring-faults exposed in the RVO solutions is probably an artifact of the 1-D velocity model. The re-located solutions for the post-1994 eruption earthquakes and the regional earthquakes have been relatively good. It seems quite obvious that earthquakes located close to the network array have less error compared to those located further away.

Based on the outcomes of some parts of this study and information from other studies I have proposed a possible plumbing system and possible eruption model for Rabaul Caldera.

Chapter 1

Introduction

1.1 Background

My study is based on Rabaul Caldera, an active volcanic complex located on the eastern tip of New Britain Island, Papua New Guinea. It is part of the Bismarck Volcanic Arc system that spans from the offshore Bam volcano in the north-west part of Papua New Guinea to Rabaul. The Rabaul Caldera was formed from a series of major caldera forming eruptions during the last 20,000 (Nairn et al., 1995). The last event is dated about 1400 years BP. Much of the caldera floor is flooded by seawater from a 5 km long breach on the southeastern part. Following the last major event, a number of post-caldera vents formed. Some of these vents have been the focus of eruptions witnessed as early as mid-1700's by early European explorers, however, Tavurvur and Vulcan located on opposite sides of the harbour have been the most active of the vents having erupted a few times in the last 250 years. Both volcanoes erupted simultaneously on three occasions in 1878, 1937 and the latest one in 1994. During the last eruption Vulcan ceased to erupt on 2 October 1994 and Tavurvur ceased on 16 April 1995. Tavurvur resumed eruption in November 1995. Besides two other stoppages in September 2001 and February 2004 for almost a year each, Tavurvur has continued to erupt variably to the time of writing this thesis.

Volcanic activity in the form of volcano seismicity was first detected at Rabaul Caldera when seismic monitoring commenced in the late 1960's (Cooke, 1972). The level of seismicity picked up in 1971 following two M_L 8.0 earthquakes that occurred in the northern Solomon Sea (Everingham, 1975) and about 100 km southeast of Rabaul Caldera. Between 1971 and the eruption in 1994 the pattern of seismicity fluctuated between periods of low and high activity. The periods of high level seismicity were characterized by earthquake swarms. The highest level of seismicity was recorded between September 1983 and July 1985. This period was dubbed the Rabaul seismo-deformation crisis (Mori

et al., 1988). Earthquake swarms became very frequent during this period. The high seismicity was accompanied by high rates of surface deformation, the vertical uplift being the main component. Approximately 0.7-0.8 meters of vertical uplift was recorded at a benchmark on Matupit Island in the central part of the caldera during the crisis period alone. An eruption was imminent then (McKee et al., 1984) but failed to occur and activity returned to background levels after July 1985. Similar crises as described above were also observed at the Long Valley caldera and the Phlegraean Fields (Newhall and Dzurasin, 1988; Barberi et al., 1984). Moreover, these two systems also failed to produce eruptions.

Seismic and surface deformation data recorded before, during and after the crisis period have been used to model this active caldera structure (Mori and McKee, 1987; McKee et al., 1987; Mori and Eberhart-Phillips, 1992; Jones and Stewart, 1997; Saunders, 2001). Point source modeling (Mogi, 1958) by McKee et al., (1984) indicated two shallow sources located slightly south beneath the area between Tavurvur and Matupit Island, and east of Vulcan headland. They proposed that these two small reservoirs were fed from a bigger body beneath them. The spatial and temporal distribution of earthquakes inside the caldera revealed an outward-dipping elliptical ring-fault (Mori and McKee, 1987). Furthermore the depths for the earthquakes were restricted to the upper four kilometers, thereby suggesting that the cut-off of earthquakes at this depth marked the roof of a possible caldera-wide magma reservoir. Further analyses of the seismic data by Jones and Stewart (1997) with the collapsing method identified two ring-faults instead of one. Essentially the collapsing method allows a cloud of events to move within the neighbourhood of the location uncertainty until they converge to a common solution.

Earthquakes ceased to occur inside the caldera following the eruption in 1994. This is quite logical considering a significant amount of the caldera stress was released by the erupted material. However, some anomalous seismicity emerged from a new location, northeast of Rabaul Caldera. Earthquake occurrence from this region was almost unheard of before the eruption, except the May 1992 Namanula earthquake swarm. From here on these earthquakes will be referred to as the northeast earthquakes and be abbreviated NEEqs. Between 1995 and 2005 simultaneous observations on the ongoing eruptions at Tavurvur and the NEEqs showed some strong correlation between the two.

Further developments aimed at better understanding the Rabaul Caldera structure became possible with the RELACS project. RELACS is the acronym for Rabaul Earthquake Locations and Caldera Structure. It is one component of the then RVO Volcanological Service Support Project funded by the Australian International Aid

Agency, AusAID. The survey was conducted by the then Australian Geological Survey Organisation (now Geoscience Australia), The Australian National University, Hokkaido University, University of Wisconsin - Madison and Rabaul Volcanological Observatory. The RELACS data have been used by a few groups (Finlayson et al., 2003; Gudmundsson et al., 2004; Bai and Greenhalgh, 2005) to further model the Rabaul Caldera structure mainly using travel time tomography and attenuation studies. The results of these studies are briefly discussed in Chapter 4.

On the volcanological front geological, petrological and geochemical studies (Heming, 1974, 1977; Walker et al., 1981; Nairn et al., 1995; Johnson et al., 1995; Patia et al., 2002 & Patia, 2004; McKee, in prep) have been ongoing to map the eruptive history and the magmatic processes associated with the eruptions in this active caldera. Some of these studies (Johnson et al., 1995; Patia et al., 2002 & Patia, 2004) indicated magma-mixing and proposed this process as a mechanism for triggering eruptions at this active caldera.

In my MPhil study I conducted further tomographic studies using P- and S-wave travel times and earthquake re-locations using a 3-D velocity model derived from the seismic tomography. The data I used in this study ranged between 1971 and 2005.

For the seismic travel time tomography I used the Fast Marching Method (FMM) by Rawlinson and Sambridge (2004, 2005) and the subspace inversion method (Kennett et al., 1988). The main aim for conducting the travel time tomography is to identify anomalous low velocity zones beneath Rabaul Caldera and the surrounding areas and where appropriate associate them with possible magma bodies. Another aim for the travel time tomography is to derive a 3-D velocity model for the Rabaul Caldera for 3-D earthquake location purposes. I used earthquake data recorded by the RHSN and the RELACS network to conduct the travel time tomography. Data from the RHSN includes pre and post-1994 eruption caldera earthquakes, local earthquakes outside the caldera and regional earthquakes. RELACS data consist of explosions.

The 3-D earthquake locations were done using a new algorithm, *Shak3_na*, developed in this study. *Shak3_na* is driven by the neighbourhood algorithm concepts. In essence the neighbourhood algorithm is a derivative-free method that uses the spatial properties of Voronoi cells to search a four-dimensional hypocenter space. The search is guided by a specified misfit measure (Sambridge, 1998). The initiative to derive a 3-D velocity model and relocate the earthquakes was driven by suggestions by Jones and Stewart (1997) that the stratification of the 1-D horizontally-layered velocity model

currently used by RVO for routine earthquake location may have some limitations and therefore not reflect the actual structure, and in turn have direct influence on the hypocentral solutions for the Rabaul Caldera earthquakes as noted also by Jones and Stewart (1997).

The results from some components of this study were blended together with other information to derive a possible plumbing system and an eruption model for the Rabaul Caldera in view of the NEEqs and the ongoing eruptions at Tavurvur between 1994 and 2005 and what they implied. Some questions that arose and drove the study are:

- Is there really a correlation between the NEEqs and the eruptions at Rabaul, particularly Tavurvur?
- Do the hypocenters of the NEEqs point to a possible northeasterly magma source.
- Does the geometrical trend of the NEEqs signify an intrusion path for the second magma source into the resident magma reservoir?
- Or does the occurrence of the NEEqs signify stress implications in the local environment, which is the driving mechanism for the second magma source into the resident magma reservoir? In this scenario, the second magma source could be at another location within the caldera or at depth. This issue was not addressed during the current study due to lack of information but has been highlighted for future work in the Conclusions.

In essence the main question is, is there a second magma source near or at depth in the vicinity of Rabaul caldera, and what relationship does the NEEqs have with this source.

1.2 Structure of Thesis

1.2.1 Chapter 2 – Tectonic setting and the Rabaul Caldera structure

Chapter 2 has two main parts. The first part discusses some general information about the tectonics of Papua New Guinea, New Britain and the Gazelle Peninsula, where

Rabaul Caldera is located. It points out the main plate boundaries and the source and distribution of earthquakes and volcanoes in this active part of the Pacific Ring of Fire.

The second part focuses specifically on Rabaul Caldera. It discusses some background information on the eruptive history, structure and the pre-1994 eruption seismic activity of this active caldera. The eruptive history includes information on the most recent eruption at Rabaul Caldera between 1994 and 2005.

1.2.2 Chapter 3 – The post-eruption seismicity at the Rabaul Caldera

The post-eruption seismicity for Rabaul Caldera is discussed in this chapter. It highlights the type of seismic events that have been recorded and how these events are associated with the ongoing eruption at Tavurvur.

A possible hypothesis is proposed here about the mechanism of eruptions at Rabaul caldera based on the strong correlation established between the NEEqs and the observed eruptive activity between 1994 and 2005.

1.2.3 Chapter 4 – Imaging Rabaul Caldera

This chapter is focused on seismic imaging of the Rabaul Caldera using P- and S-wave travel-time tomography. It discusses some general concepts about seismic tomography and the particular tomographic technique used in this study. The treatment of data and model parameterization of the area of study are outlined as well. The results of this study are compared with previous studies done by other people on the structure of the Rabaul Caldera.

1.2.4 Chapter 5 – 3-D hypocenter determinations

In this chapter I have applied a new 3-D hypocenter location program, Shak3-na, to conduct 3-D earthquake locations. *Shak3_na* makes use of the neighbourhood algorithm. This is a derivative-free method that searches a four-dimensional hypocenter space guided by a specified misfit measure. The re-location is tested with a synthetic data set and is then applied to a subset of pre- and post-1994 eruption Rabaul caldera earthquakes, and near regional earthquakes. The 3-D heterogeneous velocity field determined in Chapter 4 is used to locate the earthquakes. The results for the relocated events for the Rabaul caldera dataset are compared with previous locations determined with FASTHYPO (Hermann, 1979) and the 1-D horizontally-layered homogeneous velocity model.

1.2.5 Chapter 6 – Discussions

Chapter 6 gives some in depth discussions on some of the key issues that have emerged from study. One of this is the proposal for a possible plumbing system and an eruption model for the Rabaul Caldera.

1.2.6 Chapter 7 – Conclusions and possible further work

The last chapter, Chapter 7, lists the main conclusions of this study and at the same time lists some potential work for consideration to further this study in the future.

Chapter 2

Tectonic setting and information on Rabaul Caldera

2.1 Tectonic setting

This chapter discusses a general overview of the tectonic setting of Papua New Guinea and some information on Rabaul Caldera.

2.1.1 Papua New Guinea

Papua New Guinea is located on the Pacific Ring of Fire in a complex setting of subduction zones and consequently it is very active seismically and volcanically. The main plates engaged in the area are the Pacific and the Indo-Australian Plates. However, due to complicated tectonic processes along the main plate boundary other micro-plates have emerged in between. The main micro plates are the Solomon, and South and North Bismarck plates (Fig. 2.1). Plate motions at each plate boundary are as follows:

- The primary plate boundary between the Indo-Australian and the Pacific plates is defined by a collision zone. It runs along the central part of the mainland of Papua New Guinea and is clearly marked by the mountain ranges formed by the collision. Immediately north of the collision zone is the highly fractured Markham/Ramu valley fault system.
- North and South Bismarck. The boundary between these two plates is the transform type with the north part moving approximately westward with respect to the south. This boundary is known as the Bismarck Sea Seismic Lineation (BSSL). Small segments of spreading centers are also found here.

- South Bismarck, Solomon and Pacific. Convergence is the dominant plate motion at the interface between South Bismarck, Solomon and the Pacific plates. A deep oceanic trench south of New Britain Island and west of Bougainville Island marks the starting point of subduction of the Solomon Plate almost north-westward beneath South Bismarck and northeastward beneath the Pacific plate. There is a near-90° bend in the axis of the subduction at about 153° longitude and 5° latitude in the neighbourhood of the presumed triple junction. The rate of subduction is about 14 cm/yr (Tregoning, et al., 1998).

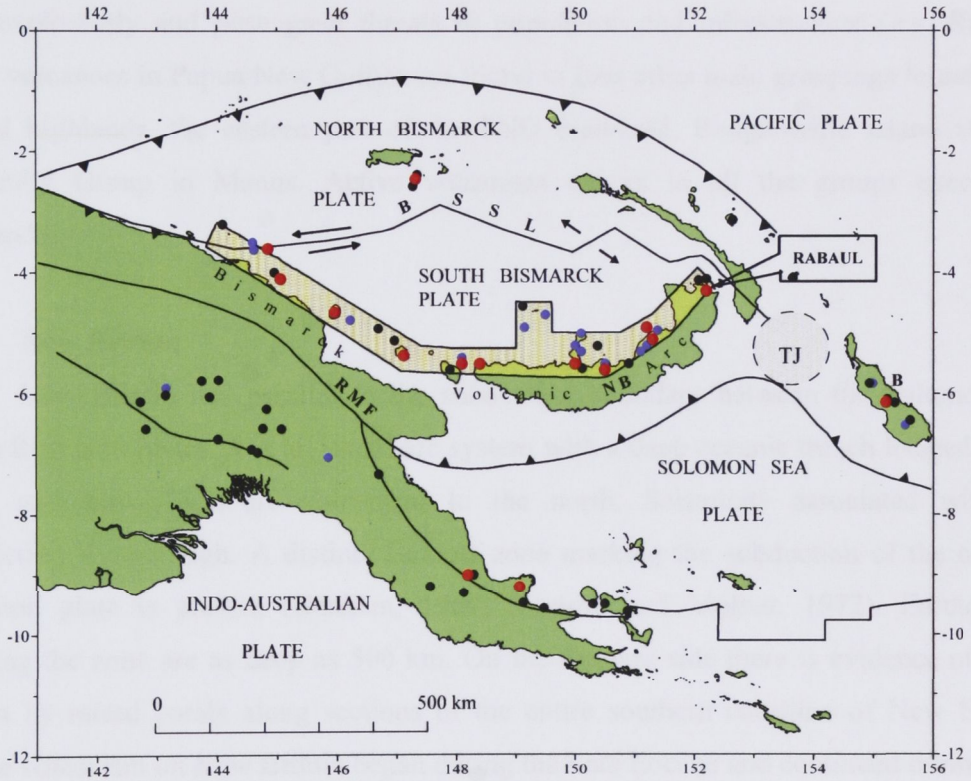

Fig. 2.1: Tectonic and volcanological map of Papua New Guinea showing the main and micro plates and their boundaries and distribution of volcanoes. The key for volcanoes is active (red circles), dormant (grey) and extinct (black). The Bismarck volcanic arc is marked by the bounded hatched region. The stippled circle marks the approximate location of the triple-junction (**TJ**). Others localities are, **BSSL** – Bismarck Sea Seismic Lineation; **MRF** – Markham-Ramu Fault; **NB** – New Britain and **B** – **B**ougainville. The location of Rabaul is marked on the map as well.

The occurrence of earthquakes along all these plate boundaries is very high. However, much more activity occurs at the subduction interface. Earthquake depths are shallowest at the North Bismarck-South Bismarck interface. They range between shallow and about 50km. At the Indo-Australian-Bismarck interface earthquake depths range between 0 and about 200 km. The deepest earthquakes are found at the subduction zone. A

distinct Benioff zone marking the rigid subducting lithosphere can be traced down to about 500 km from the earthquake locations.

In addition to the earthquake activity there is active volcanism in Papua New Guinea as well. The distribution of volcanoes is shown in Fig. 2.1. Most of the active volcanoes are located on the Bismarck Volcanic Arc System (BVAS). The arc system spans from Kadovar volcano in the northwest part of PNG to the Rabaul volcanic complex at the eastern tip of New Britain Island. Other prominent volcanoes in the chain include Manam, Karkar, Long Island, Langila, Pago, Lolobau and Ulawun. Many of these volcanoes erupt very frequently (e.g. Langila) and some of them erupt less frequently but very explosively and pose great threats to population and infrastructure (e.g. Rabaul). Other volcanoes in Papua New Guinea are found in four other main groupings found in the central highlands, the eastern part of the PNG mainland, Bougainville Island and the Admiralty Group in Manus. Active volcanism occurs in all the groups except the highlands.

2.1.2 New Britain

New Britain lies parallel to the subduction boundary between the Solomon and South Bismarck plates. It is an island arc system with a deep oceanic trench located to the south and active back-arc volcanism to the north. Seismicity associated with the subduction is very high. A distinct Benioff zone marking the subduction of the oceanic Solomon plate is present (Denham, 1969; Johnson and Molnar, 1972). Earthquakes marking the zone are as deep as 500 km. On the fore-arc side there is evidence of uplift shown by raised corals along sections of the entire southern coastline of New Britain. Active volcanism on New Britain began during the Late Eocene and continued during Late Oligocene and Mio-Pliocene (Dow, 1977; Lindley, 1988). The active back-arc volcanism and high seismicity places New Britain at the top end of the danger and risk listing for Papua New Guinea.

2.1.3 Gazelle Peninsula and its surroundings

Gazelle Peninsula is located on the eastern tip of New Britain. The geology and main structural features of the area are described in detail by various people, including Macnab (1970) who conducted the first systematic geological mapping of the area. Other people who have contributed to the understanding of the area include Wiebenga (1973), D'Addario et al. (1976), Dow (1977), Johnson (1979), Davies et al. (1984), and most

recent being Lindley (1988). All the authors point to the same synthesis that the Gazelle Peninsula is intensely fractured by a series of north-northwest trending faults (Fig. 2.2). Two of the fault systems that stand out are the Baining Mountain Horst and Graben Zone (or the Baining Fault System) and the Wide Bay Fault System (Fig. 1.3 in Patia, 2004). Initial interpretations by Macnab (1970) suggested the intense faulting is caused by compressional tectonic processes, however, Wiebenga (1973) suggested extensional tectonic forces as the cause for faulting based on seismic and gravity information. Later work by Lindley (1988) supports the latter.

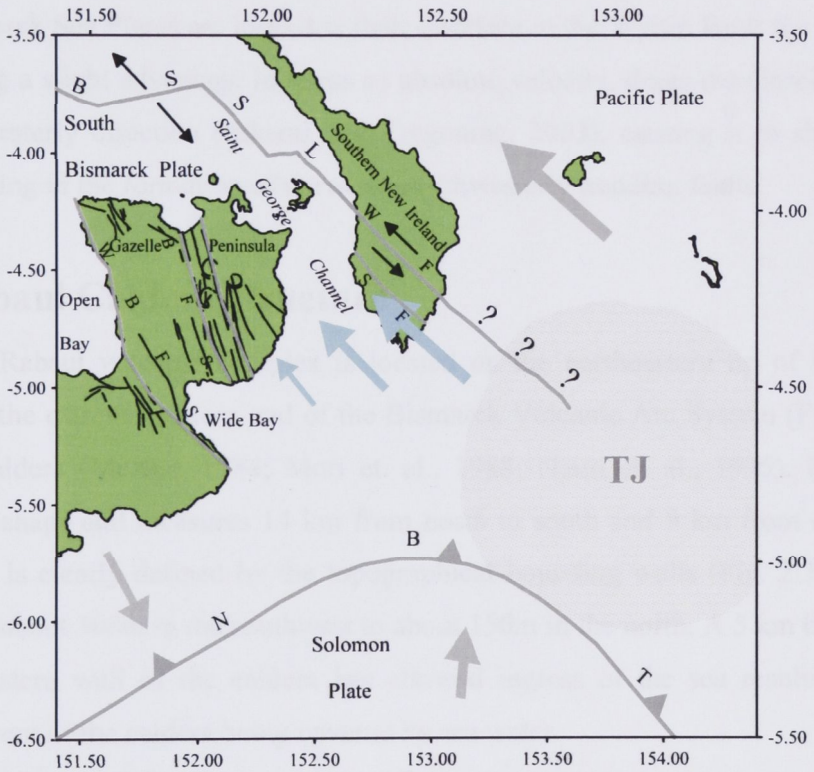

Fig. 2.2: Tectonic processes occurring near the triple junction of the Pacific-Solomon Sea-South Bismarck Sea Plate. TJ = Triple Junction – approximated by the grey shaded circle, NBT = New Britain Trench, BSSL = Bismarck Sea Seismic Lineation, WBFS = Wide Bay Fault System, BFS = Baining Fault System, WT = Weitin Fault, SF = Sapom Fault. The dark lines on the Gazelle Peninsula are faults. The black solid arrows indicate the direction of motion at the plate/fault boundary. The grey block arrows indicate the direction of plate motions. The blue-green block arrows on the southeast end of the St George Channel indicate the direction of motion for the Gazelle Peninsula during 'drag', when the two plates are locked at the interface.

To the east, not far from Gazelle Peninsula and on near-equal footing in terms of structural faulting, is the active region of the southern tip of New Ireland. This area features a couple of clearly mapped northwest trending faults namely, Weitin and Sapom. Both faults have lateral movement components just like the faults on Gazelle Peninsula.

The Weitin fault ruptured a couple of times during the last two decades (Mori, 1989; Itikarai and Tregoning, 2003). On the other hand major ruptures of faults on Gazelle Peninsula occurred only once in 1941 (Fisher, 1944). Gazelle Peninsula and the southern tip of New Ireland are separated by the Saint Georges Channel.

The close proximities of the southern New Ireland and the Gazelle Peninsula, and the similarities in the northwest trending faults in both places suggests there is probably a common northwesterly regional tectonic force driving the region. A suitable scenario depicting the whole situation is illustrated in Fig. 2.2. In fact the northwesterly motion of the two areas is justified by Tregoning et al. (2000). Simply, when the Pacific and the South Bismarck Sea Plates are locked at their interface at the Weitin Fault the rigid Pacific Plate, having a slight advantage in terms of absolute velocity, drags the Gazelle Peninsula in a northwesterly direction (Itikarai and Tregoning, 2003), causing it to shear at weak points resulting in the formation of the north-northwesterly trending faults.

2.2 Rabaul Caldera structure

The Rabaul volcanic complex is located on the northeastern tip of New Britain Island. It is the extreme eastern end of the Bismarck Volcanic Arc System (Fig. 2.1). It is an active caldera (McKee, 1984; Mori et. al., 1988; Nairn et. al., 1995). It is roughly elliptical in shape and measures 14 km from north to south and 9 km from east to west. The caldera is clearly defined by the topographical bounding walls (Fig. 2.3) varying in height from about 300m in the southwest to about 150m in the north. A 5 km breach on the east-southeastern wall of the caldera has allowed ingress of the sea resulting in about seventy percent of the caldera being covered by sea water.

Several small volcanoes have formed inside the caldera since the last major caldera-forming eruption 1400 years BP. These are Tavurvur, Vulcan, Rabalanakaia and Sulphur Creek. All these vents erupted during the last 200-300 years. The Beehive is another volcanic center inside the caldera but it is considered much older than the ones listed above. Outside the caldera there are three volcanic centers namely, Tovanumbatir, Kabiu and Turangunan. These vents are pre-1400. On the seafloor, there are few volcanic centers as well (Greene et al., 1986; Itikarai and McKee, 1990). Two lie between Vulcan and Dawapia and about four lie in the Blanche Bay area (Fig. 2.3).

Rabaul Town is located at the northern end of the caldera (Fig. 2.3), making it one of the most vulnerable towns in the world. It was severely damaged during the 1937 and

the 1941-1943 eruptions, as well as the events of World War II (WWII) between 1942 and 1945 (Johnson and Threlfall, 1985). However, following these events, the town was rebuilt and over subsequent years developed into one of the major towns of Papua New Guinea. Before the eruption in September 1994, Rabaul Town was the administrative center of East New Britain Province and its maritime port served as the hub of domestic and international shipping activities for the islands region of Papua New Guinea, due to its unique harbour setting. Before the eruption in 1994 the combined population of Rabaul Town and the surrounding villages was in the vicinity of about 60,000.

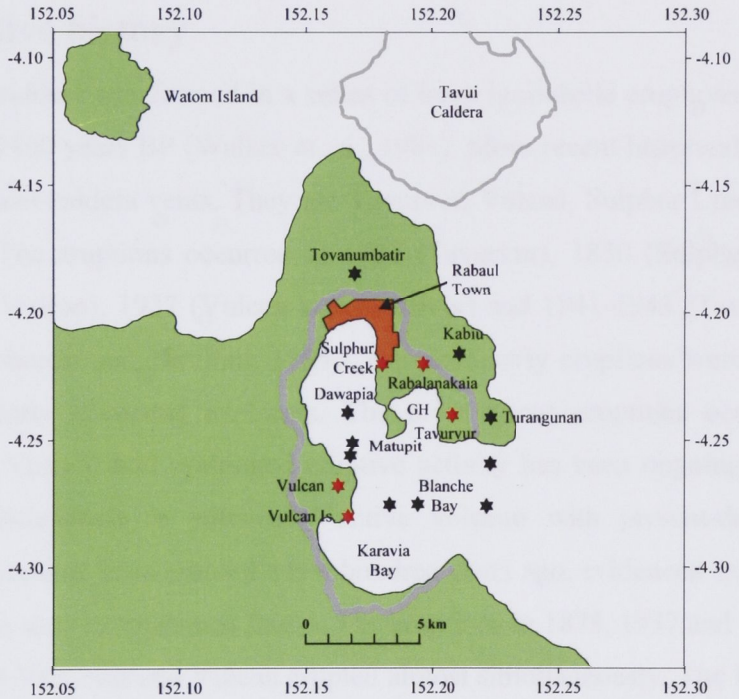

Fig. 2.3: Map showing the main structural features of Rabaul Caldera. The grey line marks the caldera margin based on the 100m contour. Volcanic centers are shown by the red (erupted in recent historical times or has active fumaroles at present time) and black (did not erupt in recent historical times) stars. GH is Greet Harbour. Tavui Caldera north of Rabaul Caldera is also marked. The boundary of the Tavui Caldera is based on the 500 m bathymetry contour.

The eruption destroyed about two-thirds of the town. After the eruption, the main administrative center for the province was moved to a new location in Kokopo (Blong and McKee, 1995), about 20 kilometers SE from Rabaul. The harbour still serves its pre-eruption role. Following the eruption the East New Britain Provincial Government sub-divided Rabaul Town into three sectors; sector one, two and three. Short-term developments have been occurring in sector one. Intermediate to long-term developments have been ear-marked for sector two. Sector three has been declared to remain

undeveloped. The undertaking by the Provincial Government is consistent with advice from scientists from RVO for limited development in Rabaul town in view of very high probabilities for future eruptions.

Immediately north of Rabaul Caldera is the recently mapped Tavui Caldera (Tiffin et al., 1990). The Tavui Caldera (Fig. 2.3) is a fully submerged submarine caldera. The deepest part is approximately 1100 m below mean sea level. There are no records of recent historical eruptions however geological studies have found eruptive material onshore and have attributed them to the Tavui Caldera (McKee, pers. comm.).

2.3 Eruptive history

Rabaul caldera was formed in a series of large ignimbrite eruptions. The last event is dated about 1400 years BP (Walker et. al., 1981). More recent historical eruptions have involved four post-caldera vents. They are Tavurvur, Vulcan, Sulphur Creek and possibly Rabalanakaia. The eruptions occurred in 1791 (Tavurvur), 1850 (Sulphur Creek), 1878 (Tavurvur and Vulcan), 1937 (Vulcan and Tavurvur) and 1941-1943 (Tavurvur) (McKee at. al., 1985; Johnson and Threlfall, 1985). The three early eruptions were witnessed and described by early European explorers. The most recent eruptions occurred in 1994 (Tavurvur and Vulcan) and prolonged eruptive activity has been ongoing between 1995 and 2005. Rabalanakaia, a potentially active volcano with present-day crater floor fumerolic activity may have erupted a few hundred years ago, evidenced by recent-looking lava flows on its west to southwest flanks. The eruptions in 1878, 1937 and 1994 were twin eruptions where Tavurvur and Vulcan erupted almost simultaneously. The limited eruption information is presented in Fig. 2.4. Fig. 2.4(a) plots the recurrence interval against the sequential order of the known eruptions and Fig. 2.4(b) has the year of eruption plotted against the same parameter as in Fig. 2.4(a). Here the recurrence interval, or sometimes known as the repose period, refers to the length of time in years between one eruption and the next. The sequence of eruption is the order in which the eruptions occurred, starting from the first reported eruption in 1767.

A number of things can be derived from Fig. 2.4. Firstly, Fig. 2.4(a) shows the recurrence interval data falls into three distinct clusters. They are 1.6, 26 and 58 years, respectively. The lower end of the scale of 1.6 years represents the ongoing eruptions that usually continue after a main event. Note that there are no such data for eruptions prior to 1937. There is only one data point associated with the 1937 eruption and three associated

with the 1994 eruption. The improvement in the increased data points is attributed to the improved record keeping and monitoring of eruptions. For purposes of long-term eruption forecasting this group is eliminated from the calculations because it is considered as part and parcel of the main eruption. The upper end of the scale of 58 years represents the twin eruption.

Fig. 2.4(b) presents three different plots. The first plot (filled blue circles) is for all the main recent historical eruptions. The second plot (filled red diamonds) is for the twin eruptions only and the third plot (filled green squares) is for all the eruptions, including the eruptions in cluster C in Fig. 2.4(a). Linear regression lines have been fitted to each plot so that the gradient for each fit represents an approximation for the recurrence interval for each dataset that has been considered. The three plots yield values of 46, 58 and 29 years, respectively. In a nutshell these results suggest the recurrence interval for main eruptions at Rabaul Caldera is anything between 29 and 58 years. It is about 58 years for the twin eruptions. These two values are not far from the values obtained for clusters **A** and **B** in Fig. 2.4(a).

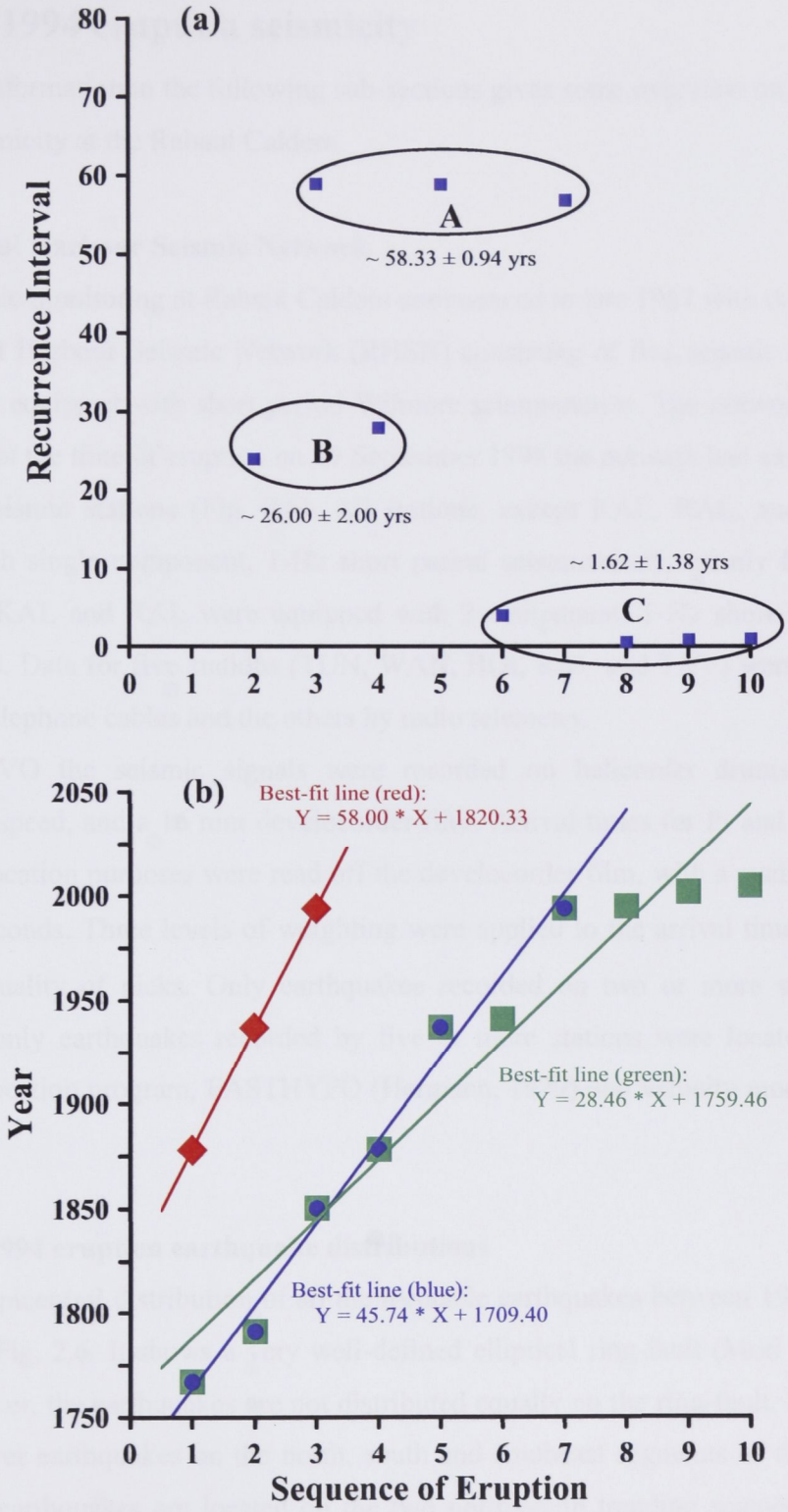

Fig. 2.4: Different ways of presenting the eruption data for Rabaul for the last 200-300 years. (a) Recurrence interval for Rabaul eruptions plotted against the sequential order of eruptions since the first known eruption in 1760. A, B and C denotes the three main groups that have emerged. (b) The year of eruption plotted against the sequence of eruptions. Green squares - all known eruptions since 1760; blue circles – the main eruptions only; Red diamonds - twin eruptions only. The green, blue and red lines are the best-fit linear regression lines for each plot.

2.4 Pre-1994 eruption seismicity

The information in the following sub-sections gives some overview on the pre-1994 eruption seismicity at the Rabaul Caldera.

2.4.1 Rabaul Harbour Seismic Network

Seismic monitoring at Rabaul Caldera commenced in late 1967 with the installation of the Rabaul Harbour Seismic Network (RHSN) consisting of five seismic stations. The stations were equipped with short period Wilmore seismometers. The network developed over time so at the time of eruption on 19 September 1994 the network had expanded to 14 permanent seismic stations (Fig. 2.5). All stations, except KAL, RAL, and VPT were equipped with single component, 1-Hz short period seismometers, mainly Mark L-4C's and S-13's. KAL and RAL were equipped with 3-component, 1-Hz short period Mark seismometers. Data for five stations (TUN, WAN, BOI, RAL and TAV) were transmitted to RVO by telephone cables and the others by radio telemetry.

At RVO the seismic signals were recorded on helicorder drums running at 180mm/min speed, and a 16 mm develocorder film. Arrival times for P- and S-waves for earthquake location purposes were read off the develocorder film, with a reading accuracy of ± 0.01 seconds. Three levels of weighting were applied to the arrival time readings to reflect the quality of picks. Only earthquakes recorded on two or more stations were logged and only earthquakes recorded by five or more stations were located using the earthquake location program, FASTHYPO (Hermann, 1979) and velocity model shown in Table 2.1.

2.4.2 Pre-1994 eruption earthquake distributions

The epicentral distribution of all the locatable earthquakes between 1971 and 1994 is shown in Fig. 2.6. It shows a very well-defined elliptical ring-fault (Mori and McKee, 1987), however, the earthquakes are not distributed equally on the ring-fault. For instance, there are fewer earthquakes on the north, south and southeast segments of the ring-fault. Most of the earthquakes are located on the two north-south trending segments on either side of the ring-fault. The depth of the earthquakes range between shallow and 5 km. East-west cross-sections of the seismicity through the central part of the caldera show outward dipping planes (Mori and McKee, 1987), however they also acknowledged inward dipping planes as well at some sections of the ring-fault.

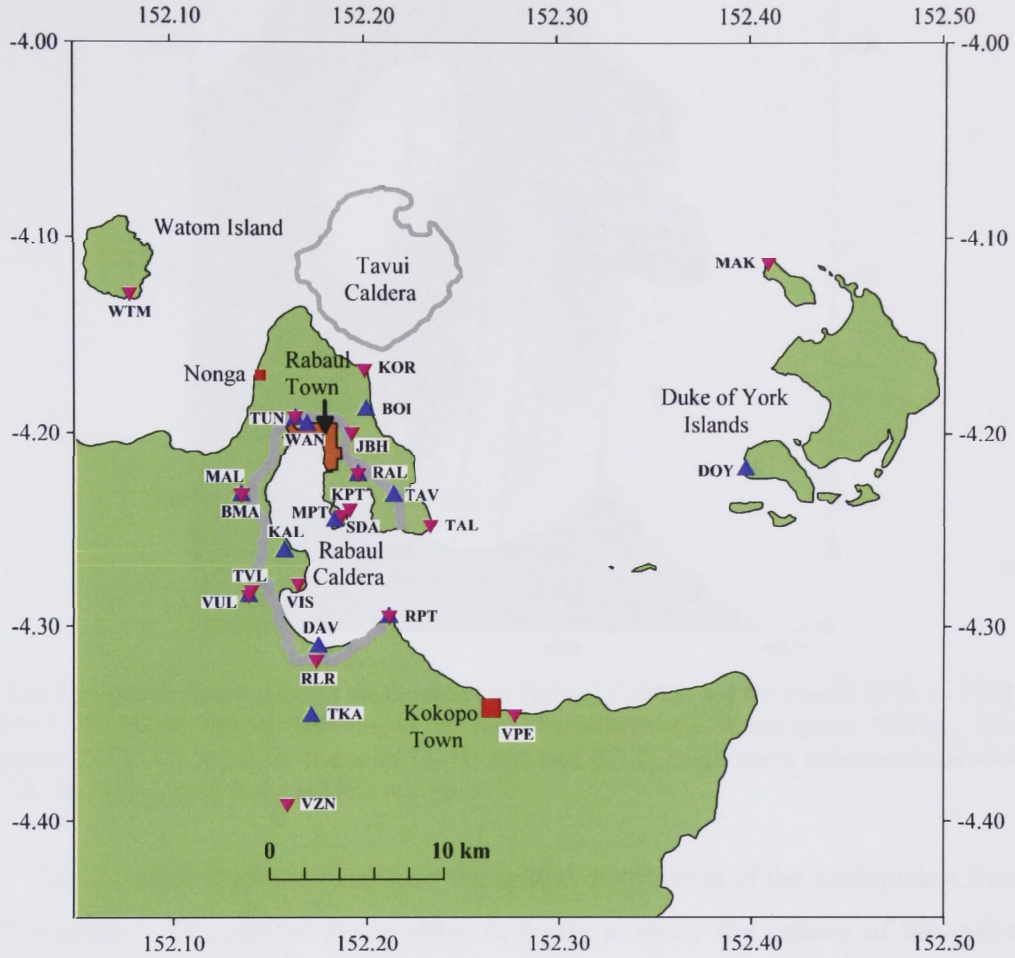

Fig. 2.5: Rabaul Harbour Seismic Network (RHSN). Blue Triangles are pre-1994 eruption seismic stations and inverted pink triangles are post-1994 eruption seismic stations. Note that some of the post-eruption seismic stations are retained at the pre-eruption sites to maintain continuity.

Table 2.1: Current 1-D velocity model used by RVO for earthquake locations.

Layer	Depth (km)	V_p (km/s)
1	0.00	1.70
2	0.25	2.06
3	0.50	2.43
4	0.75	2.79
5	1.00	3.15
6	1.25	3.51
7	1.50	3.88
8	1.75	4.24
9	2.00	4.60
10	4.00	6.11

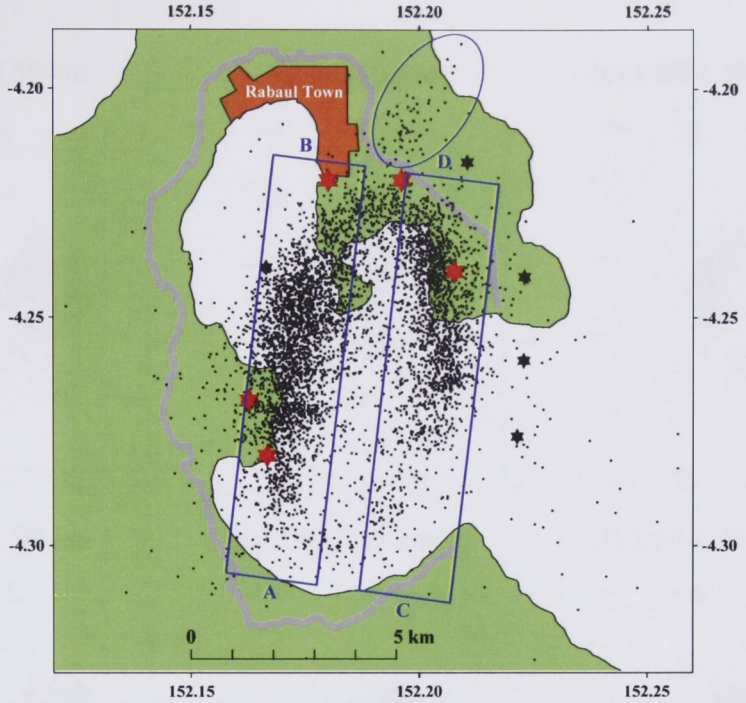

Fig. 2.6: Epicentral distribution of earthquakes at Rabaul Caldera for the period 1971 to 1994 from the RVO catalogue. Events surrounded by the blue ellipse are pre-eruption NEEqs. The blue rectangles define the areas for the west (A-B) and east (C-D) north-south cross-sections shown in Fig. 2.8. The grey curve is the caldera margin.

In this study I have re-examined the spatial distribution of the earthquakes from the RVO catalogue. The aim of the exercise is firstly to study the pattern of the epicentral distribution with increasing depth, and secondly to examine in detail the north-south cross-sections of the two north-south trending segments on either side of the ring-fault shown by the strong clustering of earthquakes. Unlike the EW-sections, the N-S sections have not been given much attention in previous studies. In order to conduct the first task the earthquakes have been divided into eight bins of 0.5 km depth slices and one of 1.0 km as follows; 0.0-0.49 km, 0.5-0.99 km, 1.0-1.49 km, 1.5-1.99 km, 2.0-2.49 km, 2.5-2.99 km, 3.0-3.49 km, 3.5-3.99 km, 4.0-5.0 km. The resulting information is displayed in the series of plots in Fig. 2.7.

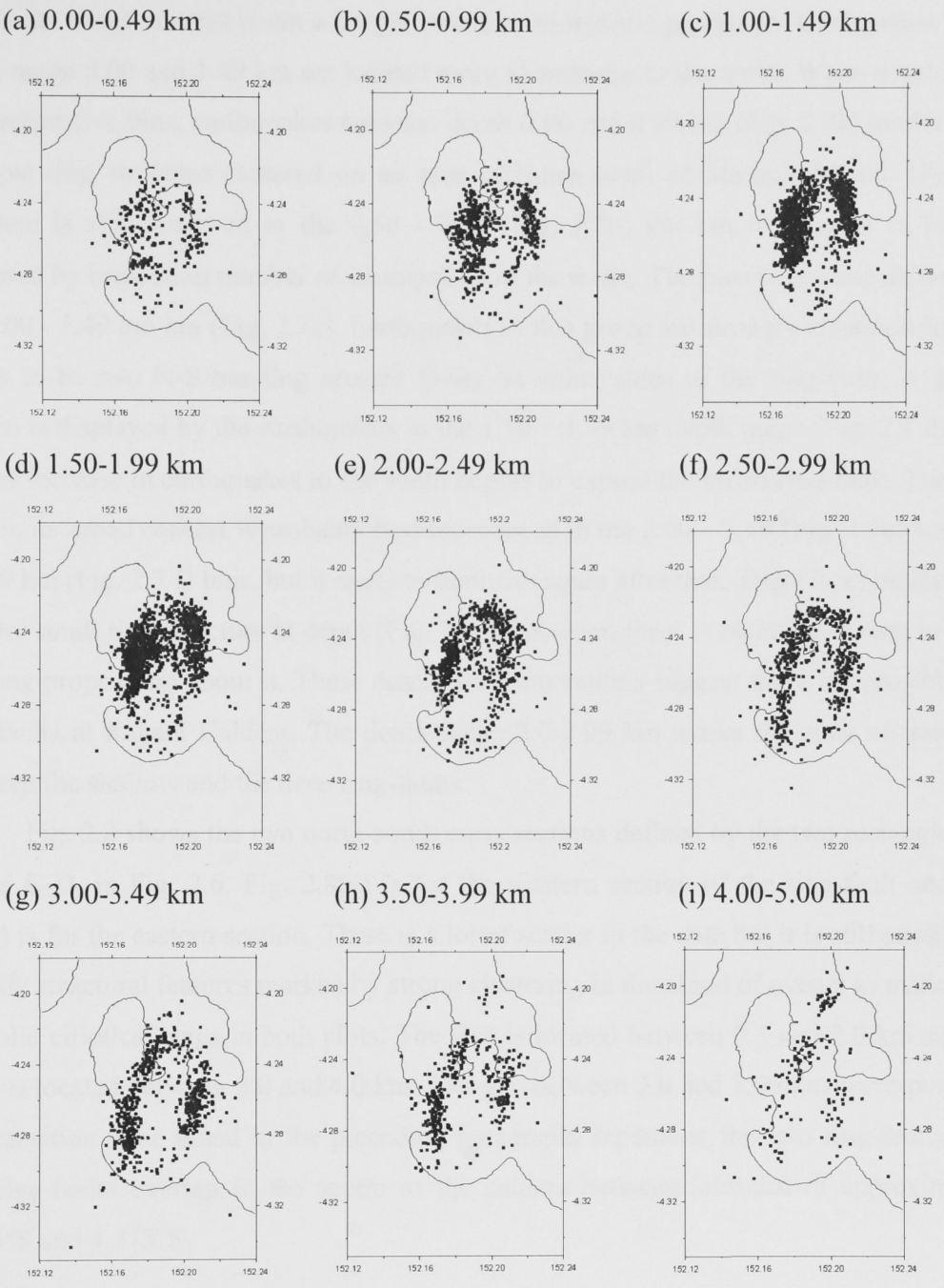

Fig. 2.7: Epicenter plots in 0.5 km depth bins from the RVO catalogue. (a) 0.00-0.49 km, (b) 0.50-0.99 km, (c) 1.00-1.49 km, (d) 1.50-1.99 km, (e) 2.00-2.49 km, (f) 2.50-2.99 km, (g) 3.00-3.49 km, (h) 3.50-3.99 km, (i) 4.00-5.00 km.

Generally the distribution of epicenters for each bin is different suggesting the ring-fault in its broad context is not a simple structure as initially perceived. Earthquakes in the depth range 0.00 and 1.49 km are located more abundantly to the north. When divided into their respective bins, earthquakes between depth 0.00 and 0.49 km (Fig. 2.7a) tend to form a vague ring structure centered on an area offshore south of Matupit Island. This ring structure is still observed in the 0.50 - 0.99 (Fig. 2.7b) km bin but begins to become obscured by increasing number of earthquakes to the south. The picture is quite different in the 1.00 - 1.49 km bin (Fig. 2.7c). Earthquakes in this group are strongly clustered on what seems to be two N-S-trending arcuate faults on either sides of the ring-fault. A similar pattern is displayed by the earthquakes in the 1.50 – 1.99 km depth range (Fig. 2.7 d) but a further increase in earthquakes to the south begins to expose the broad ring-fault. The ring-fault in its broad context is probably best reproduced in the 2.00 – 2.49 (Fig. 2.7e) and 2.50 – 2.99 km (Fig. 2.7 f) bins, but it starts to diminish again after that. There is a possibility of another small ring structure at depth (Fig. 2.7i), however, there is insufficient data to make a strong proposition about it. These descriptive annotations suggest there are possibly two ring-faults at Rabaul Caldera. The depth range 2.0-2.99 km marks the zone of transition between the shallow and the deep ring-faults.

Fig. 2.8 shows the two north-south cross sections defined by the two rectangles, A-B and C-D, in Fig. 2.6. Fig. 2.8(a) is for the western section of the ring-fault and Fig. 2.8(b) is for the eastern section. There is a lot of scatter in the data but it is still possible to identify structural features marked by strong clustering in the cloud of events as marked by the solid elliptical rings in both plots. The first is located between 0.5 and 2.0 km and the other is located between 3.0 and 4.0 km. The gap between 2.0 and 2.99 km corresponds to the transition zone noted in the preceding paragraph, separating the two ring-faults. The two ring-faults overlap in the centre of the caldera between latitudes of approximately 4.245°S and 4.275°S.

2.4.3 The double ring-fault

The systematic synthesis of the spatial distribution of the pre-1994 eruption earthquakes at Rabaul Caldera suggests that the elliptical ring-fault proposed by Mori and McKee (1987) is not a single but a pair of ring-faults. The two ring-faults were previously reported by Jones and Stewart (1997). Note that these outcomes are purely from re-processing the hypocenter solutions from the RVO earthquake catalogue. Jones and Stewart (1997) used the collapsing method. No re-locations were involved in both cases so

the outcomes do not reflect velocity changes. At this juncture it is worth mentioning that one main component of the present study is to re-locate these earthquakes. Details of this are given in Chapter 5.

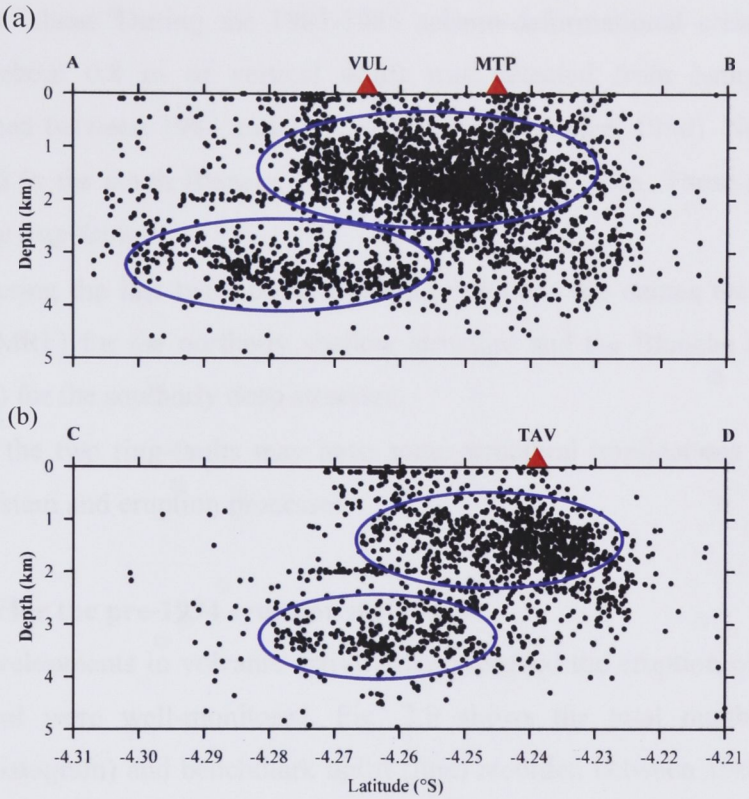

Fig. 2.8: (a) North-south cross-section on the west side of the ring-fault marked by the rectangle A-B in Fig. 2.6. (b) North-south cross-section on the east side of the ring-fault marked by the rectangle C-D in Fig. 2.6. Note the line of earthquakes at about 0.1 and 2.0 km on both plots. They are attributed to the 1-D velocity model. The blue ellipses in each plot marks strong clustering of events marking the approximate positions of the two ring-faults proposed in this study based on the original RVO solutions. The positions of Vulcan (VUL), Matupit (MTP) and Tavurvur (TAV) are marked by the red triangles.

Nonetheless if the two ring-faults actually exists some useful structural interpretation about the caldera are:

- The two ring-faults may have some association with some of the caldera forming eruptions that formed the exotic Rabaul harbour. The last event is dated about 1400 yrs BP (Walker, 1981).
- The locations of the two ring-faults may have some connection with the distribution of the volcanic centres. For instance, the positions of volcanic vents that erupted in

recent historical times and most of the submarine vents nearly coincide with the shallow ring-fault.

- Furthermore most of the active surface deformation since measurements began in 1970's has seemed to focus within the area of the shallow ring-fault centered near Matupit Island. During the 1983-1985 seismo-deformational crises (Mori et al., 1988) about 0.8 m of vertical uplift was detected from bathymetric studies conducted between 1984 and 1985 (Itikarai and McKee, 1990). No changes were detected in the south Blanche Bay and Karavia Bay areas. These areas lie within the deep ring-fault.
- Considering the last two points, this study propose the names the Matupit Ring-Fault (MRF) for the northerly shallow structure and the Blanche Bay Ring-Fault (BBRF) for the southerly deep structure.
- Lastly, the two ring-faults may have some structural implications for the caldera fault system and eruption processes.

2.4.4 Trends for the pre-1994 eruption activity

The developments in volcanic activity that preceded the eruption of 19 September 1994 at Rabaul were well-monitored. Fig. 2.9 shows the total number of monthly earthquakes (histogram) and benchmark uplift (line) recorded between 1968 and the 1994 eruption. The total monthly earthquakes include only events recorded on two or more seismic stations. The data was read from the 16 mm develocorder film. The entire period of activity is divided into five main periods based on the pattern of the seismicity and uplift. They are as follows:

- Period 1: 1968 – Oct 1971
- Period 2: Nov 1971 – Aug 1983
- Period 3: Sep 1983 – Jul 1985
- Period 4: Sep 1985 – Apr 1992
- Period 5: May 1992 – Sep 1994

A brief summary of activity for each Period is described below.

Period 1: 1968 – Oct 1971

Period 1 covers the first three years of activity since seismic monitoring commenced at Rabaul Caldera. Clearly it shows a very low level of activity. The seismicity during this period is characterized by small discrete volcano-tectonic earthquakes. Monthly earthquake totals ranged between 20 and 100.

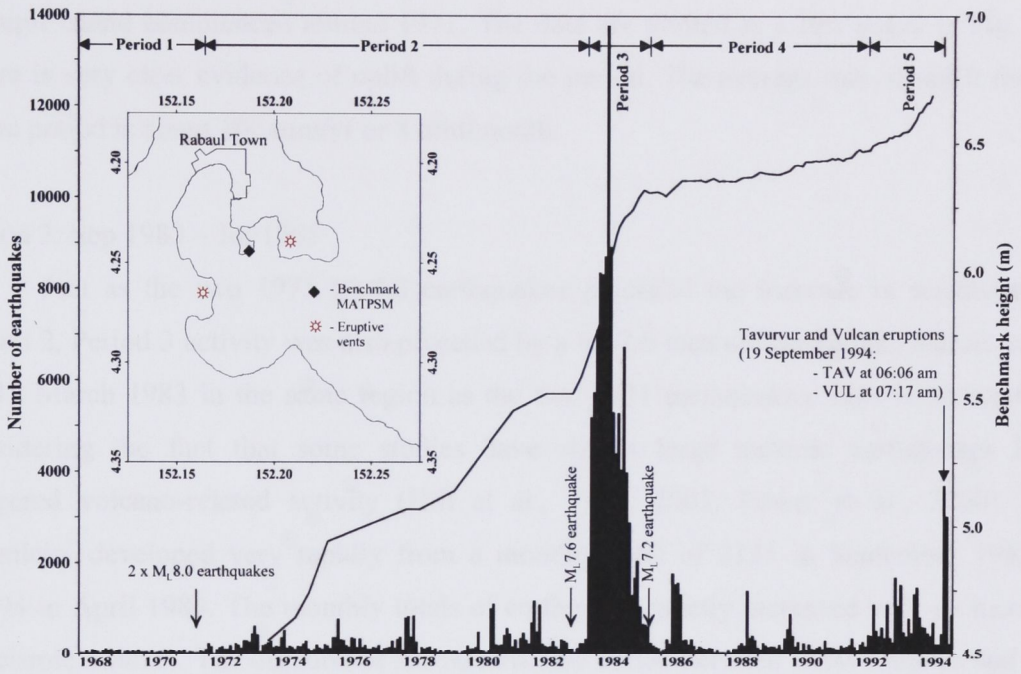

Fig. 2.9: Monthly total earthquakes (histogram) and uplift (line) between 1968 and 1994. The uplift was measured at a benchmark on Matupit Island (map inset). The activity for the entire period is divided into five periods as marked by the horizontal arrows and labels on the upper part of the plot.

Period 2: November 1971 – August 1983

Period 2 began about three months after the occurrence of two large M_L8.0 tectonic earthquakes near the Solomon Sea-Bismarck-Pacific Plate triple junction in the north Solomon Sea on 14 and 26 July 1971 (Everingham, 1975). Seismic swarms began to emerge during this period. A seismic swarm refers to the occurrence of strings of earthquakes over a very short period of time. The interval between any two earthquakes can be as small as a few seconds apart. A seismic swarm can be likened to earthquake aftershocks after a major tectonic earthquake. The difference is a seismic swarm is not necessarily triggered by a bigger earthquake.

Uneven periodic episodes of anomalously high seismicity are evident during the period. These episodes of high seismicity are associated with seismic swarms.

Furthermore, these episodes varied in duration between 13 and 26 months. The total number of monthly earthquakes during Period 2 range between 10 and 1200. The largest recorded earthquake of M_L5.2 for Rabaul caldera occurred during this period in October 1980. A comparable earthquake with M_L5.1 was also recorded during this period in March 1982.

Surface deformation measurements on a leveling benchmark on the southern end of Matupit Island commenced around 1971. The data are plotted as a line graph in Fig. 2.9. There is very clear evidence of uplift during the period. The average rate of uplift for the entire period is about 100 mm/yr or 8 mm/month.

Period 3: Sep 1983 – Jul 1985

Just as the two 1971 M_L8.0 earthquakes preceded the increase in seismicity in Period 2, Period 3 activity was also preceded by a M_L7.6 tectonic earthquake that occurred on 18 March 1983 in the same region as the two 1971 earthquakes. This is not unusual considering the fact that some studies have shown large tectonic earthquakes have triggered volcano-related activity (Hill et al., 1993, 2002; Power et al., 2000). The seismicity developed very rapidly from a monthly total of 2135 in September 1983 to 13794 in April 1984. The monthly totals of earthquake greatly increased with an increase in seismic swarms. The duration of seismic swarms varied between a few minutes and few hours. A seismic swarm that produced 150 or more events and recorded on four or more seismic stations within a 24-hour period was considered 'a seismic crisis' (Mori et. al., 1988). Based on these criteria a total of 25 seismic crises were registered. The daily earthquake totals ranged between 151 (13 July 1984) and 485 (22 April 1984). They were distributed in all sections of the caldera ring-fault, with more of them occurring in the northeast section. The largest earthquake recorded during Period 3 had a magnitude of M_L5.1. It occurred during the 3 March 1984 seismic crisis. Many earthquakes were felt by residents of Rabaul Town and nearby villages during this period and fear of an eminent eruption forced some residents of Rabaul Town to evacuate voluntarily. There was no eruption. Seismic activity declined fairly rapidly and reached pre-September 1983 levels by July 1985.

Significant co-seismic vertical surface deformation was measured on the benchmark located at the southern end of Matupit Island during Period 3 as shown by the deformation plot (Fig. 2.9). The total uplift for the entire period is about 760 mm. This

translates into about 415 mm/yr or 35 mm/month. This rate of deformation tapered off in July 1985.

Due to the rapid acceleration of seismicity and surface deformation and the prospect for an imminent eruption, Period 3 was dubbed the 'Rabaul seismo-deformational crisis' (Mori et al., 1988).

Period 4: Sep 1985 – Apr 1992

Activity subsided to pre-crisis level (Period 2) after July 1985. Interestingly, two M_L7.2 earthquakes occurred in May and July 1985 (Mori et al., 1987; Mori, 1989) at the time the activity was on the decline. The May earthquake occurred about 100 km southwest of Rabaul in central New Britain and the July earthquake occurred about 60 km east of Rabaul. The triggering effect of these earthquakes on the volcanic activity is probably the marginal increase in seismicity in April 1986 and the subsequent few months. Apparently this activity is dwarfed by the seismo-deformational crisis activity.

During Period 4 the seismicity fluctuated at comparable levels to Period 2. Seismic swarms were still evident but the total event numbers were not sufficient to qualify any as a 'seismic crisis'. Rates of vertical uplift at the concerned benchmark reduced significantly as well. The average rate of uplift during Period 4 is approximately 2 mm/month.

Period 5: May 1992 – Sep 1994

Period 5 could be considered as part of Period 4, however, it has been separated for three main reasons. Firstly, the total number of monthly earthquakes is marginally higher than the totals for Period 2 and Period 4. Secondly, this marginal increase is maintained for an extended period of about two years. Lastly, there is an increase in the rate of measured uplift coinciding with the marginal increase in seismicity in May 1992. A further increase in the rate of uplift is evident in August 1993. This rate of uplift is maintained to April 1994, the last time leveling measurements were conducted before the eruption occurred. The average rate of uplift between May 1992 and August 1993 is about 6 mm/month, and between August 1993 and April 1994 the rate is about 16 mm/month. The average rate for the entire period is approximately 9 mm/month.

A significant feature during this period is the occurrence of a seismic swarm of high frequency volcano-tectonic earthquakes northeast of the caldera and well away from the ring-fault. The locatable earthquakes from this seismic swarm are plotted in Fig. 2.6, and marked by the blue ellipse. The strongest earthquake had a magnitude of M_L4.7.

Incidentally, the occurrence of these earthquakes coincided with the increased trend of uplift during the same month, as mentioned earlier.

2.5 1994-2005 Tavurvur eruption

The eruption at Rabaul Caldera between 1994 and 2005 can be divided into four main phases. The break-down is based on the cessation and resumption of eruptions during the period. The duration of cessation has to be greater than three months in order for the resumption of eruption to qualify as a new phase of eruption. The four phases are as follows:

- Phase 1: September 1994 – April 1995
- Phase 2: November 1995 – September 2001
- Phase 3: October 2002 – February 2004
- Phase 4: January 2005 – December 2005

This breakdown is different from Patia (2004) where he listed only two phases between 1994 and 2003. The Phase 1 identified in this study is the same as the Phase 1 of Patia (2004). However Phase 2 and 3 identified in this study falls into a single phase, Phase 2, in the work of Patia (2004).

I present brief overviews of the eruptive activity for each phase in the following sections. Additional information is available in the various GVN reports, Blong and McKee (1995), and Lauer (1995).

2.5.1 Phase 1: September 1994 – April 1995

Phase 1 includes the initial onset of the eruptions from Tavurvur and Vulcan on 19 September 1994. Tavurvur erupted first at about 06:06 a.m. Vulcan eruption followed later at about 07:17 a.m.

The eruption from Tavurvur was almost noiseless with very billowing cauliflower-shaped dark ash clouds that rose slowly to a few hundred meters before they were quickly driven in a northwesterly direction toward Rabaul Town by moderate southeast winds (BGVN). Within an hour after the eruption the low moving ash clouds brought darkness over Rabaul Town. The intensity of the eruption gained momentum with increased ashfall, and became noisier at the same time with low rumbling noises as time progressed. During

the ensuing few days a moderate volume of ash fell, most of it in a narrow northwesterly corridor (compared to Vulcan ash deposits) that passed through Rabaul Town. In the main part of town the ash thickness was about 70 cm. Ash deposited on roofs of buildings turned into mud after some precipitation causing many buildings within the first several kilometers of Tavurvur to collapse from the added weight (Blong and McKee, 1995). The eruption column from Tavurvur reached a maximum height of about 6 km. After the first week the eruption began to exhibit a slow decline. The pattern of eruption also changed from subcontinuous ash emissions to vulcanian-type activity with reduced ash content. Projections of incandescent lava fragments were clearly visible at night. Fluctuating vulcanian activity exhibiting further decline continued until the eruption ceased on 16 April 1995. Besides the ash, Tavurvur also produced a small volume of lava flow on its western flank.

The eruption at Vulcan was more powerful and explosive. Soon after the initial onset the eruption changed into a strong phase of plinian activity sending a thick column of eruption cloud well into the stratosphere. It reached a maximum height of approximately 20 km. Small pyroclastic surges were produced at the base of the eruption column and upon entering the sea they generated a small localized tsunami (Nishimura et al., 2005). Ash deposits from Vulcan were more widespread than Tavurvur. Ash from Vulcan appeared much lighter in colour compared to the darkish colour of Tavurvur ash. The eruption at Vulcan ceased on 2 October 1994. A similar explosive and short-lived eruption was also observed during the 1937 Vulcan eruption.

2.5.2 Phase 2: November 1995 – September 2001

Renewed eruptive activity resumed at Tavurvur on 28 November 1995 after seven months of inactivity. It marked the beginning of Phase 2. The eruption was preceded by weak roaring sounds. The initial activity consisted of forceful emissions of gas and dark ash at 2-6 minute intervals. After that it changed into a long-term pattern of activity characterized by irregular vulcanian eruptions where ash emissions occurred at intervals ranging between minutes during high activity, and hours during very subdued activity. Sometimes the activity became highly energized with powerful explosions.

The highlight of activity in Phase 2 is eight strombolian eruptions that occurred on 11 May 1996, 4 October 1996, 9 January 1997, 14 March 1997, 12 April 1997, 1 June 1997, 11 July 1997 and 17 August 1997. Strombolian eruptions are full of energy characterized by very frequent powerful explosions that produce strong airwaves. At the

peak of these eruptions the rate of explosions can be one per second. The explosions can drive bright incandescent lava fragments tens of meters into the atmosphere above the erupting vent and hundreds of meters away from the vent laterally. Usually ash content is very low. The eruptions in October 1996 and January, March and April 1997 produced a significant volume of lava and buried much of the original land surface south of Tavurvur. The accumulated volume of lava is considered to be the greatest in any one series of eruptions in the last few hundred years. The behaviour and the pattern of the strombolian eruptions are best demonstrated by the RSAM plots in Fig. 2.10 and the series of plots in Appendix A. RSAM (Endo and Murray, 1991) stands for Real-time Seismic Amplitude Measurements and as the name says it, it is a real-time monitoring tool that keeps track of the changes in seismic amplitudes. The RSAM data plotted is the average amplitude of the seismic signal over a 10 minute period recorded on KPT station. KPT is located about 2.0 km west from Tavurvur volcano. In plots the lowest values correspond to the background seismic noise and individual spikes correspond to one or more events, usually explosions, during the 10-minute window. It is obvious from Fig. 2.10 and the series of plots in Appendix A that the build-up of strombolian eruptions can be very rapid as soon as they begin however, the tail end of the eruption can vary a lot. Sometimes the eruption can taper off very quickly (Fig. A-1 in Appendix A) and at other times they can drag on longer for many more hours (Fig. A-3 in Appendix A). Another characteristic about the strombolian eruptions is the transition between the start and the peak of the activity is not always constant. Sometimes the build-up of a strombolian eruption to its peak is punctuated by episodes of high and low activity as portrayed in Fig. 2.10.

Besides the strombolian eruptions, other notable activity during Phase 2 is the sustained ash eruptions in September and October 2000 over a two to three weeks period. The periods marking intense ashing during this activity were recorded as continuous non-harmonic volcanic tremors on the helicorders. A significant volume of ash fell during the period and probably exceeded the total volume of accumulated ash since the eruption resumed in November 1995. Most of the ash from this activity was deposited within a few kilometers from Tavurvur in a northwesterly direction, which also covered Rabaul Town.

Since the 17 August 1997 strombolian eruption, and apart from the September/October 2000 activity, fluctuating vulcanian eruptive activity persisted at Tavurvur until September 2001. Eruptions ceased once more in September to mark the end of Phase 2.

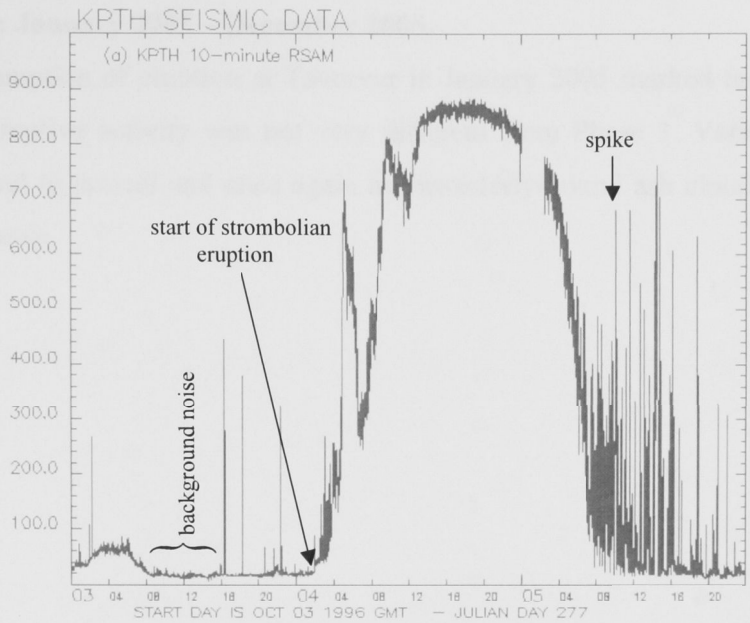

Fig. 2.10: RSAM (Real-time Seismic Amplitude Measurements) plot for KPT station for the 4 October 1996 strombolian eruption. The time axis is Universal Time (UT). Note the episodic up and down of activity during the build-up to the peak of activity. With the benefit of hindsight, the flat plateau at the peak of the activity is associated with lava flow.

2.5.3 Phase 3: October 2002 – February 2004

The activity during Period 3 was not as eventful as Period's 1 and 2. However during the initial weeks of the eruption constant ash eruptions blowing to the southeast affected the Provincial airport resulting in the suspension of flight services for about one-two weeks. After that the activity subsided and for most part of the period it was characterized mainly by variable vulcanian activity consisting of discrete ash-laden explosions. During high activity the vulcanian explosions occurred within minutes of each other and at times of low activity the frequency was much longer. Thick columns of dark ash clouds from the explosions reached between couple of hundred meters to two km above the summit before they were blown to directions determined by prevailing winds. The southeasterly winds prevailed between May and October and the northwesterly winds prevailed between November and April. Northwesterly-bound ash clouds continually affected the population of Rabaul Town. This activity was interspaced by quiet periods of days and sometimes as long as one-two weeks, and marked by weak emissions of white vapour only of variable amounts, or without any emissions at all.

2.5.4 Phase 4: January 2005 – December 2005.

The resumption of eruption at Tavurvur in January 2005 marked the beginning of Phase 4. The eruptive activity was not very different from Phase 3. Variable vulcanian activity continued to prevail and once again northwesterly-bound ash clouds continued to affect Rabaul Town.

Chapter 3

The post-1994 eruption seismicity at Rabaul caldera

3.1 Post-1994 eruption seismic monitoring

Effective seismic monitoring at the Rabaul Caldera came to a halt several hours after the onset of the twin eruptions after 90% of the RHSN was destroyed by thick ash fallout. Only three seismic stations located upwind from the erupting volcanoes were spared, and they were used to track the number and type of earthquakes that continued to occur during the eruption, but the reduced network was not ideal for locating the hypocenters. Then almost three weeks after the destruction of the seismic network and ultimately the general monitoring capabilities of RVO, the United States international aid agency came to the assistance of RVO through the United States Geological Survey Volcano Disaster Assistance Program (VDAP). A new seismic network consisting of eight stations was re-established (Fig. 2.5 in Chapter 2), and by 10 October 1994 full seismic monitoring was restored. For purposes of continuity some of the stations were re-established at the old sites and others were relocated to new sites. Except for RAL and VIS stations all the sites had single component, short period (1Hz) Mark seismometers. RAL and VIS sites had short-period 3-component Mark seismometers. The installation also included a few electronic tiltmeters to monitor surface deformation. Further improvements to the seismic network were undertaken between 1997 and 2000 under a major AusAID-funded aid program for RVO. The improvements included upgrades to the equipment and strengthening of the post-eruption network with four additional seismic stations located outside the main caldera array (Fig. 2.5). Three of these sites were equipped with 3-component, short period Mark seismometers. The installation of the stations away from the main array increased the aperture of the network and thus improved location for events away from the caldera.

The signals from these field sites were transmitted as analogue signals to the base at RVO by radio telemetry. At the base the signals were recorded on helicorder papers and, for the first time, a newly installed PC-based data acquisition system. The data acquisition system had an 8-bit AD card that converted the analogue signals to digital signals at a sampling rate of 100 samples per second. The AD card was later upgraded to a 16-bit card. The installation of the new data acquisition system enabled seismogram readers at RVO to process earthquake data much faster than for the old pre-eruption data processing system.

3.2 The post-1994 eruption seismicity

The seismic activity at Rabaul Caldera changed dramatically soon after the eruption began and thereafter. The change became obvious soon after full seismic monitoring was restored in October 1994 and earthquake locations resumed. The epicenter and depth distribution for the earthquakes recorded between October 1994 and December 1998 are shown in Fig. 3.1. Only earthquakes recorded on five or more stations and having horizontal and vertical uncertainties of less than 1.0 km are plotted. The following sections describe some general aspects of the types of post-eruption seismicity. Note that the scope of this study does not extend to modeling of the generation of the earthquakes concerned.

3.2.1 Volcano-tectonic Caldera ring-fault seismicity

The most prominent change about the post-eruption seismicity is the lack of it inside the caldera, but more interestingly on the active elliptical ring-fault. Before the eruption in September 1994 all the earthquakes associated with the ring-fault were high frequency or volcano-tectonic (VT) earthquakes. These events are volcano-tectonic because the cause and the stress conditions in which they occur are similar to normal tectonic earthquakes. Studies of volcanic earthquakes in general and more specifically VT earthquakes (Minakami, 1960; Chouet, 1979; Shaw, 1980; Weaver et al., 1981; Takeo, 1983) have attributed the occurrence of VT earthquakes to regional or local tectonic forces acting on the medium surrounding a magma source. The more macro- or micro- local tectonic forces in the volcanic environment can be driven by magma intrusion, withdrawal, cooling or any of the combinations caused by thermal, volumetric or indirect geochemical changes in the magma body, gravitational loading, pore-pressure effects and hydrofracturing.

Unlike the pre-eruption seismicity where at least a handful of earthquakes or more were recorded each month, during the post-eruption period between October 1994 and December 2005 the total number of VT earthquakes that occurred inside the caldera is significantly low. Most of these earthquakes occurred between 1994 and 1996. Notable concentrations of these earthquakes are located on the southern and western parts of the ring-fault (Fig. 3.1).

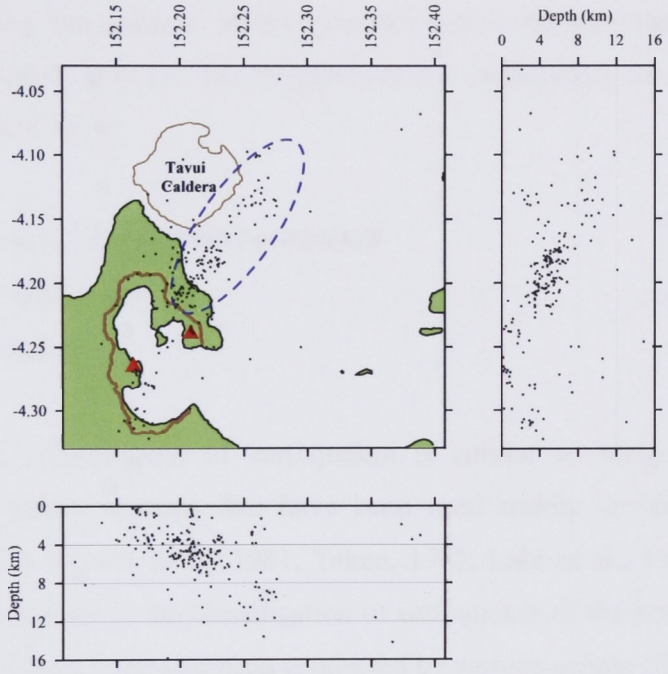

Fig. 3.1: Hypocenter distribution of earthquakes for the post-eruption period between October 1994 and December 1998. Only earthquakes recorded on five or more stations and having horizontal and vertical uncertainties of less than 1.0 km are plotted. The earthquakes surrounded by the ellipse are the northeast earthquakes (see text below).

The lack of VT earthquakes in this previously active area, and especially the ring-fault, can probably be explained by the relaxation of this once over-pressurised caldera system after the eruption of approximately 0.4 km^3 of material.

The VT earthquakes that occurred between late 1994 and 1996, immediately after the main eruption, are most likely the result of structural re-adjustment of the caldera fault system following the release of the erupted material noted above rather than due to positive stress changes associated with renewed magma intrusion. The concept of caldera relaxation is supported by the caldera-wide subsidence of about 16-20 cm (de Saint Ours, pers. comm.) immediately after the main phase of the eruption in 1994. Hence it is probably fair

to speculate that the resumption of any significant VT seismicity inside the caldera in the future would be indicative of renewed stress resurgence.

3.2.2 Eruption-related seismicity

Besides the VT earthquakes mentioned above, other recorded seismicity inside the caldera between October 1994 and December 2005 was dominated by earthquakes directly associated with the eruptive activity from Tavurvur. This assessment is made with the benefit of conducting simultaneous on the spot observations between the seismic recording and the actual eruptive activity. The eruption-related earthquakes can be classified into three main types, as follows:

- Low frequency (LF) volcanic earthquakes
- Explosion earthquakes
- Volcanic tremors

The above classification of earthquakes is similar to many generic volcanic earthquake classification systems that have been used widely in other volcanic areas (Okada et al., 1981; Weaver et al., 1981; Takeo, 1983; Lahr et al., 1994; Chouet, 1979, 1994). Further breakdown in the classification of earthquakes of the same type, especially LF volcanic earthquakes, have also been conducted by various people (Green and Neuberg, 2006) based on similarities of waveforms. It should be noted that here the term low frequency is used. In the literature people have also used the term long-period earthquakes for the same type of earthquakes.

Unlike VT earthquakes where the causes are fairly well-understood, the cause or source of LF, explosion earthquakes and volcanic tremors are still not very well understood. However some studies (Nishimura et al., 2000; Chouet et al., 1994; Neuberg et al., 2006) on the seismic signals for these earthquakes have linked their cause with fluid processes associated with the gas and volatile-rich viscous magma at the main magma chamber, the conduits leading to the vent, or dykes. Some features of the eruption-related earthquakes recorded at Rabaul Caldera during the post-eruption period are discussed below.

3.2.2.1 Low frequency (LF) volcanic earthquakes

The LF earthquakes recorded at the Rabaul Caldera between October 1994 and December 2005 can be classified into two main groups; earthquakes unaccompanied by ash emissions from Tavurvur and those associated with ash emissions. Further classification of these earthquakes can be made based on the waveforms but it is not the scope of this study to delve into this.

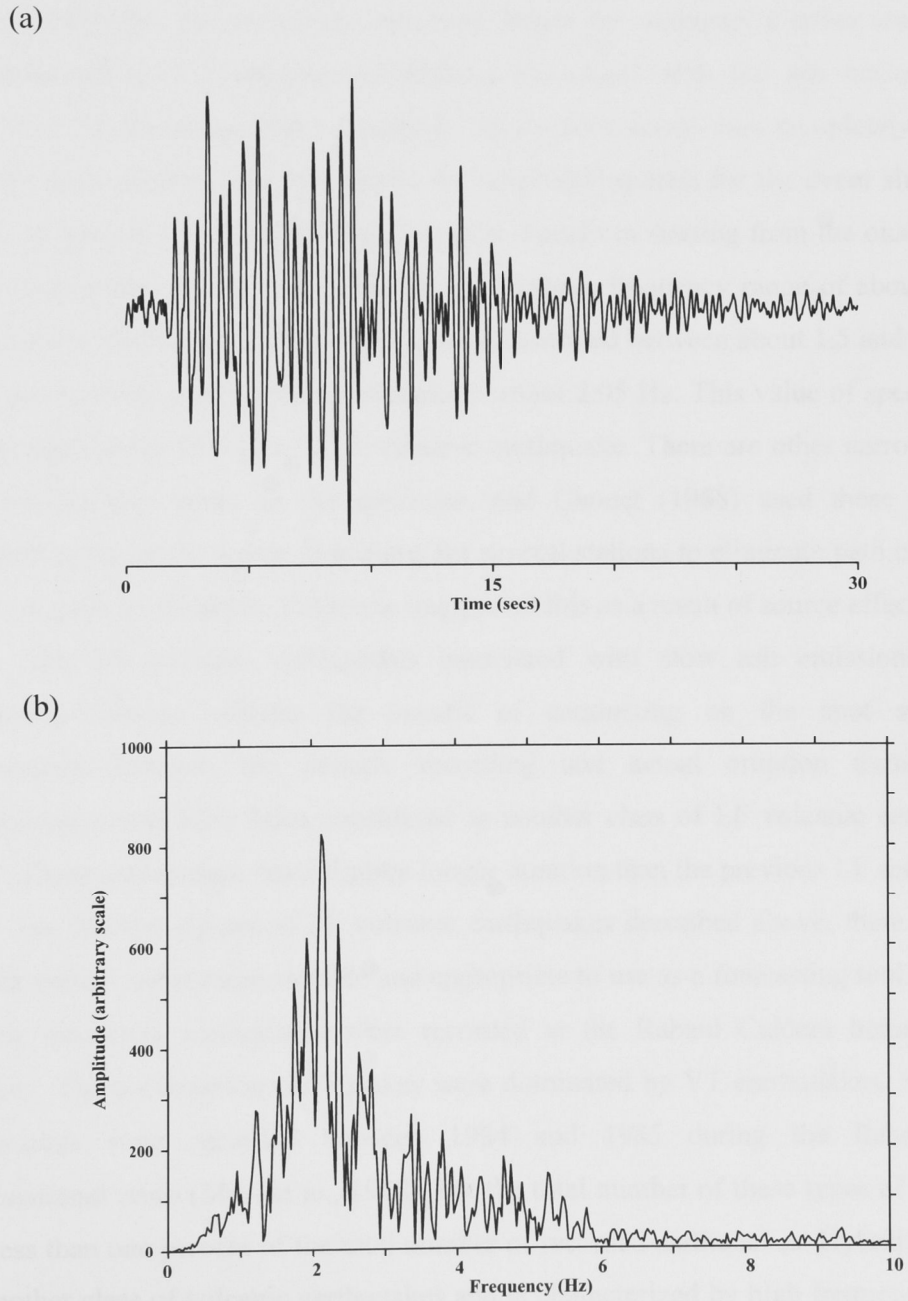

Fig. 3.2: (a) Low frequency earthquake recorded on TAL station. The signal is filtered using the Butterworth bandpass filter with frequency cutoffs at 0.1 and 5.0 Hz. (b) The corresponding amplitude spectra. The peak frequency is about 2.05 Hz. The vent is dated 2 October 2002.

The LF earthquakes unaccompanied by ash emissions have very distinct monochromatic low frequency signals (Fig. 3.2a) compared to the high frequency content of the volcano-tectonic (VT) earthquakes. The durations of these earthquakes range between 10 and 30 seconds. These earthquakes featured very prominently in the period about 1-2 months to days prior to the renewed eruptions of Phase 2, 3 and 4 discussed in Chapter 2. In all cases there was very good evidence of the earthquakes increasing in count and size as indicated by the signal duration and the amplitude leading up to the start of the renewed eruptions. As soon as the eruptions began the earthquakes either ceased or were overshadowed by LF volcanic earthquakes associated with the ash emissions. Their occurrence at any other time, especially when the volcano was completely quiet, was virtually non-existent. Fig. 3.2b shows the amplitude spectra for the event shown in Fig. 3.2a. The spectrum is calculated for the entire waveform starting from the onset to the tail of the earthquake. The energy is distributed across a frequency range of about 0.5 to 6.0 Hz. However the higher energy envelop is concentrated between about 1.5 and 2.7 Hz. The dominant spectral peak for the earthquake is about 2.05 Hz. This value of spectral peak is not uncommon for this type of LF volcanic earthquake. There are other narrow dominant and subdominant peaks in the spectrum, and Chouet (1988) used these overlapping common peaks on the power spectrums for several stations to eliminate path effects as the cause for such a waveform. Rather he interpreted this as a result of source effect.

The LF volcanic earthquakes associated with slow ash emissions are quite interesting because without the benefit of conducting on the spot simultaneous observations between the seismic recording and actual eruption these particular earthquakes would have been considered as another class of LF volcanic earthquakes at depth. These earthquakes have slightly longer duration than the previous LF earthquake.

For the two classes of LF volcanic earthquakes described above, there is no doubt that the earlier one is more suitable and appropriate to use as a forecasting tool. Apparently no low frequency earthquakes were recorded at the Rabaul Caldera before the 1994 eruption. The pre-eruption earthquakes were dominated by VT earthquakes. Some hybrid earthquakes were recorded between 1984 and 1985 during the Rabaul seismo-deformational crisis (Mori et al., 1988), but the total number of these types of earthquakes was less than one percent of the total number of recorded earthquakes. Hybrid earthquakes are another class of volcanic earthquakes and is characterized by high frequency signals in the early part of the waveform, and followed a few seconds later by low frequency signals. The non-occurrence of LF earthquakes during the pre-eruption period and just before the

eruption in 1994 is quite distinct considering the generic pattern of seismicity that is usually recorded prior to an eruption in most volcanoes. This observation suggests that all volcanic systems behave quite differently from each other, and in this case a caldera system certainly behaves very differently to a strato- or other composite volcanoes. Some examples of volcanoes in Papua New Guinea where the pre-eruption seismicity is dominated by the first type of LF earthquake described above includes Manam and Ulawun. Both are island arc strato-volcanoes.

3.2.2.2 Volcanic explosions

Volcanic explosion(s) are normally characterized by the rapid and forceful release of thick dark ash plumes from a volcanic vent during an eruption. An ash plume from the volcanic explosion is similar in shape to the plume produced by an artificial explosion. Ideally most volcanic explosions would produce an acoustic boom and an accompanying pressure or air-wave as does the artificial explosions, so on the seismogram they are clearly distinguishable from the other types of volcanic earthquakes with the distinct recording of an air-phase, which arrives well after the seismic wave that propagates through the earth (Fig. 3.3). But this does not always happen due to the complexities in their generation. Even if the air-phases are produced they may not be recorded by the standard seismic stations due to the limited bandwidths of the short-period seismic equipment. Under these circumstances seismogram readers would normally mistake these events for normal LF earthquakes. This shortcoming has been overcome in recent times with the installation of broadband and infrasonic microphones or infrasonic pressure sensors (Johnson, 2000) in volcanic regions. These instruments have recorded the air-phase with very good clarity at great distances from the source.

At RVO simultaneous observations conducted between the physical occurrence of the volcanic explosions and the recorded seismicity between 1994 and 2005 provided an ideal opportunity to study this problem and distinguish the classes of seismicity. There was fairly conclusive evidence that air-phases were produced more readily in explosions during intense strombolian eruptions than at any other time. At other times discrete vulcanian eruptions also produced air-phases but this did not happen on a 1:1 basis. That is an air-phase did not necessarily accompany each vulcanian eruption. This outcome could be explained by the physical and geochemical properties of the magma and the physical internal volcanic environment in which the explosions occur. Indeed some studies (Nishimura et al., 2000; Caplan-Auerbach and McNutt, 2003; Nishimura and Chouet,

2003) have been conducted to understand volcanic explosions and some have attributed this cause to the source depth and the nature of coupling of the acoustic energy between the ground and air.

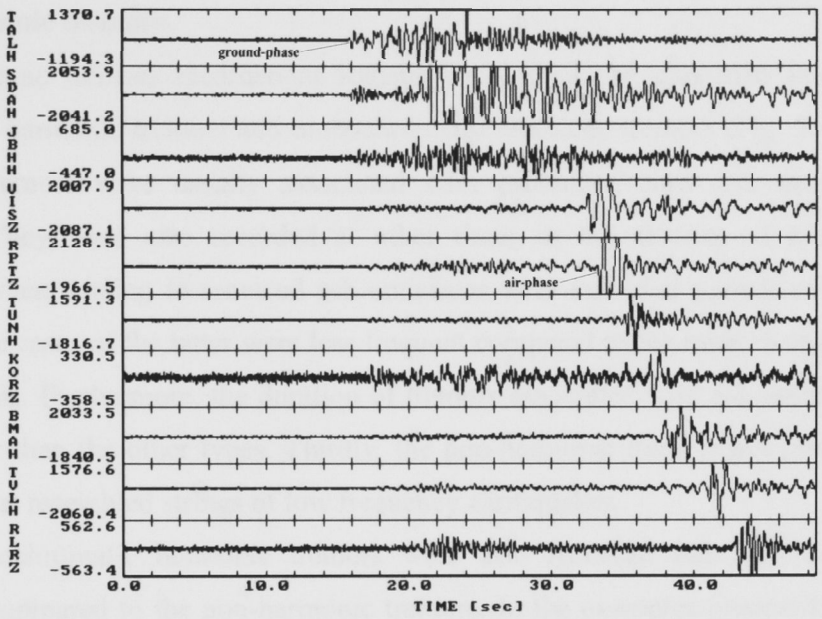

Fig. 3.3: Seismogram of an explosion recorded across the RHSN in 1997. The initial arrival corresponds to the energy that traversed the ground. The prominent phase that follows is the air-phase.

The scope of this study does not extend to modeling of the generation of volcanic explosions and air-phases, however, the few years of simultaneous visual and seismic observations at RVO suggests the following simplified conclusions about the air-phases:

- Strombolian eruptions have a higher tendency to produce air-phases than other eruption types.
- Volcanic explosions and any accompanying air-phases are generated more readily in less viscous and gas-rich magma than very viscous magma.
- Air-phases are very readily generated by volcanic explosions that occur near the surface because the coupling of the acoustic wave between the source in the ground and air is more efficient.
- Explosions occurring at greater depth have very little chance of producing air-waves because most of the energy from the explosion is transmitted into the surrounding medium. If there is any acoustic energy, this energy is trapped by the overlying cap of the vent and prevents it from coupling with the air.

- The average velocity of the air-phase recorded across the array from a single explosion is varied and not uniform. This variability is most likely controlled by the atmospheric conditions at the time of the explosion.

3.2.2.3 Volcanic tremors

Volcanic tremors recorded at Rabaul Caldera can be classified into two main groups; non-harmonic tremors and monochromatic harmonic tremors (Fig. 3.4). The non-harmonic tremors were usually associated with prolonged slow ash emissions from Tavurvur. They were also recorded at other times in the absence of ash emissions, especially when leading to renewed ash emissions after extended periods of quiescence. However the cases of the latter were less frequent compared to the tremors associated with ash emissions. Furthermore, the duration of tremors associated with ash emissions tended to be longer than the other types. Thirdly, the non-harmonic tremors not associated with ash emissions resembled strings of low frequency earthquakes.

Monochromatic harmonic tremors were also recorded but they occurred less frequently compared to the non-harmonic tremors. In the examples observed none of the harmonic tremors preceded renewed or higher levels of eruptive activity. The most conspicuous harmonic tremors ever recorded during the period concerned were on 14 April 1997. These tremors occurred a few days after the 12 April 1997 strombolian eruption. Incidentally this strombolian eruption also marked the last of the four lava effusion strombolian eruptions from Tavurvur. The three earlier strombolian eruptions also produced lava flows. Gauging from the RSAM plot in Fig. A-3 of Appendix A, the tail end of this particular eruption is quite different from the others as shown by the highly energized sustained eruptive activity characterized by non-stop explosions in the ensuing several hours. Fig. 3.4 shows a forty seconds duration of the waveform for the harmonic tremor recorded on TAL seismic station, showing the complex beating pattern, and the corresponding amplitude spectra. The waveform is filtered using the Butterworth bandpass filter with frequency cutoffs at 0.1 and 5.0 Hz. Note the resonating frequencies at 1.30, 2.50, 3.75, 5.0 and 6.3 Hz, shown in the spectral figure. This resonating characteristic synchronised very well with the pulsating or slow-motion piston-action movement that was evident in the low audible noises that accompanied the tremor signal. From a very simplistic viewpoint the audible noise source would tend to favour a partially fluid-filled cavity or conduit where the fluid, most likely not very viscous so it is easy to flow, would rise and fall giving rise to the piston or pulsating effect.

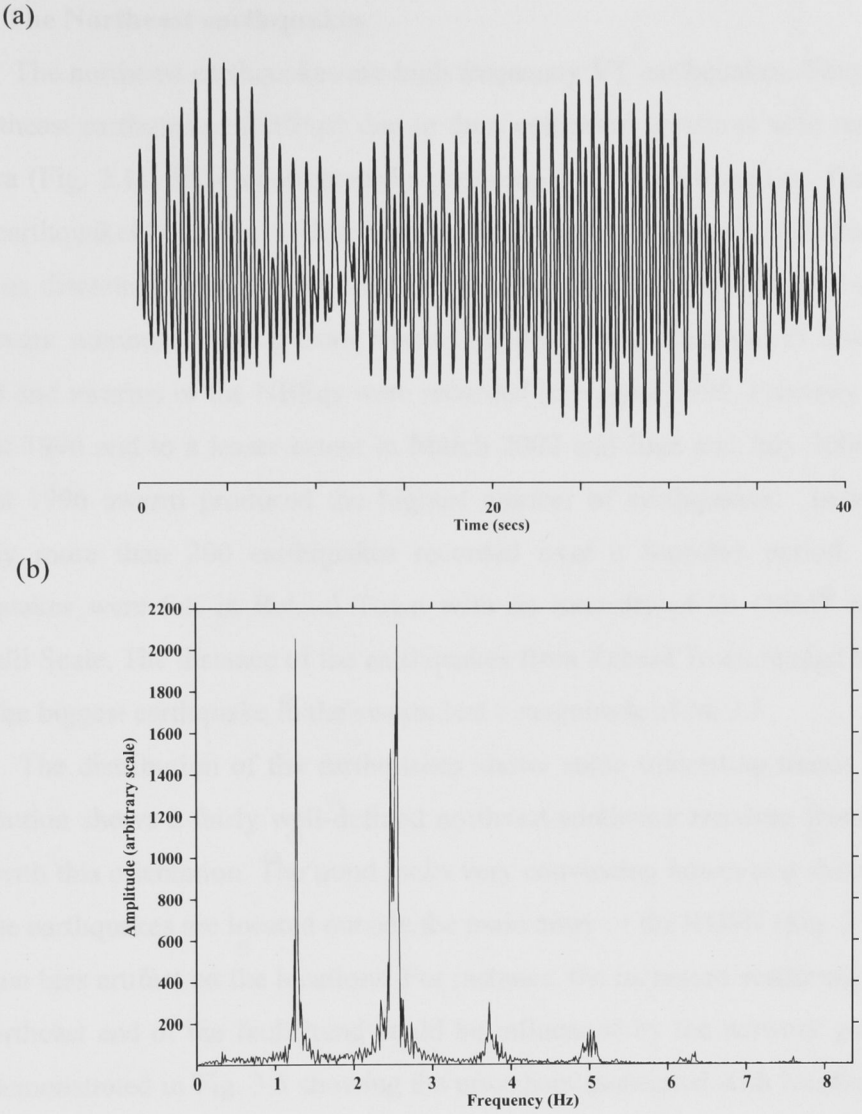

Fig. 3.4: (a) Section of a seismogram showing a harmonic tremor recorded on TAL station on 14 April 1997. The event code in the RVO earthquake catalogue is 9704140J.DMX. The signal is filtered using the Butterworth bandpass filter with frequency cutoffs at 0.10 and 5.0 Hz. (b) The corresponding amplitude spectrum. Note the multiple envelops of energy at frequencies of about 1.25 Hz, 2.55 Hz, 3.75 Hz, 5.0 Hz and 6.3 Hz. These repeated envelops of energy denotes the resonating frequencies of the tremor.

The nearly evenly spaced spectral peaks shown in Fig. 3.4 are observed systematically with time. This feature is referred to as gliding in tremor analysis and some studies (Garces et al., 1998; Neuberg and O'Gorman, 2002; Neuberg, 2000) have attributed the gliding effect to changing source lengths, bubble concentrations and pressures. Hellweg (2000) conducted similar studies and introduced some other mechanisms which include periodic degassing, turbulent slug flow and vortex shedding.

3.2.3 The Northeast earthquakes

The northeast earthquakes are high frequency VT earthquakes. They are referred to as northeast earthquakes (NEEqs) due to their epicentral locations with respect to Rabaul Caldera (Fig. 3.1). They dominated the post-eruption VT earthquakes. The occurrence of these earthquakes has been random but during the period it became clear that they occurred either as discrete events, strings of few to several events during a day or seismic swarms with event numbers ranging from tens to hundreds over a couple to few days. Notable strings and swarms of the NEEqs were recorded in August 1995, February 1996, July and August 1996 and to a lesser extent in March 2002 and June and July 2004. The July and August 1996 swarm produced the highest number of earthquakes. In total there were slightly more than 200 earthquakes recorded over a four-day period. Some of the earthquakes were felt in Rabaul Town with an intensity of III (MM) on the Modified Mercalli Scale. The distance of the earthquakes from Rabaul Town ranged between 2 and 6 km. The biggest earthquake in the swarm had a magnitude of M_L3.5.

The distribution of the earthquakes shows some interesting trends. The epicentral distribution shows a fairly well-defined northeast-southwest trending feature, or simply a fault with this orientation. The trend looks very convincing however it should be cautioned that the earthquakes are located outside the main array of the RHSN (Fig. 2.5) so there may be some bias artifact on the locations. For instance, the increased scattering of events at the far northeast end of the fault trend could be influenced by the network geometry. This is best demonstrated in Fig. 3.5 showing the error bars associated with location uncertainties. The error bars are smaller near the station array and it increases away from it. Earthquakes between the mid-section of the fault and the southwest end are considered well-located because they are closer to the main network array and furthermore some of the earthquakes were recorded by MAK and WTM stations as well. These two stations are to the northeast and northwest, respectively, from the main array. The two depth sections also show interesting trends. Both indicate deepening of the earthquakes away from the Rabaul Caldera. In general the NEEqs are slightly deeper than the Rabaul Caldera earthquakes.

The earthquakes are located well away from the centre of Tavui Caldera so it would appear that any connection of the earthquakes with possible fresh magmatic activity beneath this caldera is remote. This view is supported by the fact that Tavui Caldera is currently considered inactive. The last eruption from the caldera occurred about several thousand years ago (McKee, pers. comm.). On the contrary, the idea of VT earthquakes occurring well away from a volcano and hence isolated from volcanic connections is not

always true as demonstrated by Toda et al., (2002) during the 2000 Izu Islands earthquake swarm in Japan. At the Izu Islands the initial seismic swarm began beneath Miyakejima Volcano and after that they migrated away from the volcano in a northwesterly direction with time. Toda et al. (2002) associated the swarm to stress imparted by magma intrusion.

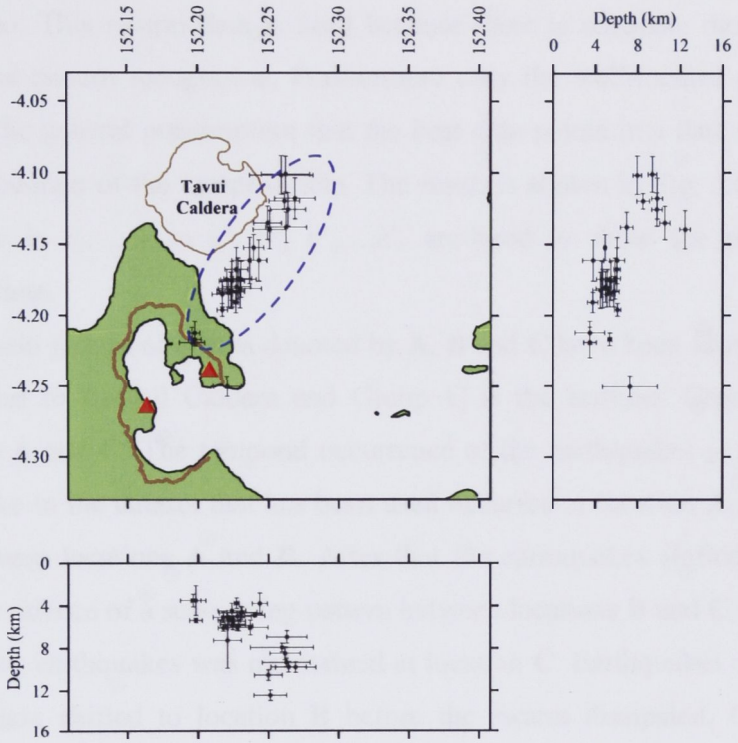

Fig. 3.5: Demonstration of the effects of the station array on the earthquake locations. Earthquakes located near the landmass, where the stations are concentrated, have smaller error bars compared to those located further away, towards the northeast. The data plotted are from the late July-early August 1996 northeast seismic swarm.

The orientation of mapped faults for this area (Lindley, 1988) are discussed in Chapter 2 and shown in Fig. 2.2. Generally they do not agree with the alignment defined by the northeast seismicity. Instead they are nearly perpendicular to each other. So this makes it unlikely that the northeasterly trend is a tectonically driven fault. In contrast, the orientation of the northeasterly fault is quite comparable to the echelon faults defining the spreading centres on the BSSL (Fig. 2.2). However, this is located tens of kilometers away from the BSSL so it does not seem likely to be part of that system. Furthermore there is no physical evidence resembling spreading centre features found in any portions of this northeast-trending fault, especially at the onshore parts as defined by the seismicity, to

suggest it is a segment of the spreading centre. Hence, this feature or its cause may be best explained by the same mechanical processes as Toda et al., (2002), i.e. dyke intrusion.

Well-located earthquakes from the July-August 1996 northeast earthquake swarm are plotted to investigate whether there is any migratory patterns on the earthquake hypocenters that could be associated with possible magma migration towards Tavurvur, the erupting volcano. This swarm data is used because there is adequate number of data to draw meaningful pattern recognition. Furthermore only the well-located earthquakes are used based on the general presumption that the best data points in a data set usually give the best representation of the sampled data. The result is shown in Fig. 3.6. The letters of the alphabet, a, b, c,…..,z to a', b', c',….z', are used to show the evolution of the earthquakes in time.

Three main groups of events denoted by **A**, **B** and **C** have been identified. Group **A** is located closest to Rabaul Caldera and Group **C** is the furthest. Group **B** is located between Group **A** and **C**. The temporal occurrence of the earthquakes is as follows. The initial earthquake in the dataset that has been used occurred at location **A**, then the events see-sawed between locations **A** and **B**. After that the earthquakes shifted to location **B**. There is some evidence of a see-sawing pattern between locations **B** and **C**, before a steady occurrence of the earthquakes was maintained at location **C**. Earthquakes during the latter part of the swarm shifted to location **B** before the swarm dissipated. Considering the circumstances that gives rise to VT earthquakes, the above annotations suggests there is common stress at location **B** and it transfers to the northeast or southwest as indicated by the earthquake locations. At this point in time there is no information to link the stress to any particular mechanism, however, if this swarm is likened to the Izu Islands super swarm (Toda et al., 2002), dyke intrusion by some magma source is the best speculative candidate for this particular swarm, other minor northeast swarms mentioned above, and the numerous occurrences of the NEEqs at other times.

Significant NEEqs during the pre-eruption period were recorded only once in May 1992. The occurrence of these earthquakes marked the beginning of Period 5 of the five periods of activity between 1968 and 1994 discussed in Chapter 2. The earthquakes occurred during a swarm over three days. About three hundred earthquakes were recorded, but only a handful was locatable. The located earthquakes are marked by the blue ellipse in Fig. 2.6. The strongest earthquake in the swarm had a magnitude of M_L4.2 and was felt with MMIV in Rabaul Town on the Modified Mercalli Scale. Again these earthquakes are marginally deeper than the earthquakes located inside Rabaul Caldera.

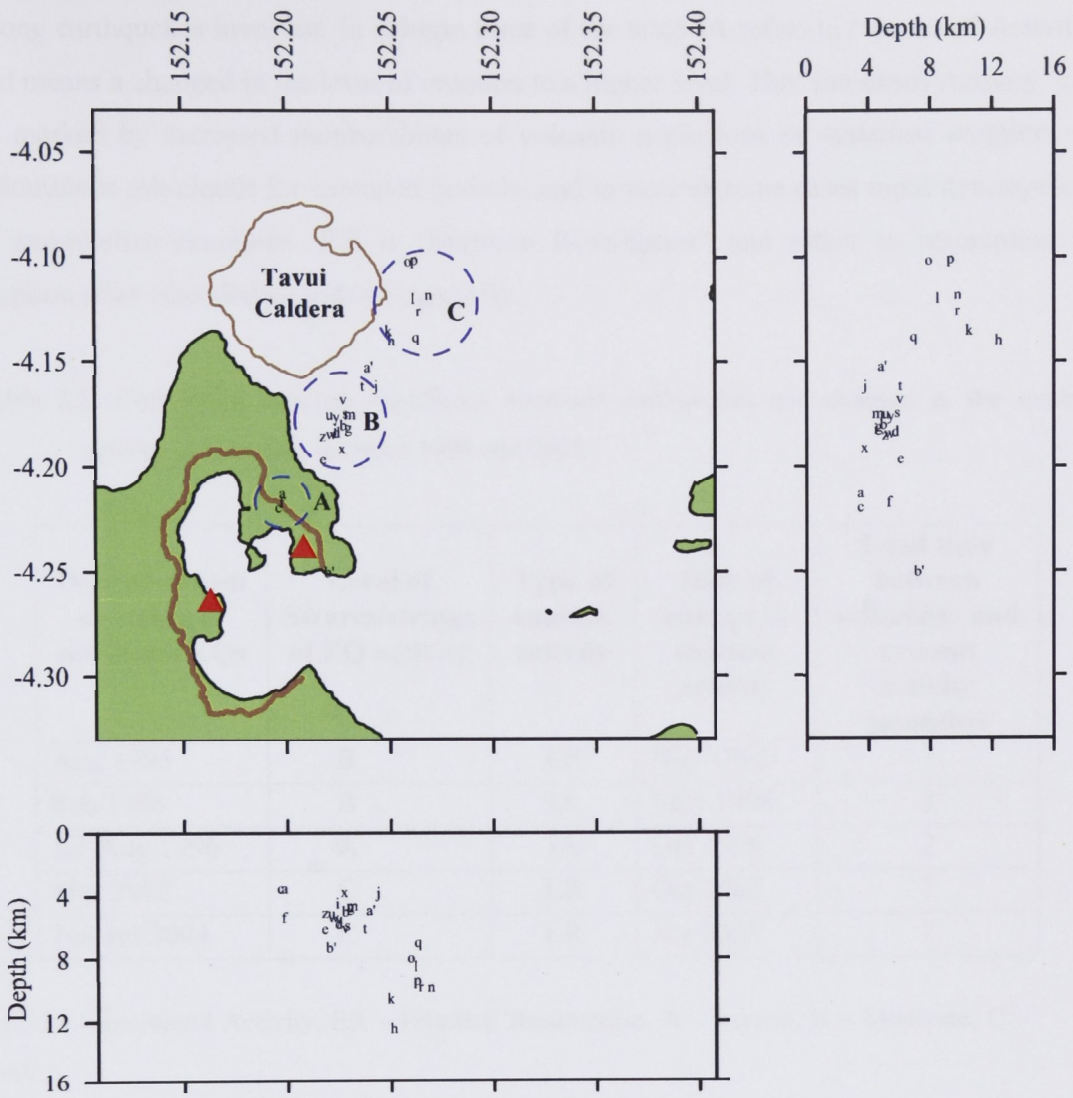

Fig. 3.6: Plot showing the progression of earthquakes in time during the July-August 1996 northeast earthquake swarm. The same data that is used in Fig. 3.5 is used here as well. The progression is denoted by the alphabetical letters a, b, c,..., and a' ,b', c',.... The letters are centered at the earthquake epicenters and hypocenters. The three dashed blue circles marked by **A**, **B** and **C** mark the three main groups that have been identified.

3.3 The NEEqs and the ongoing eruptions at Tavurvur

The eruptive activity at Rabaul Caldera between 1994 and 2005 has been discussed in some detail in Chapter 2. These eruptions and the temporal occurrence of the NEEqs have been analysed. There is some intriguing correlation between the two. Table 3.1 gives a summary of the correlation. In the table the codes **A**, **B**, and **C** in the second column denotes some measure of empirical weighting for the earthquake swarms or a string of them, based on the number of earthquakes and their corresponding magnitudes. **A** corresponds to 'Intense', meaning the number of earthquakes is plentiful and there are

strong earthquakes involved. In column three of the table **IA** refers to 'Increased Activity' and means a changed in the level of eruption to a higher level. The 'Increased Activity' can be marked by increased numbers/rates of volcanic explosions or sustained eruptions of voluminous ash clouds for extended periods, and in very extreme cases rapid development to strombolian eruptions. **ER** is 'Eruption Resumption' and refers to resumption of eruption after extended periods of inactivity.

Table 3.1: Correlation between significant northeast earthquakes and changes in the summit activity at Tavurvur between 1995 and 2005.

Date of swarm or string of northeast EQs	Level of Swarm/strings of EQ activity	Type of summit activity	Date of change in summit activity	Lead time between seismicity and summit activity (months)
Aug 1995	B	ER	Nov 1995	3
Feb 1996	B	IA	May 1996	3
Jul-Aug 1996	A	IA	Oct 1996	2
Mar 2002	C	ER	Oct 2002	7
Jun-Jul 2004	C	ER	Jan 2005	7

Key: IA – Increased Activity, ER – Eruption Resumption, A – Intense, B – Moderate, C – Low.

The information in Table 3.1 conveys the following:

- In all the cases listed the NEEqs preceded increased eruptive activity during ongoing eruptions. Besides the main events listed in Table 3.1, there were many other examples of less prominence.
- Between 1995 and 2005 three out of three case studies showed the NEEqs preceded renewed eruptions.
- The lead-time between the occurrence of the NEEqs and increased eruptive activity or renewed eruptions is inversely proportional to the level of the NEEqs. Here level refers to the number and size of earthquakes during a swarm or string of events. When the level of NEEqs is high, for instance an intense seismic swarm, the lead-time tends to be short. On the other hand, the lead-time is long for low level NEEqs.

- The lead-time is also dependent on the status of the volcano. Three conditions for the status of the volcano are considered; open, choked and a closed system. An open system refers to an erupting vent. A choked system refers to the vent being in a 'resting state' for a short period only and a closed system refers to the vent being in a non-eruptive state for many years. For a given swarm of NEEqs, the lead-time is short for an open system, intermediate for a choked system and long for a closed system.

These observations strongly suggest there is a correlation between the NEEqs and the ongoing eruptions at Tavurvur. Moreover, with the benefit of hindsight this correlation strongly suggests the May 1992 northeast earthquake swarm and the onset of the twin eruptions in 1994 could be linked. In this case the lead-time is about 28 months. The lengthy lead-time is not surprising considering the system had been closed for nearly 50 years.

3.4 Magma intrusion from the northeast

The correlation between the NEEqs and the ongoing eruptions at Tavurvur implies magmatic implications on two fronts. Firstly there is a strong possibility the earthquakes signify strain from possible magma intrusion from a northeast source into the resident caldera magma body. This interpretation could be likened to the Izu Islands earthquake swarm (Toda et al., 2002) where the earthquakes, numbering many thousands, occurred many kilometers away from Miyakejima volcano. The volcano erupted. Secondly, if there is magma intrusion into the resident magma body then magma mixing is probably involved.

The non-eruption of Tavurvur and Vulcan, or either one of them during or immediately after the Rabaul seismo-deformational crisis between 1983 and 1985 (Mori et al., 1988) raises crucial questions as why there was no eruption even though the caldera was perceived to be over-pressurised at that time as evidenced by the 1-2 meters of vertical uplift since the early 1970's, and more so the 0.8 meters of uplift during the crisis period alone, and the frequent seismic swarms.

Chapter 4

Imaging the Rabaul Caldera

4.1 Tomography - a tool for imaging the earth

The term "tomography" refers to "writing slices" but has come to mean, in a geophysical context, the construction of 2-D and 3-D images of subsurface structures particularly using seismic waves.

Tomography has been used in a number of disciplines to image or illuminate special features in a medium. The concept was brought to prominence in the medical profession with the use of x-rays to illuminate bone structures within the human body. It has also been used to diagnose sicknesses in the body as well. Further advancement in this technology resulted in CT-scan (computerized tomography).

Tomography was introduced into the field of earth sciences only in the last two to three decades. It has been used on a variety of scales to map the earth's shallow velocity and attenuation structure (Brzostowski and McMechan, 1992) to the deep dynamic interior structure using seismic waves produced by earthquakes and travelling through the earth's interior, then recorded by an adequate coverage of receivers on the earth's surface. However, unlike in the medical applications where the equipment is designed to provide uniform sampling, in seismic tomography involving the study of the earth, the sampling is very irregular. It is dependent on the distribution of the receivers and sources. Furthermore, the sensors are usually located on the surface of the earth so the information is at its best for the recovery of structures near the surface and can be poor for deeper structures. Seismic tomographic studies have led to a better understanding of the earth's 3-D structure. Seismic tomography has also been used for more specific purposes like lithospheric studies, mineral deposit exploration, engineering, and mapping magma bodies in active volcanic regions (Sudo and Kong, 2001; Finlayson et al., 2003; Husen et al., 2004; Bai and

Greenhalgh, 2005). For some of these activities, especially mineral exploration, active sources such as explosives have been used to generate seismic waves and where appropriate temporary receiver deployments have been made to give a good coverage of the target area.

4.1.1 The basis for seismic tomography

Seismic tomography depends on the presence of contrast in seismic properties of a structure or medium. These differences are reflected directly in the arrival times of seismic phases, or, through the shape and amplitude of seismic waveforms recorded by receivers (Kennett, 2002, p426). In order to detect these differences the observed arrival times are compared with predicted times from some reference model like the ak135 (Kennett et al., 1995). Any perturbation from the reference model is considered as an anomaly. This anomaly is the basis for constructing the 2-D and 3-D structure for a region or area.

4.1.2 Data

Seismic tomography can be done using full waveform inversion (Debayle and Sambridge, 2004) or travel times (Rawlinson and Sambridge, 2003) for certain seismic phases. Waveform inversion uses the full observed waveform or selected seismic phase segments. The observed waveform is compared with synthetic waveforms constructed from some reference model. Travel time tomography uses travel times for P and S-waves or other appropriate phases. The travel time is basically the amount of time it takes a seismic phase to travel from the source to receiver. The observed travel times are compared with predicted values obtained from some reference model. In the latter case, which is what has been used in this study, the acquisition and processing of preliminary raw data is very important. Some factors that must be considered when planning tomographic studies are firstly, the study or target area needs to be adequately covered by sufficient number of receivers. Secondly, the receivers need to be well-distributed across the target area, and thirdly the incoming rays from earthquakes into the seismic array have a good azimuth and depth coverage. To improve the receiver distribution factor, dense arrays of temporary seismic stations are usually deployed in the field for many months in order to record as many earthquakes as possible from a wide range of azimuthal angle and depth. Fourthly, the travel time information must be as accurate as possible. Studies have shown that relatively large travel-time errors can lead to unreliable tomographic results. So in the first instance the P and S-wave or other appropriate phases must be read with good precision. In

small datasets analysts do manual picking of the phases and in the process are able to pick and weigh the quality of picks fairly accurately. However in big datasets manual phase picking is practically impossible so people have developed tools to do automatic phase picks. For example, automatic phase picking algorithms have been developed using the energy function. The energy function is based on the ratio of the short-term-average energy (STA) to the long-term-average (LTA) energy (STA/LTA) levels derived from the same seismogram for the same event.

4.1.3 Model discretisation

In seismic tomography the model discretisation involves the division of the volume of the study area in the horizontal and vertical (depth) planes into some form of grid system. The grid spacing can be regular or irregular, or even a combination of both. The grid depends on the purpose of the study and the tomography method used. The grid structure produces cells with sides that correspond to the size of the grid spacing. For some methods finer nodes are introduced in the coarse cells and the velocity values in the cells are estimated by interpolation by, for example, b-spline methods by linking back to values at grid points. Having some *a priori* information like a good 1-D starting velocity model and what is expected to be modeled with respect to the available information, like receiver and source distribution, are prerequisites when devising the model discretisation. There is usually some trade-off between the output resolution and the model discretisation. For instance dividing the region of study into many small cells may over-parameterise the problem and produce unstable and unconstrained results. Likewise having fewer cells may under-parameterise the problem and result in not being able to resolve fine structures that may exist.

Model discretisation also impinges on the performance of the computer. Having a large study area discretised into many small cells and therefore solving for more unknowns will take a lot more time to execute than the same study area discretised into bigger cell sizes. However, with increasing computer power these days, this problem is becoming less of an issue.

4.2 Previous modeling of the Rabaul Caldera

Several studies have been conducted to model and/or image possible magma bodies in the shallow structure beneath the Rabaul caldera. The following sections give an overview of results for some of these studies.

4.2.1 McKee et al. (1984)

McKee et al. (1984) modeled onshore dry tilt and EDM surface deformation data using the point source model (Mogi, 1958) and derived two shallow magma reservoirs at the entrance to Greet Harbour at a depth of about 2 km (later revised to 1.8 km) and east of Vulcan headland at slightly greater depth. They stated further that these shallow reservoirs are fed from a common source, most likely the residuum of the 1400 yr BP magma body.

4.2.2 McKee et al. (1987)

McKee et al. (1987) studied the gravity and other deformation data. The observed data indicated a principle source of inflationary deformation beneath the offshore area between Matupit Island and Tavurvur. They indicated that the source of the inflationary deformation is presumably magmatic intrusion. The application of a simple point source model (Mogi, 1958) derived the source of the uplift at a depth of 1.8 km.

4.2.3 Mori and McKee (1987)

Mori and McKee (1987) studied the inner-caldera seismicity between 1971 and 1986 following improved earthquake locations. They derived the elliptical ring-fault and the outward dipping fault structure. They also acknowledged inward dip in some sections of the ring-fault. Furthermore they also noted the lack of seismicity below 4 km depth and inferred the presence of a magma body below this depth. In their discussions they pointed out the possibilities of magma intrusion into the ring-fault system. The ring-fault having a D-shape was initially observed by Cooke (1972).

4.2.4 Saunders (2001)

Saunders (2001) modeled some of the onshore surface deformation data using the Finite Element Modeling and suggested that the pattern of observed deformation could be caused by dykes located in some sections of the ring-fault system. Furthermore, the model suggested intrusion of the dykes by magma and causing compression in the region

bounded by the ring-fault. The end result is up-warping in some areas of the center of the caldera.

4.2.5 Seismic tomography

A few tomographic studies have been conducted for the Rabaul caldera. The first study was conducted by Mori and Eberhart-Phillips (1992). This was followed by the studies of Finlayson et al. (2003), Gudmundsson et al. (2004) and Bai and Greenhalgh (2005). The latter studies were outcomes of a major four-month long geophysical project explicitly conducted for imaging the shallow structure of the Rabaul Caldera. Known as RELACS (Rabaul Earthquake Location and Caldera Structure), the project involved the deployment of onshore seismic recorders and offshore OBS's (Ocean Bottom Seismographs) in order to record natural earthquakes during the duration of the project (Finlayson et al., 2001). In addition to the earthquakes, thirty controlled explosives were detonated at selected offshore sites. The project was conducted by Geoscience Australia, The Australian National University, Hokkaido University and the University of Wisconsin - Madison with financial support provided by AusAID (Australian Aid Agency for International Development) and JICA (Japanese International Co-operation Agency). Rabaul Volcano Observatory assisted in the project. Details of the project concept and operational procedures are described in Gudmundsson et al. (1999) and Finlayson et al. (2001).

4.2.5.1 Mori et al., (1992)

The first tomographic study for the Rabaul Caldera was conducted my Mori & Philipps (1992). They used the Rabaul Caldera earthquakes and the RHSN that was present at that time. The outcome of this study showed a fairly well-defined low velocity anomaly in the center of the caldera at depths between 3 and 7 km.

4.2.5.2 Finlayson et al. (2003)

Finlayson et al. (2003) conducted the first detailed tomographic study for the Rabaul Caldera using information recorded during the duration of the RELACS project. The forward modeling was done using the ray-bending method of Um and Thurber (1987) and the inverse problem was done using the damped least squares method of Thurber (1993), where the inversion for earthquake locations and velocity structure are performed simultaneously using an iterative approach.

The main outcome of this study is a low velocity anomaly immediately beneath the central part of the caldera at a depth of 3-6 km (Fig. 4.1). They related this anomaly to a magma reservoir. They used the dimensions of the P-wave velocity anomaly from a 3-D perspective to estimate a volume of 30-35 km^3 for the magma body.

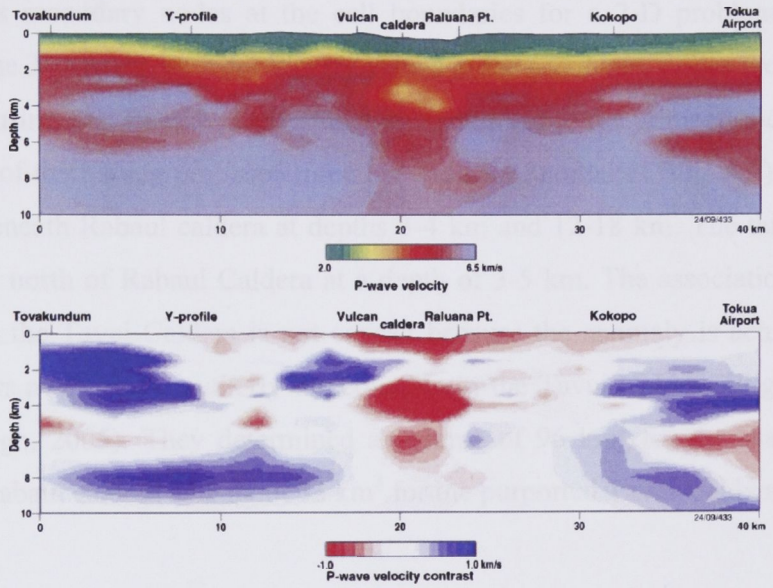

Fig. 4.1: Tomographic result of Finlayson et al. (2003) along a NW-SE profile that runs through the central part of Rabaul Caldera. The top panel is the velocity and the bottom panel is the velocity perturbation from a reference model in percentage. Note the distinct low velocity region beneath the centre of the caldera in the lower panel which they consider as a magma body.

4.2.5.3 Gudmundsson et al. (2004)

Gudmundsson et al. (2004) conducted P and S wave seismic attenuation studies using data recorded by two broadband recorders during the duration of the RELACS project. The first station was located about 50 km southwest from the caldera and the second station was located inside the caldera and about 1 km north of the ring-fault seismicity.

The results from the first site showed weak P- and S-wave attenuation. On the other hand the station inside the caldera showed very anomalous P- and S-wave attenuation immediately towards the south in the direction of the central part of the caldera compared to waves approaching from other azimuthal directions. They suggested that the attenuation is due to fracturing of rocks and the presence of geothermal fluids.

4.2.5.4 Bai and Greenhalgh (2005)

Bai and Greenhalgh (2005) conducted P- and S-wave travel time tomography using the same data as Finlayson et al. (2003) but expanded it by picking additional earthquakes

from the RELACS dataset. They used 3-D ray-tracing with an 'irregular' shortest path method for the forward modeling and a damped minimum norm, and constrained least-squares conjugate gradient approach to solve the inverse problem. The 'irregular' approach employed to solve the forward problem involves maintaining a relatively large cell size, but introduces secondary nodes at the cell boundaries for a 2-D problem, or onto cell surfaces for the 3-D problem. The velocity values at the secondary nodes are calculated by interpolation using a tri-linear velocity function and linked to the primary nodes.

The outcome of their study proposed three low velocity anomalies (Fig. 4.2). Two of them are located beneath Rabaul caldera at depths 3-4 km and 12-18 km. The third anomaly is located to the north of Rabaul Caldera at a depth of 3-5 km. The association of the latter anomaly with the Tavui Caldera is not correct because the anomaly is actually located a few kilometers away, in a southerly direction, from the Tavui Caldera (Fig. 13(b) of Bai and Greenhalgh, 2005). They determined a volume of 96 km^3 for the shallow anomaly beneath the Rabaul caldera and about 32 km^3 for the purported Tavui Caldera anomaly.

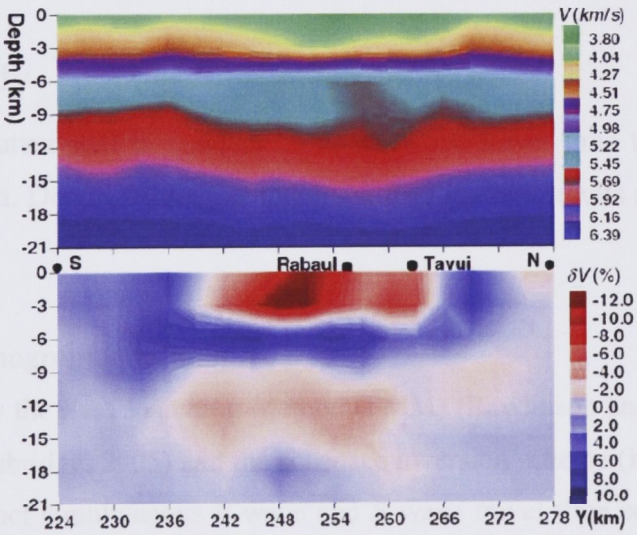

Fig. 4.2: Tomographic result of Bai and Greenhalgh (2005) along a S-N profile that runs through the central part of Rabaul Caldera. The upper panel shows the velocity and the lower panel shows the velocity perturbation from the reference model in percentage. Note the two layers of anomalous low velocity regions in the lower panel which they interpret as magma bodies.

4.2.5.5 Comparison between Finlayson et al. (2003) and Bai and Greenhalgh (2005) results

A comparison between the results of Finlayson et al. (2003) and Bai and Greenhalgh (2005) yields the following features. Firstly Finlayson et al, (2003) identified only one anomaly located at 3-6 km beneath the Rabaul Caldera. On the other hand, Bai

and Greenhalgh (2005) identified three anomalies. Two are located beneath the Rabaul Caldera at depths of 2-4 km and 12-18 km, respectively, and the third is located north-northeast of Rabaul but not necessarily beneath the Tavui Caldera, at a depth of about 2-4 km. It would appear that the shallow anomaly of Bai and Greenhalgh (2005) beneath the Rabaul Caldera could correspond to the anomaly mapped by Finlayson et al. (2003). The depths for the anomalies from both studies are not quite the same although they have a common depth of 3-4 km. Secondly, the volume for the anomaly estimated by the two studies is very different. Finlayson et al. (2003) estimated a volume at about 30-35 km^3. The volume estimated by Bai and Greenhalgh (2005) is 2-3 times higher than the volume estimated by Finlayson et al. (2003).

The differences in the depth and volume for both studies could be attributed firstly to the tomographical methods, the velocity model and lastly the location of the profiles where the slices were made. It is quite clear from Fig. 4.2 and Fig. 13(a) of Bai and Greenhalgh (2005) that the result of Bai and Greenhalgh (2005) for this particular anomaly appears more stretched than Finlayson et al. (2003), which gives rise to a greater volume.

4.3 This study

This study attempted to conduct P- and S-wave travel time tomography for the Rabaul Caldera area. Details of the methodology, data and the results are discussed in the following sections.

4.3.1 Seismic tomographic technique

In this study the Fast Marching Method (FMM) (Rawlinson and Sambridge, 2004; Rawlinson and Sambridge, 2005) and the subspace inversion scheme (Kennett et al., 1988) were used to conduct simultaneous P-wave and S-wave travel time seismic tomography. The FMM was used to solve the forward problem and the subspace inversion scheme was used for the inverse problem. Some description for both methods is described in the following subsections.

4.3.1.1 Fast Marching Method

FMM is a grid-based numerical algorithm ideal for wavefront construction from which travel times are deduced. It does this by tracking an evolving interface along a narrow band of nodes that are updated by solving the eikonal equation. The eikonal

equation, which governs the propagation of seismic waves in the high-frequency limit may be written as;

$$\nabla_x T = s(\mathbf{x}) \tag{4.1}$$

where ∇_x is the gradient operator, T is the travel time, and $s(\mathbf{x})$ is the slowness as a function of position.

The FMM deals with problems of discontinuities by enforcing an entropy condition where the wavefront evolves because it can only pass through a point once. The travel time associated with a particular grid point is updated using a finite difference scheme. The implementation of the scheme requires that the order in which the nodes are updated be consistent with the direction of the flow as time progresses. The FMM achieves this by systematically constructing travel times ahead of the wavefront from known values behind the wavefront using a narrow-band approach. In the narrow-band concept the grid points are labeled as either *alive, close* or *far*, where the *alive* points lie in front of the wavefront, *far* points lie behind the wavefront and the *close* points lie within the narrow band itself. The narrow-band is thus identified with points with minimum travel time and its shape approximates the first arrival wavefront. The above explanation is illustrated in Fig. 4.3.

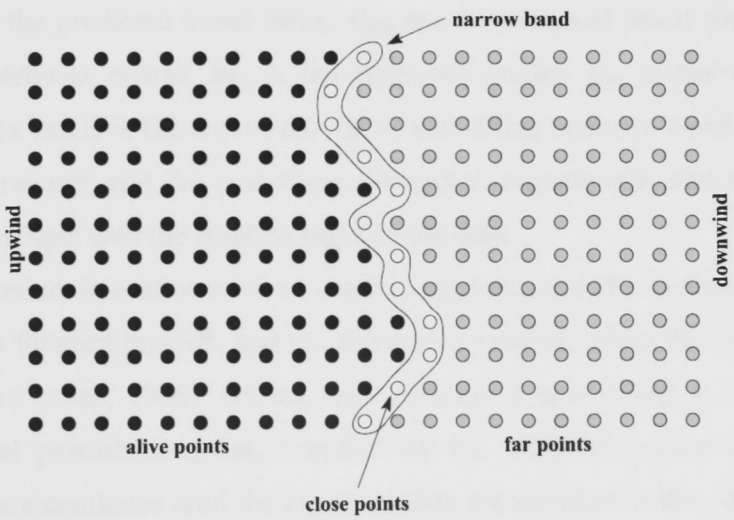

Fig. 4.3: Illustration showing how the travel time is calculated in an evolving wavefront marked by the *narrow band*. The traverse is from left to right so that the *alive points* (black circles) have their travel times correctly computed already, the *closed points* (white) have trial travel times and the *far points* (grey) still have their travel times to be computed (after Rawlinson and Sambridge, 2004).

4.3.1.2 Subspace inversion

The subspace inversion method described by Kennett et al., (1988) and applied by Rawlinson and Sambridge (2003) is used here to solve the inverse problem. Basically the inverse problem involves the analysis of departures of the observed parameters studied from the predictions for a reference model. In my problem the observed parameters are the P- and S-wave travel times between a receiver and a source. The essence of seismic tomography is to relate these departures back to the structure from which they arise and subsequently construct the meaningful 2-D and 3-D structures for the areas or regions studied. Details of the subspace inversion are described in Kennett et al., (1988) and Rawlinson and Sambridge (2003), however for the purpose of this thesis, I have extracted or quoted some information from Rawlinson et al., (2006) to give the reader of this thesis some overview of the procedure.

The inverse problem can be solved by specifying an objective function S(**m**), where **m** are the model parameters which are to be minimised. Here the objective function has the form;

$$S(\mathbf{m}) = (\mathbf{g}(\mathbf{m})-\mathbf{d}_{obs})^T\mathbf{C}_d^{-1}(\mathbf{g}(\mathbf{m})-\mathbf{d}_{obs}) + \epsilon(\mathbf{m}-\mathbf{m}_0)^T\mathbf{C}_m^{-1}(\mathbf{m}-\mathbf{m}_0) + \eta\mathbf{m}^T\mathbf{D}^T\mathbf{D}\mathbf{m} \quad (4.2)$$

where g(**m**) are the predicted travel times, $\mathbf{d}_{obs}$ are the observed travel times, $\mathbf{C}_d$ is the *a priori* data covariance matrix, $\mathbf{m}_o$ is the reference model, $\mathbf{C}_m$ is the *a priori* model covariance matrix and **D** is the second derivative smoothing operator. ϵ and η are known as the damping parameter and the smoothing parameter, respectively, and they govern the trade-off between how well the solution satisfies the data.

The procedure is conducted in an iterative approach in order to minimise S(**m**). The FMM solves the forward problem and the subspace inversion solves the linearised inverse problem (Kennett et al., 1988). During each iteration a new model is derived with an associated model perturbation, $\delta\mathbf{m}$, supplied by the subspace inversion method. The iterative procedure continues until the observed data are satisfied or the change in S(**m**) is significantly small.

The subspace inversion method works by projecting the quadratic approximation of S(**m**) onto an *n*-dimensional subspace of model space. For an objective function of the form given in (2), the perturbation $\delta\mathbf{m}$ is given by;

$$\delta \mathbf{m} = -\mathbf{A}[\mathbf{A}^T(\mathbf{G}^T\mathbf{C}_d^{-1}\mathbf{G} + \epsilon\mathbf{C}_m^{-1} + \eta\mathbf{D}^T\mathbf{D})\mathbf{A}]^{-1}\mathbf{A}^T\boldsymbol{\gamma} \quad (4.3)$$

where $\mathbf{A} = [\mathbf{a}^j]$ is the M x n matrix projection matrix, $\mathbf{G}$ is the matrix of Fréchet derivatives and $\boldsymbol{\gamma}$ is the gradient vector ($\boldsymbol{\gamma} = \partial S/\partial \boldsymbol{m}$).

4.3.2 Data and model parameterization

4.3.2.1 Data

The following sets of data were used in this study:

- A subset of the pre-1994 eruption Rabaul caldera earthquakes

This dataset includes earthquakes that originated inside Rabaul caldera between 1971 and 1985 that were recorded by the pre-eruption Rabaul Harbour Seismic Network (RHSN). Nearly all the earthquakes occurred on the elliptical ring-fault (Mori et al., 1988). Only earthquakes recorded on seven or more stations are selected. All the earthquakes had only P-wave arrival readings. The phase readings were picked manually on a 16-mm develocorder film to the 1/100th of a second with some weighting associated with each pick to reflect the pick quality. No S-waves were read, noting that the seismic network had only short-period vertical component seismometers so the identification of S-waves in the vertical component data was difficult. However Mori (1988) did identify S-waves from a special array of three 3-component stations that operated for a short period. The total number of earthquakes in this subset is about 3244.

- Post-1994 eruption Rabaul caldera earthquakes

The post-1994 eruption dataset consists of earthquakes recorded by the post-1994 eruption RHSN. Because of the scarcity of post-eruption inner-caldera seismicity the threshold for the number of stations recording an event was reduced to five stations instead of seven. Once again the P-wave is the primary phase that has been picked, but the emergence of the northeast earthquakes outside of the caldera provided some S-wave picks. The pick precision is to the 1/100th of a second and some weighting was

associated with each pick to reflect the pick quality. The total number of earthquakes is about 223.

- Regional earthquakes.

The regional earthquake dataset consisted of tectonic earthquakes detected by the RHSN between 1994 and 2005 and located within 250 km from the center of the caldera. These earthquakes had a magnitude threshold of M_L5.0 and greater.

The RELACS survey coincided with this period so data recorded by the RELACS stations are part of this dataset. The station detection threshold and picking resolution is similar to the post-eruption dataset. The total number of earthquakes in this subset is about 400.

- RELACS shots.

The RELACS shot data were used, however instead of using the original phase picks, all the shot data were re-picked. Out of a possible thirty shots only 28 of them were used. The other two were omitted because not many stations recorded them and for many of the stations the signal to noise ratio was very low. The picks were read to $1/100^{th}$ of a second.

The distribution of the earthquakes and seismic receivers is shown in Fig. 4.4.

Travel times for both the P and S-waves used in the tomography are observed data determined by;

$$T_{obs} = P_{arr} - OT \tag{4.4}$$

where T_{obs} is the observed travel time, P_{arr} is the P-wave arrival time for a particular earthquake at a particular station and OT is the corresponding calculated origin time for the earthquake. S-wave travel times are determined in a similar manner. The travel time-distance and the corresponding velocity curves for both the P and S-waves are shown in Fig. 4.5. The velocities are determined using the Wiechert-Herglotz inversion method. The purpose for this exercise is to generate a suitable base velocity model to be used in the tomography. In Fig. 4.5 (c) the solid blue curve gives the best fit for the scattered points.

The curve is not smooth. It has some velocity jumps. One of these jumps is from about 7.9 km/s to 8.5 km/s at about 35 km depth. This could be the Moho. In general the Moho depth varies generally between 10 and 50 km (Collins et al., 2003). It is shallower in the oceanic plates and deeper in the subcontinents.

(a)

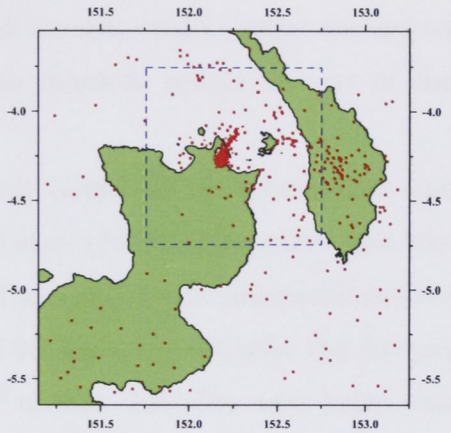

(b)

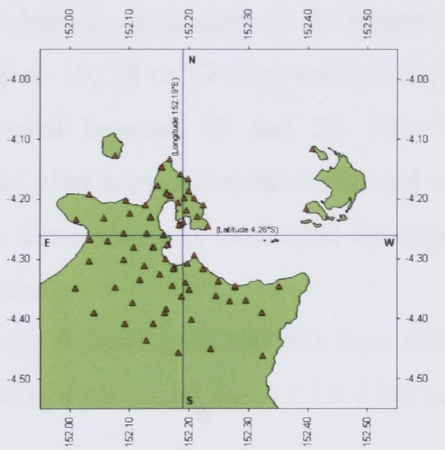

Fig. 4.4: (a) The regional model with distribution of all the earthquakes (solid black circles) used in the travel time tomography. The blue dashed box defines the local model region. (b) The distribution of seismic stations (brown triangles). In (b), the two blue lines which intersect at the center of the caldera marks the profiles where the N-S and E-W depth cross-sections were determined for the tomographic images.

4.3.3 The approach to the tomography and the outcomes

The travel time tomography via the FMM scheme was conducted for both the regional and local models. The regional model tomography involved the simultaneous inversion of the first three datasets listed in Subsection 4.3.2.1. The FMM scheme was

executed three times with each execution applying a different cell size of (3 x 3 x 3) km, (2 x 2 x 2) km and (1 x 1 x 1) km. The local model tomography was done in three stages. The first stage involved the simultaneous inversion of the first three datasets listed in Subsection 4.3.2.1, noting that for the regional earthquake dataset only those that fell within the region of the local model was used. The RELACS shots data was not used. The second stage involved only the RELACS shots data. The third stage involved the simultaneous inversion of all the data used in stages one and two. For each stage the FMM scheme was executed three times to reflect the use of the three different cell sizes mentioned above.

The reference velocity model for the tomography was derived from Fig. 4.5 and information from Finlayson et al. (2003). Other parameters shown in equations 4.2 and 4.3 had the following values. The *a priori* data covariance and the *a priori* model covariance were set to 0.1 seconds and 0.1 km/s, respectively. The damping parameter, ϵ, was 0.1 and the smoothing parameter, η, was 1.0. The two latter values were fixed. All these parameters were determined from a vigorous testing of different combinations. The above combinations gave the best trade-off. The inversion procedure was carried out in five iterations with a starting subspace dimension of 20 however during the inversion the subspace dimension reduced to 19, 18 or 17 after each of the five iterations. So in effect the subspace dimension varied between 17 and 20. Note that the starting subspace dimension of 20 was selected after some exhaustive trial and error over a range of values. The change in the subspace dimension was conducted dynamically by the SVD (singular value decomposition) algorithm.

The results given in the following subsections were obtained from executions with 2 x 2 x 2 km cell size for the regional model and 1 x 1 x 1 km cell size for the local model.

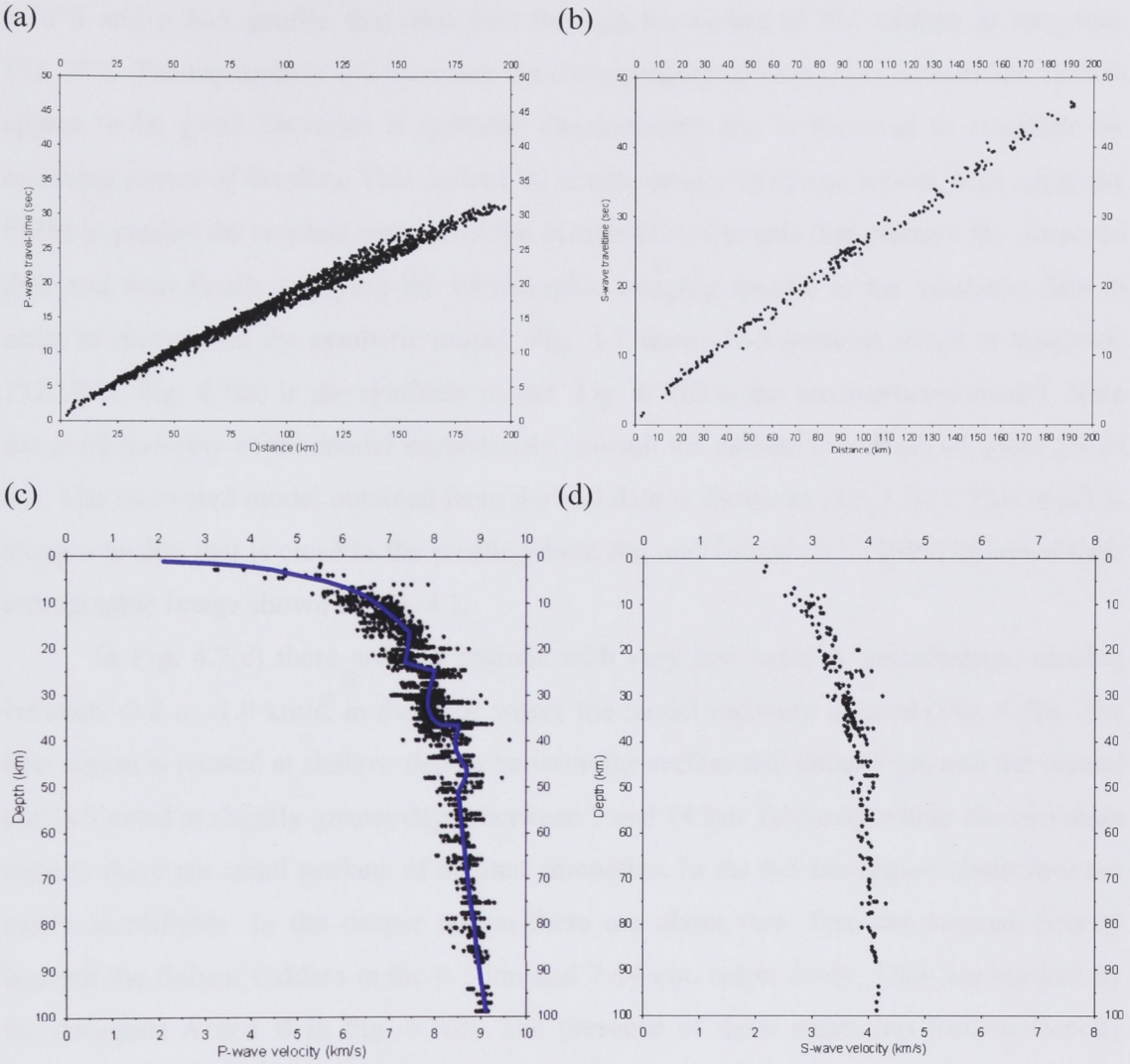

Fig. 4.5: Travel time-distance curves for P- and S-waves are shown in (a) and (b), respectively. The plots are constructed from near and distant regional earthquake information used in this study. The corresponding 1-D P- and S-wave velocity curves are shown in (c) and (d), respectively. The blue solid line in (c) is the best fit. The velocities are determined using the Wiechert-Herglotz inversion method. The 1-D reference velocity model for the tomography was derived from this and information from Finlayson et al. (2003).

4.3.3.1 Regional model

Fig. 4.6 shows a 2-D distribution of the P-wave ray paths in the regional model at 10 km depth, a W-E profile that cuts through the central part of the caldera at latitude 4.26°S and a N-S profile that also cuts through the centre of the caldera at longitude 152.19°E. The ray density and therefore the cross-pathing between rays beneath the caldera appear to be good. However a synthetic checkerboard test is essential to establish the resolving power of the data. This is done by constructing a synthetic model, then using the FMM to predict the residual pattern for the distribution of events that produce the observed data and then finally applying the tomographic imaging routine to the synthetic data in order to reconstruct the synthetic model. Fig. 4.7 shows N-S sections sliced at longitude 152.19°E. Fig. 4.7(a) is the synthetic model. Fig. 4.7(b) is the reconstructed model. Note the good recovery of the model immediately beneath the caldera to a depth of about 15-20 km. The recovered model obtained from the real data is shown in Fig. 4.7(c). This result is along a profile that is close to the profile where Bai and Greenhalgh (2005) obtained their tomographic image shown in Fig. 4.2.

In Fig. 4.7(c) there are two regions with very low velocity perturbation, ranging between -0.8 to -1.0 km/s, in the zone where the model recovery is good (Fig. 4.7b). The first region is located at shallow depths between the surface and about 5 km and the second one is located at slightly greater depth between 7 and 14 km. However within the two main regions there are small pockets of distinct anomalies. In the 0-5 km region about four are easily identifiable. In the deeper region there are about two. Two are located directly beneath the Rabaul Caldera at the 0-5 km and 7-14 km, respectively. They are marked by the polygons **A** and **B** in Fig. 4.7(c). The presence of these anomalies located directly beneath the Rabaul Caldera strongly suggests they are possibly magma bodies. However, there may be some doubt about linking the shallow anomaly to a magma body because it is not very different from the other three anomalies on either side of it. However, the results from the local model tomography were able to resolve this uncertainty (see subsection 4.3.3.2 below).

(a)

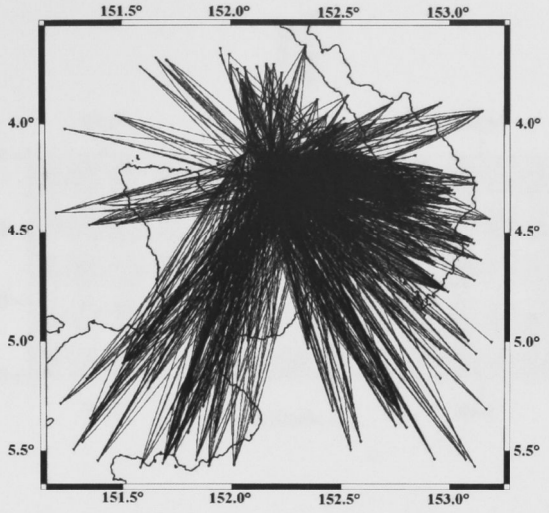

(b)

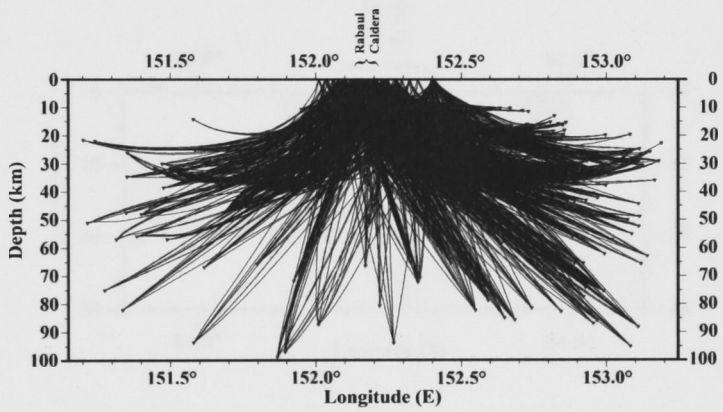

(c)

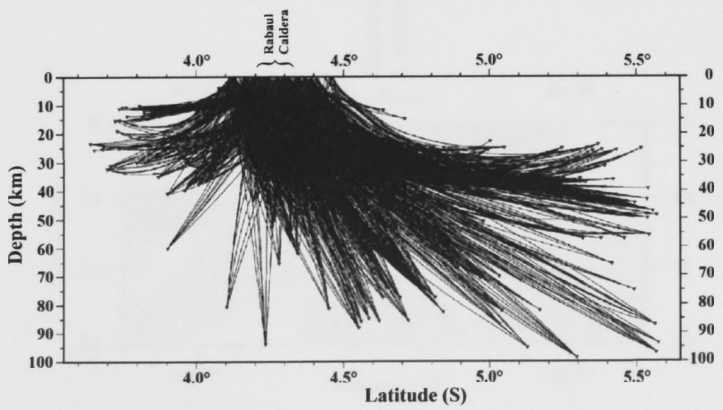

Fig. 4.6: Raypaths for the P-waves in the regional model. (a) Slice at 10 km depth, (b) E-W depth profile sliced at latitude 4.26°S, and (c) N-S depth profile sliced at longitude 152.19°E. In plots (b) and (c) the location of Rabaul Caldera is shown.

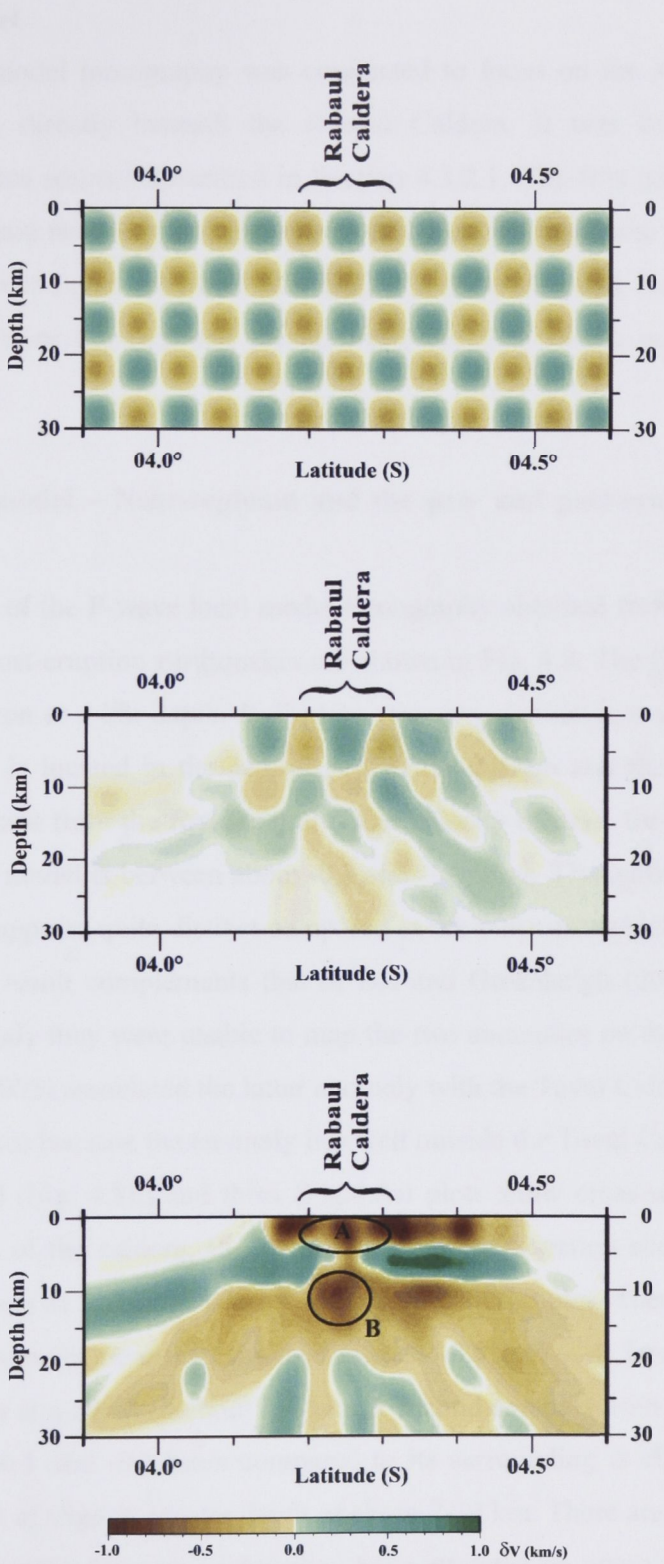

Fig. 4.7: (a) Input checkerboard model for the regional model. (b) Recovered checkerboard model that is obtained by inverting the data used. (c) The P-wave solution model obtained with real data showing the velocity perturbation in km/s. All the data sources described in Section 4.3.2.1 were used. The two zones marked in (c) directly beneath Rabaul Caldera are inferred to be magma bodies.

4.3.3.2 Local model

The local model tomography was conducted to focus on the structure in the top several kilometers directly beneath the Rabaul Caldera. It was done in three parts according to the data sources described in Section 4.3.2.1. The first part utilized the pre- and post-eruption and near-regional earthquake data that fell inside the blue box shown in Fig. 4.4(a). The second part used only the RELACS shots data and the last part used the combined dataset from the first and the second parts. The results are presented in the following sections.

4.3.3.2.1 Local model – Near-regional and the pre- and post-eruption earthquake data

The results of the P-wave local model tomography obtained from the near-regional and the pre- and post-eruption earthquakes are shown in Fig. 4.8. The first plot (Fig. 4.8a) is a depth slice taken at 4 km depth. It displays two very distinct low velocity anomalies. The first anomaly is located in the central part of the caldera and the second is located north but slightly east from the first anomaly. The velocity contrast for the two anomalies from the reference model is between about -0.8 and -1.0 km/s. The outline for the anomaly inside the caldera appears quite distinct compared to the other one which seems vague due to smearing. This result complements that of Bai and Greenhalgh (2005) but unlike the outcome of this study they were unable to map the two anomalies on the same model. Bai and Greenhalgh (2005) associated the latter anomaly with the Tavui Caldera. In this study I dispute this reference because the anomaly lies well outside the Tavui Caldera.

The second (Fig. 4.8b) and third (Fig.4.8c) plots show cross-sections that passes through the centre of the caldera. Fig. 4.8b is a W-E cross-section sliced at 4.26°S. The approximate position of Rabaul Caldera is also shown in the plot. There is a distinct low anomaly with a velocity contrast ranging between -0.5 and -1.0 km/s located directly beneath the caldera at a depth of about 3-6 km. A second anomaly with a velocity contrast ranging between -0.1 and -0.3 km/s compared to its surrounding is also located directly beneath the caldera at slightly greater depth of about 7-12 km. There are other low velocity anomalies in the surrounding region but they have attracted no attention mainly because they fall outside the network array where the resolution recovery is very poor. Even the 7-12 km deep anomaly mentioned above is mapped in an area where the ray coverage is relatively poor so its existence may be slightly ambiguous. However its proximity to the 7-

14 km deep anomaly in Fig 4.7c, denoted by **B**, directly beneath the caldera strongly suggests this anomaly is a genuine structure.

Fig. 4.8c is an N-S cross-section sliced at 152.20°S. It also passes through the centre of the caldera, but slightly to the east. Slicing at 152.20°E was deliberate and the reason was to determine whether the north-northeast anomaly determined both by Bai and Greenhalgh (2005) and this study and the shallow Rabaul Caldera anomaly could appear on the same section. The polygon denoted by **A**, with a velocity contrast between -0.7 and -0.9 km/s, is located directly beneath the Caldera. The dashed polygon denoted by **C** with a velocity contrast of about -0.4 km/s coincides very well with the position of the north-northeasterly low velocity anomaly shown in Fig. 4.8a.

The local model tomography has resolved the shallow structure beneath the Rabaul Caldera far better than the regional model. The result has identified three distinct low velocity anomalies within the caldera. Two are located directly beneath the caldera and the third is located outside of the Rabaul Caldera in a north-northeasterly direction.

4.3.3.2.2 Local model – RELACS shot data

The P-wave tomography result for the RELACS shots only is shown in Fig. 4.9. Again the interpretation of the results is focused in the area directly beneath the Rabaul Caldera. However, some attention is also given to the area north-northeast of the Rabaul Caldera. Fig. 4.9(a) shows the velocity contrast map at 5 km depth. There is a low velocity anomaly with a velocity contrast of about -0.7 km/s located at the center of the caldera. The anomaly is distorted by SE-NW smearing. This anomaly is related to the one located at the center of the caldera in Fig. 4.8a.

Fig. 4.9(b) is a W-E cross-section sliced through latitude 4.27°S. The profile passes through the centre of the caldera. A few areas showing low velocity contrast are present. Three of them are located between shallow and about 3 km. These zones are within the network array and therefore in regions of good ray coverage. They are most likely associated with dense sampling directly beneath the receivers that lie along the profile. Besides these very shallow anomalies there is another anomaly, denoted by the polygon **A**, at about 4-6 km depth directly beneath the Rabaul Caldera. Again this anomaly is probably related to the 3-6 km anomaly discussed in Subsection 4.3.3.2.1 above. This anomaly has been interpreted as the shallow magma body beneath the Rabaul Caldera. It also features in the N-S cross-section in Fig. 4.9(c). The section is sliced at longitude 152.19°E and passes through the centre of the caldera.

(a)

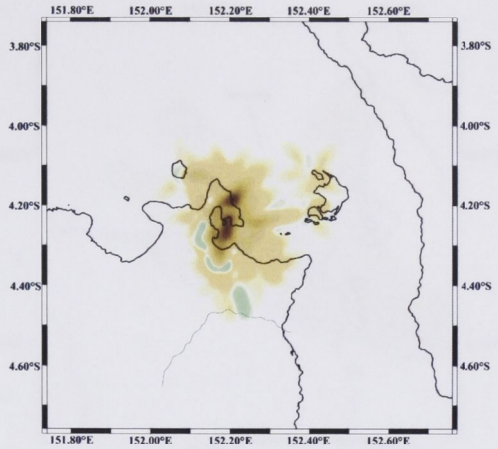

(b)

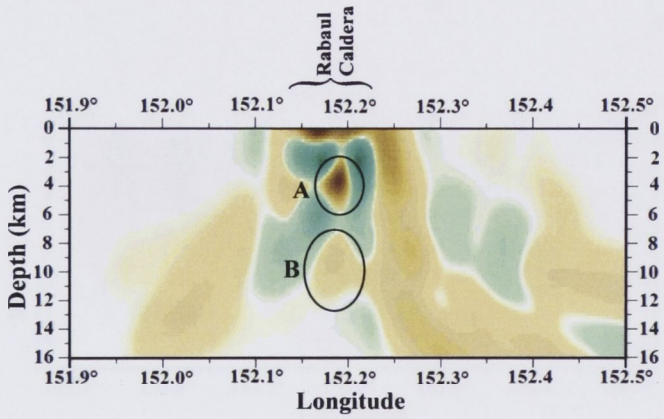

(c)

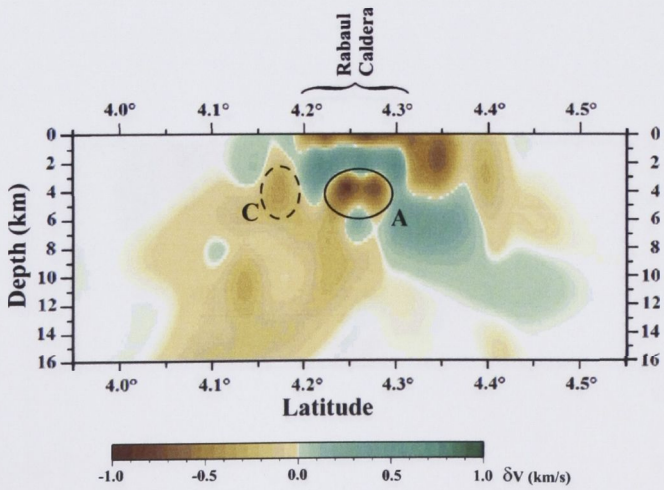

Fig. 4.8: P-wave velocity perturbation from the reference model in km/s for the local model using the pre- and post-eruption caldera earthquakes and all the regional earthquakes that fell within the local model domain. (a) Depth slice at 4.0 km. (b) W-E profile that passes through the centre part of the caldera at latitude 4.26°S. (c) N-S profile that passes through the centre of the caldera at longitude 152.20°E. The dashed and solid polygons marked by the letters A, B and C directly beneath Rabaul Caldera are possible magma bodies.

(a)

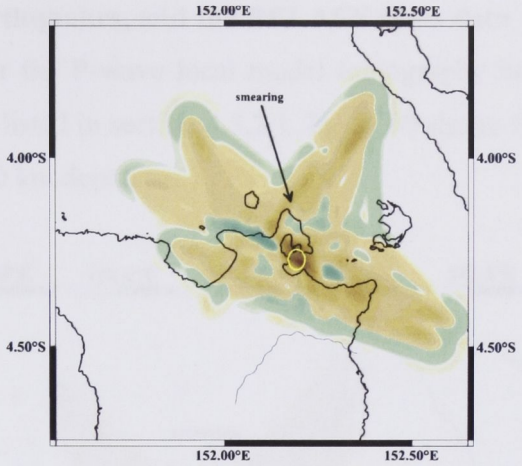

(b)

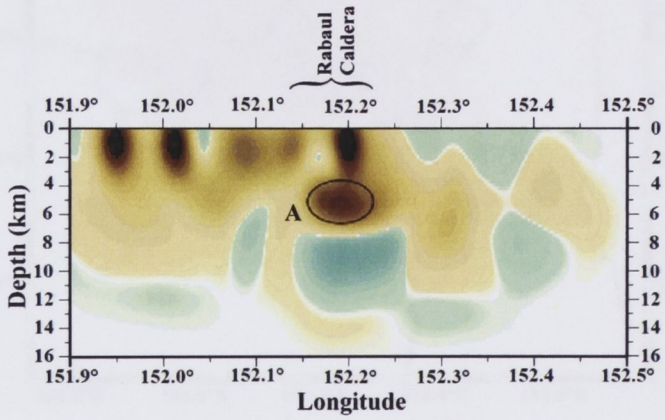

(c)

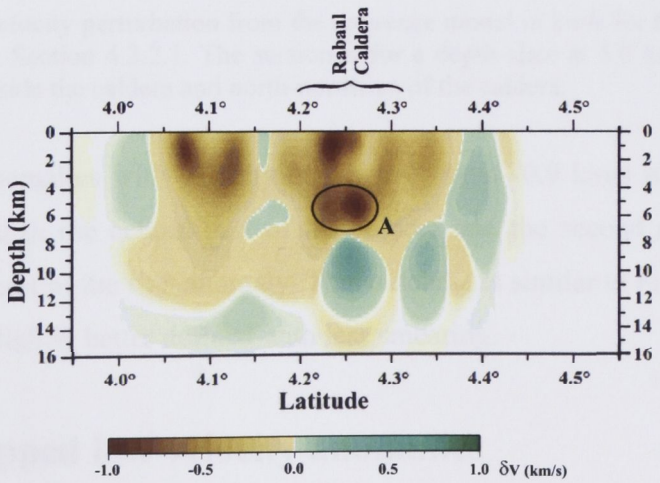

Fig. 4.9: P-wave velocity perturbation from the reference model in km/s for the local model using the RELACS data only. (a) Depth slice at 5.0 km. (b) E-W profile that passes through the centre part of the caldera at latitude 4.27°S. (c) N-S profile that passes through the centre of the caldera at longitude 152.19°E. The polygons in all three plots directly beneath the Rabaul Caldera mark a possible common magma body. Its depth is about 4-6 km.

4.3.3.2.3 Local model – Combined data of the regional and pre- and post-1994 eruption earthquakes, and the RELACS shots data

The final run for the P-wave local model tomography involved the simultaneous inversion of all the data listed in section 4.3.2.1. Fig. 4.10 shows the tomographic image of the outcome sliced at 5.0 km depth.

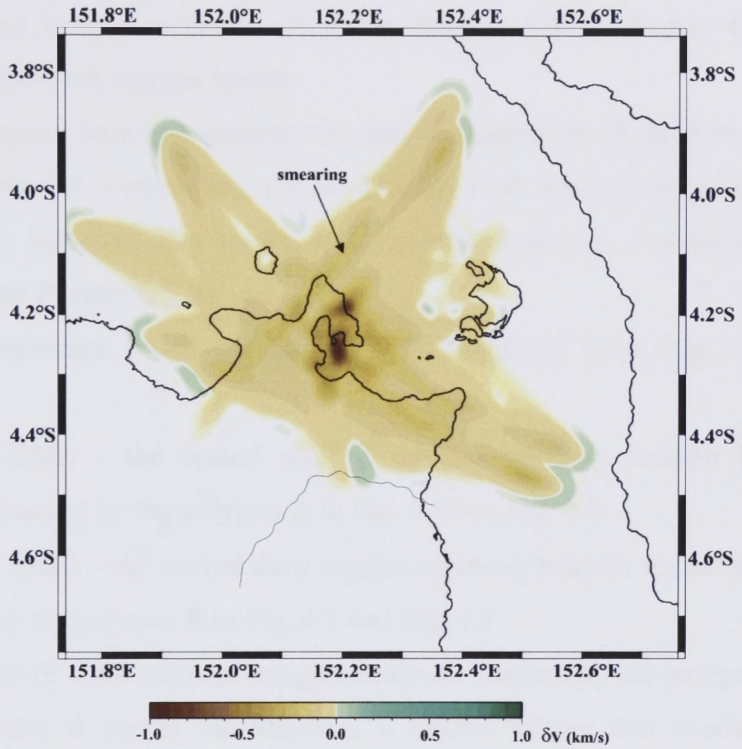

Fig. 4.10: P-wave velocity perturbation from the reference model in km/s for the local model using all the data listed in Section 4.3.2.1. The section is for a depth slice at 5.0 km. Note the two low velocity contrasts inside the caldera and north-northeast of the caldera.

Two prominent anomalies with velocity contrast of about -0.9 km/s stands out. The first anomaly is located in the central part of the caldera and the second anomaly is located north but slightly east of the first anomaly. This outcome is similar to Fig. 4.8a but here the latter anomaly is slightly better defined with less smearing.

4.4 The mapped low velocity anomalies

In this study three fairly well-defined low velocity anomalies have been mapped. They are denoted by the polygons **A**, **B** and **C** in Fig. 4.7, Fig. 4.8 and Fig. 4.9. Two are located directly beneath Rabaul Caldera at depths 3-6 km and 7-14 km. The third anomaly is located outside the caldera in a north-northeast direction (Fig. 4.8a) at similar depth to

the shallow body beneath the caldera. I have associated these anomalies with magma bodies in the same way other volcano-related tomographic studies (Husen et al., 2004; Pearson, 2000) have associated low velocity anomalies with magma bodies. But in this study some of the key reasons for linking the anomalies to magma bodies are because they are located directly beneath or in the proximity of Rabaul Caldera, their location with respect to the active volcanic centres, and the fact that physical phenomena like volcanic earthquakes have been associated with them. Section 6.4 in Chapter 6 presents more thoughts about the three magma bodies.

S-wave travel time tomography was also conducted for all the data sets. Due to the inadequate number of S-wave data a V_p/V_s ratio of 1.78 was used to provide an estimate for the S-wave velocity. The tomographic results from the S-wave information are comparable to the P-wave results.

For convenience I will use the following notations from here on for the three magma bodies:

- CSMR – the central shallow magma reservoir beneath Rabaul Caldera denoted by the polygon **A** in Fig. 4.8 and Fig. 4.9.
- CDMR – the central deep magma reservoir beneath Rabaul Caldera denoted by the polygon **B** in Fig. 4.7 and Fig. 4.8.
- RMR – the northeast magma reservoir denoted by the polygon C in Fig. 4.8. Here R stands for Rabuana, a coastal village that overlies this magma reservoir.

It is difficult to determine absolute dimensions of anomalous structures from tomographic images due to issues associated with data and model parameterization, the choices of ϵ and η, also known as the damping and smoothing parameters, and the smearing effects in the image itself. In this study I attempted some dimension estimates for the three magma reservoirs using the ±0.6 - ±0.7 km/s velocity contrast mark as the cut-off point. However, this threshold is reduced below the cut-off mark if there is great contrast between an anomalous feature and the surrounding region. An example for this is the anomaly denoted by **B** in Fig. 4.8b.

The estimated dimensions for the three magma bodies are as follows:

- CSMR: 30 – 40 km^3
- CDMR: 180 – 240 km^3
- RMR: 10 – 20 km^3

4.5 Comparison with previous tomographic studies

Finlayson et al. (2003), Bai and Greenhalgh (2005) and this study all mapped the CSMR. Finlayson et al. (2003) determined a depth of 3-6 km for the CSMR. Bai and Greenhalgh (2005) had a depth of about 3-4 km. This study has a depth that is similar to Finlayson et al. (2003). This study and Bai and Greenhalgh (2005) also mapped the CDMR. This study had a depth of about 7-14 km for the CDMR. Bai and Greenhalgh (2005) determined a depth of about 12-18 km. Furthermore this study and the Bai and Greenhalgh (2005) also mapped the RMR.

Some estimate for the volumes of the supposedly mapped magma bodies were conducted by Finlayson et al. (2003), Bai and Greenhalgh (2005) and this study. Finlayson et al. (2003) estimated the volume of the CSMR to be about 30-35 km^3. Bai and Greenhalgh (2005) estimated a much bigger volume of about 96 km^3 for the same body. This study has estimated a volume of 30-40 km^3, which is quite comparable to the estimate by Finlayson et al. (2003).

The depths for the magma bodies determined by the three studies are quite different however there is a depth range that is common to all. For instance, the three studies suggest the depth of the CSMR range between 3 and 6 km. The common depth range that they all have is between 3 and 4 km. Similarly, the common depth range for the CDMR between Bai and Greenhalgh (2005) and this study falls between 12 and 14 km.

The volume estimates for the three magma bodies are as follows. The volume of the CSMR determined by Bai and Greenhalgh (2005) is nearly three times the volumes determined by Finlayson et al. (2003) and this study. As for the RMR, the volume determined by Bai and Greenhalgh (2005) is nearly twice the volume determined in this study. Generally the volumes determined by Bai and Greenhalgh (2005) are greater than the values determined by the other two studies.

4.6 The 3-D velocity model for 3-D earthquake location

As mentioned in an earlier part of this chapter, due to the inadequate number of S-wave arrivals a V_P/V_S ratio of 1.78 was used to determine the corresponding 1-D V_S. This 1-D V_S was used to construct the 3-D S-wave velocity model. The resulting 3-D P- and S-wave velocities were used to conduct the 3-D hypocenter determinations that are discussed in the next chapter.

Chapter 5

3-D earthquake hypocenter determination

5.1 Hypocenter determination

The precise location of earthquake hypocenters is an ongoing research problem for many seismologists. The spatial location and origin time of the initial seismic disturbance is sought indirectly from the arrival times for suitable seismic phases. A further requirement to determine these parameters is an appropriate velocity model. The arrival times correspond to the times at which an array of receivers picks up the first seismic disturbance from a seismic source. The velocity model contains information on the speed at which seismic waves propagates through the medium between the source and the receiver. In essence, a high speed medium would allow a seismic wave to propagate faster than a slow speed medium. Arrival times from the receiver array and the velocity information are used to invert for the seismic wave travel times in order to estimate the hypocenter parameters. The hypocenter parameters include the three spatial coordinates (latitude-x_h, longitude-y_h and depth-z_h) and the origin time (t_h) of the seismic disturbance. Usually a minimum of four receivers are needed to obtain a reasonable location, however, with the advancement in seismological equipment and data processing algorithms in recent times, the same information, but with less accuracy, can be obtained using information recorded by a single 3-component receiver.

Many routine traditional hypocenter location algorithms like HYPO71 (Lee and Lahr, 1975) and HYPOINVERSE (Klein, 1978, 2000) use velocity models comprising homogeneous horizontal layers. However in real life the actual earth is far from this ideal state, and so unavoidable location uncertainties or errors are usually introduced. The heterogeneous properties of the earth are evident from tomographic and other related studies of the globe and the smaller regional and local models (Kennett et al., 1995; Widiyantoro et al., 2000; Debayle and Sambridge, 2004; Kennett et al., 2004; Fishwick,

2005). Uncertainties in the estimate of earthquake hypocenters can also be introduced by other sources as discussed in Section 5.3

5.2 3-D hypocenter determination

To overcome the limitations of earthquake hypocenters associated with horizontally layered homogeneous velocity models, people are beginning to move towards the routine application of 3-D velocity models. This is not to say that the application of 3-D velocity models for hypocenter determination is completely new. People have been conducting simultaneous relocation of large amounts of earthquake datasets during seismic tomography, while attempting to determine more realistic 3-D P- and S-wave travel times to represent the 3-D velocity field (Aki and Lee, 1976). Since such tomographic inversion is conducted iteratively, the relocated hypocenters are improved after each iteration as the velocity field improves. In more recent times people have developed single-event 3-D earthquake location algorithms for routine applications (Lomax et al., 2001; Husen et al., 2003; Chen et al., 2006). These developments arise from knowledge of improved 3-D velocity fields due to improvements in data acquisition systems, receiver array geometries, large volumes of high quality data and faster computer power.

5.3 Sources of error in hypocenter determination

Errors in earthquake hypocenters are inevitable no matter what level of care is undertaken to eliminate them. So the hypocentral solution that is obtained by the location algorithm is usually the best representation of the hypocenter with the given data and knowledge of the earth, and not the actual location. Different earthquake location algorithms express this error in different ways, however most of them usually assign a number to each of the four main hypocentral parameters (latitude, longitude, depth and origin time) to define the error level. For the spatial parameters given by the latitude, longitude and depth, these errors define the principal axis of an ellipsoid, so the hypocentral solution can be located anywhere within the bounds of the ellipsoid.

Errors can arise from various sources. I have discussed some of the more common ones below.

5.3.1 Location of seismic receivers.

5.3.1.1 Location

The location of a receiver is defined by the latitude and longitude. One to two decades ago these parameters were derived from topographic maps and there would have been a tendency to introduce errors of the order of tens to a couple of hundred meters, depending on the scale of map used. Errors associated with receiver location have reduced significantly with the introduction of GPS measurements.

5.3.1.2 Elevation

Receiver elevation is usually referenced to the mean sea level. Likewise the receiver location, receiver elevations were, and are still today, derived from topographic maps. This error source becomes critical when receivers are located at very high altitudes in mountainous regions. The differences in elevation between different receivers can also be important.

Errors arising from receiver locations are more critical in cases where the area for the receiver array is small and the number of receivers is small. It decreases as the array area and the number of receivers increases. These errors can be controlled by obtaining more accurate measurements for the receiver locations and elevation by using differential GPS measurements and also by increasing the number of receivers in a well-laid out array geometry by taking into consideration the purpose and area of study.

5.3.2 Array geometry

The geometry of receiver arrays can have a lot of influence on the hypocentral parameters determined by any one hypocenter determination algorithm. It is widely acknowledged that earthquakes that occur within an array tend to have smaller errors than earthquakes located far away from the receiver array. The thumb of rule is the greater the distance of the earthquake is from the receiver array the greater the error of the solution becomes. This is because the azimuth coverage between the array and the source starts to dwindle.

5.3.3 Phase picking

Errors associated with phase picking can be quite important. The errors depend very much on two factors. The first is the signal to noise ratio on the seismogram and the

second is how the phase picking is done; manual or automatic. Manual picking is considered to be more accurate, however it can be very labour-intensive if the number of seismograms to be read is large. Even if the number of seismograms is small and the picking is done manually, when the signal to noise ratio is low the chances for picking the correct onset can be quite far from the true onset. This is where analysts make their best guesses based on judgment but these guesses can be off as much as 1-2 seconds, particularly for emergent arrivals. In these circumstances filtering is normally applied to remove the noise and hopefully improve the signal to noise ratio (Fig. 5.1) for better picks. Automatic phase picking is good when many seismograms are to be read, and the signal to noise ratio is high. In practice, analysts normally re-read automated arrival picks if the residual for any particular station appear anomalous.

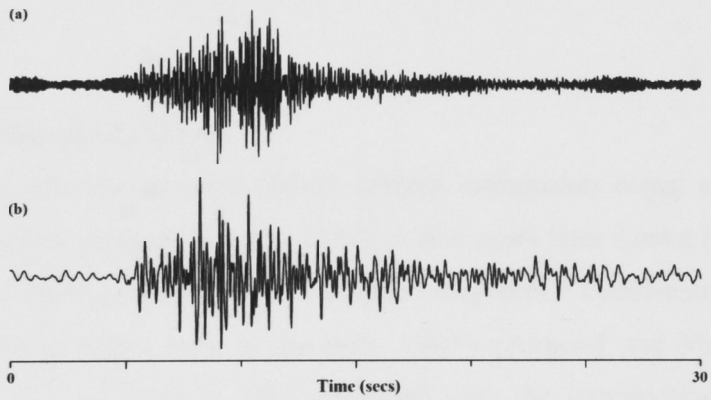

Fig. 5.1: Seismogram from RAL station for a high frequency earthquake. (a) Original signal. Note the very high frequency background noise. (b) The same signal after filtering. Here a Butterworth bandpass filter is applied. The cut-off frequencies are 0.1 and 5.0 Hz.

5.3.4 P- and S-wave velocity models.

P-wave velocities are calculated from the above information and interpolations and approximations are applied in the calculations. So any errors in the station locations and phase picks, together with the interpolations and approximations, are passed on to the calculated velocities, which sometimes can be far from the true velocity. Errors attributed to S-wave velocities are more critical because when there is not enough S-wave information the ratio, V_p/V_s, is usually used to estimate the V_s. People have used V_p/V_s ratios ranging between 1.5 to 2.0 to determine S-wave velocities for environments similar to Rabaul.

It is worth re-iterating that 1-D horizontally-layered homogeneous velocity models are usually far from the true earth and so earthquake hypocenter errors, especially the depth, associated with them are no doubt greater than errors associated with 3-D heterogeneous velocity models because the latter represent the earth more appropriately.

5.3.5 P- and S-wave travel times

Calculation of travel times directly or indirectly uses most of the information listed above. Therefore any errors embedded in them will be passed onto the calculated travel times.

5.4 Earthquake locations at RVO

The following sections give a brief history of earthquake locations at RVO since the early 1970's.

5.4.1 1-D earthquake locations

Epicenter determination for Rabaul caldera earthquakes began as early as 1970's using manual scaling methods (Cooke, 1972). A few years later Cooke (1977) produced a seismic pattern that resembled a D-shaped ring-fault. Consistent computer-based earthquake locations began only in the early 1980's (Almond and McKee, 1982). The introduction of PC's at RVO in 1985 coincided with the introduction of an improved earthquake location algorithm, the FASTHYPO (Herrmann, 1979). All the previous earthquakes were relocated thereafter using the velocity model shown in Table 5.1. The epicentral distribution for the earthquakes up to 1994 is shown in Fig. 5.2.

The velocity model is a horizontally layered homogeneous one derived from three seismic experiments conducted in 1966 (Cifali, 1969), 1969 (Finlayson and Cull, 1973) and 1982 (Almond and McKee, 1982). The top nine layers of the velocity model are derived from Almond and McKee (1982). The model has strong velocity gradients with depth. The deeper interface at 4 km is derived from Finlayson and Cull (1973). Cifali (1969) puts this interface at 6 km.

Table 5.1: Current 1-D velocity model used by RVO for earthquake locations.

Layer	Depth (km)	V_p (km/s)
1	0.00	1.70
2	0.25	2.06
3	0.50	2.43
4	0.75	2.79
5	1.00	3.15
6	1.25	3.51
7	1.50	3.88
8	1.75	4.24
9	2.00	4.60
10	4.00	6.11

Jones and Stewart (1997) pointed to possible ambiguities in this velocity model. They noted the distinct banding of earthquakes at 0 and 2 km depth, and demonstrated the shift of events associated with the 4km interface simply by changing this value in the model.

The opportunity to check the reliability of the velocity model and to improve or determine an alternative model was realised in the form of the RELACS project. RELACS is the acronym for Rabaul Earthquake Locations and Caldera Structure Survey. The project was one component of the AusAID-funded Twinning Program for RVO and managed by Geoscience Australia (Finlayson, 2003). Geoscience Australia, The Australian National University, Hokkaido University, University of - Madison and RVO conducted the project in 1997/1998.

5.4.2 3-D earthquake locations

3-D earthquake location was first introduced at RVO in 1999 (Mori, pers. comm.). The algorithm named RAB3D was generated from a modified version of FASTHYPO (Herrmann, 1979) that used a 3-D velocity model. The 3-D velocity model was the outcome of the RELCAS project (Finlayson et al., 2003) and was constructed from receiver travel time residuals. The use of the algorithm did not mature due to changes in the data acquisition system at RVO and also changes to some of the seismic stations of the network array. The ineffective use of RAB3D was more of a technicality rather than the failure of the algorithm itself.

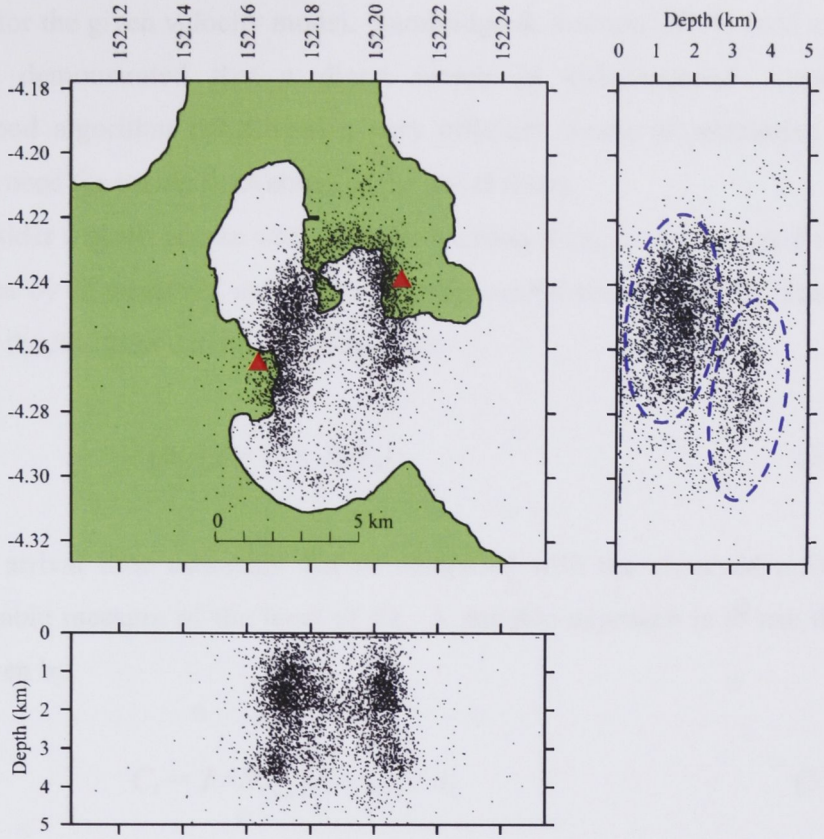

Fig. 5.2: Distribution of earthquakes at Rabaul Caldera between 1971 and 1994 located with FASTHYPO (Herrmann, 1978) and the 1-D velocity model shown in Table 5.1. The data is unfiltered. Note the concentration of events at 0 and 2 km depth.

5.5 The 3-D earthquake location algorithm – *Shak3_na*

In this study I have developed a new non-linear 3-D earthquake location algorithm, *Shak3_na*, for routine applications. The program is based on the Neighbourhood Algorithm (NA). The 3-D P- and S-wave travel time fields derived from the local model in Chapter 4 are used in the program for the velocity field. The next section describes some aspects of the neighbourhood algorithm, the engine that drives *Shak3_na*.

5.5.1 Spatial search and travel times

Shak3_na is a 3-D earthquake location program developed for routine applications. It makes use of the Neighbourhood Algorithm and builds on the concepts developed by Sambridge & Kennett (2001) for teleseismic location.

The estimation of an event hypocenter can be regarded as a search in a 4-dimensional space (spatial location and origin time) for the region where the best fit is achieved between the observed arrival times and those predicted from the proposed

hypocenter for the given velocity model. Sambridge & Kennett (2001) used a 1-D velocity model and demonstrated that a direct search in 4-dimensional space using the neighbourhood algorithm constituted a very efficient means of estimating hypocenters without any need for taking derivatives of the travel times.

Consider a given source with a spatial location at (x_s, y_s, z_s) = x_s and origin time t_s, and recorded by N receivers with corresponding arrival time picks, N_t. The arrival time estimate for the ith phase can be constructed as;

$$t_{ci}(x_s,t_s) = t_s + t_{ri}(x_s) \tag{5.1}$$

The arrival time estimates can be compared with the observed arrival times (t_i) using a suitable measure of the level of fit. A suitable approach is to use the robust L1 measure given by,

$$C_t = 1/N_t \sum \left| t_i - t_{ci} \right| / \sigma_i \tag{5.2}$$

where σ_i is the estimate of the error in the ith observed arrival time. The use of a L_1 measure minimizes the influence of outliers with a limited dataset (Sambridge and Kennett, 2001).

For the case of a three-dimensional velocity model a fast method is needed to calculate the travel times. In shak3-na the travel times are constructed by interpolation in a grid of pre-computed times generated by the use of the fast-marching method that was employed in the tomographic inversions in Chapter 4. Using the concept of seismic reciprocity each receiver station is treated as a source and travel times for the first arriving energy of the particular wave type is calculated to all the points on a regular spatial grid. The full time field is stored for each of the set of possible receivers. When a hypocenter is tested 3-D linear interpolation is made in the stored array of times associated with the grid points to provide the requisite travel time to each receiver. There is a considerable overhead in calculating the time fields for both P- and S-waves for each possible receiver, but interpolation in the stored tables is very quick. As a result it is entirely practical to test many potential locations directly through the associated times rather than undertake the even more time consuming task of calculating derivatives for the 3-D model.

5.5.2 The Neighbourhood Algorithm

The search of the four-dimensional hypocentral space (t_s, x_s) to find the region where the best match to the observations occur (i.e. where C_l is least) is conducted using the neighbourhood algorithm method.

In essence the neighbourhood algorithm is a derivative-free method that searches a multi-dimensional space guided by a specified misfit measure (Sambridge, 1998). Full details of the neighbourhood algorithm are discussed in Sambridge (1999), however for the purpose of my thesis I have presented some of the key elements very briefly to give the reader some idea about the method.

The key idea behind the neighbourhood algorithm is the use of the spatial properties of Voronoi cells to directly guide the search in parameter space. Voronoi cells can be considered as the nearest neighbour regions (Fig. 5.3) to a point as defined by a suitable distance norm (Voronoi, 1908).

The neighbourhood algorithm uses some simple geometrical concepts. It makes use of two tunable parameters and does randomized, or stochastic, sampling of the parameter space. The two tuning parameters are the initial set of modes, n_s, and the number of models generated with the least misfit, n_r. Here is a summary of how the procedure works:

1. A initial set of n_s models are generated in parameter space.
2. The corresponding misfit for each model generated in Step 1 is calculated. The parameter space is then divided into a set of Voronoi cells. Each cell is characterized by the misfit within it.
3. The number of models with the least misfit, n_r, are determined and a uniform random walk is performed in each Voronoi cell to generate a new set of n_s models for each of the chosen n_r models.
4. The second step is repeated until some predefined criterion, like the lowest misfit, is achieved.

For my application to the earthquake hypocenter problem the neighbourhood algorithm has approximately the character of a contracting irregular grid in four-dimensional hypocenter space. In this case the irregular grid is represented by the Voronoi cells and the four-dimensional parameters are the spatial hypocenter location given by the latitude (x_s), longitude (y_s) and depth (z_s), and the origin time (t_s).

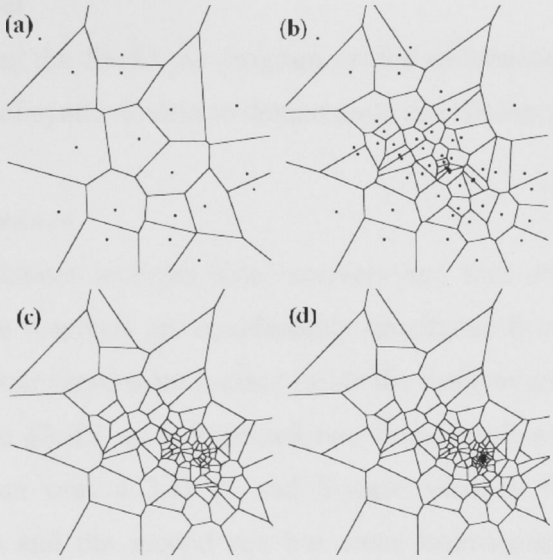

Fig. 5.3: Voronoi cells produced by the neighbourhood algorithm after (a) 1, (b) 5, (c) 10 and (d) 20 iterations. Note the contraction of the Voronoi cells to a central point shown in (d).

5.6 Application of *Shak3_na* for hypocenter determination

I have used *Shak3_na* to test its capability for conducting routine single-event locations with 3-D velocity models using four different datasets. The first is a synthetic dataset and this was used to verify the correct operation of the newly developed program. The other three datasets are a subset of pre-1994 eruption Rabaul Caldera earthquakes between 1971 and 1985, the post-1994 eruption Rabaul Caldera earthquakes and lastly some near-regional earthquakes recorded by the RHSN receiver array.

In all four cases the L_1 measure has been used to calculate the misfit between the actual and calculated arrival times. Furthermore, based on the experience of Sambridge & Kennett (2001) I have used n_s=9 and n_r=2 in the application of the neighbourhood algorithm so that 9 new hypocentral trials are inserted at each iteration and these points are placed into the two Voronoi cells that currently are associated with the least misfit. Since all of the hypocenter estimates to date are used to generate the next generation of Voronoi cells, the algorithm rapidly gains information on the character of the misfit distribution across the 4-D hypocenter space. I have worked consistently with a limited number of random number seeds that determine the placement of the initial 9 points in the 4-D space. Although, in principle, the outcome of the neighbourhood algorithm should be independent of the initial distribution of points, in practice the rate of convergence can be significantly accelerated by a good choice of seed for the random number generator. In this case I used 5590.

5.6.1 Synthetic Model

Prior to applying the *Shak3_na* program on the re-location of real earthquakes, I have applied it to a set of synthetic data to demonstrate its efficiency and effectiveness.

5.6.1.1 Data and procedure

The synthetic dataset includes nine receivers and four sources. The sources are listed in Table 5.2. The receivers are equidistantly distributed from each other in latitude and longitude and the four sources are located inside the receiver array (Fig. 5.4).

For the exercise *Shak3_na* is executed two times, each with 30, 60, 90 and 120 iterations. The first run uses a 3-D P- and S-wave velocity field calculated from a homogeneous medium and the second run has some heterogeneity introduced into the velocity field (Fig. 5.4). The starting hypocentral parameters (latitude, longitude and depth) where the search begins are located inside the receiver array and they are all different for each case. The horizontal starting points are at least 1-2 degrees away from the actual location and the starting depth is varied between ±5 to ±10 km from the actual depth. Since the locations of the sources are known, the main aim of the synthetic test is to determine how well *Shak3_na* is able to reproduce the original source parameters and how the misfit measure behaves for the two mediums with different velocity properties.

Table 5.2: Hypocentral parameters for the sources used in the synthetic test.

Event	Lat. (°S)	Long. (°E)	Depth (km)	Origin Time (secs)
1	41.100	139.200	30.0	0.00
2	41.000	140.700	20.0	0.00
3	39.900	139.400	60.0	0.00
4	39.900	140.700	70.0	0.00

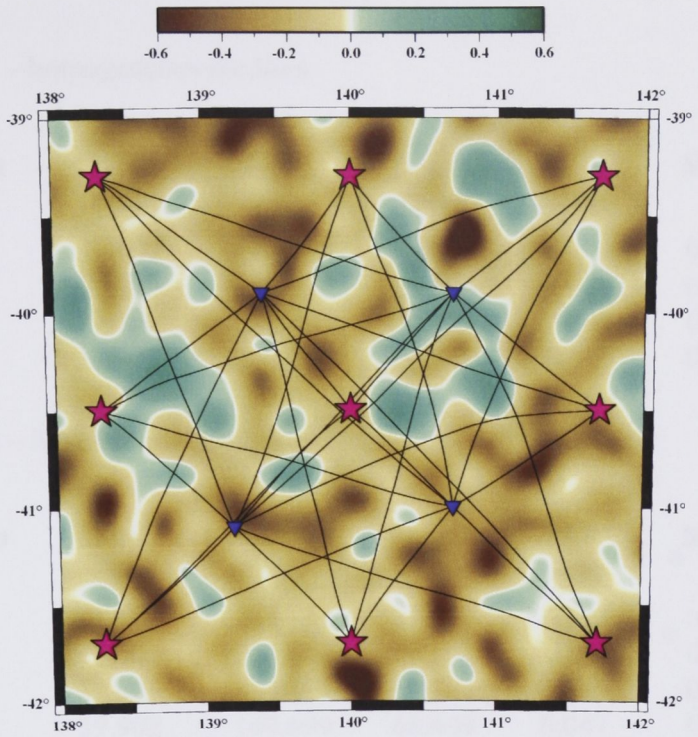

Fig. 5.4: Map view of receivers (pink stars) and sources (blue triangles) used in the synthetic test. They are over-laid on the 3-D-heterogeneous velocity model sliced at a depth of 10 km.

5.6.1.2 Recovered solutions

Generally the recovered information and the misfit measure improved dramatically with increased number of iterations for both mediums. Secondly the solutions for the homogeneous medium converged much faster than the heterogeneous medium. The re-located hypocentral parameters and the corresponding misfit measures for 120 iterations are shown in Table 5.3. The search results converged extremely well for the case of the homogeneous medium. In fact the original latitude and longitude values for all four sources are reproduced precisely. The depth estimates are very good, but not precise. This is not surprising, knowing well that depth is more difficult to resolve by any location algorithm due to vertical velocity ambiguities. Similarly, the misfit values are significantly smaller for the homogeneous medium compared to the heterogeneous medium. The non-recovery of the exact epicentral parameters and the slightly higher misfit values associated with the heterogeneous medium is not unexpected and could be attributed to the complexity of ray tracing in the heterogeneous medium.

Table 5.3: Relocated hypocentral parameters for the 120 iterations.

(a) Run 1 – homogeneous medium

Event	Lat. (°S)	Long. (°E)	Depth (km)	OT (secs)	Misfit
1	41.100	139.200	30.089	-0.011	0.006
2	41.000	140.700	19.504	-0.029	0.010
3	39.900	139.400	59.951	-0.008	0.004
4	39.900	140.700	69.834	+0.003	0.007

(b) Run 2 – heterogeneous medium

Event	Lat. (°S)	Long. (°E)	Depth (km)	OT (sec)	Misfit
1	41.103	139.198	31.863	-0.011	0.091
2	41.000	140.699	19.169	-0.017	0.021
3	39.901	139.401	59.324	0.013	0.024
4	39.902	140.699	68.409	0.047	0.072

Fig. 5.51 to Fig.5.53 shows the results of the 4-D parameter space search at different map scales for Events 3 obtained with the heterogeneous medium after 120 iterations. The search result is presented in three different map scales to conveniently demonstrate the manner in which the Voronoi cells contract rapidly to the best possible solution and in doing so trace the evolution of sampling as the location is refined. In this case the map scales considered are 400 x 400 (Fig. 5.31), 30 x 30 (Fig. 532) and 8 x 8 kilometers (Fig. 5.53). In Fig. 5.51 the centre of the plot corresponds to the starting point - 40.5°S, 140.0°E, and in Fig. 5.52 and Fig. 5.53 the centre of the plot is set to the epicenter of the source. The dots in the plots represent the tested epicenters and the change in colour reflects the level of misfit during convergence. In this case the purple dots represent higher misfits and each gradation in colour from blue, green, yellow to orange represent an improvement in the misfit. The black or grey area or region in the centre is an approximation of the error ellipse in the conventional scheme. The slices besides the main figure illustrate the manner in which the depth and the origin time converge to the best solution. The colour for the dots is the same as explained above.

The misfit measure tracking the pattern of convergence is shown in Fig. 5.54. The misfit value starts from about 39 and convergence becomes exhausted at 0.024 after about 40 iterations. The accuracy of the solution is about ±0.15 km.

The relocation of the synthetic dataset by *Shak3_na* reproduced the hypocentral parameters extremely well. The misfit measure representing the goodness of the locations also converged extremely well to a very small value. This demonstrates the effectiveness of the neighborhood algorithm technique in earthquake location problems, and in this case in a 3-D heterogeneous medium.

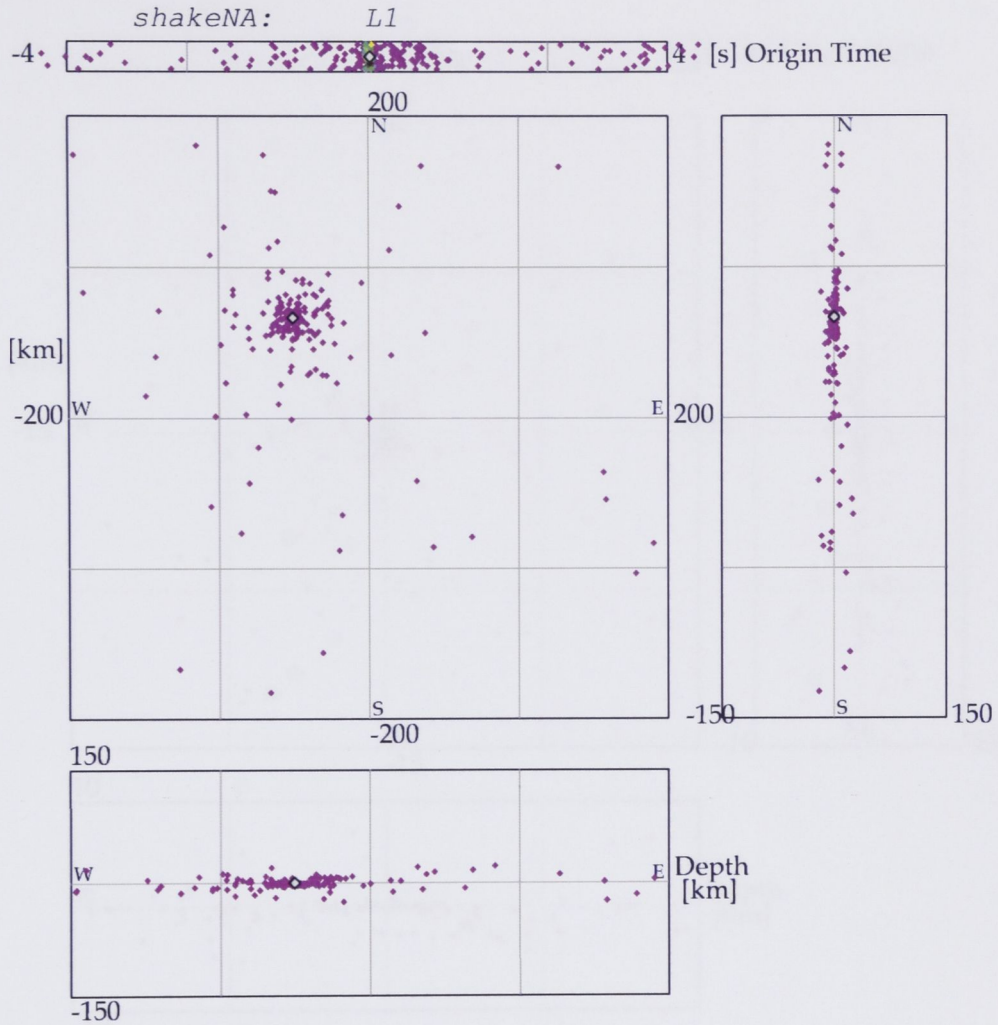

Fig. 5.51: Illustration of the neighbourhood algorithm progression towards convergence for Event 3 in the synthetic dataset. The search area is (400 X 400) km. The centre of the plot marks the starting search point. The area of strong clustering marks the best misfits.

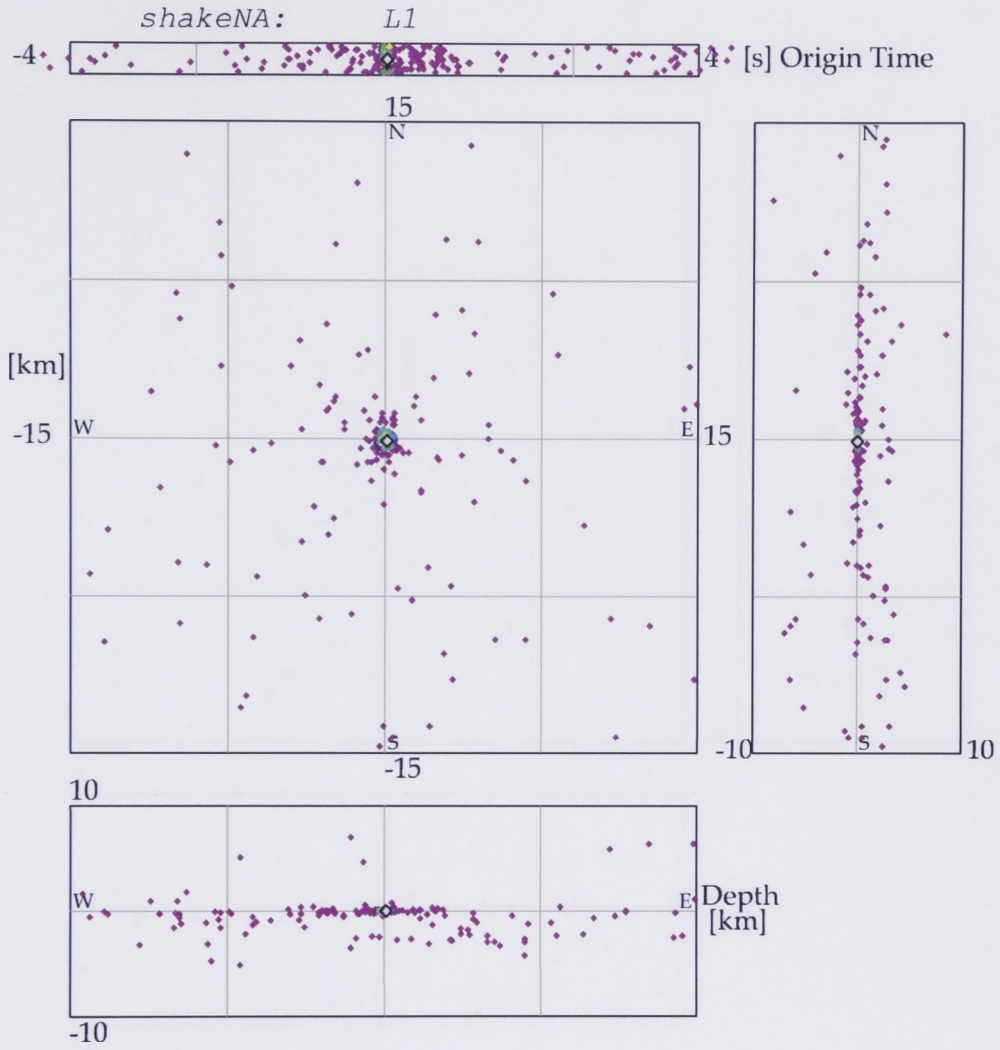

Fig. 5.52: Illustration of the neighbourhood algorithm progression towards convergence. The search area is (30 X 30) km. Here the centre of the plot is the source location. Note the spread of tested epicenters representing poor misfits and zooming in into the green zone showing the best misfits, almost overlapping with the source location.

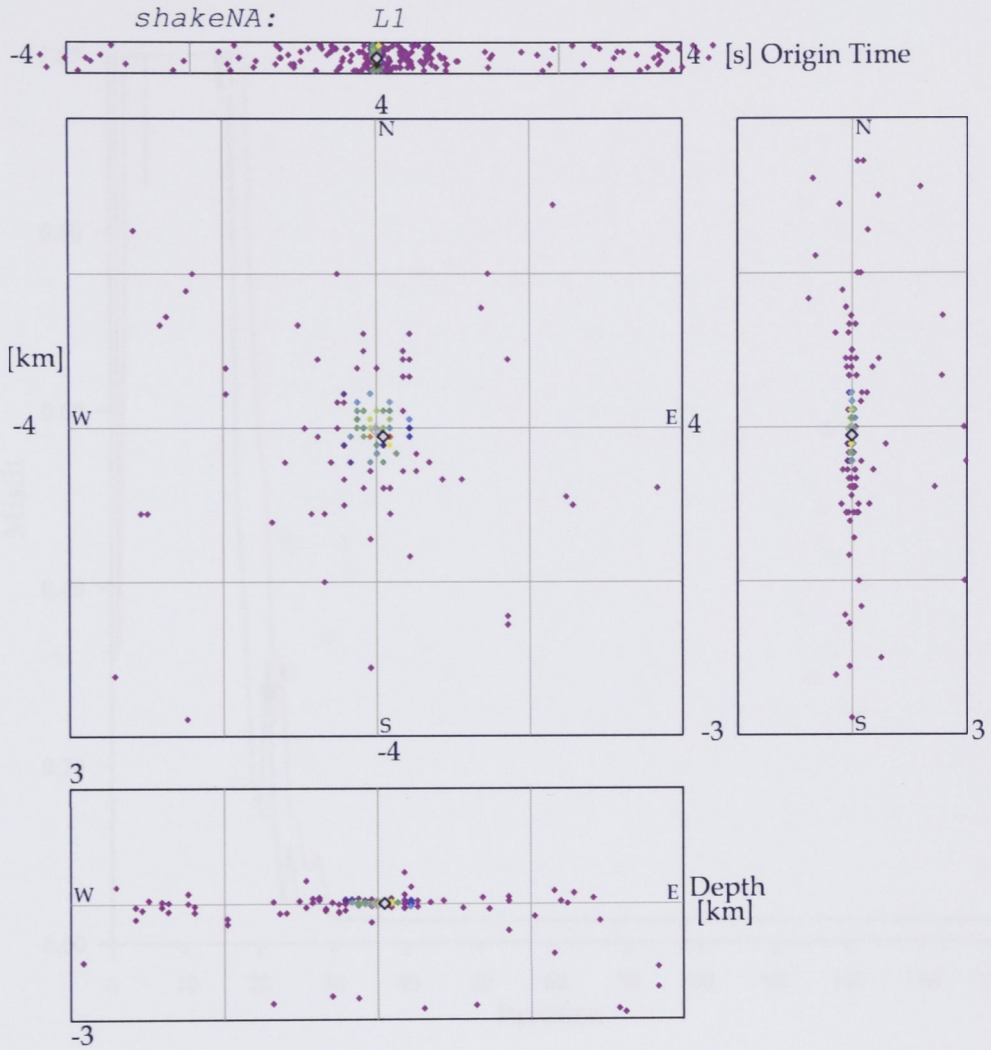

Fig. 5.53: Illustration of the neighbourhood algorithm progression towards convergence. The search area is (8 X 8) km. Here the centre of the plot is the source location. Note the change in colour from purple (poor misfits) to orange (good misfits) converging into the centre. The dark polygon near the centre is a representation of the error ellipse as in conventional schemes.

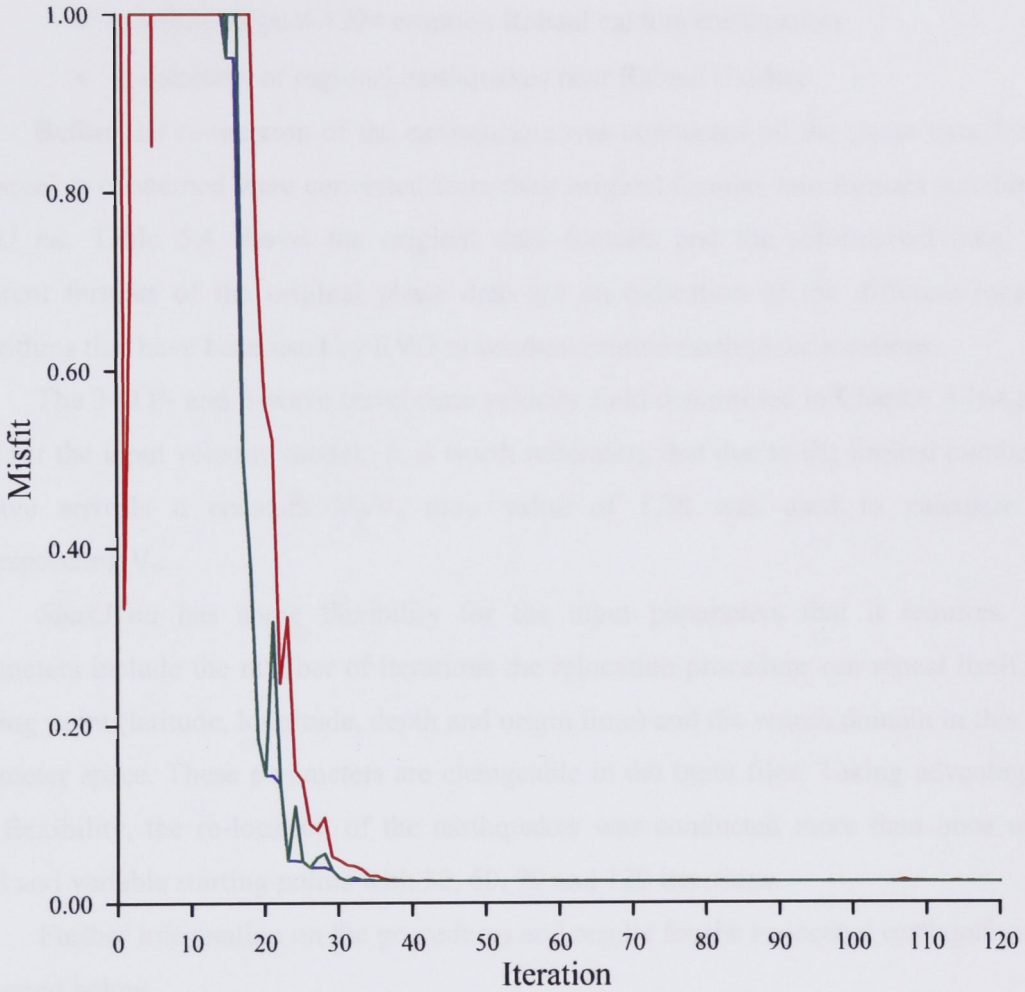

Fig. 5.54: Plot of misfit measure tracking the convergence of the neighbourhood algorithm for Event 3 in the synthetic dataset located with the heterogeneous velocity model for 120 iterations. Blue line is for the lowest misfit in the model, red is the average misfit and green is the current misfit. Convergence is exhausted between 30 and 40 iterations.

5.6.2 Re-location of earthquakes from Rabaul and the surroundings

Three groups of earthquakes were re-located with *Shak3_na* after its successful application with the synthetic data. The earthquakes include:

- a subset of pre-1994 eruption Rabaul Caldera earthquakes
- a subset of post-1994 eruption Rabaul caldera earthquakes
- a selection of regional earthquakes near Rabaul Caldera

Before the re-location of the earthquakes was conducted all the phase data for the earthquakes concerned were converted from their original formats into formats suitable for *Shak3_na*. Table 5.4 shows the original data formats and the reformatted data. The different formats of the original phase data are an indication of the different location algorithms that have been used by RVO to conduct routine earthquake locations.

The 3-D P- and S-wave travel-time velocity field determined in Chapter 4 has been used for the input velocity model. It is worth reiterating that due to the limited number of S-wave arrivals a constant V_p/V_s ratio value of 1.78 was used to calculate the corresponding V_s.

Shak3_na has some flexibility for the input parameters that it requires. The parameters include the number of iterations the relocation procedure can repeat itself, the starting point (latitude, longitude, depth and origin time) and the search domain in this 4-D parameter space. These parameters are changeable in the input files. Taking advantage of this flexibility, the re-location of the earthquakes was conducted more than once using fixed and variable starting points with 30, 60, 90 and 120 iterations.

Further information on the procedures and results for the re-located earthquakes are discussed below.

5.6.2.1 Pre-eruption Rabaul Caldera earthquakes

The subset of pre-1994 eruption Rabaul Caldera earthquakes includes 3600 earthquakes recorded by five or more stations by the RHSN between 1971 and July 1985. Almost all the earthquakes are located inside the RHSN array.

Due to the enormous number of pre-eruption earthquakes *Shak3_na* was executed in a batch (or Script) file to re-locate the earthquakes. In doing so a systematic quality check on the solutions for individual earthquakes was not conducted.

Table 5.4: Examples of the original phase data (a, b) and the reformatted data suitable for *Shak3_na* (c).

(a) Pre-1994 eruption data format

```
84  4 20 18  5
tav  12.12    1    .00  4
mtp  12.20    1    .00  4
ral  12.27    1    .00  4
rpt  12.60 d  0    .00  4
kal  12.75    1    .00  4
boi  13.25    1    .00  4
wan  13.26    1    .00  4
vul  13.37 c  0    .00  4
tka  13.85    1    .00  4
```

(b) Post-1994 eruption data format

```
RALZ P 1 960730092835.91
TALHIPU0 960730092836.17       38.63 S 2
KPTHEP+0 960730092836.47
VISZ P 2 960730092837.28
TUNHIPD0 960730092836.12
MALHEP 1 960730092836.97
JBHHIPD0 960730092835.85
BOIZIPD0 960730092835.51
         10
```

(c) *Shak3_na* phase data format

```
 EVENT
 RAB
  96   VII 30 09 28  33.51    0.50
   -4.265      5.0000
  152.190      5.0000
    4.000      3.0000
RAL  P         09 28 35.91  0.50
TAL  P         09 28 36.17  0.25
KPT  P         09 28 36.47  0.25
VIS  P         09 28 37.28  0.95
TUN  P         09 28 36.12  0.25
MAL  P         09 28 36.97  0.50
JBH  P         09 28 35.85  0.25
BOI  P         09 28 35.51  0.25
TAL  S         09 28 38.63  1.25
end
```

The earthquakes were re-located using fixed and variable starting points. For a fixed starting point, a point given by -4.265°S and 152.190°E was adopted for the horizontal position with a range of depths. This point is located almost at the centre of the Rabaul Caldera. For the other case, the variable starting point, the original 1-D hypocentral solutions of RVO were used for each earthquake.

The hypocentral distribution for the re-located earthquakes with different combinations of starting epicenter and depth for 120 iterations are shown in the series of plots in Appendix B (Fig. B-1 to Fig. B-6). Note that this is only a sample of the solutions from more than a dozen runs. Others were eliminated due to similarities with others, uncontrolled scattering and misfit considerations. There are two plots for each case. The first plot is for all the re-located earthquakes and the second plot is only for earthquakes with misfit values of less than 0.015. Data filtering is applied in many research areas and in most cases it is done in order to eliminate data with very anomalous uncertainties. However, it has been demonstrated that comparable results can still be obtained without filtering of data (Jones and Stewart, 1997; Nicholson et al., 2000). The choice of the above misfit value (0.015) to select the best results was made after exhaustive examination of a range of values with the aim of reducing the scatter of events, but at the same time retaining sufficient number of earthquakes that could be used to infer useful structural information about the caldera.

Generally all the plots, inclusive of the complete and the selected dataset, reproduced the elliptical ring-fault extremely well irrespective of the different starting points employed during each re-location procedure. Besides the general outlook, the strong concentration of earthquakes on the two N-S trending arcuate faults on either side of the ring-fault and the fewer number of earthquakes on the south to southeast quadrant of the ring-fault are reproduced considerably well. But as mentioned earlier the main difference between each pair of plots is the significant reduction in the scatter of epicenters away from the main axis of the ring-fault for the selected results. This is a clear demonstration on how filtering can improve a blurry image. Fig. 5.6 is an alternative colour-coded plot for Fig. B-5(a) based on the misfit values. The number of earthquakes for each misfit range is listed in Table 5.5.

Note the distinct scattering of earthquakes denoted by the purple, brown and black circles. This corresponds to earthquakes with misfit values greater than 0.020. Also note the location of Tavurvur with respect to the ring-fault. There is a marginal shift in the

locations from the original RVO solutions. The relocated solutions put Tavurvur almost on the ring-fault. The position of Vulcan with respect to the ring-fault is virtually unchanged. These positions may have some implications on the eruptive patterns for both volcanoes.

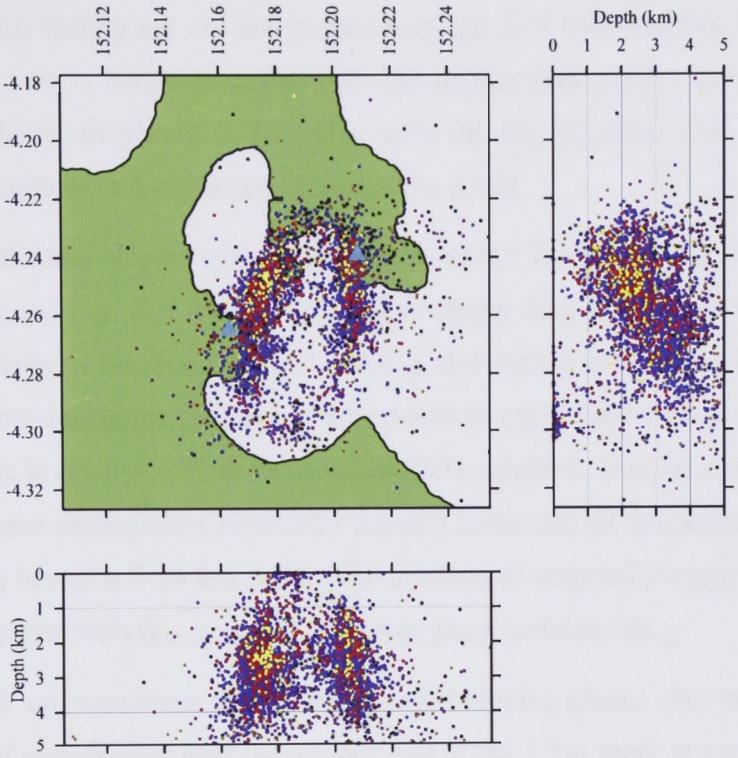

Fig. 5.6: Colour-coded plot showing the distribution of re-located epicenters and depths from a fixed starting position of -4.265°S and 152.190°E and depth 4 km. The search domains are $\pm 0.20°$ and ± 4.0 km, respectively. The aim of the plot is to emphasise the impact of scattering which is controlled by the location misfits. The description for the colour codes are given in Table 5.3.

Table 5.5: The particulars of the data plotted in Fig. 5.6.

Colour Code	Misfit range	No. of earthquakes
Yellow	0.000 – 0.005	163
Red	0.006 – 0.009	413
Blue	0.010 – 0.019	1423
Purple	0.020 – 0.029	832
Brown	0.030 – 0.039	371
Black	0.040 – 0.100	351

A range of starting depths and corresponding search domain were applied during the re-location of the earthquakes. The resulting depth sections are again displayed in the series of plots in Appendix B. As a special case Fig. B-1 mimics those of Fig. 5.2 quite

well and the reason is because during the relocation the depths were fixed to the original RVO depths. Note the strong concentration of earthquakes on the N-S cross-section near the surface and 2.0 km depth still present in the unfiltered data, but are eliminated from the selected hypocenters. The rest of the N-S cross-sections are different from Fig. B-1. Instead of having two layers as clearly shown in the S-N cross-section in Fig. B-1, the others seem to have a single structure with the earthquakes getting deeper towards the south. This is better displayed in the plots with the filtered data. The earthquakes are shallow at the northern end and deepen towards the south.

The earthquake depths range between about 0.5 km and about 5.0 km for most except Fig. B-2 and Fig. B-4 where earthquakes deeper than 4.0 km are far less than the others. The differences between Fig. B-2 and Fig. B-4 and the others could be attributed to the starting points during the location or they could be attributed to the 3-D velocity field. This depth range is consistent with the original RVO solutions. It is interesting though that there are no deeper earthquakes, especially beneath or around the proposed second magma reservoir sitting between 7-14 km depth. The absence of seismicity suggests any changes in activity associated with this magma body takes place aseismically.

The E-W cross-sections feature the outward dipping planes very well. The distinct concentration of earthquakes near the surface and at the 2 km mark is not shown. Instead the information displays a uniform depth transition. Jones and Stewart (1997) attributed the two lines of concentration to the 1-D velocity model that was used to locate the earthquakes.

To investigate the stability of the *Shak3_na* solutions for the various starting points a number of earthquakes were selected randomly to compare their horizontal and vertical positions and determine how they differed from one another. The earthquakes were selected from the list with misfits less than 0.15. The outcome of this investigation is shown in Fig. 5.7. It is evident from the figure that except for earthquake 8405040100, the horizontal positions of the other earthquakes are fairly tightly clustered within a 0.5 km radius. This value is within acceptable limits of error bars of 1.0 to 1.5 km that most people allow during qualitative and quantitative analysis. Moreover, the tight clustering of the horizontal positions of the earthquakes from *Shak3_na* is a good measure of the stability of the horizontal solutions, irrespective of the starting point. Earthquake 8405040100 has a fair scatter of about 1.0 km on the longitudinal axis and about 0.5 km on latitudinal axis.

The only earthquake that plotted well out of position is earthquake 8312282101 located with fixed horizontal starting point and fixed starting depth of 0.0±15.0 km.

The same stability cannot be accorded to the vertical positions. There is more scatter in the vertical positions, with most of them within 1.0 km. The earthquake with the greatest scatter in the vertical position is again earthquake 8405040100. The greater scatter in the vertical axis is not unusual considering the similar outcomes that were observed with the synthetic dataset. It reflects the complexities of heterogeneous media in the vertical axis.

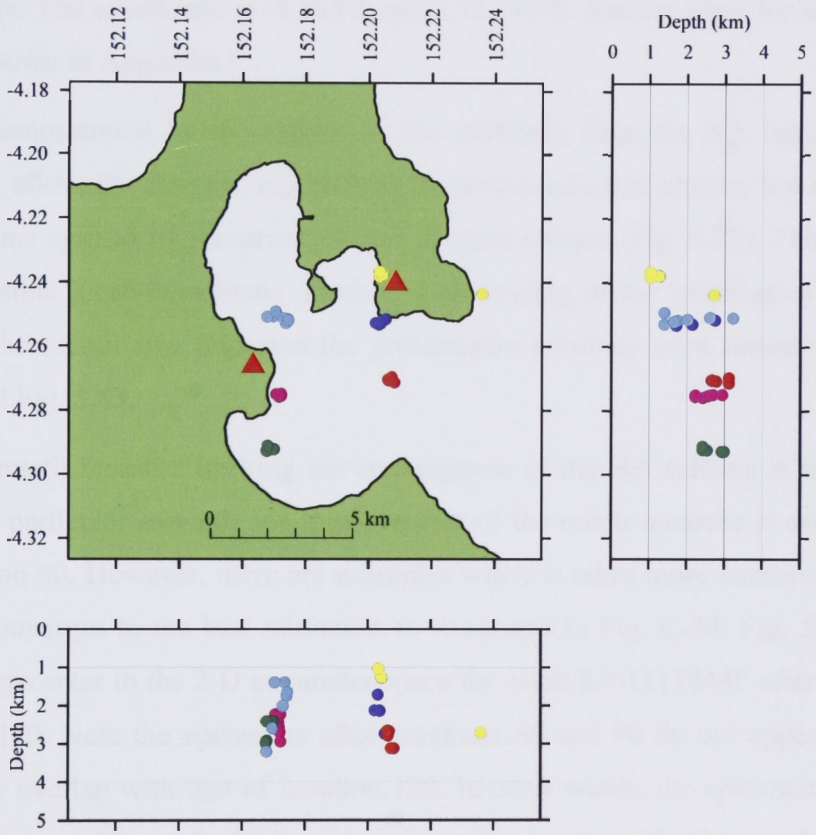

Fig. 5.7: The horizontal and vertical positions of the selected earthquakes to investigate the stability of the *Shak3_na* solutions using different starting points. The colour codes correspond to the earthquakes studied. Blue – 8101111444, red – 8103241806, magenta – 8310241800, purple – 8312282101, green – 8402180015, cyan – 8405040100. There are seven data points for each colour code, each corresponding to the different starting points and the Rabhypo solution, inclusive.

5.6.2.1.1 Behaviour of convergence for the NA procedure and misfits

The behaviour of convergence for the NA procedure and misfits has been studied using a handful of events selected randomly from different sections of the ring-fault. The events are selected from the re-location procedure that used a fixed starting horizontal

position of -4.265°S and 152.190°E and ±0.20 search domain, and 4.0 km depth with a ±4 km search domain. The progress of the NA scheme and the corresponding misfit measure towards the best fitting location by means of projection onto the spatial axes and a time bar for Event 8101111444F are shown in Fig. 5.81 to Fig. 5.84. The progress of the NA scheme is presented in three different map scales. The purpose for presenting the information in this manner is similar to the reasons given for the synthetic data. The size of the search areas that have been used are 40 x 40 km, 10 x 10 km and 4 x 4 km. In each plot the centre of the horizontal axis plot is fixed to the starting epicenter located at the center of the caldera. The coordinate is -4.265°S and 152.190°E. Similar plots for the rest of the events are shown in Appendix C.

As demonstrated by the results for the synthetic data, the NA initially explores much of the allowable domain, represented by purple-coloured circles, but rapidly shifts focus to a zone marked by the strong cluster of other colours (Fig. 5.81). This zone marks the best possible location estimate. Further re-processing of the information by reducing the size of the search area improves the presentation accuracy even further as shown by Fig. 5.82 and Fig. 5.83.

The misfit measure tracking the convergence of the NA scheme is shown in Fig. 5.84. In this particular example the improvement of the misfit measure is exhausted after about iteration 60. However, there are examples where it takes more iterations before this parameter converges to the best minimum as illustrated in Fig. C-34. Fig. 5.9 shows the shift of the epicenter in the 2-D parameter space for event 8101111444F after iteration 30, 60, 90 and 120. Note the epicenters after iterations 60 and 90 do not appear in the plot because they overlap with that of iteration 120. In other words, the epicenter cannot shift anymore because it has reached full convergence after iteration 60. This result is consistent with the observation derived from Fig. 5.84. For comparison, the original RVO epicenter is also plotted. The re-located epicenter is offset from the RVO location by 0.033 km on the latitudinal axis and 0.067 km on the longitudinal axis. These offsets are within the horizontal error bars of the RVO solution, which happen to be ±0.15 km and ±0.18 km for the latitude and longitude, respectively. Similar plots for the list of earthquakes studied are shown in Appendix D. Table 5.6 lists the latitudinal and longitudinal differences between the *Shak3_na* and RVO solutions for these earthquakes. It also lists the RVO horizontal error bars. Some of the differences are within the RVO error bars and the others are outside the error bars. However, the differences which lie outside the RVO error bars are still very

small so that it does not make a great degree of difference in the actual location. From the examples studied the earthquake that has the biggest difference between a *Shak3_na* solution and a RVO earthquake catalogue is Event 8405040100 with 0.189 km and 0.300 km, but in general these values are well within acceptable error limits.

Table 5.6: Latitudinal and longitudinal differences between the *Shak3_na* and the RVO solutions for the list of earthquakes studied. The RVO uncertainties are also listed.

Earthquake	**Difference (km)**		**RVO error bars (km)**	
Code	**Latitude**	**Longitude**	**Latitude**	**Longitude**
8101111444	0.033	0.067	0.15	0.18
8103241806	0.100	0.122	0.08	0.08
8310241800	0.011	0.122	0.31	1.40
8312282101	0.122	0.222	0.11	0.13
8402180015	0.178	0.011	0.80	1.20
8405040100	0.189	0.300	0.18	0.17

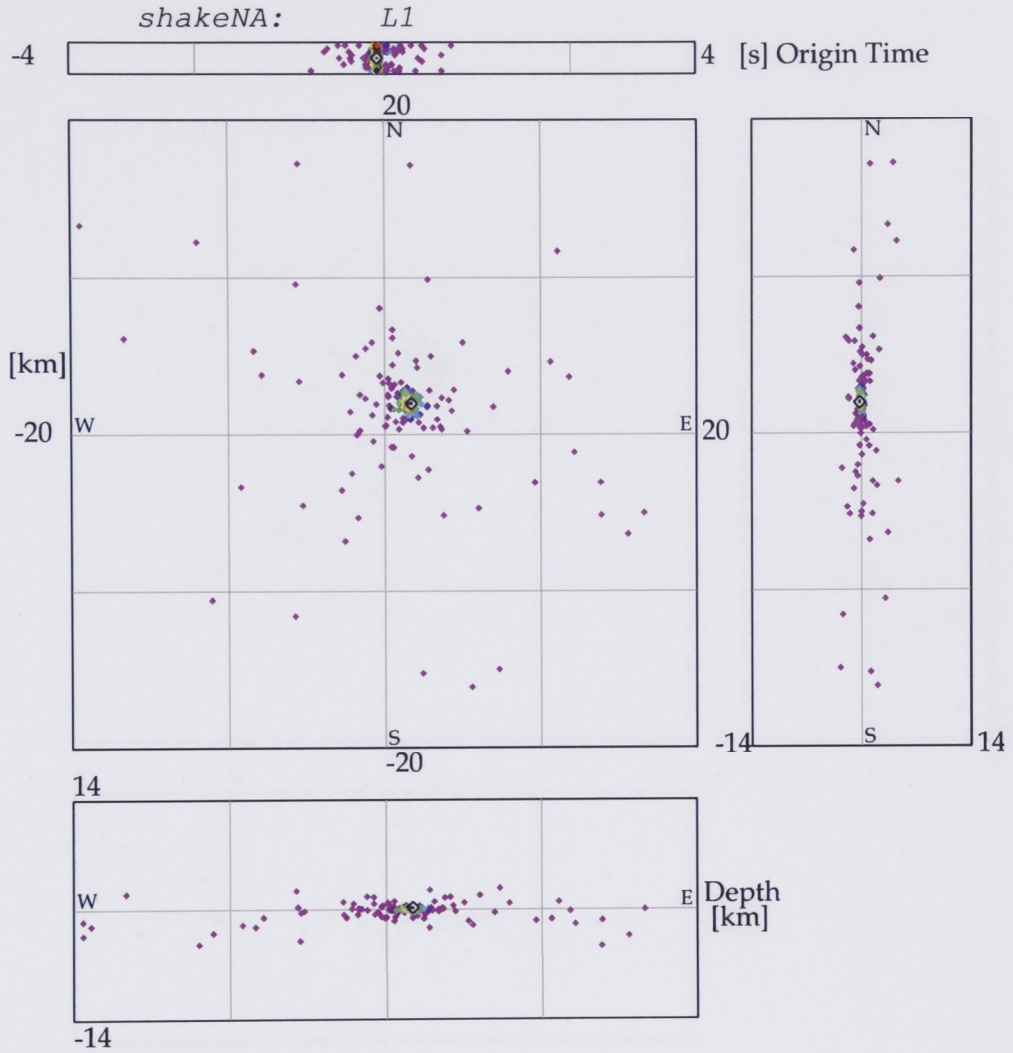

Fig. 5.81: Illustration of the neighbourhood algorithm progression towards convergence for Event 8101111444F in the 4-D parameter space. The horizontal search area is 40 x 40 km. The centre of the plot is the starting search point and is given by the coordinate -4.265°S and 152.190°E. Each circle, irrespective of colour, denotes the tested epicenters. Note the spread of the purple circles. These are tested epicenters with high misfits. The area of strong clustering marked by the coloured circles gives the best location estimate. Where they appear, the black circles have the least misfits.

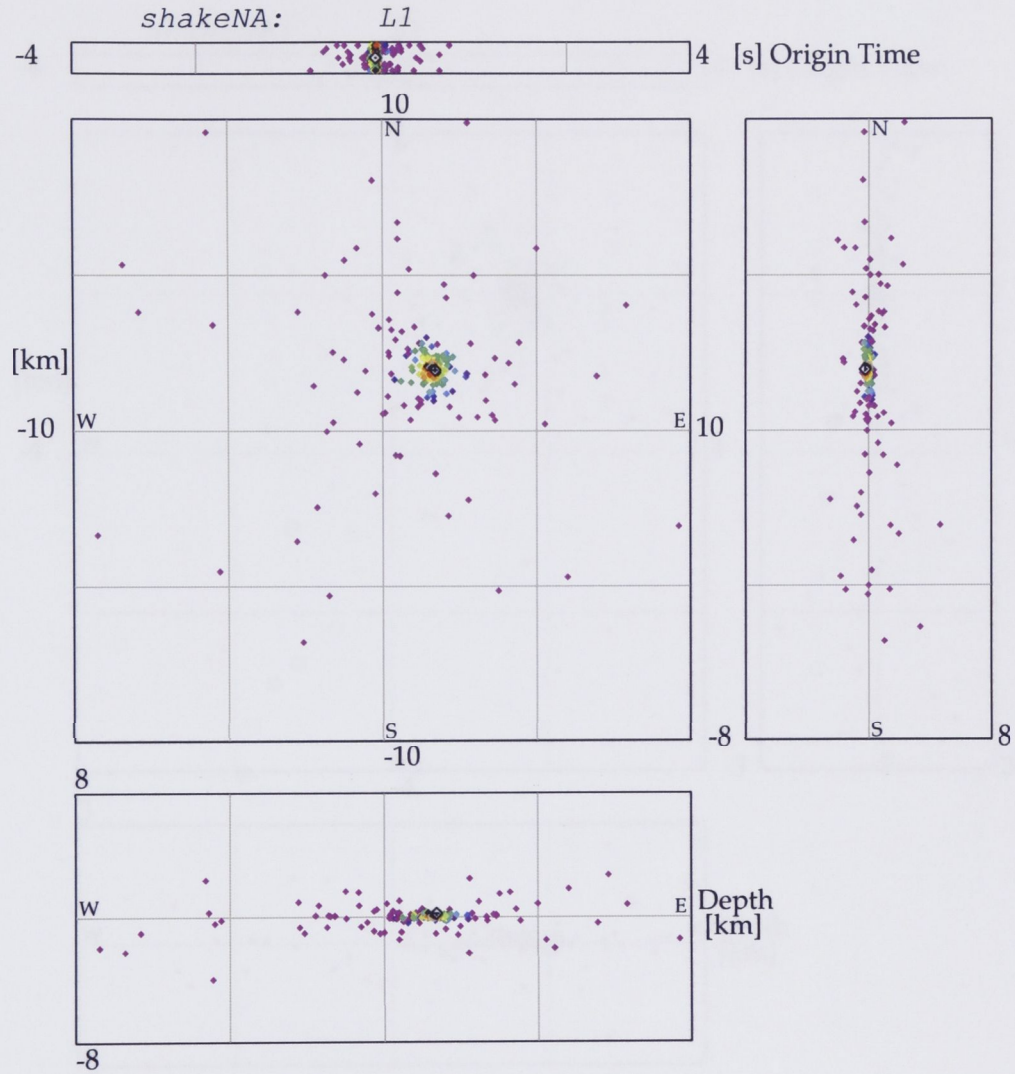

Fig. 5.82: Illustration of the neighbourhood algorithm progression towards convergence for Event 8101111444F in the 4-D parameter space. The horizontal search area is 20 x 20 km. The centre of the plot is the starting search point and is given by the coordinate 4.265°S and 152.190°E. Each circle, irrespective of colour, denotes the tested epicenters. Note the spread of the purple circles. These are tested epicenters with high misfits. The area of strong clustering marked by the coloured circles gives the best location estimate. Where they appear, the black circles have the least misfits.

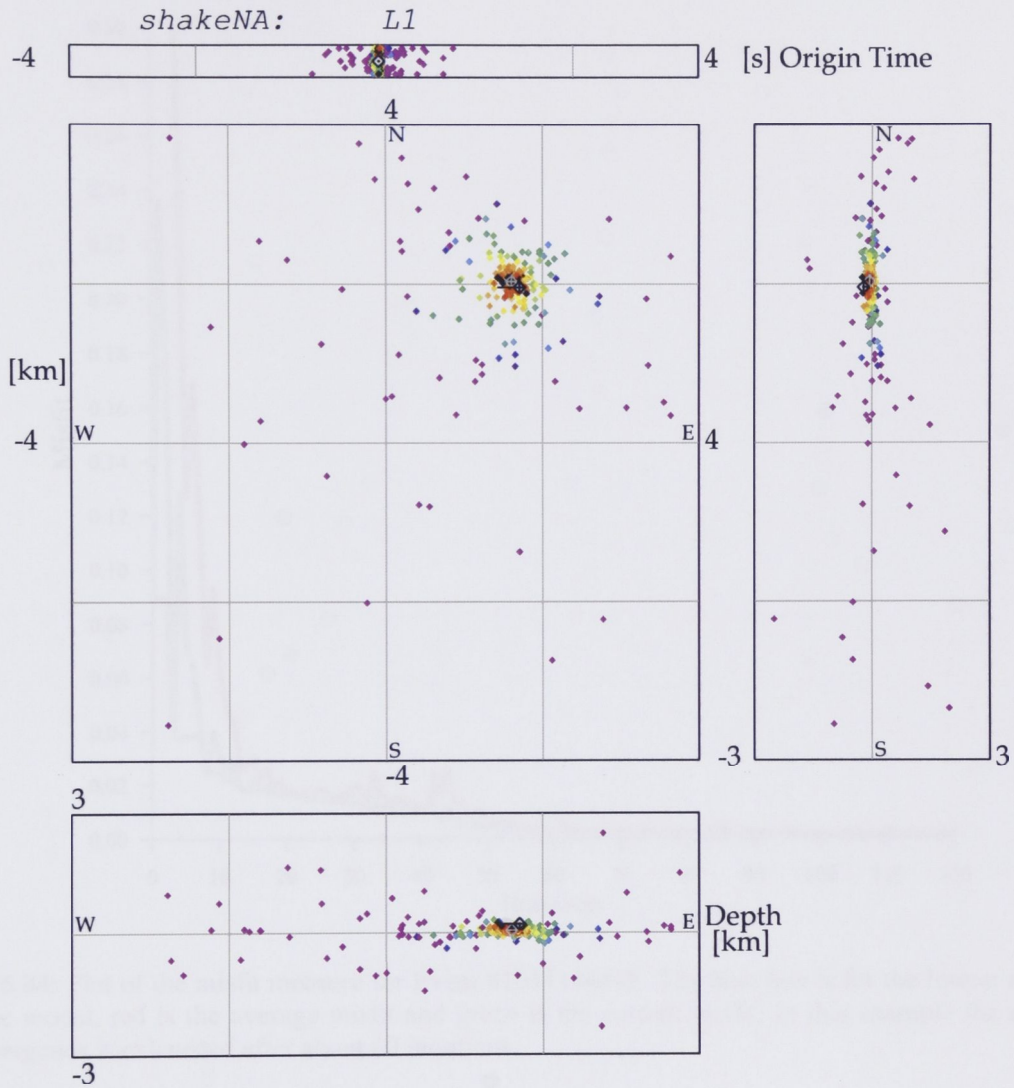

Fig. 5.83: Illustration of the neighbourhood algorithm progression towards convergence for Event 8101111444F in the 4-D parameter space. The horizontal search area is 8 x 8 km. The centre of the plot is the starting search point and is given by the coordinate -4.265°S and 152.190°E. Each circle, irrespective of colour, denotes the tested epicenters. Note the spread of the purple circles. These are tested epicenters with high misfits. The area of strong clustering marked by the coloured circles gives the best location estimate. Where they appear, the black circles have the least misfits.

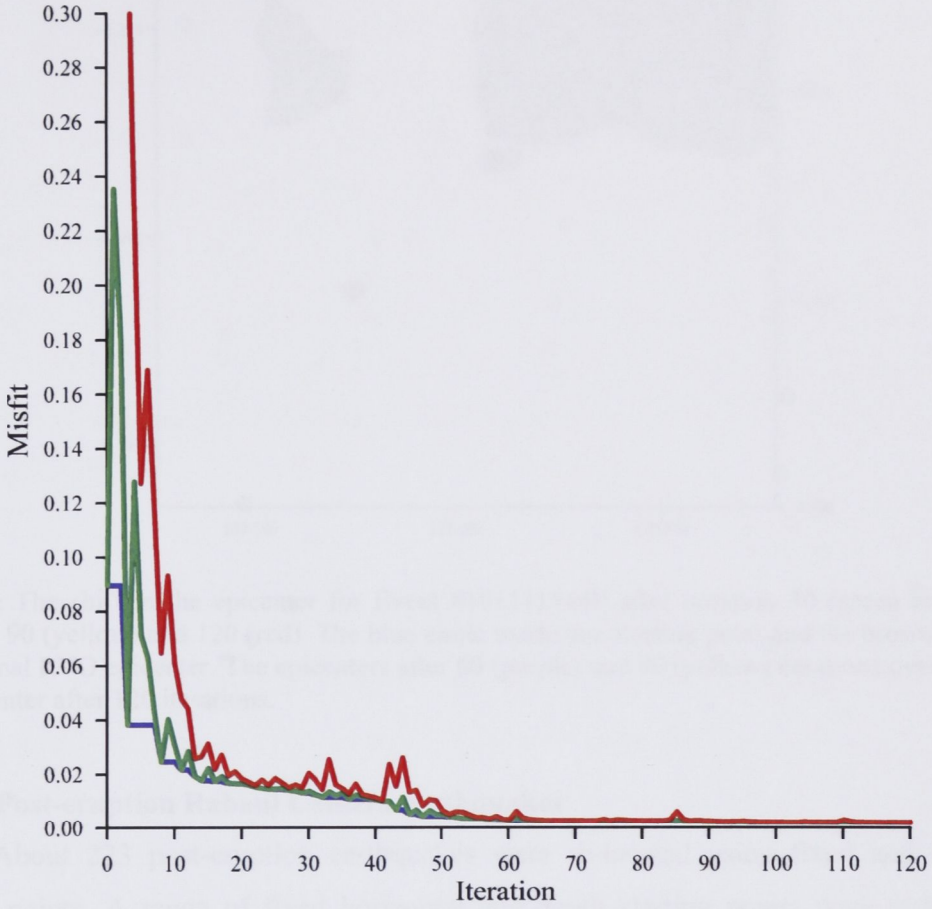

Fig. 5.84: Plot of the misfit measure for Event 8101111444F. The blue line is for the lowest misfit in the model, red is the average misfit and green is the current misfit. In this example the misfit convergence is exhausted after about 60 iterations.

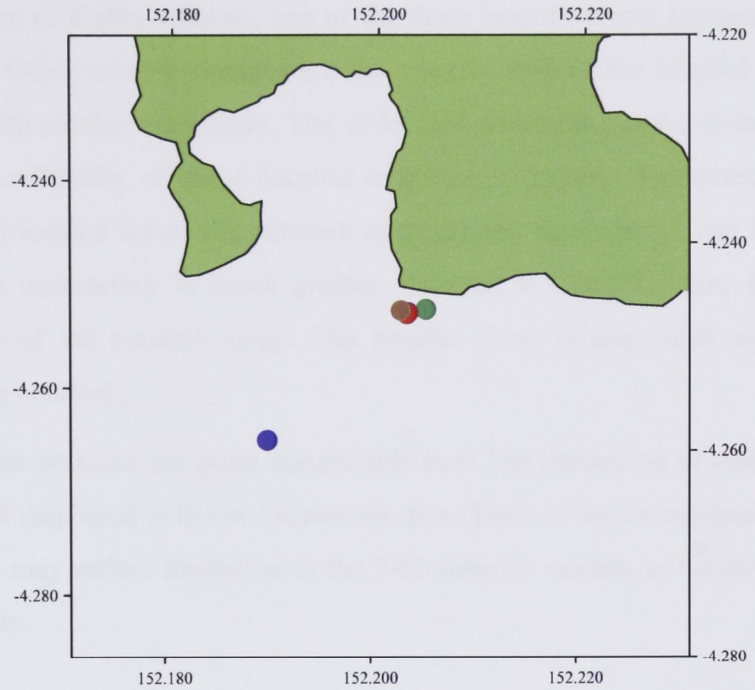

Fig. 5.9: The shift in the epicenter for Event 8101111444F after iteration 30 (green circle), 60 (purple), 90 (yellow) and 120 (red). The blue circle marks the starting point and the brown circle is the original RVO epicenter. The epicenters after 60 (purple) and 90 (yellow) iterations overlap with the epicenter after 120 iterations.

5.6.2.2 Post-eruption Rabaul Caldera earthquakes

About 223 post-eruption earthquakes were re-located using fixed and variable starting points. A range of fixed horizontal and depth starting points were tested. The horizontal search domain was set to ± 0.4 and the depth search domain was set to ± 5 km. For the variable starting points, the original RVO solutions were used. The same search domains as stated above were used.

Generally all the solutions from the different procedures were very comparable to the RVO solutions, however the solutions obtained with variable starting points (Fig. 5.10(a)) matched the RVO solutions far better than the others. The RVO solutions are reproduced again in Fig. 5.10(b) for direct comparison with the re-located solutions. Only earthquakes recorded on five or more stations and having horizontal and vertical uncertainties of less than 1.0 km are plotted. But when comparing results for specific events the shift for any one parameter between the re-located and the *Shak3_na* solution is as much as 1.5 km for the best solutions. For instance, the NE-SW lineament observed in the original solutions is still maintained in the re-located solutions, however it has shifted

slightly to the southeast by about 1.0 km so the southwest end of the lineament coincides with the position of Kabiu volcano, one of the three inactive cones located north and east of the caldera. Other notable changes are the easterly shift of the handful of earthquakes near Vulcan with similar magnitude. The re-located solutions put the events closer to the ring-fault. The reliability of the re-located solutions is variable. Estimates of uncertainty for earthquakes located inside the network array ranged between 0.1 and 0.6 km. On the other hand the uncertainty is much greater, between 0.1 and 1.5 km, for earthquakes located outside of the network array. The smaller value is associated with earthquakes located near the network.

The cross-sections are quite comparable too. The deepening of earthquakes to the northeast is still displayed in the re-located solutions but it is not as convincing as the RVO solutions. This may reflect limitation in the 3-D velocity models as the distance from the caldera increases.

5.6.2.3 Near-regional earthquakes

About fifteen local and near-regional earthquakes were selected systematically based on the RVO solutions and relocated with *Shak3_na*. However, instead of running the location algorithm in a script that would have located all the earthquakes in a single sweep like the pre- and post-eruption earthquakes, these earthquakes were located one at a time so it provided more control on the values for the initial starting point and the search domain in the 3-D space. Various starting points and search domains were tested. The solutions plotted in blue triangles in Fig. 5.11 had the best misfits and convergence. They had the following. The starting points were fixed to the RVO solutions. The horizontal search domain was ±0.5° for earthquakes near the network array and ±1.5° for those far from the array. The vertical search domain was set at ±10.0 km. The RVO solutions are plotted in red diamonds. Also plotted in brown circle are two earthquakes which had NEIC solutions. The arrows linking the RVO and the *Shak3_na* solutions show the shift from one to the other.

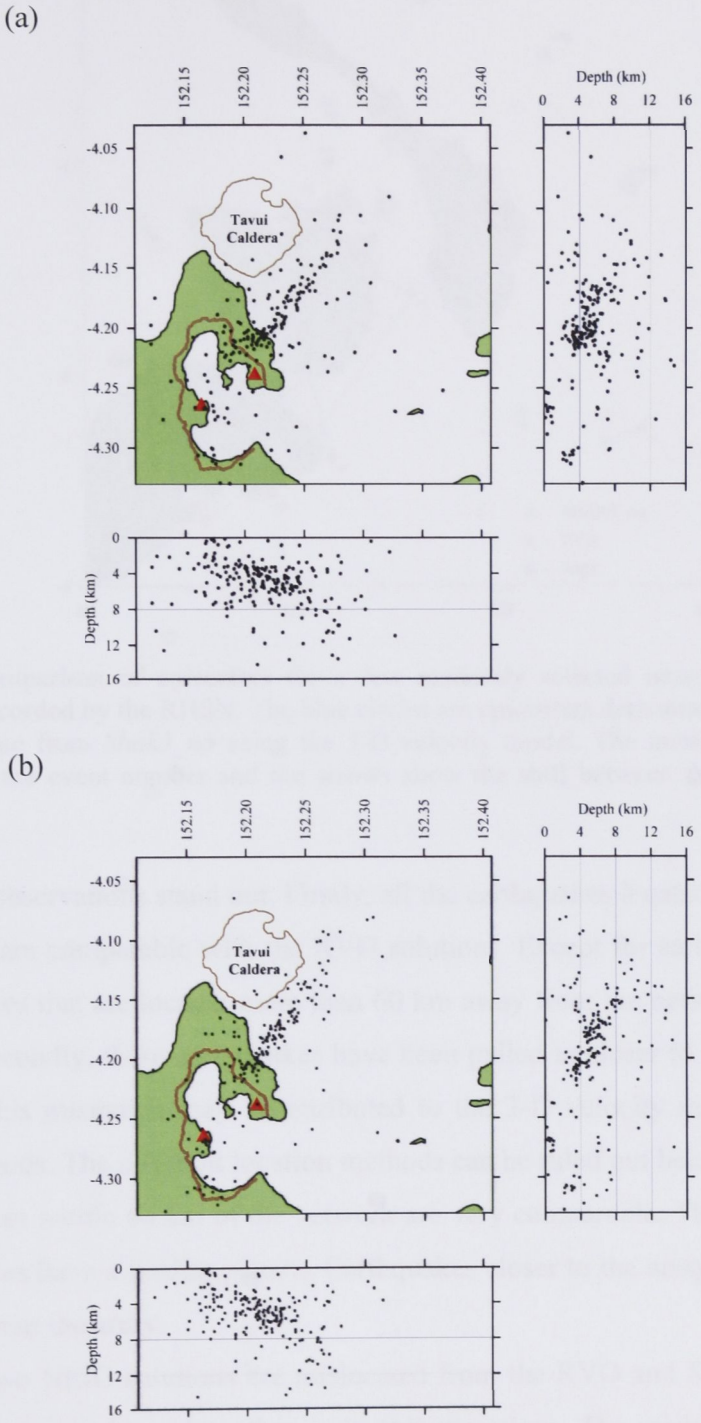

Fig. 5.10: (a) The re-located post-eruption Rabaul Caldera seismicity with *Shak3_na* using variable starting points. (b) The original RVO hypocentral solutions.

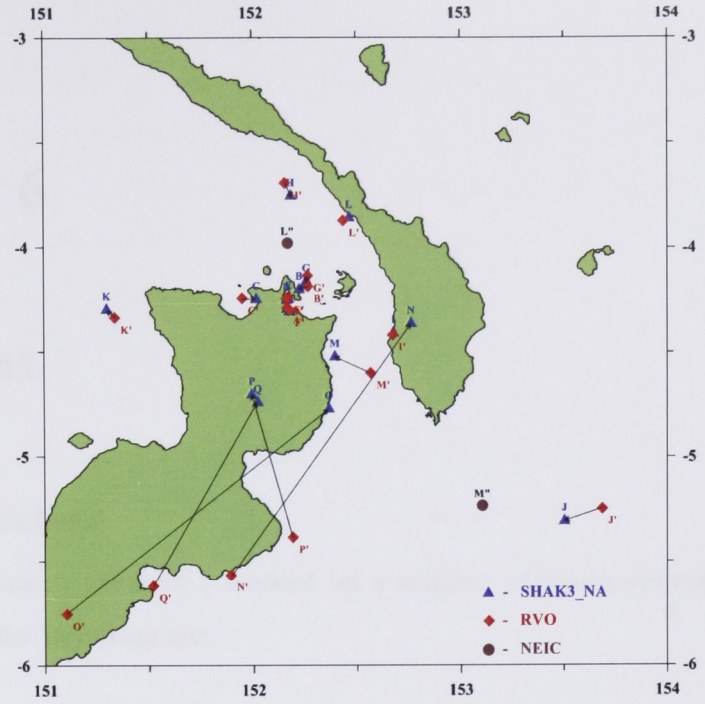

Fig. 5.11: Comparison of epicenters for a few randomly selected near and distance regional earthquakes recorded by the RHSN. The blue circles are epicenters determined by RVO and the red circles are those from *Shak3_na* using the 3-D velocity model. The numbers above each circle correspond to the event number and the arrows show the shift between the RVO and *Shak3_na* epicenters.

Two observations stand out. Firstly, all the earthquakes located within 60 km of the RHSN array are comparable with the RVO solutions. Except for earthquake **J**, the rest of the earthquakes that are located more than 60 km away from the network array have a big mismatch. Secondly, these earthquakes have been pulled in closer to the network array by *Shak3_na*. This mismatch may be attributed to the 3-D velocity model or the different location methods. The different location methods can be ruled out because the solutions for the earthquakes within 60 km of the network are very comparable. The depth solutions for the earthquakes have a similar pattern. Earthquakes closer to the array matched better than those away from the array.

The two NEIC solutions are mislocated from the RVO and *Shak3_na* solutions in southwesterly (event L) and southeasterly (M) directions. The mislocations are probably coincidence rather than a genuine pattern. There is not enough data to draw any general mislocation pattern.

Chapter 6

Discussions

6.1 Introduction

In my research program I worked on a number of topics concerning the Rabaul Caldera. Four of the key areas are:

- The pre-1994 eruption seismicity.
- The post-1994 eruption seismicity, and in particular the NEEqs VT earthquakes, and the ongoing eruptions at Tavurvur between 1994 and 2005.
- The 3-D structure of the Rabaul Caldera from travel time tomography.
- The 3-D location of the Rabaul Caldera earthquakes using a newly developed 3-D earthquake location algorithm, *Shak3_na*.

In the following sections I have provided some discussions focused on a few key issues that emerged either directly or indirectly from some of the above areas. They are as follows.

6.2 The correlation between the NEEqs and the ongoing eruptions at Tavurvur

The strong correlation between the ongoing eruptions at Tavurvur and the NEEqs between 1994 and 2005 (Table 3.1) has some practical implications.

Firstly, the NEEqs occur as a result of strain. The strain is presumably caused by intrusion of magma from a northeast source into the resident caldera magma body. This speculation is supported by mapping of the RMR. This magma body was also mapped by Bai and Greenhalgh (2005). Moreover, this speculation promotes further speculation about

possible magma mixing beneath the Rabaul Caldera. This speculation is supported by Patia et al. (2002) and Patia (2004) from the 1994 Tavurvur eruptives.

Secondly, this correlation could probably explain the reasons for the non-eruption of Tavurvur and Vulcan volcanoes or any one of them during or immediately after the 1983-1985 Rabaul seismo-deformational crises even though the caldera system was perceived to have been over-pressurised. It is noted in Section 3.2.3 that the only notable NEEqs before the 1994 eruptions occurred during a seismic swarm in May 1992. Besides these earthquakes no other NEEqs were recorded prior to or during the crisis. The non-occurrence of any NEEqs before or during the crisis suggests no magma intrusion from the RMR occurred at any time to facilitate magma mixing in order to trigger an eruption. On a different context, the non-eruption at that time could also be explained by considering the eruption repose periods. The repose period for twin-eruptions is about 58 years. May be at that time an eruption was probably not yet due. Some general information on eruption forecasting and specific case studies on the Rabaul Caldera is discussed in Section 6.5 of this chapter.

Thirdly, this correlation could be used as a forecasting tool for future eruptions at the Rabaul Caldera. The examples listed in Table 3.1 and many others that did not make the table strongly suggest there is a link. Obviously the ongoing monitoring parameters like the inner caldera seismicity, ground deformation, temperature and gas measurements, etc., will form the basis for long, intermediate and short term eruption forecasting, however, this observation warrants every consideration.

6.3 The 3-D earthquake locations and the double ring-fault

The results of the 3-D earthquake locations presented in Chapter 5 (see Fig. 5.6 and the series of figures in Appendix B) have some similarities and differences with the RVO solutions (see Fig. 2.6 and 2.8). The main similarity is with the epicenter distribution for the earthquakes. The 3-D solutions replicated the ring-fault extremely well. The main differences are with the depth sections. This is clearly shown in the S-N depth profiles (see Fig.2.8 for the RVO solutions and the series of plots in Appendix B for the 3-D solutions). The RVO solutions show two distinct clusters. The first is located between shallow and about 2 km and more or less to the north, and the second is located deeper between 3 and 4 km. On the other hand the 3-D solutions show only a single structure with the earthquake depths getting deeper towards the south. Considering the RVO solutions (Fig. 2.8), the

general positions of the two main clusters could give a perception of the earthquakes getting deeper to the south.

The difference in the depth sections is obviously attributed to the velocity models used to locate the earthquakes. The RVO solutions were obtained from a 1-D velocity model (Table 2.1). The 3-D solutions were obtained from the 3-D velocity model derived from the work discussed in Chapter 4.

Jones and Stewart (1997) raised a couple of issues about the 1-D model. The first is in relation to the strong concentration of earthquakes at about 0.1 km and 2 km depth. Secondly, they demonstrated that the 4 km depth marking the termination of the earthquakes in the vertical axis shifted simply by changing this parameter in the velocity model. These observations strongly suggest the 1-D velocity model has limitations.

In contrast the 3-D velocity models are seen to represent the true earth more adequately because the model is derived inside a 3-D volume by ray tracing and other techniques. But even so they are still far from perfect. The fact that it represents the earth better probably leads to better hypocentral solutions. For this reason people are gradually moving towards using 3-D velocity models for routine earthquakes locations. The derivation of 3-D velocity models has been made easier with improved data acquisition systems and computer power.

On this note it is probably fair to state that the 3-D hypocenter solutions determined in this study represent the Rabaul Caldera seismicity better. However it is also acknowledged that this velocity model is far from perfect and could require further improvement. This statement is supported by the differences shown in the series of depth section plots in Appendix B.

The foregoing discussion raises doubts about the double ring-fault mentioned in Chapter 2. In order to investigate this with the 3-D solutions I conducted similar depth slicing spatial analysis as done Section 2.4 of Chapter 2. The results are shown in Fig. 6.1 and Fig. 6.2.

The series of plots (a) to (h) in Fig. 6.1 generally suggests that most of the shallow earthquakes are located on the northern half of the elliptical ring-fault. However note also the group of shallow earthquakes in the depth range 0.0 to 0.99 km located on the southern part between latitude 4.28°S and 4.30°S and longitude 152.17°E and 152.20°E. Deep earthquakes begin to emerge towards the south but they are not plentiful as the shallow earthquakes.

It is difficult to draw any distinct ring-faults from any of the individual plots to associate with the MRF and BBRF discussed in Chapter 2. The main reason is the amount of data used here is far less than the data used to construct Fig. 2.7. However when some of the plots are merged, some patterns arise. For example, Fig. 6.1 (b to d) would best fit the MRF and Fig. 6.1 (g & h) best illuminate the BBRF. Here the BBRF does not appear convincing due to lack of earthquakes on the south and southeast parts of the ring-fault. However, merging the plots puts the MRF between 0.5 and 2.5 km depth and the BBRF between 3.5 and 4.5 km depth. Fig. 6.1(e & f) defines the elliptical ring-fault best in its entirety and could be considered the transition zone between the two ring-faults. The depth is between 2.5 and 3.5 km. The alternative, and probably the most convincing scenario, is the relocated solutions are pointing to a single ring-fault only, and not two. Fig. 6.1(h) is the combined plot for all the data.

Fig. 6.2 shows the two north-south cross-sections running through the strong concentration of earthquakes on the east and west sides of the ring-fault. It is equivalent to Fig. 2.8. It clearly shows only one structure instead of two as discussed in Chapter 2. The earthquakes get deeper towards the south. This scenario is in good agreement with the alternative view expressed in the foregoing paragraph. This study will adopt this interpretation. However, the two ring-fault structure could still exist noting the discussions pertaining to Fig. 6.1 above.

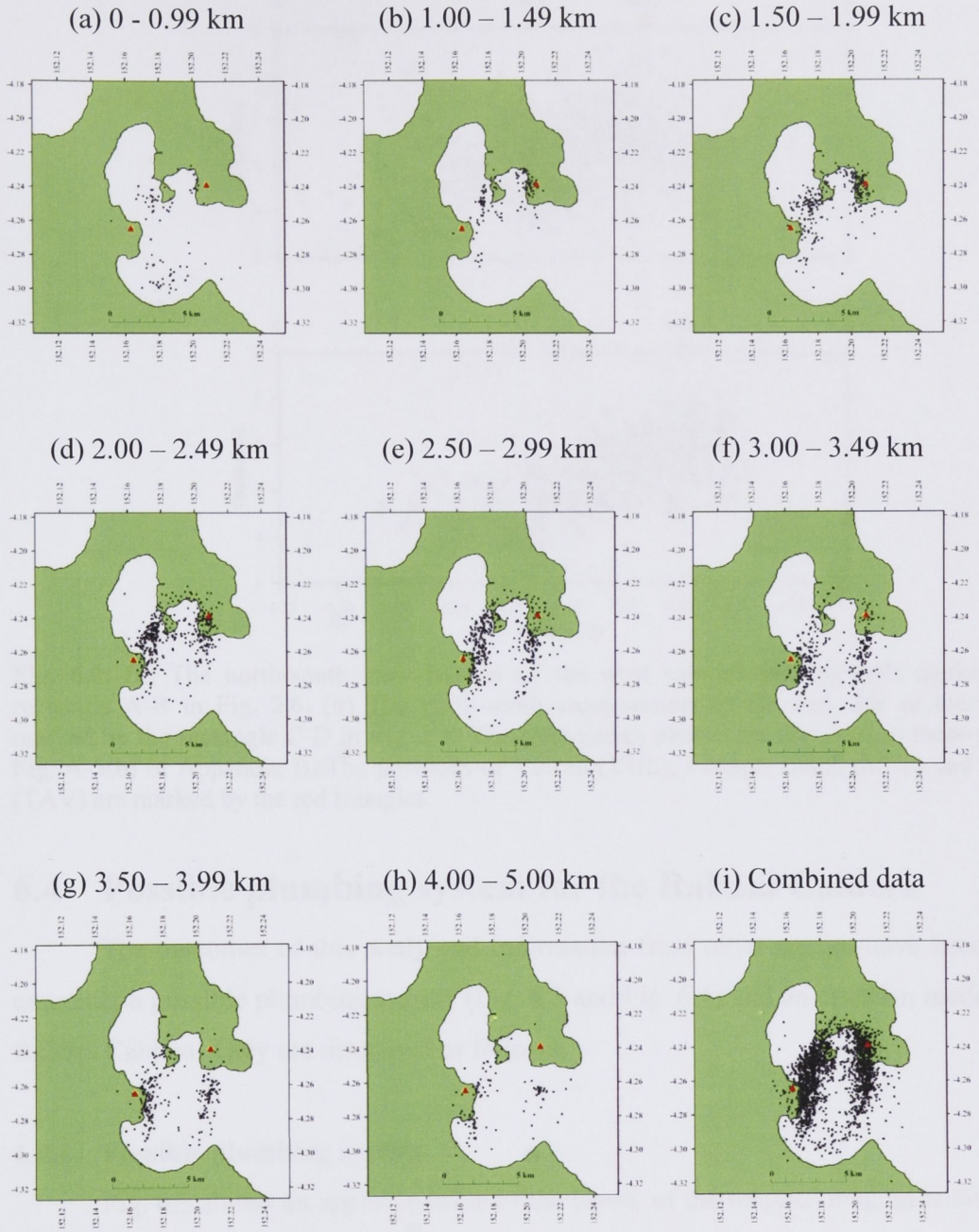

Fig. 6.1: Distribution of epicenters for various depth intervals. (a) 0.00 – 0.99 km, (b) 1.00 – 1.49 km, (c) 1.50 – 1.99 km, (d) 2.00 – 2.49 km, (e) 2.50 – 2.99 km, (f) 3.00 – 3.49 km, (g) 3.50 – 3.99 km, (h) 4.00 – 5.00 km, (i) the combined data. The earthquake data plotted are the same as those plotted in Fig. A-5(b) of Appendix B. The red triangles show the locations of Tavurvur and Vulcan on the east and west side of the ring-fault, respectively.

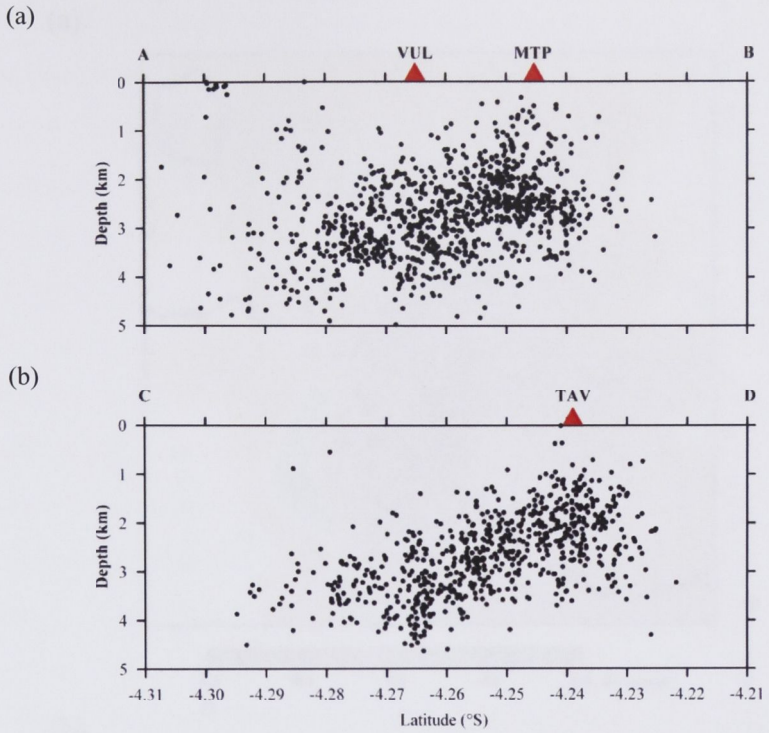

Fig. 6.2: (a) The north-south cross-section on the west side of the ring-fault marked by the rectangle A-B in Fig. 2.6. (b) The north-south cross-section on the east side of the ring-fault marked by the rectangle C-D in Fig. 2.6. The earthquakes plotted are the same as those plotted in Fig. A-5(b) of Appendix B. The positions of Vulcan (VUL), Matupit Island (MTP) and Tavurvur (TAV) are marked by the red triangles.

6.4 Possible plumbing system for the Rabaul Caldera

The outcomes of this study and information from other studies have been used to construct a possible plumbing system (Fig. 6.3 and Fig. 6.4) and an eruption model for the Rabaul Caldera. They are discussed as follows.

6.4.1 Possible plumbing system

Fig. 6.3 shows an approximation of the layout of the mapped magma bodies from a birds-eye perspective (Fig. 6.3a) and along an S-N profile that cuts through all the three bodies (Fig. 6.3b). All the three bodies are connected in one way or another. This study perceives the three magma bodies as follows:

(a)

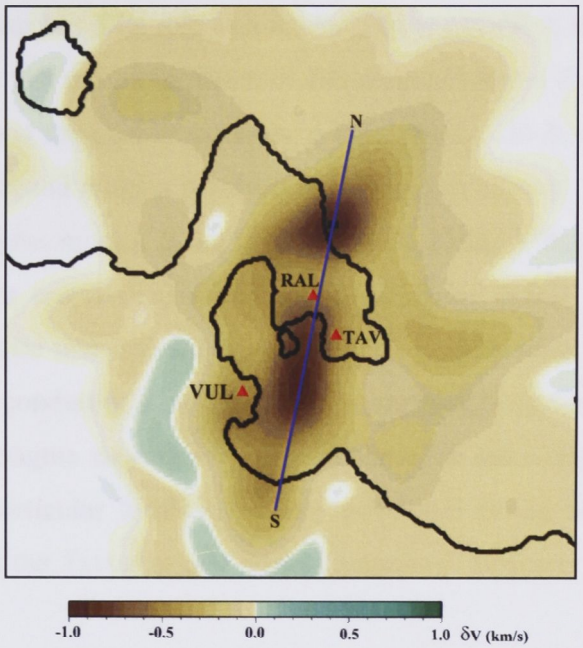

(b)

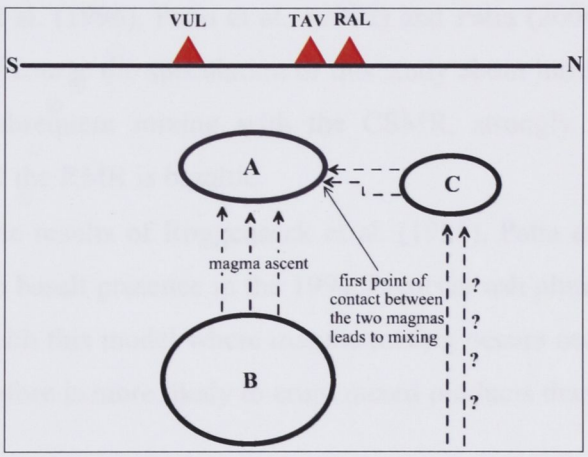

Fig. 6.3: (a) P-wave velocity perturbation in km/s for a 5 km depth slice for the local model. Note the two low velocity anomalies inside Rabaul Caldera and north-northeast of it. The positions of Tavurvur, Vulcan and Rabalanakaia are marked by the red triangles. (b) Cartoon illustrating the S-N cross-section along the blue line in (a). It portrays the configuration of the three magma bodies as perceived by the tomography study and how they relate to each other. **A** and **B** are the CSMR and CDMR. **C** is the RMR. ? speculates **C** linked to a deeper source. The figure is not drawn to scale.

- The CSMR is a storage body. This is the same body that is referred to as the residual of the 1400 year BP caldera-forming event (Walker et al., 1981). It feeds the eruptive vents that have been active during the last 250 years. The composition of this magma is primarily dacite (Fisher, 1939; Heming, 1974; Walker et al., 1981; Wood et al., 1995; Patia et al., 2002 and Patia, 2004).

- The CDMR is a feeder body that feeds the CSMR above it. The composition of the CDMR is unclear but if its role as a feeder for the CSMR is taken into account then it is very likely that the composition of this magma body is similar to the CSMR. The alternative is the CDMR could be a basalt body which, in this scenario, is the source of the second magma involved in the magma mixing. The drawback for this scenario is magma mixing is not very dominant in the Vulcan eruptives compared to the Tavurvur eruptives (Patia et al., 2002; Patia, 2004). Hypothetically if the CDMR is basaltic and it is ascending directly from beneath the CSMR through a narrow central conduit or a broad leaky system, there would be some expectation of caldera-wide magma mixing in the peripheries of the caldera ring-fault and not focused at a particular location. In this case there would be comparable magma mixing in both the Tavurvur and Vulcan eruptives. However this has not been the case.
- The RMR is a separate entity but is connected to the CSMR. The results by Roggensack et al. (1996), Patia et al., (2002) and Patia (2004) pointing to magma mixing, and of course the speculation of this study about intrusion from a northeast source and subsequent mixing with the CSMR, strongly suggests the magma composition of the RMR is basaltic.
- Furthermore the results of Roggensack et al. (1996), Patia et al. (2002) and Patia (2004) point to basalt presence in the 1994 Tavurvur ash plume and eruptives. This equates well with this model where magma mixing occurs nearer to Tavurvur (Fig. 6.3b) and therefore is more likely to erupt mixed products than Vulcan.

Fig. 6.4 presents another aspect of the plumbing system. Fig. 6.4a shows a W-E cross-section sliced through the centre of the caldera. The main focus here is to illustrate how the CSMR and the CDMR interact with each other and hence influence some of the physical processes, e.g. surface deformation, that occur within the ring-fault system. Some of the ideas are presented below:

- The CDMR feeds the CSMR. This process allows the CSMR to maintain its internal heat structure. The process also contributes to replenishing the CSMR with new magma. By doing so two things happen. Firstly, it slows down the crystallisation process that would otherwise occur due to natural heat loss and heat

loss from the short-cycle eruptions, and water intervention. Secondly, the pressure gradient in the CSMR is maintained by the new added material.

(a)

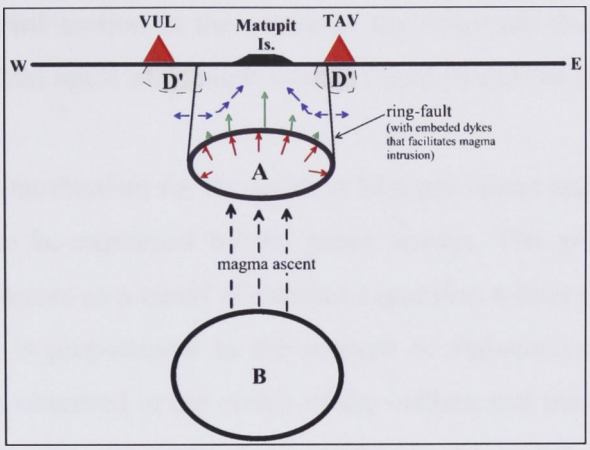

(b)

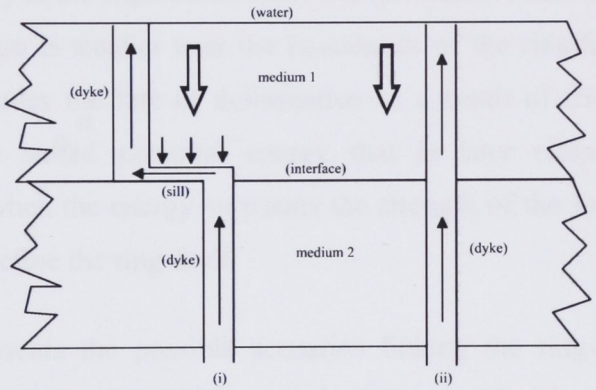

Fig. 6.4: (a) Cartoon illustrating the W-E cross-section sliced through the centre of the caldera. **A** and **B** are the CSMR and the CDMR beneath the Rabaul Caldera. The blue arrows depict the deformation vector proposed by Saunders (2001), resulting from a partially intruded ring-fault. The green arrows depict the deformation vector resulting from the expansion of the CSMR shown by the red arrows. The size of the green arrows is proportional to the amount of deformation. (b) Cartoon illustrating the possible forms of connection linking the ring-fault to the conduit system of the eruptive vents at point **D'**. Here (i) denotes the situation beneath Vulcan and (ii) is for Tavurvur. The arrows in the dykes show the direction of magma flow and the block arrows pointing downwards denotes the vertical downward loading driven by the gravitational force and the overriding mass. The small arrows pointing downwards on the sill denote the compressional force exerted on the sill by the gravitational force and the overriding mass.

- In this model a positive gradient pressure is vital because it provides the kinetic energy to drive the magma upward (Fig. 6.4a), or in the case where there is no way out the body expands. Buoyancy also contributes to the upward movement of magma. In Fig. 6.4a the red arrows indicates expansion of the magma body. When the body expands the magma intrudes into fractures or dykes in the ring-fault

system. Further fracture or dyke intrusion in the ring-faults develops a stress pattern with deformation vectors that is depicted by the blue arrows (Saunders, 2001). According to the model of Saunders (2001) the region inside the ring-fault becomes compressed. The compression from both sides converges and gives a net result that shows an upward motion at the centre of the ring-fault that probably causes the long-term vertical uplift of Matupit Island (Fig. 2.9) and the area immediately south of it.

- An alternative mechanism for the uplift at Matupit Island and the area immediately south of it can be explained by the green arrows. The green arrows depict the deformation vectors as a result of internal expansion within the CSMR. The length of the arrows is proportional to the amount of deformation so that the greatest deformation is observed at the centre of the caldera and the least is observed near the ring-faults. The deformation is greater at the centre because the medium responds freely to the expansion forces with an elastic behaviour. On the other hand the deformation is smaller near the boundaries of the ring-fault because the fault interface impedes the rate of deformation as a result of friction. This resistance converts into stored potential energy that is later released in the form of earthquakes when the energy surpasses the strength of the ring-fault material. The earthquakes define the ring-fault.

Fig. 6.4b presents the possible scenarios linking the ring-fault to the eruptive conduit systems for Tavurvur and Vulcan at the points marked by **D'**. This is important because the behavior of eruptions for the two volcanoes is very different and this model may have some influence. Here the ring-fault is seen to host dykes or fractures that facilitate magma transport to the eruptive vents. Also the locations of Tavurvur and Vulcan with respect to the ring-fault (Fig. 5.6 and Fig. 6.1i) are considered. Tavurvur is located almost on the ring-fault whereas Vulcan is located about 0.5-1.0 km from it. This is slightly different from the fine ring-fault structure of Jones and Stewart (1997), and this study has deliberately ignored it because it is seen to be an over-simplification of the actual ring-fault structure. The two logical scenarios of the connecting structures considered are as follows (Fig. 6.4b):

(i) Connection by a combination of dyke(s) and sill(s). i.e. dyke-sill-dyke. The dyke(s) can be vertical or dipping.

(ii) Connection by dyke(s) only. Again the dyke(s) can be vertical or dipping.

Naturally both scenarios can be present beneath both volcanoes but the critical factor is probably the distance of the two volcanoes from the ring-fault because this determines the type and the geometry of the connecting structures which in turn control the flow pattern of the magma to the eruptive vents during an eruption.

In scenario (i) both dykes and sills are considered. Beneath Tavurvur the lengths for the sills would be relatively short due to the short distance between the ring-fault and the vent, or it could even be negligible and therefore give rise to a near-vertical dyke connection. On the other hand, the sill components beneath Vulcan would be much longer or alternatively, there would be more step-like dyke-sill-dyke structures to accommodate the slightly longer distance between the ring-fault and the vent.

In scenario (ii) any dyke linking Tavurvur to the ring-fault would be vertical or near vertical because the distance separating the vent from the ring-fault is very short. In contrast, dykes beneath Vulcan would possibly dip at greater angles from the vertical because the distance between the ring-fault and the vent is much longer. Literally the dipping dykes would be more susceptible to shutting from vertical compression than the vertical dykes.

These geometries have important controlling factors on the behavior of magma flow during eruptions for both volcanoes.

6.4.2 Possible eruption model

This study presents a possible eruption model for Rabaul Caldera based on magma mixing and the eruption patterns.

6.4.2.1 Magma mixing

Evidence for magma mixing of dacite and basalt composition at the Rabaul Caldera has been presented by Patia et al. (2002) and Patia (2004). This study has strongly speculated on intrusion of magma from a northeast source into the resident caldera magma and results in mixing. The mapping of the RMR (Fig. 6.3a) goes well with this speculation.

Patia (2004) proposed magma mixing as the primary cause for triggering eruptions. The author of this study has been promoting this mechanism since 1995 as evidenced by the correlation between the NEEqs and the ongoing eruptions at Tavurvur (Table 3.1). This study is of the view that the NEEqs signify intrusions of basalt magma into the CSMR,

noting each time the volume of the intruded magma is variable and can be measured indirectly by the levels of the NEEqs (Table 3.1). This view contradicts the view of Patia (2004) about a single basaltic intrusion into the CSMR at the time of the 1983-1985 seismo-deformational crises. According to the hypothesis presented in this study if there was basalt intrusion into the CSMR back then, an eruption would have occurred at the time of the crisis or soon after it ended. So, on the basis of this hypothesis the lack of NEEqs prior, during and soon after the crisis suggests there was no basaltic intrusion. The only NEEqs prior to the 1994 eruption occurred in May 1992 and this may have marked the beginning of the intrusion and consequently the mixing and eventually the trigger of the eruptions 28 months later. Unlike the short lead-times listed in Table 3.1, the long lead-time of 28 months could be attributed to the system being closed for nearly 51 years.

6.4.2.2 Eruption patterns

The eruption styles at Tavurvur and Vulcan are completely different. Vulcan erupts violently for very short periods then stops for many decades. On the other hand Tavurvur has a tendency to produce ongoing eruptions after a main event. In addition, the recent historical eruptions at Rabaul Caldera show Vulcan has never erupted alone by itself but has erupted simultaneously with Tavurvur on three occasions. On the other hand Tavurvur has erupted by itself once.

This study presents a possible explanation for this based on Fig. 6.3 and Fig. 6.4. It is an alternative to the model presented by Saunders (2001).

Tavurvur has a tendency to produce ongoing eruptions for the following reasons. The first and also the main reason are probably due to magma mixing occurring in its neighbourhood (Fig. 6.3). This study speculates that Tavurvur will erupt in all eruption cycles and also produce ongoing eruptions as long as favourable magma mixing conditions prevail. The second reason is associated with the connecting structures that facilitate magma transport from the source to the erupting vent. Fig. 6.4 suggests the structures beneath Tavurvur are not complex and so are very conducive for magma transport to maintain sustained eruptions.

In complete contrast the same view cannot be accorded to Vulcan. Vulcan is far from where magma mixing occurs so the potential for a Vulcan eruption due to magma mixing is very remote. However, magma mixing can indirectly trigger Vulcan to erupt if the system is over-pressurised and volatile saturated. This is probably how the twin eruptions happen.

The short-lived eruptions at Vulcan could be attributed to the complex connecting structures beneath the volcano. Here dipping dykes or the dyke-sill-dyke structures probably dominates. At all times the dipping dyke(s) and the sill(s) are subjected to compression from vertical loading of the gravitational force. During an eruption different things can happen at different stages of the eruption. For instance just prior to and during the early stages of the eruption these structures are filled by intrusions of fresh voluminous magma en route to the eruptive vent. The voluminous intrusions overcome the downward compressional gravitational force and allow the structures to remain open. The structures can remain open as long as these intrusions are maintained at a constant rate. However, as soon as the intrusions feeding the eruption start to decline the compressional gravitational force becomes dominant and slowly acts on the dipping dykes and sills until they eventually close, forcing the eruption to stop.

6.5 Forecasting eruptions

Successful forecasting of volcanic eruptions is the ultimate goal of any volcanological observatory and other relevant institutions responsible for monitoring volcanoes. The success of forecasting an eruption is measured primarily by how well in advance an eruption is forecasted and how effective that information is conveyed to the civil authorities who are responsible for the practical implementation of the volcanic disaster management plan. The disaster management plan also entails an evacuation plan.

There have been some success stories of eruption forecasting like the 1989-1990 Mount Redoubt (Chouet et al., 1994; Chouet, 1996) and the 2000 Hekla eruption in Iceland, (Agustsson, et al., 2000).

6.5.1 Forecasting tools

Scientists forecast volcanic eruptions using information acquired from various kinds of monitoring techniques either in real-time or after post-data processing. The primary techniques include seismicity, ground deformation (leveling, tiltmeters, strainmeters, electronic distance measurements, global positioning system) and ground-based geochemical monitoring techniques.

Developments in new technology during the last one to two decades have improved some of the above monitoring techniques (broadband seismology, pressure sensors and gas spectrometers). At the same time some completely new techniques have been introduced as

well. One of the new techniques is remote sensing and this has enabled some aspects of volcano monitoring to be conducted remotely. An example of this is the satellite radar interferometry, but at this point in time results from this are not in real-time.

Further developments in forecasting have evolved around the modeling of recorded information. For instance, seismologists have classified (Minakami, 1960; Green and Neuberg, 2006) and modeled (Chouet, 1988; Chouet, 1996; Neuberg et al., 2006) the different types of volcanic earthquakes to understand their causes and how they relate to the dynamicity of the magma leading up to an eruption. The correlation of these parameters has contributed very positively towards improved forecasting. Forecasts of volcanic eruptions can be divided into three main groups: long-term, intermediate and short-term forecasts. All the three types of forecast are based on temporal and spatial trends of the monitored parameters. The short-term forecasts become more critical because they take into account the immediate precursors on time scales of days to hours, and how they relate to the dynamics of the magma leading to an eruption and more importantly whether these processes actually produce an eruption.

6.5.2 Forecasting eruptions at Rabaul Caldera

Volcano monitoring in Papua New Guinea began in the 1940's following the eruptions of Tavurvur and Vulcan in 1937. During a period of inactivity soon after the eruptions stopped in 1937 and 1940 Norman Fisher, the person tasked to set up the first volcanological observatory in Papua New Guinea, conducted temperature measurements on the floor of the 1878 crater at Tavurvur. He noted an anomalous rise in temperature (Fig. 6.5) beginning in early December 1940 and forecasted that an eruption was imminent (Fisher, 1939). The forecasted eruption occurred several months later in June 1941.

Some aspects of the results of the pre-1994 eruption monitoring at the Rabaul Caldera have been discussed in Chapter 2. Fig. 2.9 shows the monthly total number of earthquakes and vertical uplift between 1968 and 1994. The figure shows clear evidence of increased seismicity since 1971 and again in September 1983, and increased rates of vertical uplift since 1970 and again in September 1983, coinciding with the increased seismicity.

Based on this information and the recent historical eruptions at the Rabual Caldera scientists at the RVO forecasted an eruption was expected before the end of the century (McKee et al., 1984). This forecast and other technical considerations led to the formation of the East New Britain Provincial Disaster Committee in 1984 and subsequently led to the

commencement of regular mock evacuation exercises soon after. The mock exercises continued but became less frequent until the time of the eruption. This forecast was a long-term one. The eruption occurred in September 1994. The experience gained during the mock evacuation exercises resulted in five human losses only. The loss of fixed infrastructure worth millions of PNG Kina was unavoidable.

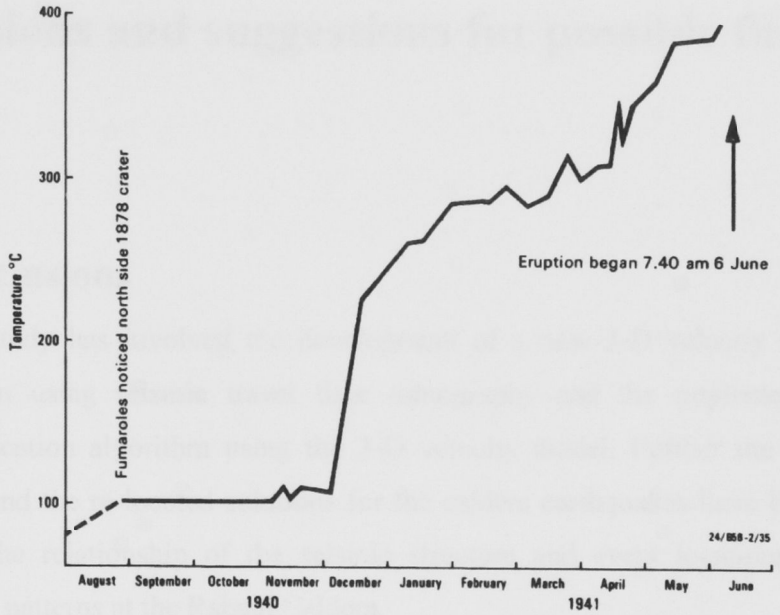

Fig. 6.5: Temperature measurements of the hot ground on the floor of the 1878 crater at Tavurvur Volcano by Norman Fisher. Note the rise in temperature starting at the beginning of December 1940. An eruption followed several months later in June 1941. (Reproduced from Johnson and Threlfall, 1985).

Some overview of the ongoing eruptive activity at Tavurvur between 1994 and 2005 has been discussed in Section 2.5 of Chapter 2. Also some aspects of the post-1994 eruption seismicity have been discussed in Chapter 3. Table 3.1 presents some correlation between these two parameters. This correlation was applied to forecast the resumption of the eruption in January 2005 (Itikarai, 2004a & 2004b). The intermediate-term forecast was based on the Jun-Jul 2004 northeast earthquakes. The short-term forecast was based on the emergence of the small low frequency earthquakes beneath Tavurvur one to two months earlier and the increasing trend that they displayed leading up to the eruption.

Chapter 7

Conclusions and suggestions for possible further work

7.1 Conclusions

This study has involved the development of a new 3-D velocity model for the Rabaul region using seismic travel time tomography and the implementation of an earthquake location algorithm using the 3-D velocity model. Further the results of the tomography and the re-located solutions for the caldera earthquakes have been employed to examine the relationship of the seismic structure and event locations to eruptions processes and patterns at the Rabaul Caldera.

The main conclusions are:

1. The P- and S-wave travel-time tomographic study generated a new 3-D velocity model for the Rabaul region with the highest resolution in the area around the caldera where the density of stations had been highest. The velocity model has been used for 3-D earthquake location. The tomography has identified three magma sources in and around the Rabaul Caldera. Two such sources are located beneath the Caldera, the CSMR and the CDMR, at depths of 3-6 km and 7-14 km. The third, the RMR, is located north-northeast of the Rabaul Caldera, but not beneath Tavui Caldera.
2. A new 3-D hypocenter determination algorithm, *Shak3_na*, was developed during this study. Using the 3-D seismic velocity model mentioned above, subsets of the pre- and post-eruption earthquakes in the Rabaul Caldera have been re-located, along with a sample of near-regional events. The convergence of the location algorithm has been generally good, with closely reproducible results for different starting conditions for the best events. The performance of the 3-D location algorithm has

been good for the pre-eruption events and the post-eruption within the network array. Reasonable results have been achieved for the near-regional earthquakes outside the network for which there is limited azimuth control from the network. The 3-D velocity model is at its best in the neighbourhood of the caldera and is less well constrained on the regional fringe and so the limitations of the model may well influence the quality of the locations.

3. For events within the caldera the agreement in the spatial position of the earthquakes between the RVO catalogue and the *Shak3_na* solutions has been very good. The main differences occur in the depth of the events where the velocity model has a strong influence; Jones & Stewart (1997) highlighted the possibility that the 1-D velocity model currently used by RVO may have some limitations. The 3-D velocity tomographic model uses all available information to include both vertical and horizontal variations and so should give a better representation of the structure beneath the Caldera than the 1-D model. The RVO solutions indicate banding at the discontinuities in the 1-D reference model (especially around 0.1 and 2 km depth). These bandings are absent in the 3-D solutions which should provide a better representation of the depth distribution of the earthquakes. This is demonstrated quite clearly in Fig. 2.8 and Fig. 6.2. It would therefore be logical that the *Shak3_na* solutions be preferred over the RVO solutions. Subsequently, it is recommended that all Rabaul Caldera earthquakes should be re-located with a new 1-D velocity model and the locations compared to the original RVO catalogue and the *Shak3_na* results. The outcome should then determine the way in which routine caldera earthquake locations are conducted. 3-D locations should be carried out for any unusual events and as a means of subsequently refining depth estimates.

4. The results from the RVO earthquake catalogue strongly suggest the presence of a well-defined ring-fault as noted by Mori and McKee (1988). Re-analysis of the same data by Jones and Stewart (1997) and this study, prior to doing the 3-D locations, have identified two ring-faults instead of one. This study has given the names Matupit Ring Fault (MRF) and the Blanche Bay Ring Fault (BBRF). The two ring-faults are not replicated by the *Shak3_na* solutions. It reveals only one ring-fault structure and this study will adopt this outcome. The earthquakes get deeper towards the south. However, it is possible the two ring-fault phenomena may still exist but they are strongly bonded in the single unit.

5. There has been a strong correlation between the NEEqs and the ongoing eruptions at Tavurvur between 1994 and 2005. This study has shown that the NEEqs have always been followed by increased eruptive activity or renewed eruptions, with variable lead times. This observation provides an important parameter for intermediate to long-term forecasting for new volcanic eruptions at the Rabaul Caldera.
6. Furthermore, this study has associated the NEEqs with possible dyke intrusion originating from a magma source of basaltic composition located in a north-northeast direction from the Rabaul Caldera, but not located beneath the Tavui Caldera, into the resident caldera reservoir of dacite composition. Here the north-northeast magma source is the RMR and the resident caldera reservoir is the CSMR. This interpretation indirectly infers that magma mixing consequently occurs and becomes the driving force for triggering increased eruptive activity or renewed eruptions, particularly at Tavurvur. The idea of magma mixing is supported by Walker et al., (1981) and Patia et al. (2002) and Patia (2004).
7. Lastly, based on some of the outcomes of this study and information from other studies I have proposed a possible plumbing system and an eruption model for the Rabaul Caldera.

7.2 Suggestions for possible further work

Possible suggestions for future work that have emerged from this study are:

1. The NEEqs should continue to be monitored. To improve the locations the island stations WTM and MAK need to be operational as much as possible. This will improve azimuth coverage and lead to improved location parameters.
2. Conduct focal mechanism investigations for some of the large NEEqs that are detected by a maximum number of stations (including WTM and MAK). The best fitting double-couple representations should help to confirm or nullify the hypothesis of a northeast trending fault suggested by the epicenter distribution.
3. Conduct stress field analysis on the earthquakes and determine the distribution pattern of these stress fields. This may shed some light on the actual cause of the earthquakes. In this study the earthquakes have been attributed to stress induced by dyke intrusion.
4. The differences in the earthquake depths exposed by the north-south depth sections between the RVO and the *Shak3_na* solutions clearly indicate that one of the velocity

models has a problem. Jones and Stewart (1997) highlighted the possibility of the velocity model currently used by RVO for routine earthquake locations to having limitations. The 3-D velocity model derived in this study probably represents the structure better than the 1-D model. Nonetheless, further work is recommended to look into this. It would be useful to have some calibration events to test the suitability of the 3-D model. Some well-located explosions with good timing control would be helpful.

5. The hypothesis proposed in this study linking the NEEqs and the eruptions at Tavurvur should be used as a tool to conduct intermediate to long term forecasting of future volcanic eruptions at Rabaul Caldera.

References

Agustsson, K., Steffansson, R., Linde, A. T., Einarsson, P., Sacks, I. S., Gudmundsson, G. B. and Thorjarndottir, B., 2000. Successful prediction and warning of the 2000 eruption of Hekla based on seismicity and strain changes, *EOS Trans.* AGU U81, F1337.

Aki, K. and Lee, W. H. K., 1976. Determination of three-dimensional velocity anomalies under a seismic array using first P arrival times from local earthquakes: 1. A homogeneous initial model. *J.Geophys. Res.*, 81, 4381-4399.

Almond, R. A. and McKee, C. O., 1982. Location of volcano-tectonic earthquakes within the Rabaul Caldera. *Geol. Surv. Papua New Guinea*, Report 82/19.

Bai, C. and Greenhalgh, S., 2005. 3-D multi-step travel time tomography: Imaging the local, deep velocity structure of Rabaul volcano, Papua New Guinea. *Physics of the Earth and Planetary Interiors*, 151, 259-275.

Barberi, F., Corrado, G., Innocenti, F. and Luongo, G., 1984. Phlegraean Fields 1982-1984: Brief chronicle of a volcano emergency in a densely populated area. *Bull Volcanol.*, 47(2), 175-185.

Blong, R. and McKee, C. O., 1995. Destruction of a Town – The Rabaul eruption 1994. *Natural Hazards Research Centre*, Macquarie University, 52p.

Brzostowski, M. A. and McMechan, G. A., 1992. 3-D tomographic imaging of near-surface seismic velocity and attenuation. *Geophysics*, 57, 3, 396-403.

Caplan-Auerbach, J. and McNutt, S. R., 2003. New insights into the 1999 eruptions of Shishaldin Volcano based on acoustic data. *Bull. Volcanol.*, 65, 405-417.

Chen, H., Chin, J. M., Pujol, J., Kim, K., Chen, K. C., Huang, B. S., Yeh, Y. H. and Chin, S. C., 2006. A simple algorithm for local earthquake location using 3D Vp and Vs models: Test examples in the Central United States and in Central Eastern Taiwan, *Bull. Seismol. Soc. Am.*, 6(1), 288-305.

Chouet, B., 1979. Sources of seismic events in the cooling lava lake of Kilauea Iki, Hawaii, *J. Geophys. Res.*, 84, 2315-2330.

Chouet, B., 1988. Resonance of a fluid-driven crack: radiation properties and implications for the source of long-period events and harmonic tremor. *J. Geophys. Res.*, 101, 4375-4400.

Chouet, B. A., Page, R. A., Stephens, C. D., Lahr, J. C. and Power, J. A., 1994. Precursory swarms of long-period events at Redoubt Volcano (1989-1990), Alaska: Their origin and use as a forecasting tool. *J. Volcanol. Geotherm. Res.*, 62, 95-135.

Chouet, B. A., 1996. Long-period volcano seismicity: its source and use in eruption forecasting. *Nature*, 380, 309-316.

Cifali, G., D'Addario, G. W., Polak, E. J. and Wiebanga, W. A., 1969. Rabaul preliminary crustal seismic test, New Britain 1966, *Bur. Mineral Resour. Aust. Rec.* 1969/125 (unpubl.).

Collins, C. D. N., Drummond, B. J. and Nicoll, M. G., 2003. Crustal thickness patterns in the Australian continent. *In – Evolution and the Dynamics of the Australian Plate* (Ed., R. R. Hills and R. D. Muller), Geol. Soc. of America, 121-128.

Cooke, R. J. S., 1972. Rabaul Caldera seismic activity progress report November 1972. *Geol. Surv. Papua New Guinea Note on investigation* 72-028.

Cooke, R. J. S., 1977. Rabaul Volcanological Observatory and geophysical surveillance of the Rabaul volcano. *The Australian Phys.*, 27-30.

Davies, H. L., Symonds, P. A. and Ripper, I. D., 1984. Structure and evolution of the southern Solomon Sea region. *BMR Journal of Australian Geology and Geophysics*, 9, 49-68.

D'Addario, G. W., Dow, D. B. and Swoboda, R., 1976. Geological Map of Papua New Guinea, 1:2 500 000. *BMR, Geology and Geophysics,* Canberra.

Debayle, E. and Sambridge, M., 2004. Inversion massive surface wave data sets; Model construction and resolution assessment. *J. Geophys. Res.*, 109, B2.

Denham, D., 1969. Distribution of earthquakes in the New Guinea-Solomon Islands region. *J. Geophys. Res.*, 74, 4290-4299.

Dow, D. B., 1977. A geological synthesis of Papua New Guinea. *BMR, Geology and Geophysics*, Canberra. Bulletin 201.

Endo, T. E. and Murray, T. L., 1991. Real-time Seismic Amplitude Measurements (RSAM): A volcano monitoring and prediction tool. *Bull. Volcanol.*, 53, 533-545.

Everingham, I. B., 1975. Faulting associated with the major North Solomon Sea earthquakes of 14 and 26 July 1971. *Journal of Geological Society of Australia*, 22, 61-70.

Finlayson, D. M. and Cull, J. P., 1973. Structural profiles in the New Britain/New Ireland region. *J. Geo. Soc. Am.*, 20, 37-48.

Finlayson, D. M., Gudmundsson, O., Itikarai, I., Saunders, S., Powel, L., Thurber, C. H., Shimamura, H. and Nishimura, Y., 2001. The Rabaul Earthquake Location And Caldera Structure (RELACS) program: operations report. *Record 1001/01. Aust. Geol. Survey Organisation.*

Finlayson, D. M., Gudmundsson, O., Itikarai, I., Nishimura, Y., Shimamura, H. and Johnson, R. W., 2003. Rabaul Volcano, Papua New Guinea: island arc structural architecture and seismic tomography imaging of an active volcanic caldera. *J. Volcanol. Geotherm. Res.*, 124, 153-171.

Fisher, N. H., 1939. Geology and vulcanology of Blanche Bay and the surrounding area, New Britain. Territory of New Guinea. *Geol. Bull.*, 1, 1-68.

Fisher, N. H., 1944. The Gazelle Peninsula, New Britain earthquake of January 14, 1941. *Bull. Seismol. Soc. Am.*, 34, 1-12.

Fishwick, S., Kennett, B. L. N. and Reading, A. M., 2005. Contrasts in lithospheric structure within the Australian Craton, *Earth Planet. Sci. Lett.*, 231, 163-176.

Garces, M. A., Hargety M. T. and Schwartz, S. Y., 1998. Magma acoustics and time-varying melt properties at Arenal Volcano, Costa Rica. *Geophys. Res. Lett.*, 25, 2293-2296.

Greene, G. H., Tiffin, D. L. and McKee, C. O., 1986. Structural deformation and sedimentation in an active caldera, Rabaul, Papua New Guinea. *J. Volcanol. Geotherm. Res.*, 30, 327-356.

Green, D. N. and Neuberg, J., 2006. Waveform classification of volcanic low frequency earthquake swarms and its implication at Soufriere Hills volcano, Montserrat. *J. Volcanol. Geotherm. Res.*, 153, 51-63.

Gudmundsson, O., Johnson, R. W., Finlayson, D. M., Nishimura, Y., Shimamura, H., Terashima, T., Itikarai, I. and Thurber, C., 1999. Multinational seismic investigation focuses on Rabaul volcano. *EOS Trans.* AGU 80, 269-273.

Gudmundsson, O., Finlayson, D. M., Itikarai, I., Nishimura, Y. and Johnson, W. R., 2004. Seismic attenuation at Rabaul Volcano, Papua New Guinea. *J. Volcanol. Geotherm. Res.*, 130, 77-92.

Hellweg, M., 2000. Physical models for the source of Lascar's harmonic tremor. *J. Volcanol. Geotherm. Res.*, 101: 183-198.

Heming, R. F., 1974. Geology and Petrology of Rabaul Caldera, Papua New Guinea. *Geol. Soc. Am. Bull.*, 85, 1253-1264.

Heming, R. F., 1977. Minerology and proposed P-T paths of basaltic lavas from Rabaul Caldera, Papua New Guinea. *Contrib. Mineral Petrol.*, 61, 15-33.

Hermann, R. B., 1979. FASTHYPO – a hypocenter location program. *Earthquake Notes*, 50, 25-38.

Hill, D. P., Reasenberg, P. A., Michael, A., Arabaz, W. J., Beroza, G. and et al., 1993. Seismicity remotely triggered by the magnitude 7.3 Landers, California earthquake, *Science*, 260, 1617-1623.

Hill, D. P., Pollitz, F. and Newhall, C., 2002. Earthquake-volcano interactions, *Phys. Today*, 55, 41-47.

Husen, S., Kissling, E., Deichmann, N., Wiemer, S., Giardini, D. and Baer, M., 2003. Probabilistic earthquake location in complex three-dimensional velocity models: Application to Switzerland. *J. Geophys. Res.*, 108(B2), 2077, doi: 10.1029/2002JB0011778.

Husen, S., Robetr, Smith, R. B. and Waite, G. P., 2004. Evidence for gas and magmatic sources beneath the Yellowstone volcanic field from seismic tomographic imaging. *J. Volcanol. Geotherm. Res.*, 131, 397-410.

Itikarai, I. and McKee, C., 1990. Comparison of results of bathymetric surveys at Rabaul Caldera, July 1983-1984. *Geol. Surv. Papua New Guinea Report*, 90/2.

Itikarai, I. and Tregoning, P., 2003. The 16 November 2000 southern New Ireland earthquake and its aftershocks. *Geol. Surv. Papua New Guinea Report*, 2003/1. 16pp.

Itikarai, I., 2004a. The northeast earthquakes; a tool to forecast future eruptions at Rabaul Caldera. *Seminar presentation* at Geoscience Australia, Canberra.

Itikarai, I., 2004b. Rebuilding Rabaul Town and the associated risks, 10th Anniversary of Rabaul Twin Eruptions; what have we learnt ? *Symposium presentation.*

Johnson, J. B., 2000. Interpretation of infrasound generated by erupting volcanoes and seismo-acoustic energy partitioning during strombolian explosions. *PhD thesis.* Univ. Wash., Seattle. 159pp.

Johnson, R. W., 1979. Geotectonics and volcanism in Papua New Guinea: a review of the late Cainozoic. *BMR Journal of Australian Geology and Geophysics*, 4, 181-207.

Johnson, R. W, and Threlfall, N. A., 1985. Volcano Town: The 1937 – 1943 Rabaul Eruptions: *Robert Brown and Associates*, 151pp.

Johnson, R. W., McKee, C. O., Eggins, S., Woodhead, J., Arculus, R. J., Chappell, W. and Sheraton, J., 1995. The 1994 eruptions at Rabaul Volcano, Papua New Guinea: taking petrologic pathways towards understanding a restless caldera. *EOS Trans.* AGU 76, 171.

Johnson, T. and Molnar, P., 1972. Focal mechanisms and plate tectonics of the southwest Pacific. *J. Geophys. Res.*, 77, 5000-5032.

Jones, R. H. and Stewart, R. C., 1997. A method for determining significant structures in a cloud of earthquakes. *J. Geophys. Res.*, 102 (B4), 8245-8254.

Kennett, B. L. N., Sambridge, M. S. and Williamson, P. R., 1988. Subspace methods for large inverse problems with multiple parameter classes. *Geophys. J.*, 94, 237-247.

Kennett, B. L. N., Engdahl, E. R. and Buland, R., 1995. Constraints on seismic velocities in the earth from travel times. *Geophys. J. Int.*, 122, 108-124.

Kennett, B. L., N., 2002. The Seismic Wavefield Volume II: Interpretation of Seismograms on Regional and Global Scales. *Cambridge University Press*, Cambridge, p426.

Kennett, B. L. N., Fishwick, S., Reading, A. M. and Rawlinson, N., 2004. Contrasts in mantle structure beneath Australia: relation to Tasman Lines? *Australian Journal of Earth Sciences*, 51, 563-569.

Klein, F. N., 1978. Hypocenter location program: HYPOINVERSE, *U.S Geol. Surv. Open-File Rep.*, 78-694, 113pp.

Klein, F. N., 2000. Users guide to HYPOINVERSE-2000, *U.S Geol. Surv. Open-File Rep.*, 02-171, 123pp.

Lahr, J. C., Chouet, B. A., Stephens, C. D., Power, J. A. and Page, R. A., 1994. Earthquake classification, location, and error analysis in a volcanic environment: implications for magmatic system of the 1989-1990 eruptions at Redoubt Volcano, Alaska. *J. Volcanol. Geotherm. Res.*, 62, 137-151.

Lauer, S., 1995. Pumice and Ash: a personal account of the 1994 Rabaul volcanic eruptions. *CDP Resources*, Ballina, Australia, 80pp.

Lee, W. H. K. and Lahr, J. C., 1975. HYPO71: A computer program for determining hypocenter, magnitude and first motion pattern of local earthquakes, *U. S. Geological Survey Open File Report 75-311*, 113pp.

Lindley, D., 1988. Early cainozoic stratigraphy and structure of the Gazelle Peninsula, East New Britain: An example of tensional tectonics in the New Britain arc-trench complex, *Australian Journal of Earth Sciences*, 35, 231-244.

Lomax, A., Zollo, A., Capuano, P. and Virieux, J., 2001. Precise, absolute earthquake location under Somma-Vesuvius volcano using a new three-dimensional velocity model. *Geophys. J. Int.*, 146, 313-331.

Macnab, R. P., 1970. Geology of Gazelle Peninsula, TPNG. *Bureau of Mineral Resources, Geology and Geophysics*, Canberra, Record1970/63 (unpubl.)

Minakami, T., 1960. Fundamental research for predicting volcanic eruptions. I-Earthquakes and crustal deformation originating from volcanic activities. *Bulletin of the Earthquake Research Institute*, University of Tokyo, 38, 497-544.

McKee, C. O., Lowenstein, P. L., de Saint Ours, P., Talai, B., Itikarai, I. and Mori, J. J., 1984. Seismic and ground deformation crises at Rabaul Caldera: prelude to an eruption ? *Bull. Volcanol.*, 47, 397-411.

McKee, C. O., Johnson, R. W., Lowenstein, P. L., Riley, S. J., Blong, R. J., de Saint Ours, P. and Talai, B., 1985. Rabaul Caldera, Papua New Guinea: Volcanic hazards, surveillance, and eruption contingency planning. *J. Volcanol. Geotherm. Res.*, 23, 195-237.

McKee, C., Mori, J. and Talai, B., 1987. Microgravity changes and ground deformation at Rabaul Caldera, 1973-1985. *Geol. Surv. Papua New Guinea Report*, 87/29.

McKee, C. O., Kuduon, J., and Patia, H., (in prep.). Recent eruption history at Rabaul.

Mogi, K., 1958. Relations between the eruptions of various volcanoes and the deformations of the ground surfaces around them. *Bull. Earthquake Res. Inst. Tokyo Univ.*, 36, 99-13.

Mori, J., McKee, C. O. and Letz, H., 1987. The central New Britain earthquake May 10, 1985: tensional stresses in the frontal arc. *Phys. Earth Planet. Inter.*, 48, 73-78.

Mori, J. and McKee, C. O., 1987. Outward dipping ring-fault structure at Rabaul Caldera as shown by earthquake locations. *Science,* 235, 193-195.

Mori, J., 1988. Re-location of Rabaul Caldera earthquakes using S-wave data. *Geol. Surv. Papua New Guinea Report,* 88/20, 13pp.

Mori, J., McKee, C., Itikarai, I., Lowenstein, P., de Saint Ours, P. and Talai, B., 1988. Earthquakes of the Rabaul seismo-deformational crisis, September 1983 to July 1985: Seismicity in a caldera ring-fault. *In – Volcanic Hazards Assessments and Monitoring* (Ed., J. H. Latter), Springer – Verlag, 429-462.

Mori, J., 1989. The New Ireland earthquake of July 3, 1985 and associated seismicity near the Pacific-Solomon Sea-Bismarck Sea triple junction. *Phys. Earth Planet. Inter.*, 55, 144-153.

Mori, J. and Eberhart-Phillips, D., 1992. Magma bodies inferred from 3-D velocity inversions at two large volcanoes: Mt Pinatubo, Philippines and Rabaul Caldera, Papua New Guinea. *EOS Trans.* AGU 73, 348.

Nairn, I. A., McKee, C. O., Talai, B. and Wood, C. P., 1995. Geology and eruptive history of Rabaul Caldera, Papua New Guinea. *J. Volcanol. Geotherm. Res.*, 69, 259-299.

Neuberg, J., 2000. Characteristics and causes of shallow seismicity in andesite volcanoes. *Philos. Trans. R. Soc. London Ser.*, A 358: 1533-1546.

Neuberg, J. and O'Gorman, C., 2002. A model of the seismic wavefield in gas-charged magma: application Soufriere Hills Volcano, Montserrat. *In - The eruption of Soufriere Hills Volcano, Montserrat, from 1995-1999* (Ed., T. H. Druitt and Kokelaar), Geol. Soc. London, Memo., 21, 602-609.

Neuberg, J., Tuffen, H., Collier, L., Gree, D., Powell, T. and Dingwell, D., 2006. The trigger mechanism of low-frequency earthquakes on Montserrat, *J. Volcanol. Geotherm. Res.*, 153, 37-50.

Newhall, C. G. and Dzurisin, D., 1988. Historical unrest at large calderas of the world, *US Geol. Surv. Bull.* 1855.

Nicholson, T., Sambridge, M. and Gudmunsson, O., 2000. On entropy and clustering in earthquake hypocenter distributions. *Geophys. J. Int.*, 142, 37-51.

Nishimura, T., Nakamichi, H., Tanaka, S., Sato M. and Kobayashi, T., 2000. Source process of very long period seismic events associated with the 1998 activity of Iwate Volcano, northeastern Japan. *J. Geophys. Res.*, 105, 19135-19147.

Nishimura, T. and Chouet, B., 2003. A numerical simulation of magma motion, crustal deformation, and seismic radiation associated with volcanic eruptions. *Geophys. J. Int.*, 153, 699-718.

Nishimura, Y., Nakagawa, M., Kuduon, J. and Wukawa, J., 2005. Timing and scale of tsunami caused by the 1994 Rabaul eruption, East New Britain, Papua New Guinea. *In – Tsunamis: Case studies and recent development* (Ed. K. Satake), Springer, Netherlands, 43-56.

Okada, H., Watanabe, H., Yamashita, H. and Yokoyama, I., 1981. Seismological significance of the 1977-1978 eruptions and the magma intrusion process of Usu Volcano. *J. Volcanol. Geotherm. Res.*, 9, 311-334.

Patia, H., Eggins, S., McKee, C. O. and Johnson, R. J., 2002. The 1994 to 2001 eruption at Rabaul, Papua New Guinea: Evidence of repeated basaltic magma influx into a sub-caldera dacitic magma reservoir. *16th Australian Geological Convention*, Adelaide, Abstract.

Patia, H., 2004. Petrology and geochemistry of the recent eruption history at Rabaul Caldera, Papua New Guinea: implications for magmatic processes and recurring volcanic activity, *MPhil. Thesis*, The Australian National University.

Pearson, A. D., 2000. The three-dimensional structure of the summit magma complex at Kilauea volcanic, Hawaii, from travel time CDI tomography. *MSc. Thesis*, Univ. of Alaska, Fairbanks, 97pp.

Power, J. A., Moran, S. C., McNutt, S. R., Stihler, S. D. and Sanchez, J. J., 2000. Triggered seismicity beneath the Katmai volcanoes following the December 6, 1999, magnitude 7.0 Karluk Lake earthquake, Alaska. *EOS*, 81, 48, p917.

Rawlinson, N. and Sambridge, M., 2003. Seismic traveltime tomography of the crust and lithosphere. *Advances in Geophysics*, 46, 181-198.

Rawlinson, N. and Sambridge, M., 2004. Wavefront evolution in strongly heterogeneous layered media using the fast marching method. *Geophys. J. Int.*, 156, 631-647.

Rawlinson, N. and Sambridge, M., 2005. The fast marching method: An effective tool for tomographic imaging and tracking multiple phases in complex layered media. *Expl. Geophys.*, 36, 341–350.

Rawlinson, N., Reading, A. M. and Kennett, B. L. N., 2006. Lithospheric structure of Tasmania from a novel form of teleseismic tomography. *J. Geophys. Res.*, 111, B02301, doi:10.1029/2005JB003803.

Roggensack, K., Williams, S. N., Schaefer, S. J. and Parnell Jr., R. A., 1996. Volatiles from the 1994 Eruptions of Rabaul: Understanding large caldera systems. *Science*, 273, 490-493.

Sambridge, M. S., 1998. Exploring multidimensional landscapes without a map. *Inverse Problems*, 14, 427-440.

Sambridge, M. S., 1999. Geophysical inversion with neighbourhood algorithm – I: Searching a parameter space. *Geophys. J. Int.*, 138, 479-494.

Sambridge, M. and Kennett, B., 2001. Seismic event location: Nonlinear Inversion using Neighbourhood Algorithm. *Pure Appl. Geophys.*, 158, 241-257.

Saunders, S. J., 2001. The shallow plumbing system of Rabaul: a partially intruded ring fault ? *Bull. Volcanol.*, 63, 406-420.

Shaw, H. R., 1980. The fracture mechanisms of magma transport from the mantle to the surface. *In: Physics of magmatic processes* (Ed. R. B. Hargraves.), Princeton University Press, Princeton, NJ, 201-264.

Sudo, Y., and Kong, L. S. L., 2001. Three-dimensional seismic velocity structure beneath Aso Volcano, Kyushu, Japan. *Bull. Volcanol.*, 63, 326-344.

Takeo, M., 1983. Source mechanisms of Usu Volcano, Japan, earthquakes and their tectonic implications. *Phys. Earth Planet. Inter.*, 32, 241-264.

Thurber, C. H., 1993. Local earthquake tomography: velocities and V_p/V_s-theory. *In: Seismic tomography: Theory and Practice* (Eds. *Iyer, H. M. and Hirahara, K.*), Chapman and Hall, London, pp. 563-583.

Tiffin, D. L., Taylor, B. D., Tufar, W. and Itikarai, I., 1990. A seabeam and sampling survey of newly discovered Tavui Caldera near Rabaul, Papua New Guinea. *SOPAC Cruise Report 132*. 18pp.

Tregoning, P., Lambeck, K., Stolz, A., Morgan, P., McClusky, S. C., van der Beek, P., McQeen, H., Jackson, R. J., Little, R. P., Liang, A. and Murphy, B., 1998. Estimation of current plate motions in Papua New Guinea from Global Position system observations. *J. Geophys. Res.*, 103, 12181-12203.

Tregoning, P., McQueen, H., Lambeck, K., Jackson, R., Little, R., Saunders, S. and Rosa, R., 2000. Present-day crustal motion in Papua New Guinea. *Earth Planets Space*, 52, 727-730.

Toda, S., Stein, R. S. and Sagiya, T., 2002. Evidence from the AD 2000 Izu Islands earthquake swarm that stressing rate governs seismicity. *Nature*, 419, 58-61.

Um, J. and Thurber, C., 1987. A fast algorithm for two-point seismic ray tracing. *Bull. Seismol. Soc. Am.*, 77, 972-986.

Voronoi, M. G., 1908. Nouvelles applications des paramètres continues à la théorie des formes quadratiques, *J. reine angew. Math.* 134, 198-287.

Walker, G. P. L., Heming, R. F., Sprod, T. J. and Walker, T. J., 1981. Latest major eruptions of Rabaul Volcano. *In: Cooke-Ravian Volume of Volcanological Papers* (Ed., R. W. Johnson), Geological Survey of Papua New Guinea. Memoir 10, 181-193.

Weaver, C. S., Grant, W. C., Malone, S. D. and Endo, E. T., 1981. Post-May 18 seismicity: volcanic and tectonic implications. *In: The 1980 eruptions of Mount St Helens, Washington* (Eds. Lipman and D. R. Millineaux), U. S. Geol. Surv., Prof. Pap., 1250, 109-121.

Widiyantoro, S., Gorbatov, A., Kennett, B. L. N. and Fukao, Y., 2000. Improving global shear-wave delay-time tomography using three-dimensional ray tracing and iterative inversion, *Geophys. J. Int.*, 141, 747-758.

Wiebenga, W. A., 1973. Crustal structure of the New Britain-New Ireland region. *In: The Western Pacific: Island Arcs, Marginal Seas, Geochemistry* (Ed. P. J. Coleman), University of Western Australia Press, 163-177.

Wood, C.P., Nairn, I.A., McKee, C.O. and Talai, B., 1995. Petrology of the Rabaul Caldera area, Papua New Guinea. *J. Volcanol. Geotherm. Res.*, 69, 285-302.

APPENDIX A – RSAM plots for the strombolian eruptions

Appendix A contains the RSAM plots for the strombolian eruptions that occurred at Tavurvur between 1997 and 2005. They are as follows:

a) 9 January 1997
b) 14 March 1997
c) 12 April 1997
d) 1 June 1997
e) 12 July 1997
f) 17 August 1997

A strombolian eruption is a very energy-filled eruption characterised by constant strong volcanic explosions accompanied by loud booming noises. Many of the strong explosions produce air waves that can be felt several kilometers from the explosion source. At the peak of a strombolian eruption, explosions can occur at a rate of one per second. At night the strombolian eruption is typified by very impressive projections of incandescent lava fragments.

The data plotted is the average amplitude over a 10 minute period recorded at KPT seismic station. The station is located about 2 km west of Tavurvur. Some brief description for each event is presented with the plots. RSAM stands for Real-time Seismic Amplitude Measurements (Endo and Murray, 1991). Some things that are common to all the plots are, firstly the individual spikes on the plots correspond to brief periods of sustained high eruptive activity, or the summation of individual explosions during the 10-minute period. From observations the latter is more common. Secondly, the length of the spike is proportional to the magnitude(s) of the activity or explosions. Thirdly, the x-axis is time expressed in Universal Time (UT). The local time is 10 hours ahead of the UT. In three of the plots the curve reaches a plateau. The plateau is associated with effusion of lava from the erupting vent.

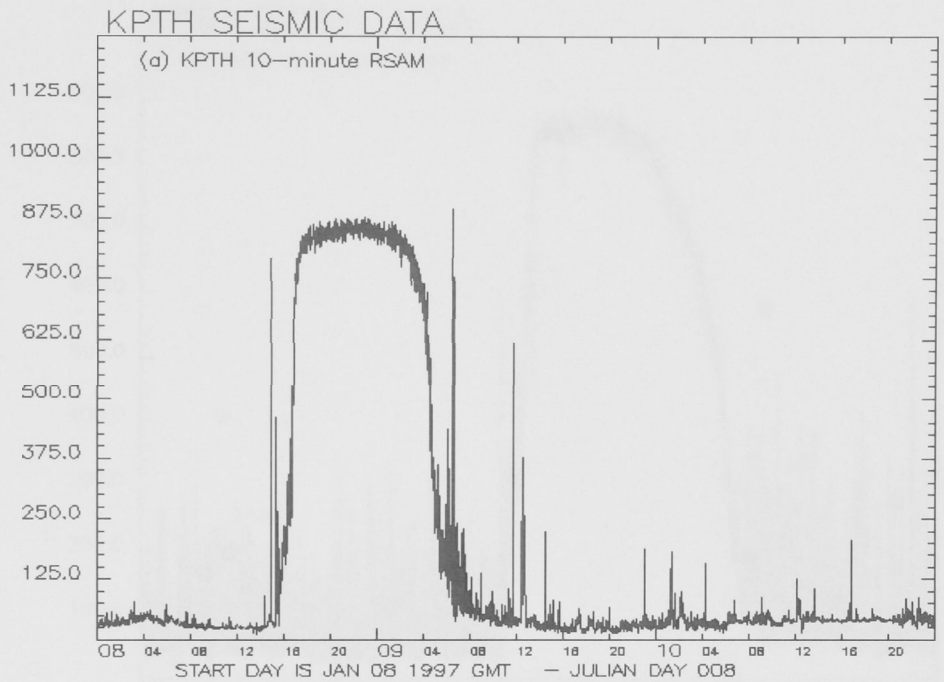

Fig. A-1: 9 January 1997. The strombolian eruption of 9 January 1997 was preceded by fairly low seismic and eruptive activity. This is indicated by the several hours of low activity characterized by the relatively quiet background noise. However some large spikes just before the onset of the eruption suggest the eruption was preceded by some large explosions. The buildup of the eruption is initially gradual but rapidly develops to its peak within less than one hour. The presence of a plateau at about 875 RSAM units in the curve corresponds to the effusion of lava during the eruption. The waning of the eruption is nearly exponential. Some milder explosive activity after the main event is evident shown by the slightly raised and spiky background.

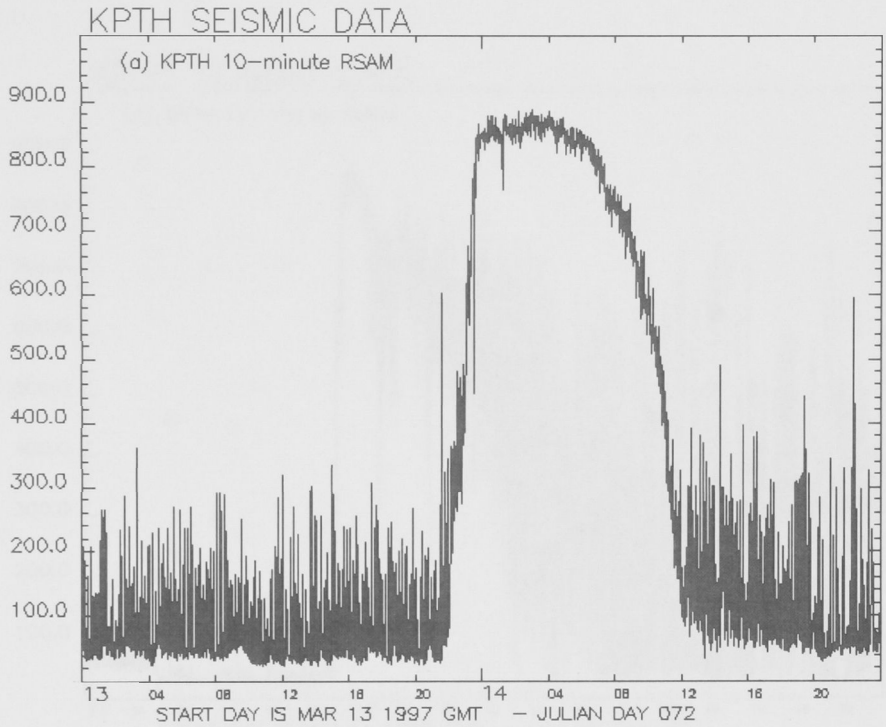

Fig. A-2: 14 March 1997. The pattern and the behavior of the 14 March strombolian eruption are quite similar to the 9 January 1997 eruption. The onset and the subsequent build-up to the peak of the eruption are rapid. However, there is evidence of pulsating/fluctuating activity during the build-up phase indicated by the breaks in the plot. This plot has a plateau at about 875 RSAM units during the peak of the activity and again this denotes lava effusion from the vent. The main difference between this and the RSAM plot for the 9 January 1997 eruption is the activity before and after the strombolian eruption. Here the pre- and post-strombolian activity is dominated by moderate RSAM values, meaning the strombolian eruption clearly developed in the midst of ongoing moderate explosive activity. Similar activity persisted after the strombolian eruption ceased.

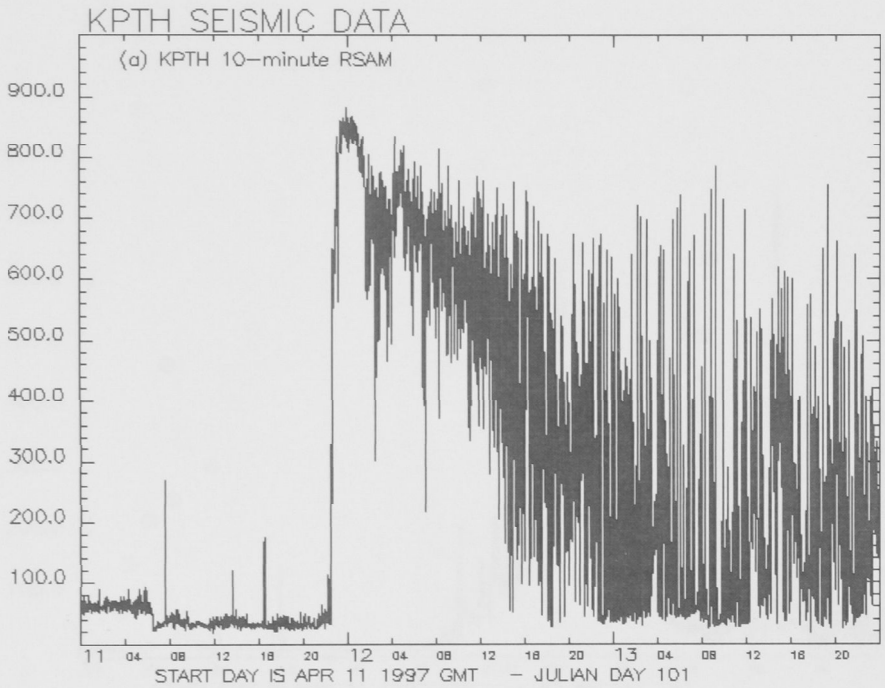

Fig. A-3: 12 April 1997. This plot marks the strombolian eruption of 12 April 1997. The curve suggests that the activity prior to the strombolian eruption is quiet. There are no immediate visible indicators on the curve to suggest notable activity before the commencement of the strombolian eruption. The rise-time from the onset of the eruption to the peak is more rapid than the two previous events. The eruption reaches a peak and maintains a plateau at about 875 RSAM units for a very short duration only compared to the two previous events. The plateau corresponds to the effusion of lava from the vent. The decay of this eruption is also very different from the two previous events. In this case the decay is prolonged over about 24 hours compared to the few to several hours only observed in the two previous events. After the strombolian eruption very intense explosive activity persisted. Minor strombolian eruptions are evident after the main event.

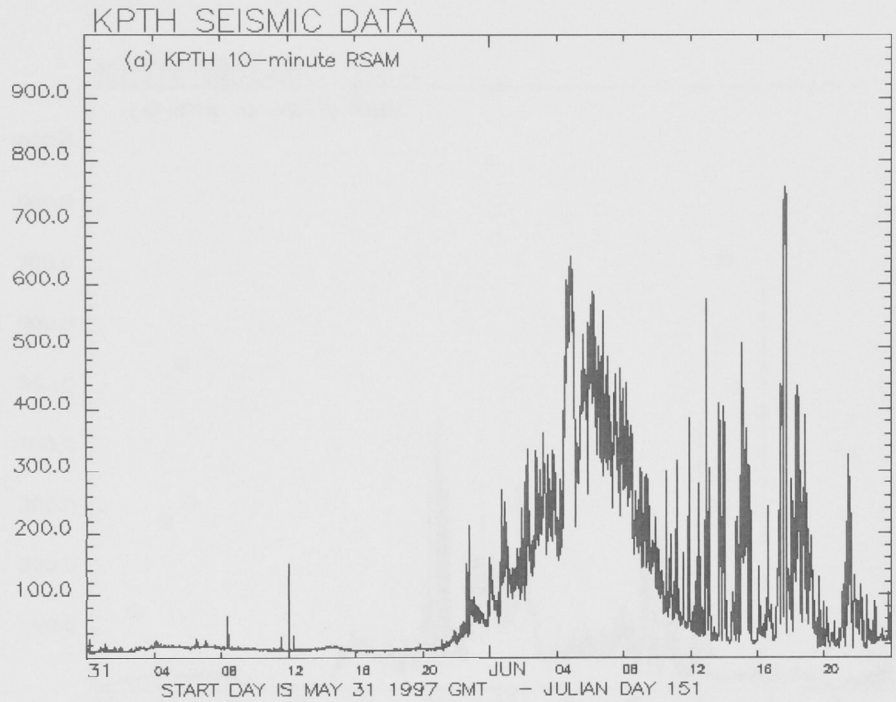

Fig. A-4: 1 June 1997. The strombolian eruption portrayed in this plot did not have the same intensity nor reached the same heights as the three previous eruptions. There is no clear evidence of prior activity before the strombolian eruption. The plot suggests that the buildup of the eruption to its peak is very slow and marked by fluctuations. The fluctuations are indicated by the rise and fall in the curve. The decay of the eruption is also rather slow. A fairly intense activity, with some minor strombolian phases, is evident after the main event. This eruption did not produce any lava flow.

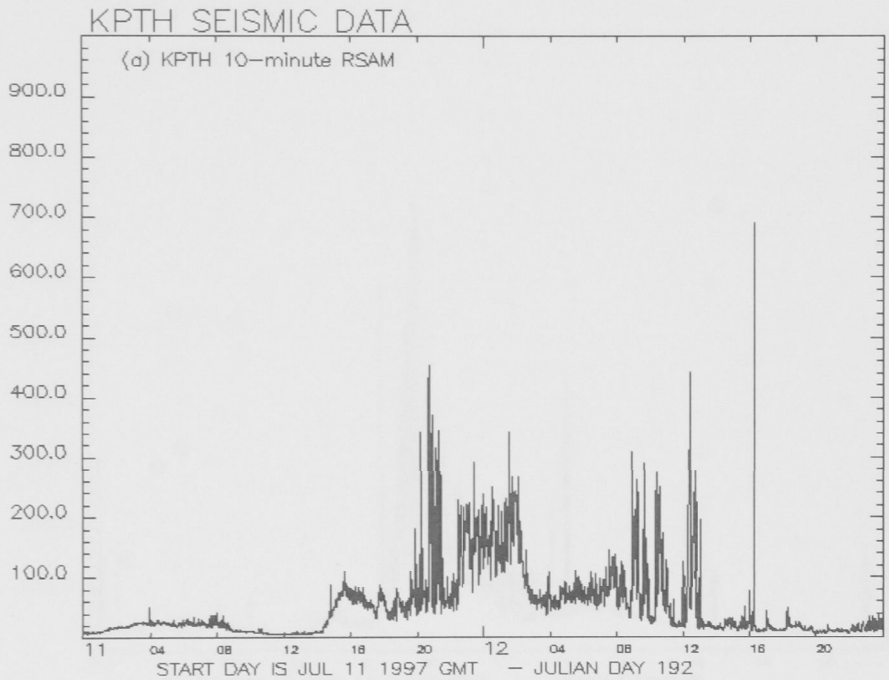

Fig. A-5: 12 July 1997. This particular strombolian eruption is very irregular as portrayed in the plot. The plot suggests that the eruption did not reach a single peak of activity. The plot also suggests that the eruption had a very irregular fluctuating pattern as indicated by the irregularity of the curve. In terms of eruption intensity this eruption is the least even though it carried on for about 24 hours. This eruption did not produce any lava flow.

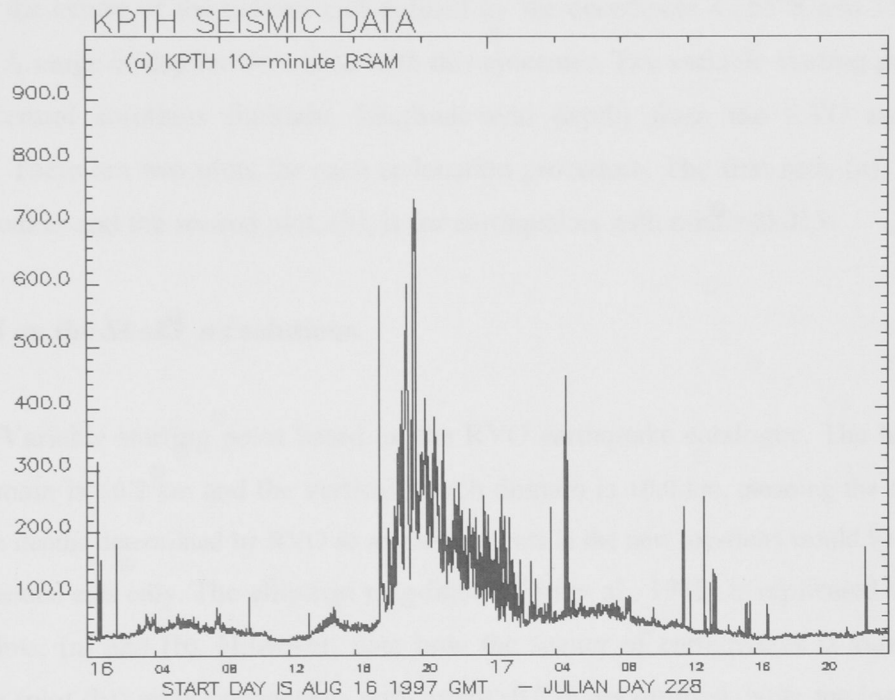

Fig. A-6: 17 August 1997. The strombolian eruption portrayed in this plot had the shortest duration and rated second last in terms of eruption intensity amongst all the eruptions listed above. This eruption did not produce any lava flow.

APPENDIX B – *Shak3_na* solutions

Appendix B contains a series of plots showing the distribution of earthquakes located with *Shak3_na* using variable and fixed epicenter and depth as the starting point. The earthquakes are for the period 1971 to 1985. For the fixed starting epicenter a point located at the centre of the caldera and defined by the coordinate 4.265°S and 152.190°E was used. A range of depths were used with this epicenter. The variable starting point used the hypocentral solutions (latitude, longitude and depth) from the RVO earthquake catalogue. There are two plots for each re-location procedure. The first plot, (a), is for all the earthquakes and the second plot, (b), is for earthquakes with misfit≤0.015.

Appraisal on the *Shak3_na* solutions.

Fig. B-1:.Variable starting point based on the RVO earthquake catalogue. The horizontal search domain is ±0.2 km and the vertical search domain is ±0.0 km, meaning the depths are fixed to the depths determined by RVO so any movements in the new locations would be observed in the horizontal axis only. The elliptical ring-fault (Mori et al., 1988) is replicated very well in both plots, (a) and (b). However, note how the scatter of earthquakes is significantly reduced in (plot (b)) after earthquakes with misfit>0.015 are omitted. Note the locations of Tavurvur and Vulcan with respect to the ring-fault. Tavurvur is located almost on the ring-fault whereas Vulcan is offset from it by nearly a kilometer. Since the depths are fixed to the RVO solutions the W-E and S-N depth sections are expected to be replicated very closely unless there is large movements in the horizontal axis. The replication is good as shown by the following three observations. They are, firstly the outward dipping planes shown in the W-E section, secondly the strong concentration of events at about 0.1 and 2.0 km depth, and lastly the two strong clusters of earthquakes shown in S-N depth section. The latter is almost identical to Fig. 2.8.

Fig. B-2: Variable starting point based on the RVO earthquake catalogue. The horizontal search domain is ±0.2 km and the vertical search domain is ±4.0 km. The elliptical ring-fault is replicated well. Again note the locations of Tavurvur and Vulcan. Tavurvur is located nearly at the center of the ring-fault. The location of Vulcan is offset from the ring-fault by about 0.5 to 1.0 km.

There are some notable differences in the depth sections. Firstly, the strong concentrations of earthquakes at about 0.1 km and 2.0 km depth have diminished. Secondly, the depth of majority of the earthquakes range between about 1.0 and 4.0 km and the earthquakes tend to be tightly clustered within this range, unlike Fig. B-1, where the earthquakes are spread out between about 0.2 and 4.0 km. Lastly, the biggest difference is displayed in the S-N depth section. Unlike the corresponding depth section in Fig. B-1, here the earthquakes form a single cluster only. From here on this cluster will be referred to as the 'structure'. Plot (b) suggests the earthquakes are shallow on the northern end of the structure and they get deeper towards the south. A trend-line through the structure gives an angle of about 12° from the horizontal.

Fig. B-3: Fixed starting point. The epicenter is defined by the point 4.26°S and 152.19°E and the search domain is ±0.2 km. The depth is 0.0 km and the search domain is ±15.0 km. The elliptical ring-fault is replicated well. The locations of Tavurvur and Vulcan with respect to the ring-fault are almost unchanged. The earthquakes seem to be scattered a lot more in plot (a) compared to the corresponding plot in Fig. B-2. The scatter is reduced significantly when earthquakes with misfit>0.15 are omitted (plot (b)). The depth section plots suggest the earthquake depths range between shallow and about 5 km. The outward dipping planes in the W-E depth section are clearly visible. The distribution of earthquakes in the S-N depth section is very scattered in plot (a) but improves significantly when earthquakes with misfit>0.15 are omitted (plot (b)). Plot (b) shows only one structure, similar to the corresponding plot in Fig. B-2. Earthquakes are shallow on the northern end and they get deeper towards the south. A trend-line through the structure gives an angle of approximately 22° from the horizontal.

Fig. B-4: Fixed starting point. The epicenter is 4.26°S and 152.19°E and the search domain is ±0.2 km. The starting depth is 2.5 km and the search domain is ±4.0 km. The elliptical ring-fault is nearly identical to those in the previous figures, and the locations of Tavurvur and Vulcan with respect to the ring-fault are also similar. The depth sections here are almost identical to those in Fig. B-2. The main similarity is the tight clustering of events between about 1.0 and 4.0 km. The outward dipping planes in the W-E depth section are visible in plot (b) but less distinct compared to the corresponding plot in Fig. B-3. The southward sloping structure in the S-N depth section is clearly displayed. A trend-line through the structure gives an angle of approximately 18° from the horizontal. Note the cluster of events between 0-0.5 km depth and latitude 4.29°S and 152.30°E in plot (a). The events are still visible in plot (b) but the number of events is reduced significantly due to filtering.

Fig. B-5: Fixed starting point. The epicenter is 4.26°S and 152.19°E and the search domain is ±0.2 km. The starting depth is 4.0 km and the search domain is ±4.0 km. The elliptical ring-fault is replicated very well and the locations of Tavurvur and Vulcan with respect to the ring-fault are similar to the previous figures. There is some scattering away from the main ring-fault axis. The outward dipping planes in the W-E depth section are still maintained. The southward slopping structure in the S-N depth section is clearly visible. A trend-line through the structure gives an angle of approximately 23° from the horizontal position.

Fig. B-6: Fixed starting point. The epicenter is 4.26°S and 152.19°E and the search domain is ±0.2 km. The starting depth is about 5.0 km and the search domain is about ±5.0 km. The epicenter and depth distribution patterns obtained here is similar to those obtained in Fig. B-5.The elliptical ring-fault, the outward-dipping planes in the W-E depth section, the southward sloping structure in the S-N depth section are all replicated very well. The location of Tavurvur and Vulcan with respect to the ring-fault is similar to the other five cases. A trend-line through the structure gives an angle of approximately 25° from the horizontal.

Summary:

The *Shak3_na* solutions from the six examples replicates the elliptical ring-fault of Mori et al., (1988) very well with only very minor differences, irrespective of the different initial starting points and the search domains. Some scattering is obvious in some of them (Fig. B-3, Fig. B-5 and Fig. B-6) but applying some filtering criteria eliminates the scattering. Between the three figures Fig. B-5 seems slightly better. The locations of Tavurvur and Vulcan with respect to the ring-fault are very similar in all cases. Vulcan is offset from the center of the ring-fault by about 0.5-0.8 km. Tavurvur is located on or on the fringe of the ring-fault.

The depth sections are mixed. The W-E depth section from the RVO earthquake catalogue defines a fairly evenly stretched out distribution between about 0.1 and 4.0 km with a fairly distinct outward dipping planes (Mori et al., 1988). The solutions from the six *Shak3_na* examples also display the outward dipping planes but the pattern of distribution is different from each other. For example, Fig. B-2 and Fig. B-4 have majority of the earthquakes distributed fairly tightly between about 1.0 and 4.0 km, whereas in Fig. B-3, Fig. B-5 and Fig. B-6, the distribution of the earthquakes is more spread out between about 0.5 and 5.0 km.

The S-N depth sections between the RVO earthquake catalogue and the *Shak3_na* solutions are completely different. The RVO earthquake catalogue displays two distinct clusters, alias structures (Fig. 2.8). On the other hand, except Fig. B-1 which has the earthquake depths fixed to the depths in the RVO earthquake catalogue, the S-N depth sections for the other five *Shak3_na* solutions (Fig. B-2 to Fig. B-6) displays only one structure. The structure slopes to the south. Best-fit straight lines were fitted to the slope of the structure to determine the slope angle. Fig. B-3, Fig. B5 and Fig. B6 had slope angles of 23°, 23° and 25° respectively. Fig. B-2 and Fig. B4 had slope angles of 12° and 17°, respectively.

The above discussions strongly suggest that the initial starting point and the corresponding search domain have a strong influence on the final solutions. The solutions shown in Fig. B-5 have been adopted in this study.

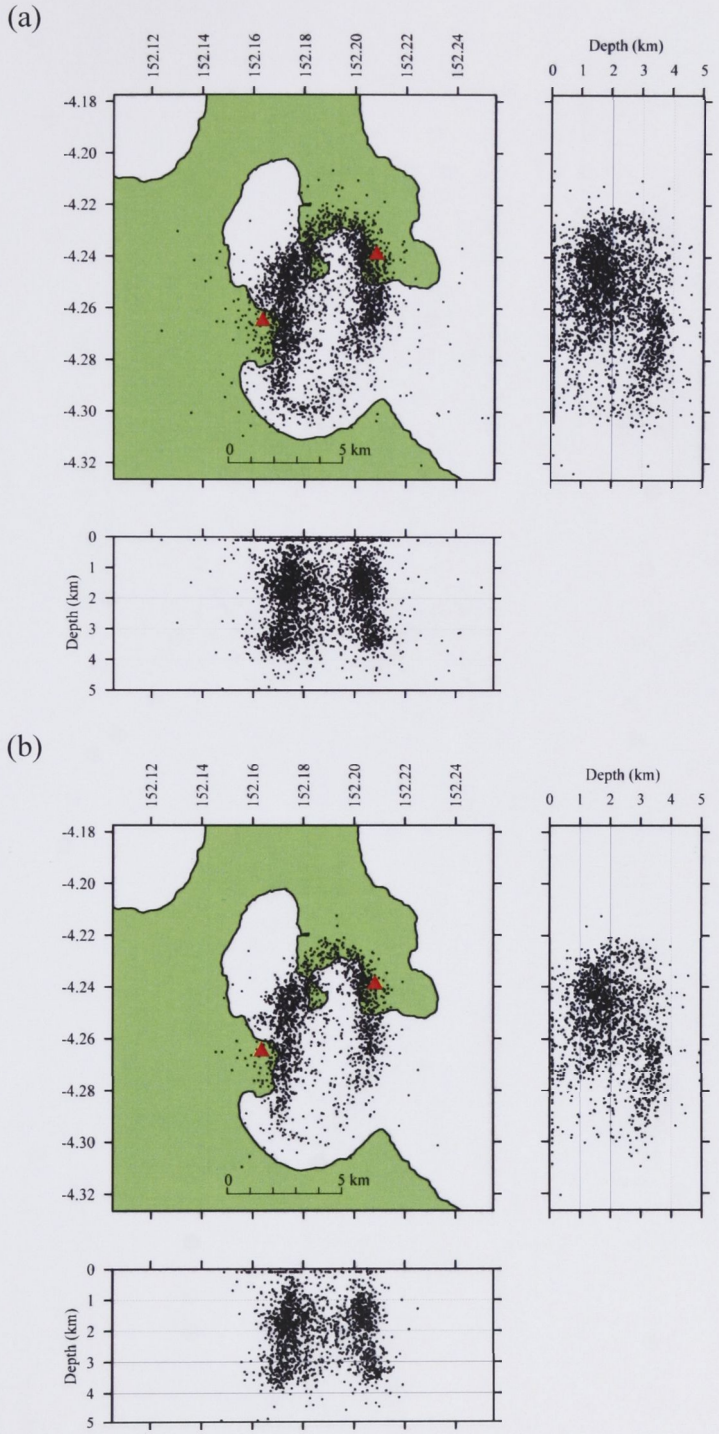

Fig. B-1: Relocated epicenters after 120 iterations using variable starting points based on the RVO solutions. The horizontal search domain is ±0.20° and the vertical search domain is ±0.0 km. The vertical search domain of ±0.0 means the depths are fixed to the RVO depths. (a) all the data and, (b) filtered data with a misfit value of $\leqslant$0.015.

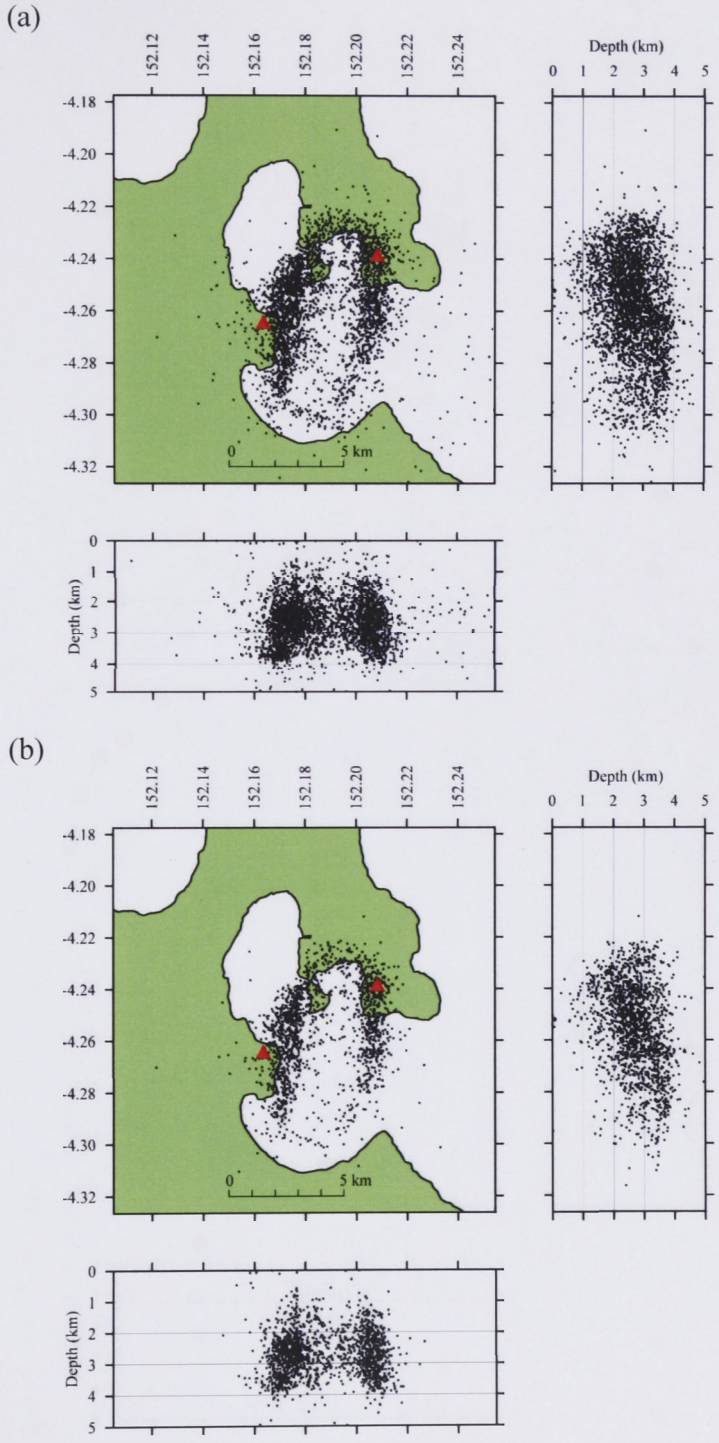

Fig. B-2: Relocated epicenters after 120 iterations using variable starting points based on the hypocentral solutions determined by RVO. The horizontal search domain is ±0.20° and the vertical search domain is ±4.0 km. (a) all the data and, (b) filtered data with a misfit value of ⩽0.015.

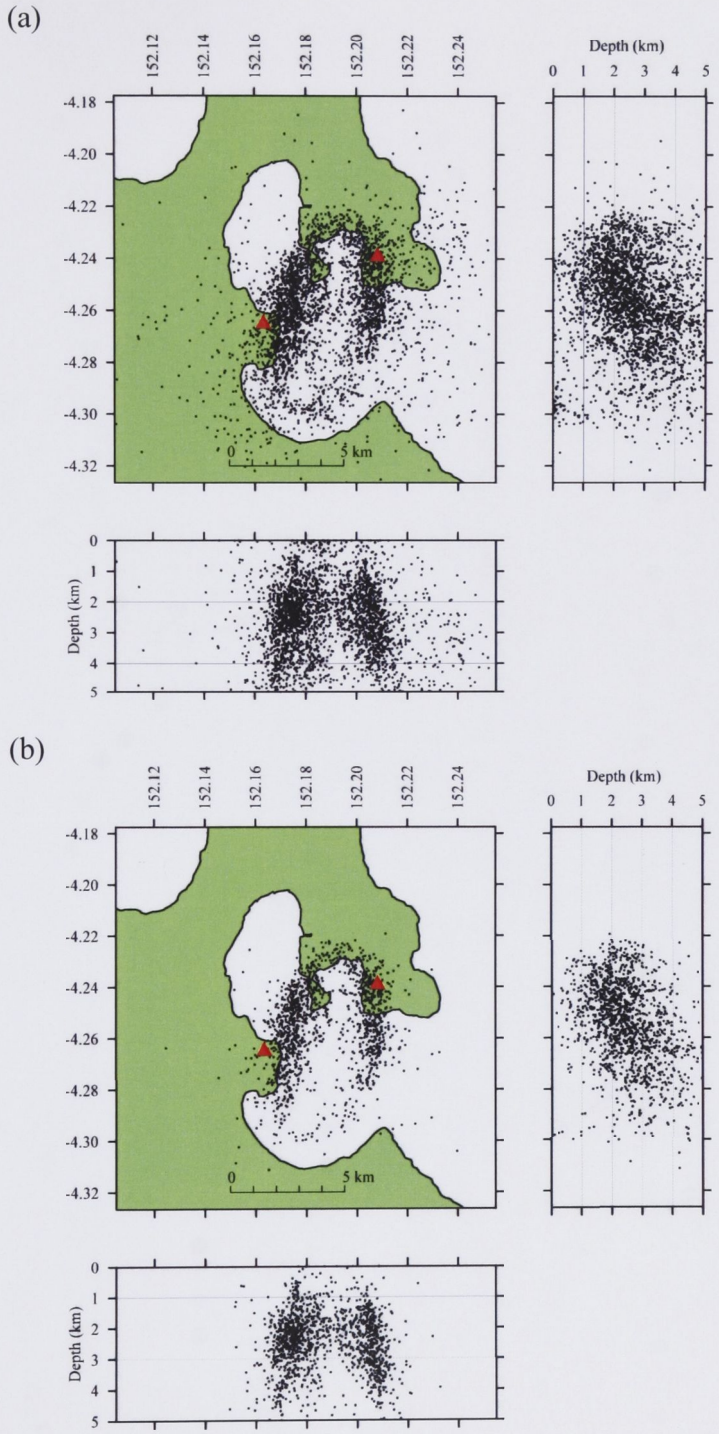

Fig. B-3: Relocated epicenters after 120 iterations using a fixed starting point at -4.265°S and 152.190°E with a search domain of ±0.20°. The starting depth is 0.0 km and the corresponding search domain is ±15.0 km. (a) all the data and, (b) filtered data with a misfit value of $\leqslant$0.015.

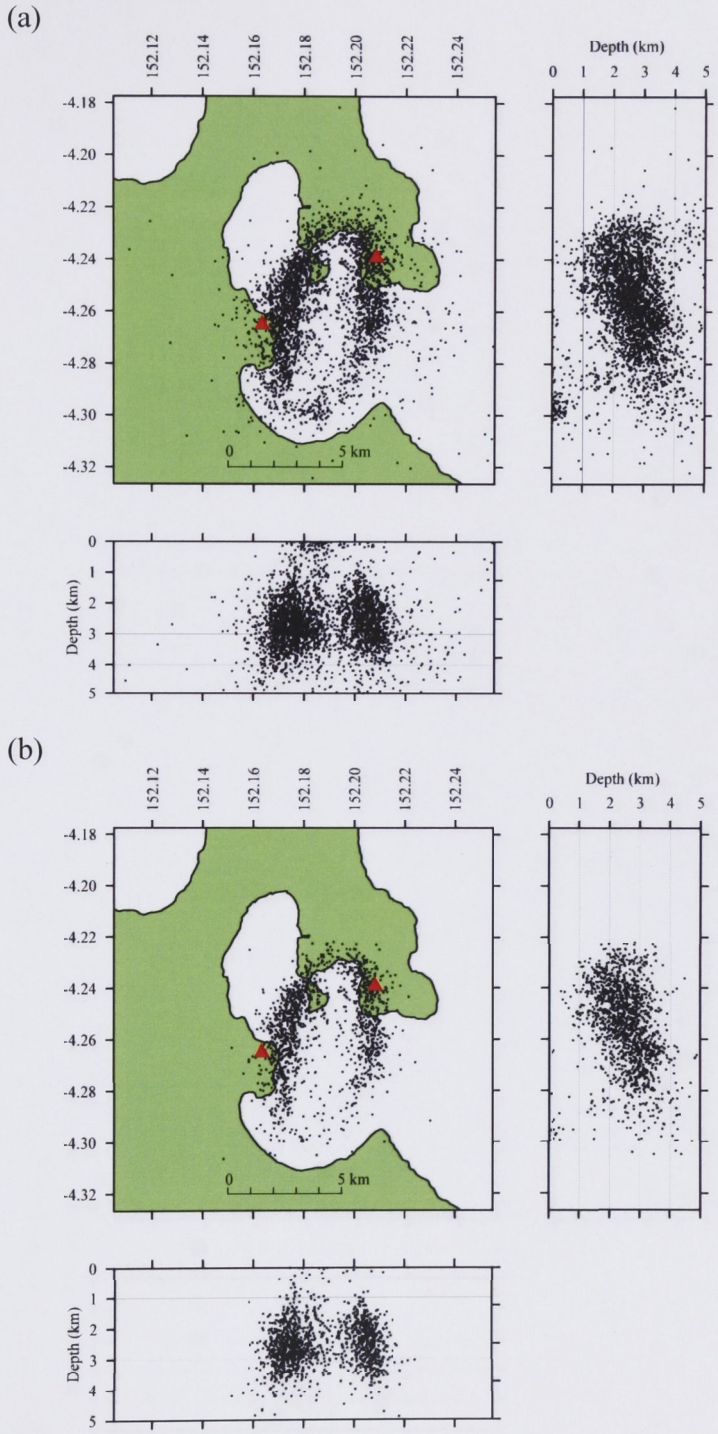

Fig. B-4: Relocated epicenters after 120 iterations using a fixed starting point at -4.265°S and 152.190°E with a search domain of ±0.20°. The starting depth is 2.5 km and the corresponding search domain is ±4.0 km. (a) all the data and, (b) filtered data with a misfit value of $\leqslant$0.015.

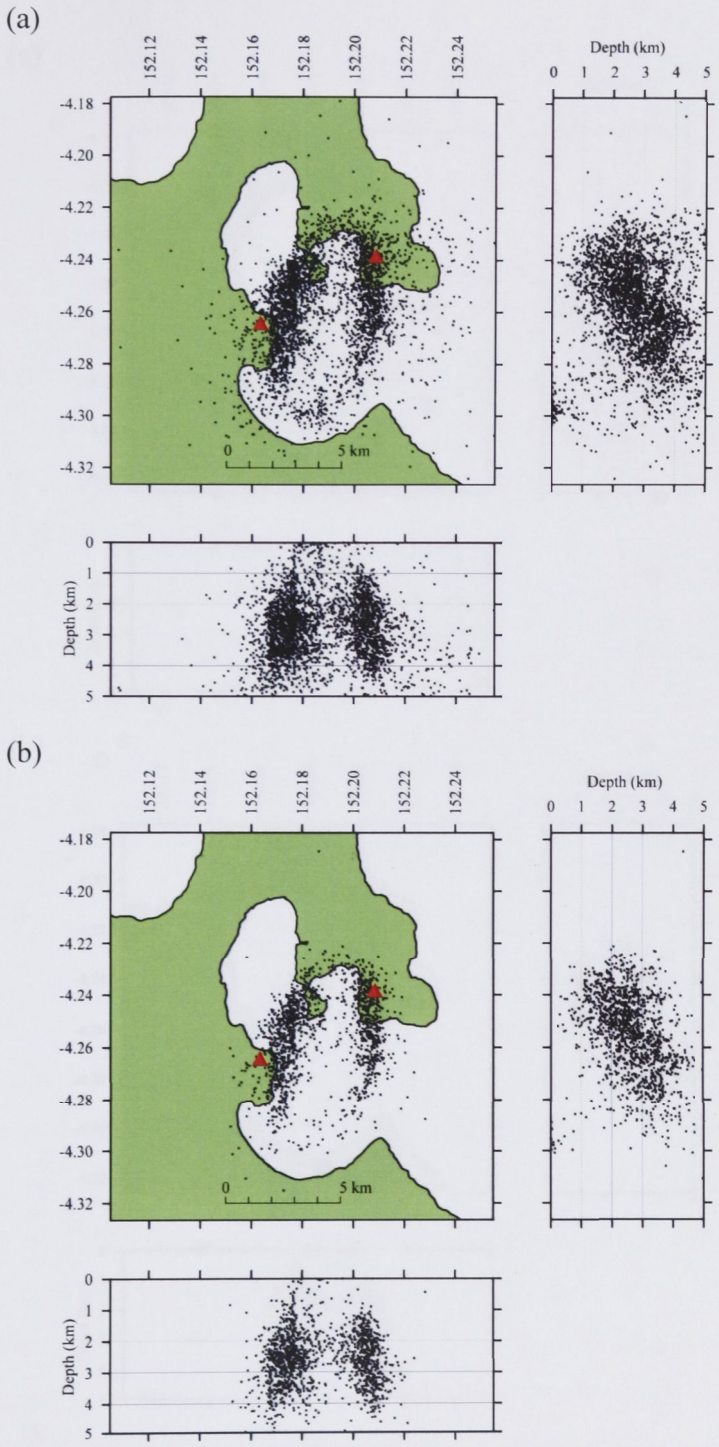

Fig. B-5: Relocated epicenters after 120 iterations using a fixed starting point at -4.265°S and 152.190°E with a search domain of ±0.20°. The starting depth is 4.0 km and the corresponding search domain is ±4.0 km. (a) all the data and, (b) filtered data with a misfit value of $\leqslant$0.015.

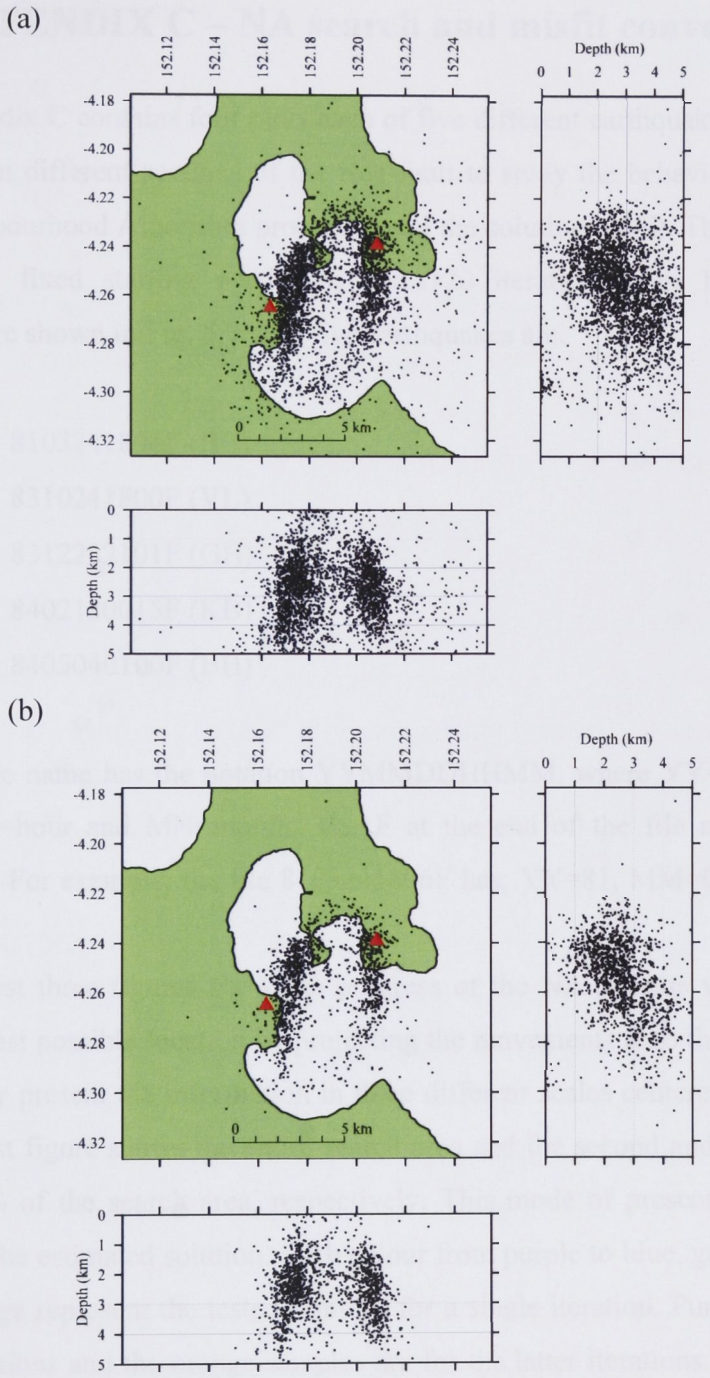

Fig. B-6: Relocated epicenters after 120 iterations using a fixed starting point at -4.265°S and 152.190°E with a search domain of ±0.20°. The starting depth is 5.0 km and the corresponding search domain is ±5.0 km. (a) all the data and, (b) filtered data with a misfit value of $\leqslant$0.015.

APPENDIX C – NA search and misfit convergence

Appendix C contains four plots each of five different earthquakes that were chosen randomly from different sections of the ring-fault to study the behaviour of convergence for the Neighbourhood Algorithm procedure and the solution misfit. The earthquakes were located using fixed starting conditions and 120 iterations. The locations for these earthquakes are shown in Fig. 5.7. The five earthquakes are:

- 8103241806F (BB)
- 8310241800F (VL)
- 8312282101F (GH)
- 8402180015F (KB)
- 8405040100F (BH)

The file name has the notation YYMMDDHHMM, where YY=year, MM=month, DD=day, HH=hour and MN=month. The F at the end of the file name denotes fixed starting point. For example, the file 8103241806F has; YY=81, MM=03, DD=24, HH=18 and MN=06.

The first three figures show the progress of the NA scheme with an L_1 measure towards the best possible location by projecting the movements onto the spatial axes and a time bar. They present the information in three different scales centered about the starting point. The first figure shows the entire search area and the second and third figures show 50% and 10% of the search area, respectively. This mode of presentation improves the resolution of the estimated solution. Each colour from purple to blue, green, yellow, brown and then orange represent the tested samples for a single iteration. Purple samples are for the early iterations and the orange samples are for the latter iterations. The black samples are for the last few iterations. An estimate of the reliability for the estimated hypocenter can be derived from the spread of the black samples. However in some a light grey polygon is plotted as well. The polygon gives an estimate of the solution reliability.

The last figure shows the progress of the NA procedure. The three plots in the figure are for the best fit model per iteration, the mean misfit across all models for each iteration and the current best fit. The main idea is to show how the models converge.

Appraisal for the NA search and misfit convergence

Event 8103241806F: The NA progression towards convergence for Event 8103241806F is very smooth as shown in Fig. C-11 to Fig. C-13. At the zoom-in scale of 8 x 8 km horizontal search space the zone representing the low misfits, indicated by the black circles, is very confined. This represents good convergence with low misfit. The uncertainty for the solution is less than 0.2 km. Fig. C-14 shows the misfit measure. This parameter converges very quickly to about 0.01 at about iteration 20. The lowest misfit measure of less than 0.002 is reached after iteration 80.

Event 8310241800F: The NA convergence for this event is marginally slow. This is indicated by the greater spread of the epicenters with good misfits (coloured circles). The spread is more apparent in Fig. 2-23. The uncertainty estimate for the event is about 0.2-0.3 km. The misfit measure (Fig. C-24) also gives a similar result. It converges at about iteration 30 and the best value is about 0.02.

Event 8312282101F: Event 8312282101F has more trouble converging. This is probably best illustrated in Fig. C34, showing the convergence of the misfit measure. The misfit measure improves considerably to less than 0.002 at iteration 100 from a value of about 0.07 at about iteration 10. The convergence is almost linear. The uncertainty for the solution is about 0.8 km. This example illustrates that the NA convergence to the best possible solution can be achieved more slowly than expected.

Event 8402180015F: The behaviour of the NA convergence for this event and event 8405040100F are almost identical. They converge fairly rapidly but the lowest misfit measure they reach is about 0.02 at about iteration 40 and 50, respectively. The uncertainty for the solution estimate is about 0.4 km.

Event 8405040100F: Same as Event 8402180015F.

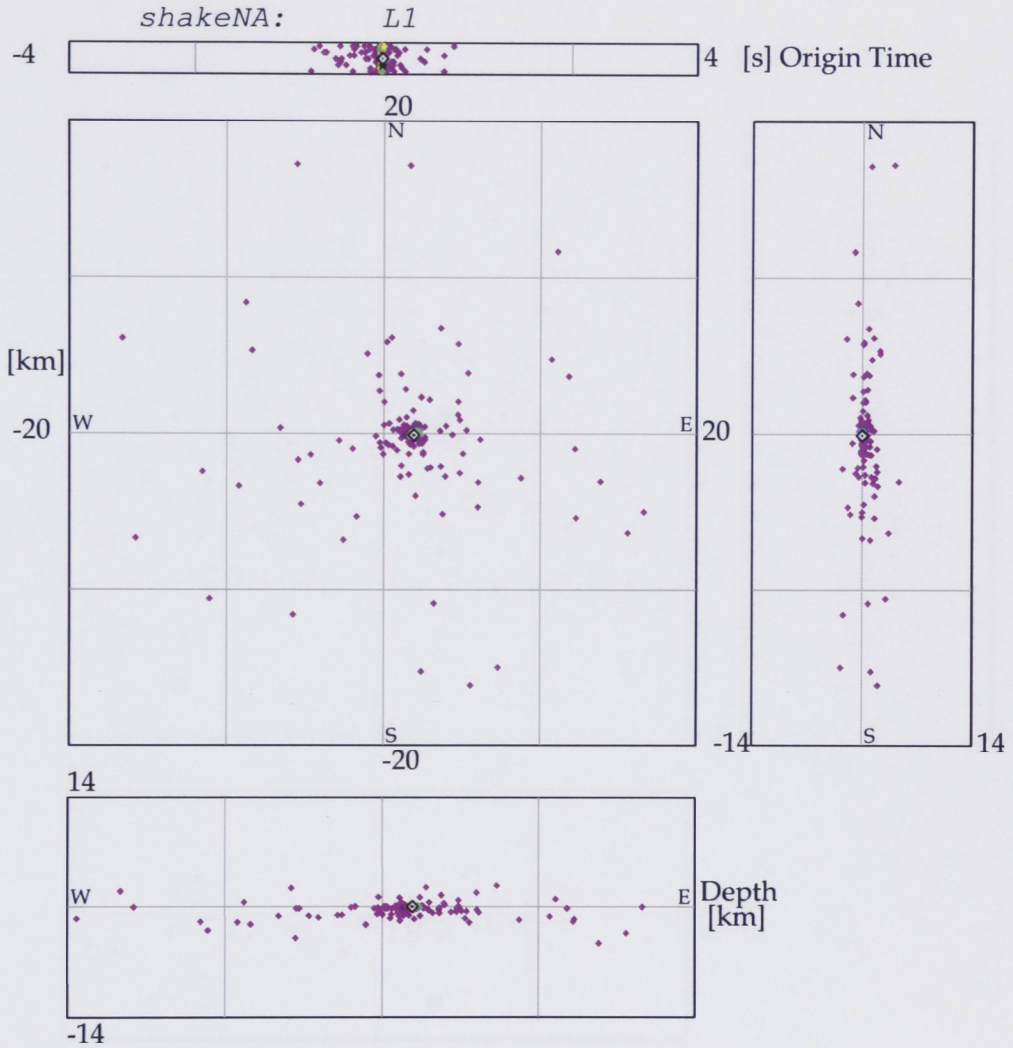

Fig. C-11: Illustration of the neighbourhood algorithm progression towards convergence for Event 8103241806F in the 4-D parameter space. The horizontal search area is 40 x 40 km. The centre of the plot is the starting search point and is given by the coordinate -4.265°S and 152.190°E. Each circle, irrespective of colour, denotes the tested epicenters. Note the spread of the purple circles. These are tested epicenters with high misfits. The area of strong clustering marked by the coloured circles gives the best location estimate. If they appear, the black circles have the least misfit.

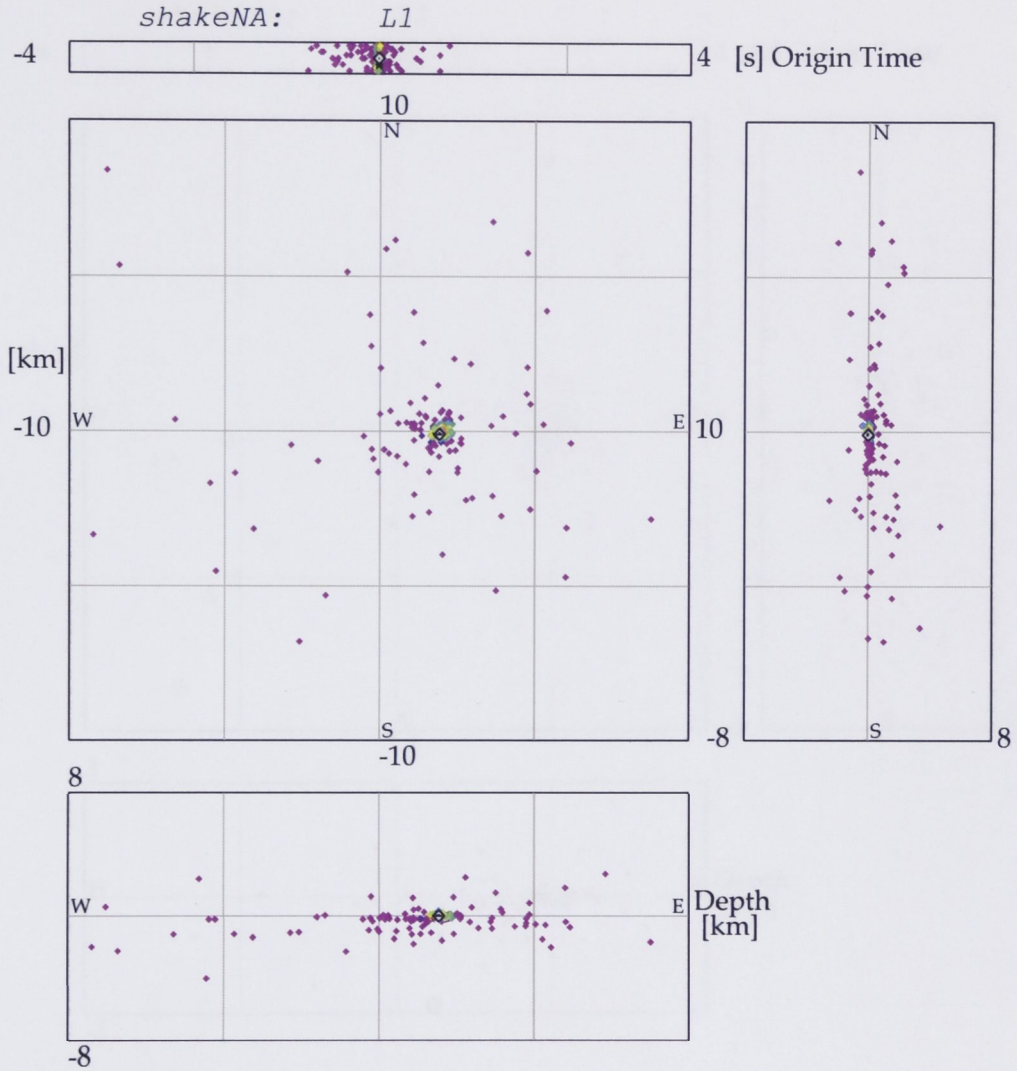

Fig. C-12: Illustration of the neighbourhood algorithm progression towards convergence for Event 8103241806F in the 4-D parameter space. The horizontal search area is 20 x 20 km. The centre of the plot is the starting search point and is given by the coordinate -4.265°S and 152.190°E. Each circle, irrespective of colour, denotes the tested epicenters. Note the spread of the purple circles. These are tested epicenters with high misfits. The area of strong clustering marked by the coloured circles gives the best location estimate. If they appear, the black circles have the least misfit.

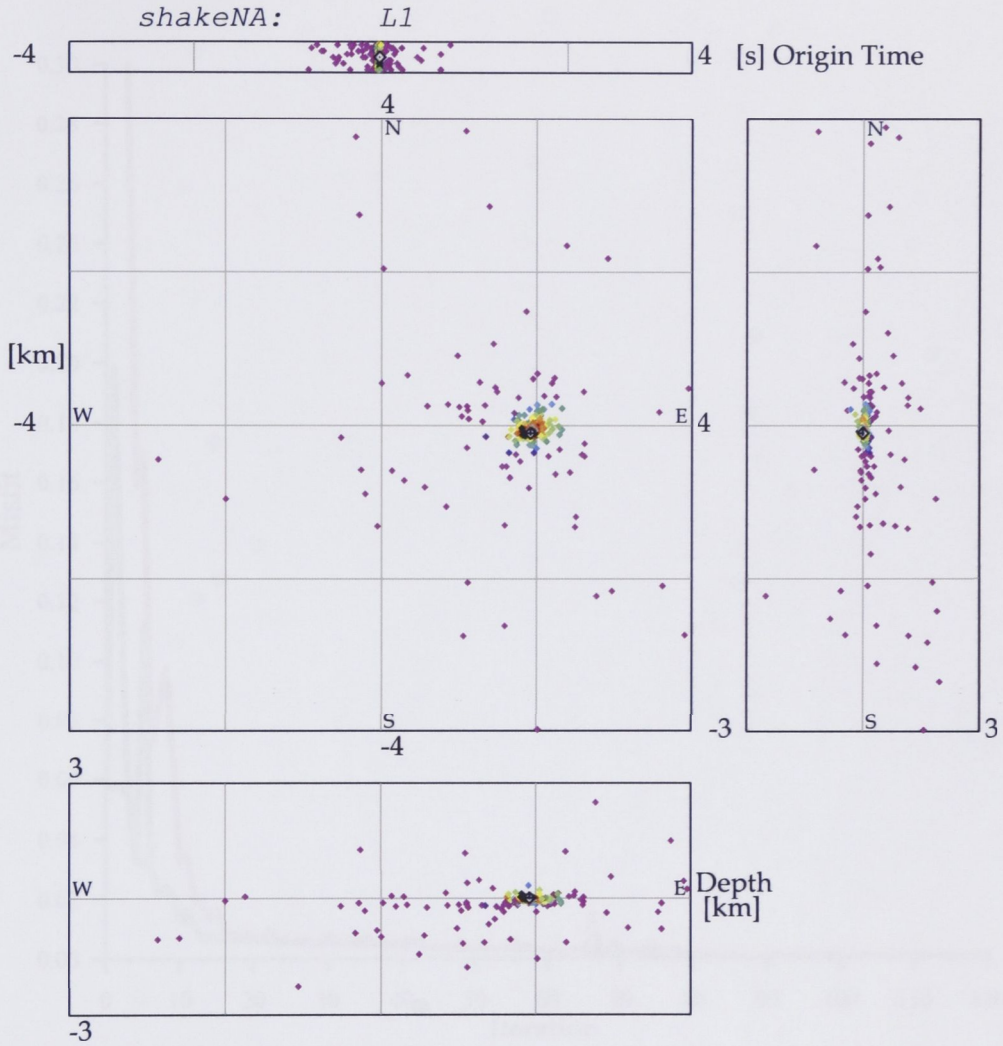

Fig. C-13: Illustration of the neighbourhood algorithm progression towards convergence for Event 8103241806F in the 4-D parameter space. The horizontal search area is 8 x 8 km. The centre of the plot is the starting search point and is given by the coordinate -4.265°S and 152.190°E. Each circle, irrespective of colour, denotes the tested epicenters. Note the spread of the purple circles. These are tested epicenters with high misfits. The area of strong clustering marked by the coloured circles gives the best location estimate. If they appear, the black circles have the least misfit.

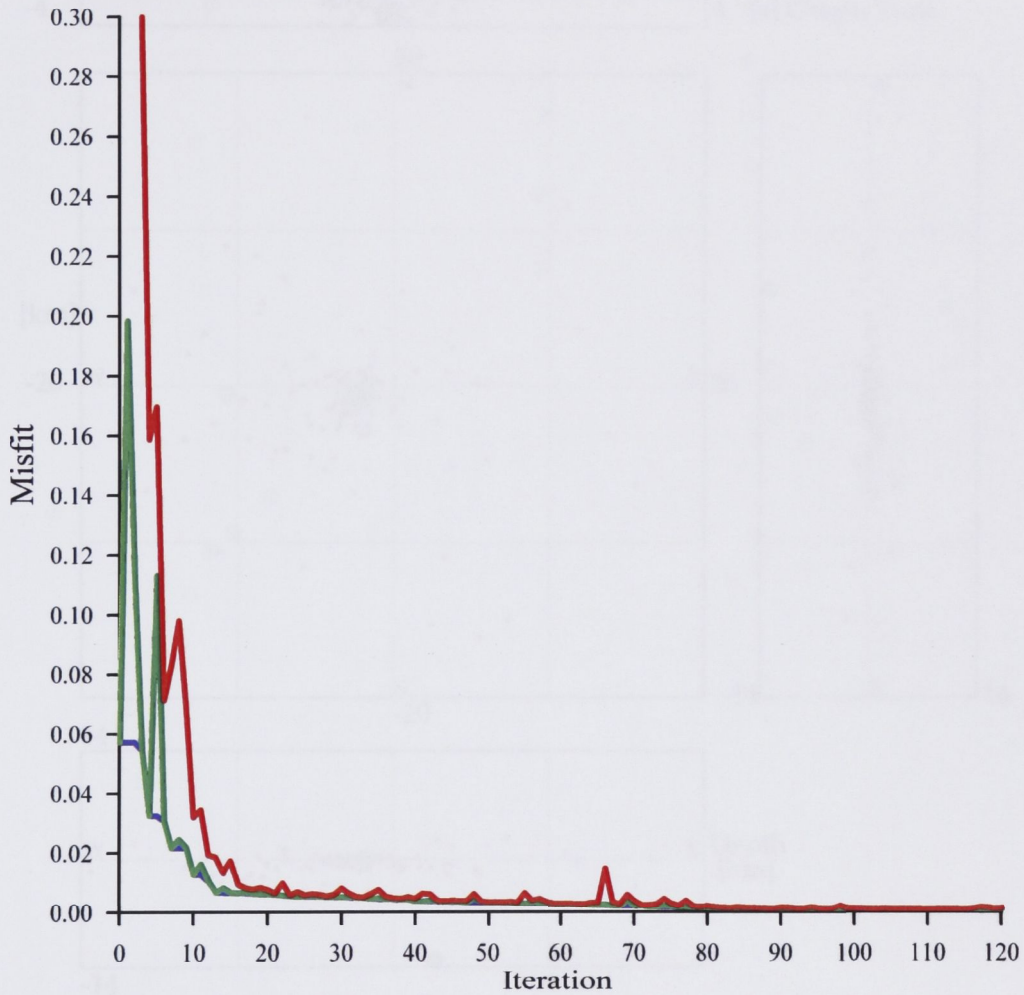

Fig. C-14: Plot of the misfit measure for Event 88103241806F. The blue line is for the lowest misfit in the model, red is the average misfit across all models and green is the current misfit. In this example all models converge at about iteration 20 but there are still minute improvements until about iteration 80.

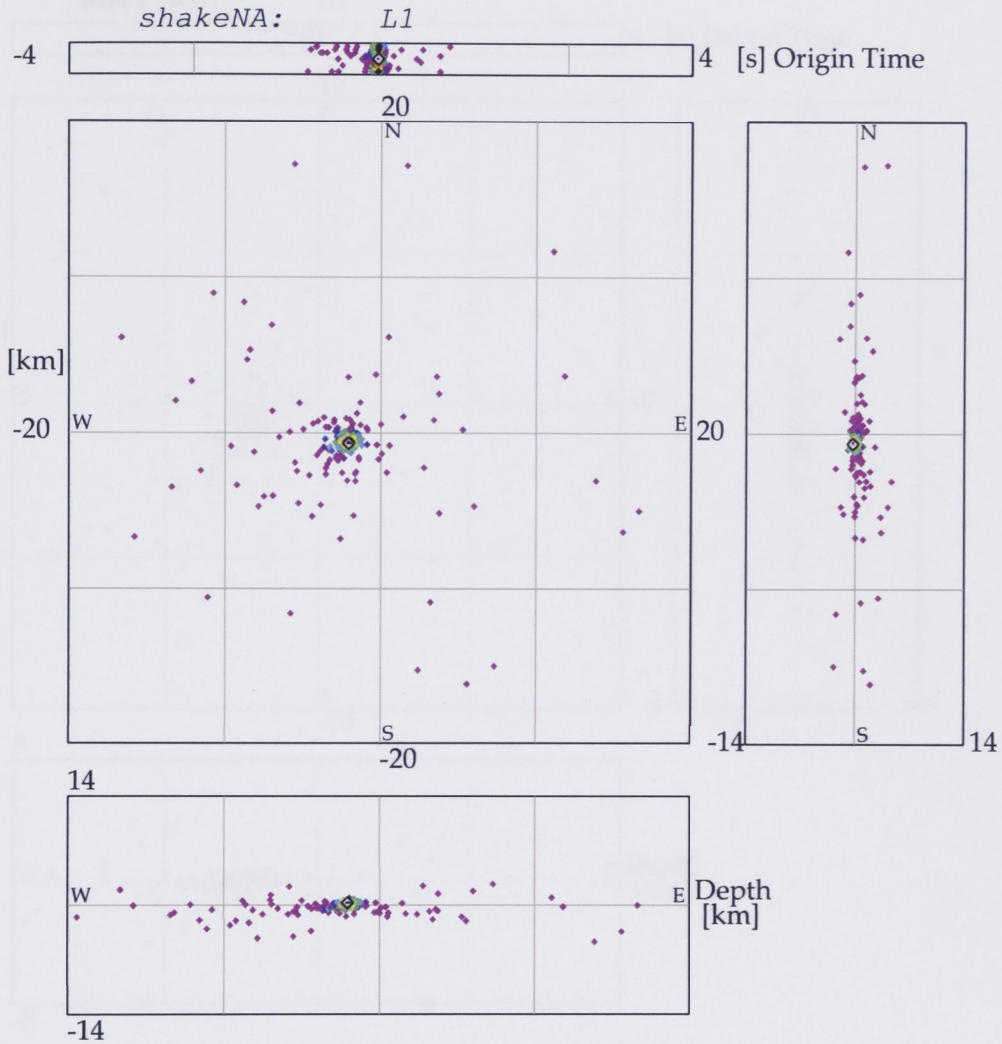

Fig. C-21: Illustration of the neighbourhood algorithm progression towards convergence for Event 8310241800F in the 4-D parameter space. The horizontal search area is 40 x 40 km. The centre of the plot is the starting search point and is given by the coordinate -4.265°S and 152.190°E. Each circle, irrespective of colour, denotes the tested epicenters. Note the spread of the purple circles. These are tested epicenters with high misfits. The area of strong clustering marked by the coloured circles gives the best location estimate. If they appear, the black circles have the least misfit.

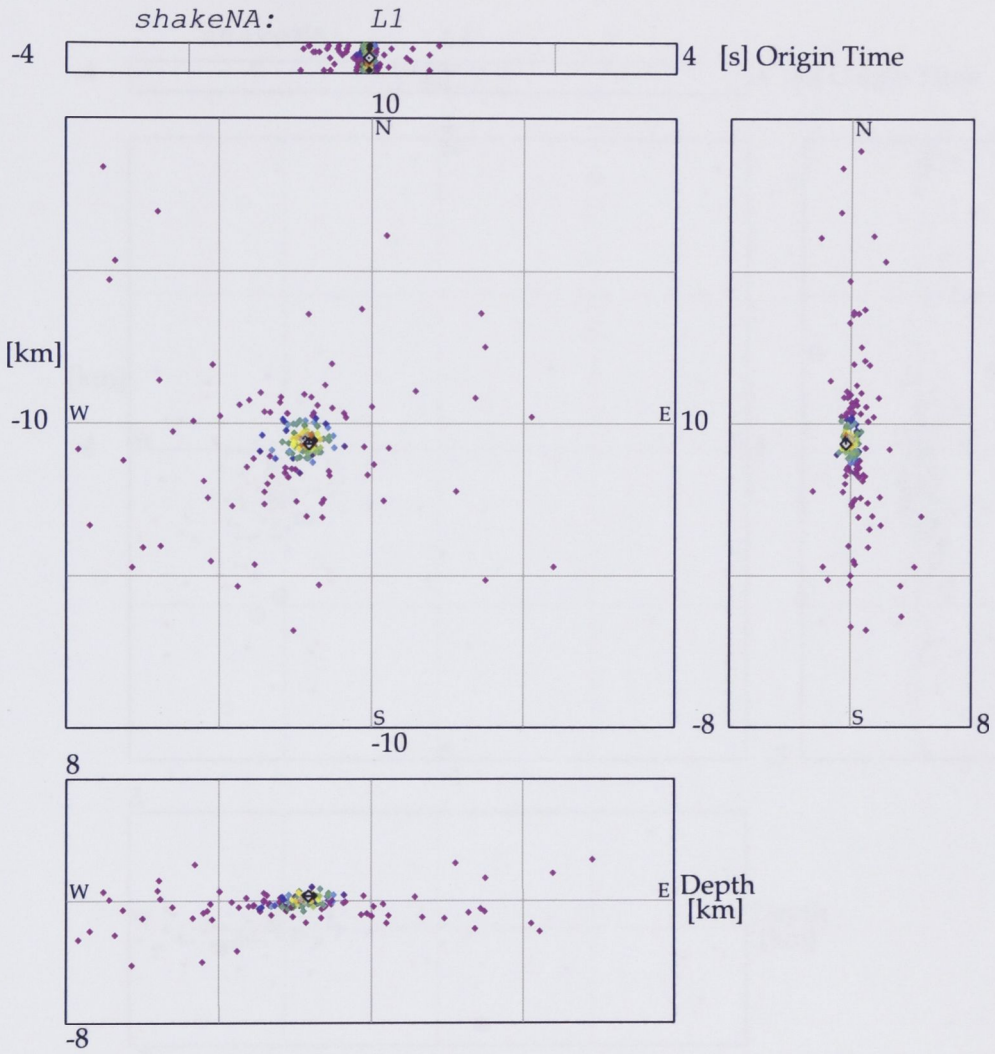

Fig. C-22: Illustration of the neighbourhood algorithm progression towards convergence for Event 8310241800F in the 4-D parameter space. The horizontal search area is 20 x 20 km. The centre of the plot is the starting search point and is given by the coordinate -4.265°S and 152.190°E. Each circle, irrespective of colour, denotes the tested epicenters. Note the spread of the purple circles. These are tested epicenters with high misfits. The area of strong clustering marked by the coloured circles gives the best location estimate. If they appear, the black circles have the least misfit.

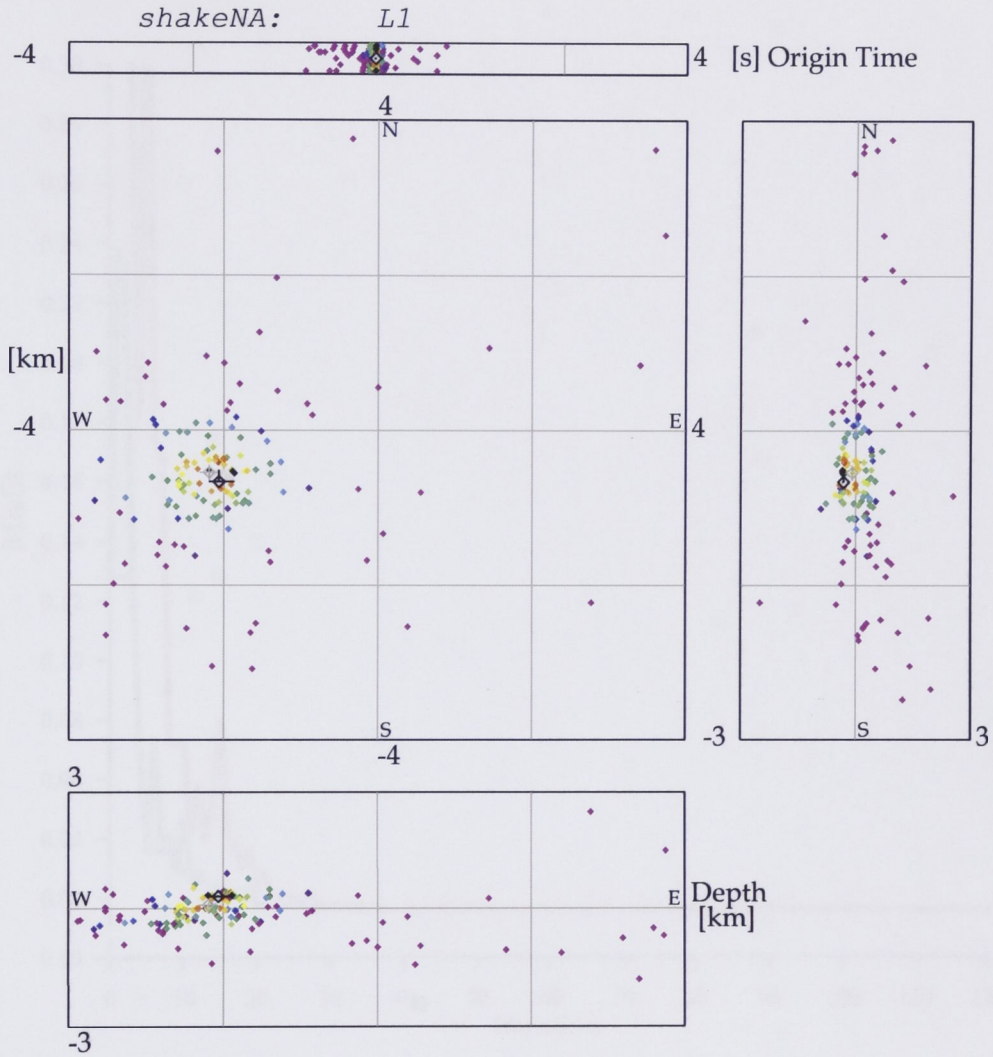

Fig. C-23: Illustration of the neighbourhood algorithm progression towards convergence for Event 8310241800F in the 4-D parameter space. The horizontal search area is 8 x 8 km. The centre of the plot is the starting search point and is given by the coordinate -4.265°S and 152.190°E. Each circle, irrespective of colour, denotes the tested epicenters. Note the spread of the purple circles. These are tested epicenters with high misfits. The area of strong clustering marked by the coloured circles gives the best location estimate. If they appear, the black circles have the least misfit.

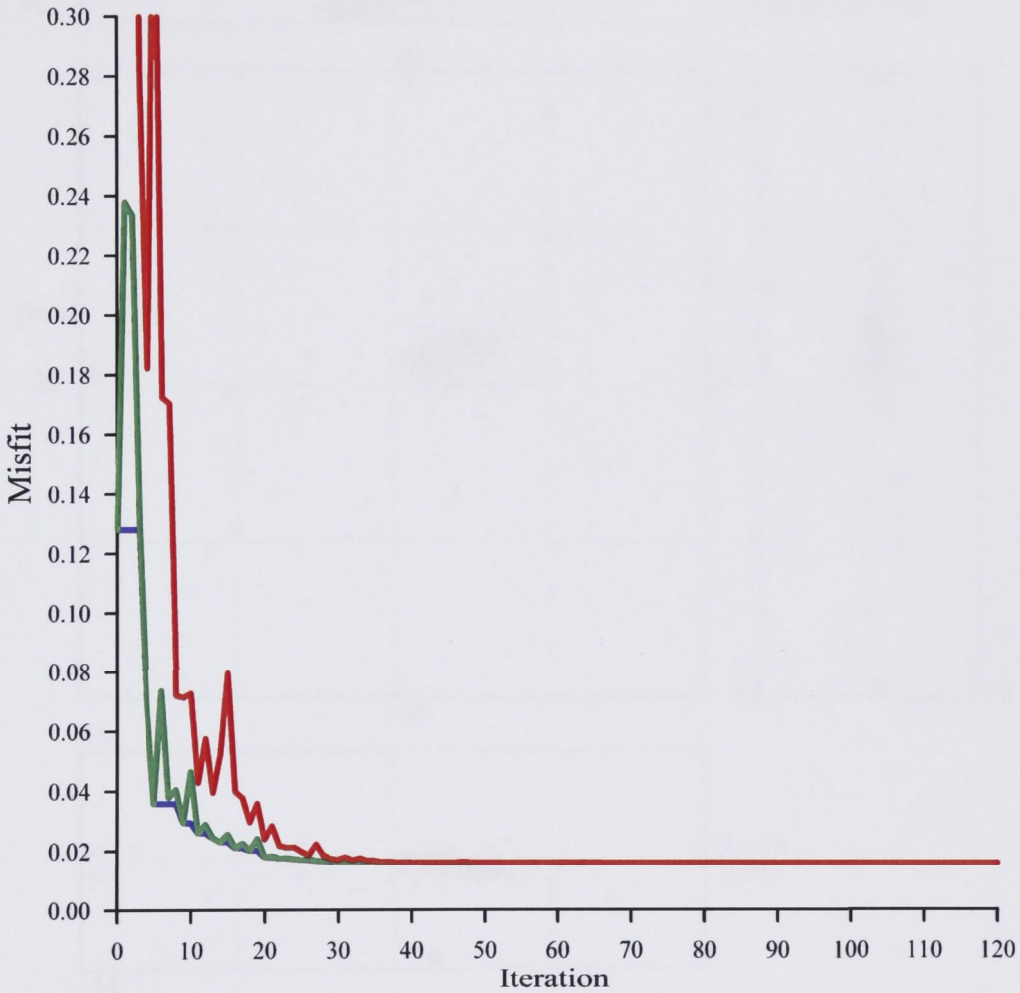

Fig. C-24: Plot of the misfit measure for Event 8310241800F. The blue line is for the lowest misfit in the model, red is the average misfit across all models and green is the current misfit. In this example all models converge at about iteration 35.

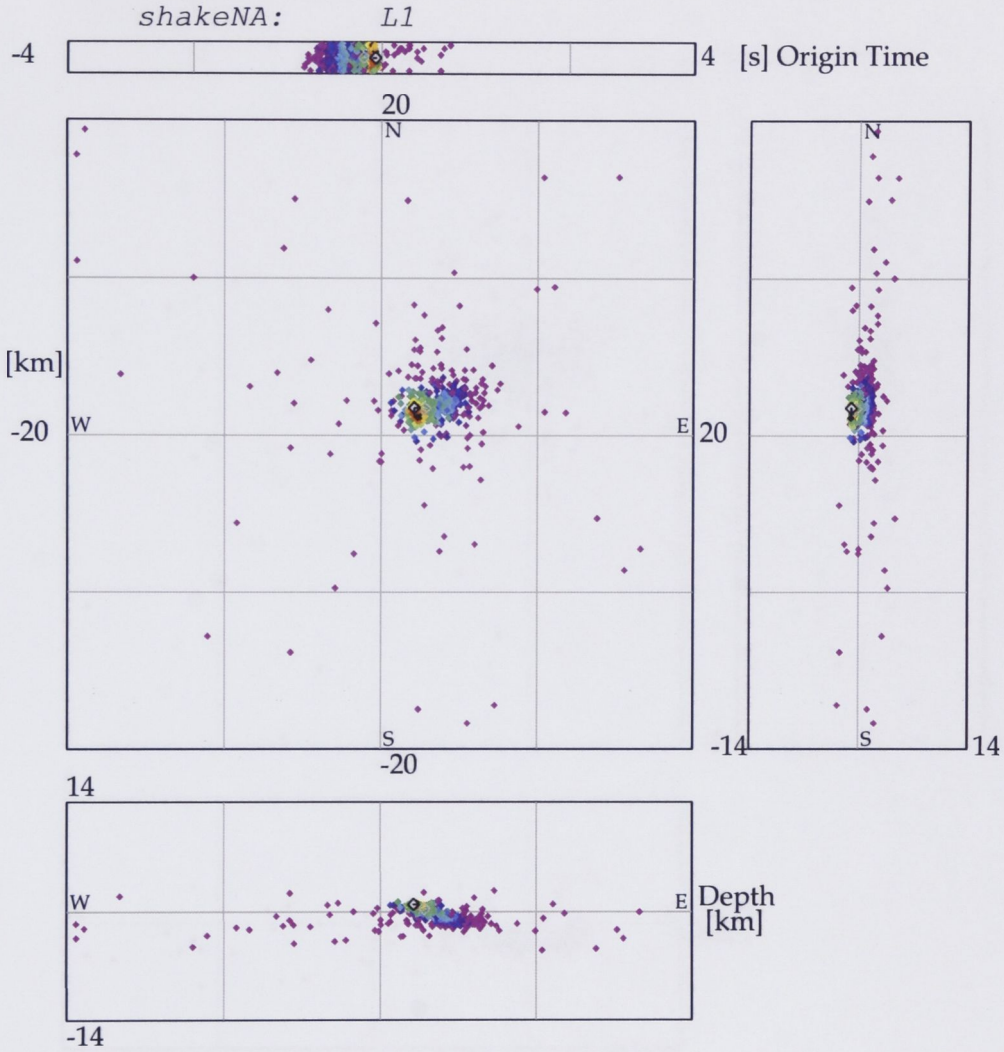

Fig. C-31: Illustration of the neighbourhood algorithm progression towards convergence for Event 8312282101F in the 4-D parameter space. The horizontal search area is 40 x 40 km. The centre of the plot is the starting search point and is given by the coordinate -4.265°S and 152.190°E. Each circle, irrespective of colour, denotes the tested epicenters. Note the spread of the purple circles. These are tested epicenters with high misfits. The area of strong clustering marked by the coloured circles gives the best location estimate. If they appear, the black circles have the least misfit.

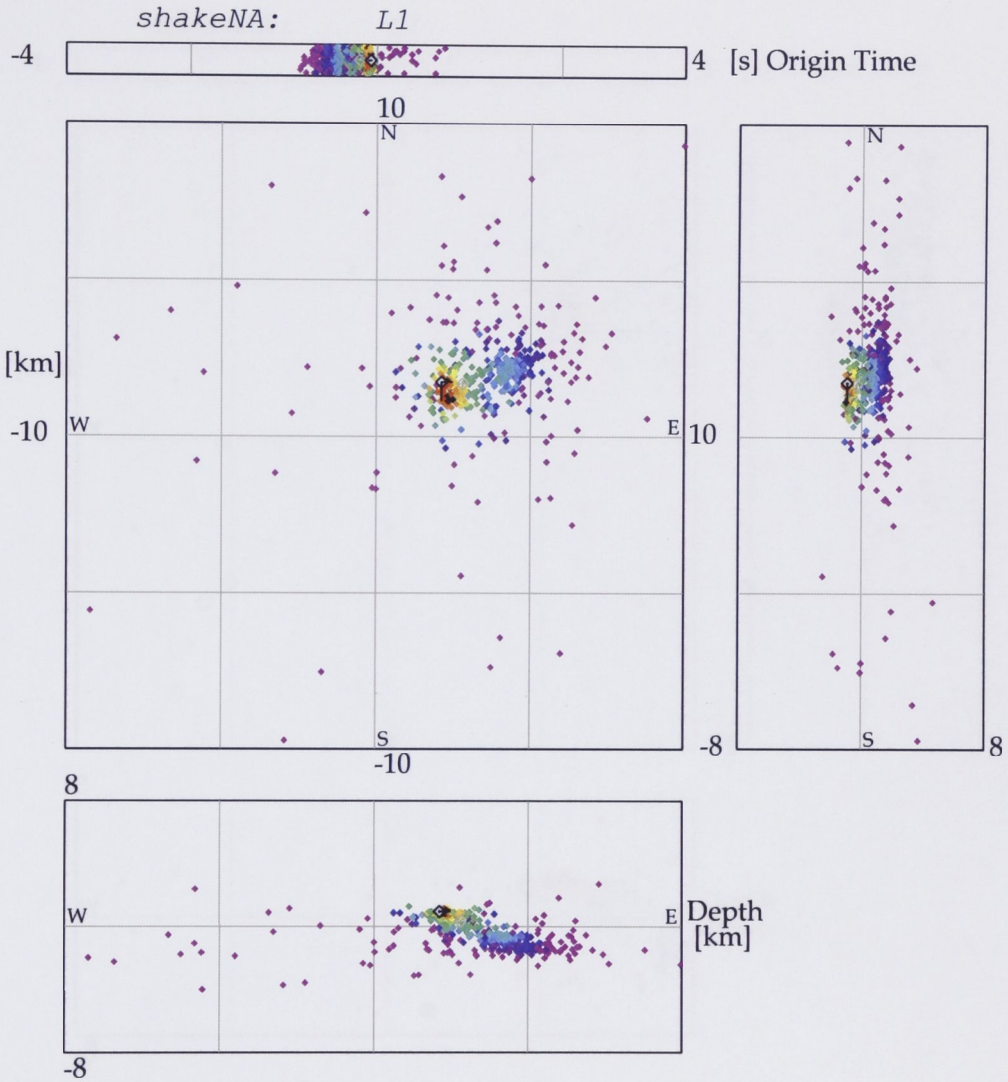

Fig. C-32: Illustration of the neighbourhood algorithm progression towards convergence for Event 8312282101F in the 4-D parameter space. The horizontal search area is 20 x 20 km. The centre of the plot is the starting search point and is given by the coordinate -4.265°S and 152.190°E. Each circle, irrespective of colour, denotes the tested epicenters. Note the spread of the purple circles. These are tested epicenters with high misfits. The area of strong clustering marked by the coloured circles gives the best location estimate. If they appear, the black circles have the least misfit.

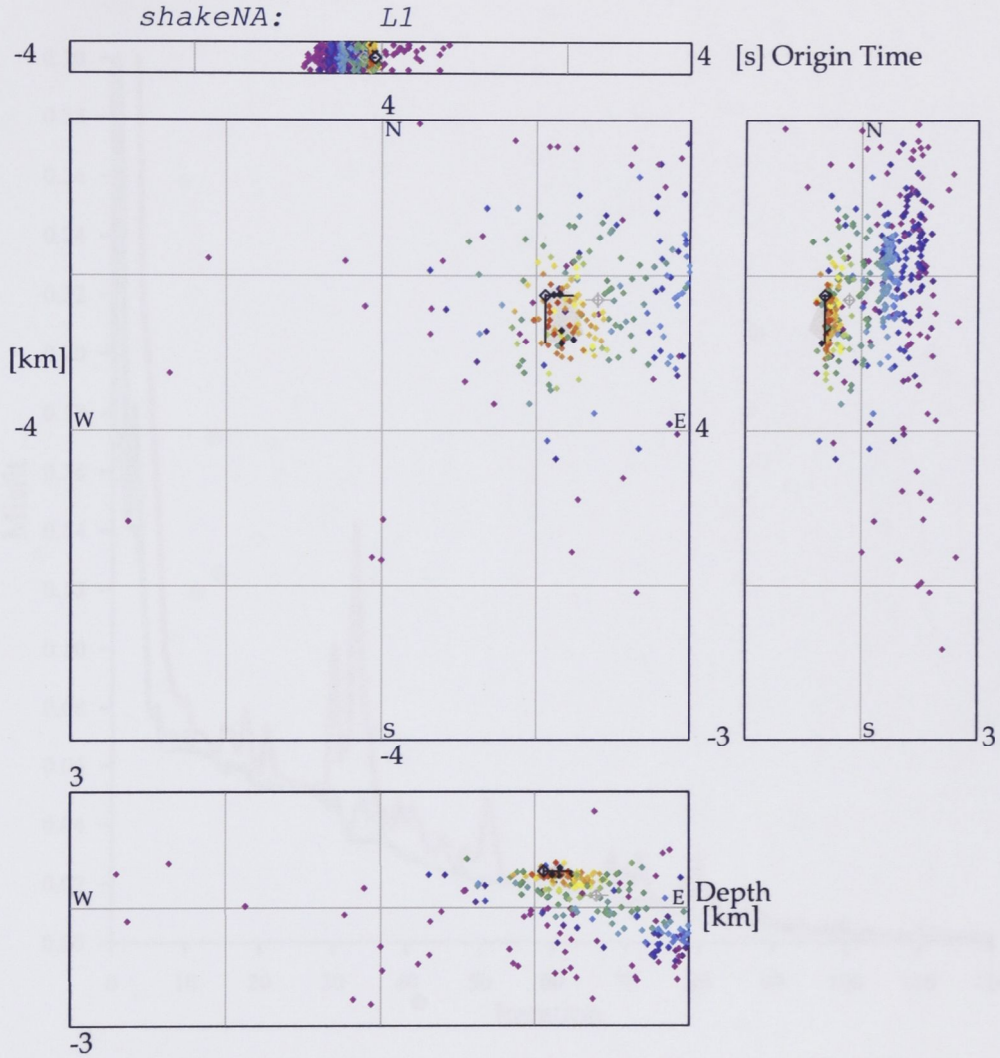

Fig. C-33: Illustration of the neighbourhood algorithm progression towards convergence for Event 8312282101F in the 4-D parameter space. The horizontal search area is 8 x 8 km. The centre of the plot is the starting search point and is given by the coordinate -4.265°S and 152.190°E. Each circle, irrespective of colour, denotes the tested epicenters. Note the spread of the purple circles. These are tested epicenters with high misfits. The area of strong clustering marked by the coloured circles gives the best location estimate. If they appear, the black circles have the least misfit.

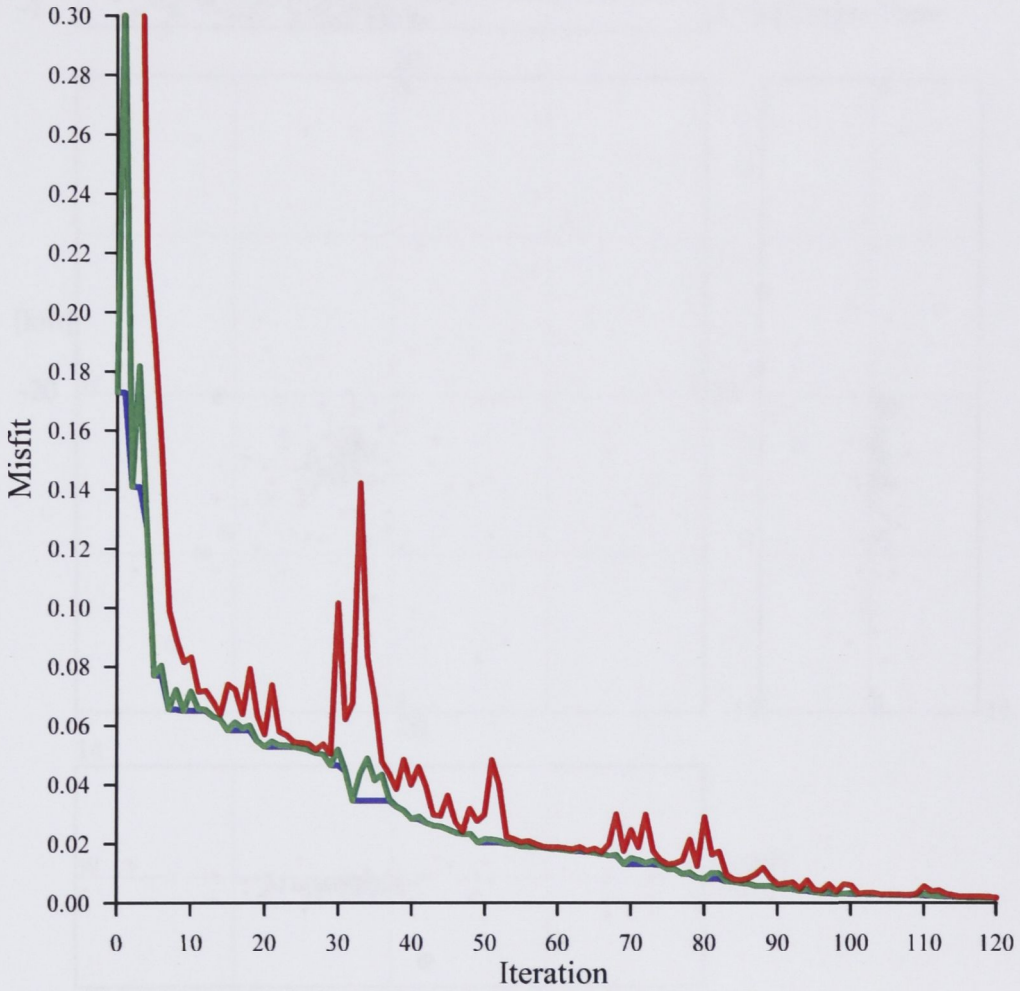

Fig. C-34: Plot of the misfit measure for Event 8312282101F. The blue line is for the lowest misfit in the model, red is the average misfit across all models and green is the current misfit. In this example the convergence is fairly slow. It converges fully at about iteration 117.

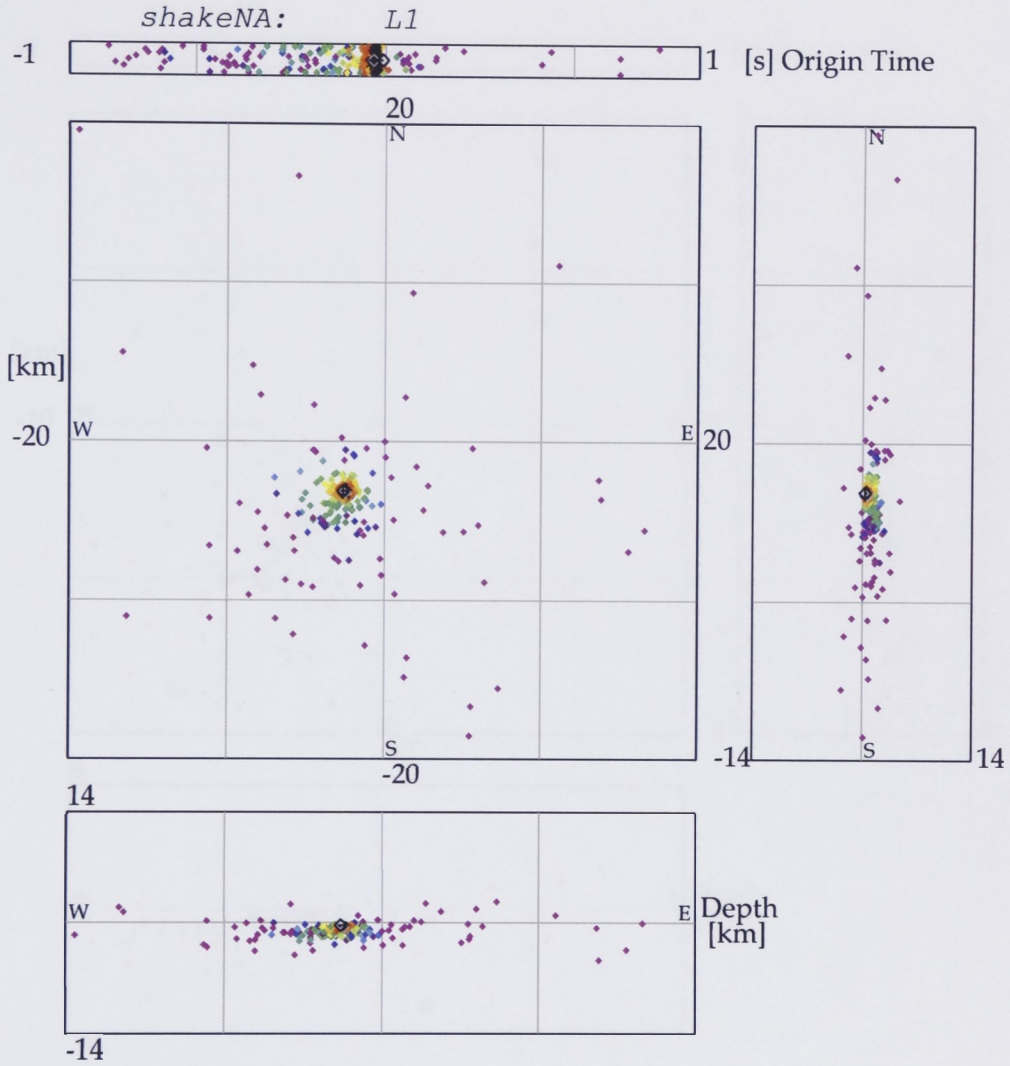

Fig. C-41: Illustration of the neighbourhood algorithm progression towards convergence for Event 8402180015F in the 4-D parameter space. The horizontal search area is 40 x 40 km. The centre of the plot is the starting search point and is given by the coordinate -4.265°S and 152.190°E. Each circle, irrespective of colour, denotes the tested epicenters. Note the spread of the purple circles. These are tested epicenters with high misfits. The area of strong clustering marked by the coloured circles gives the best location estimate. If they appear, the black circles have the least misfit.

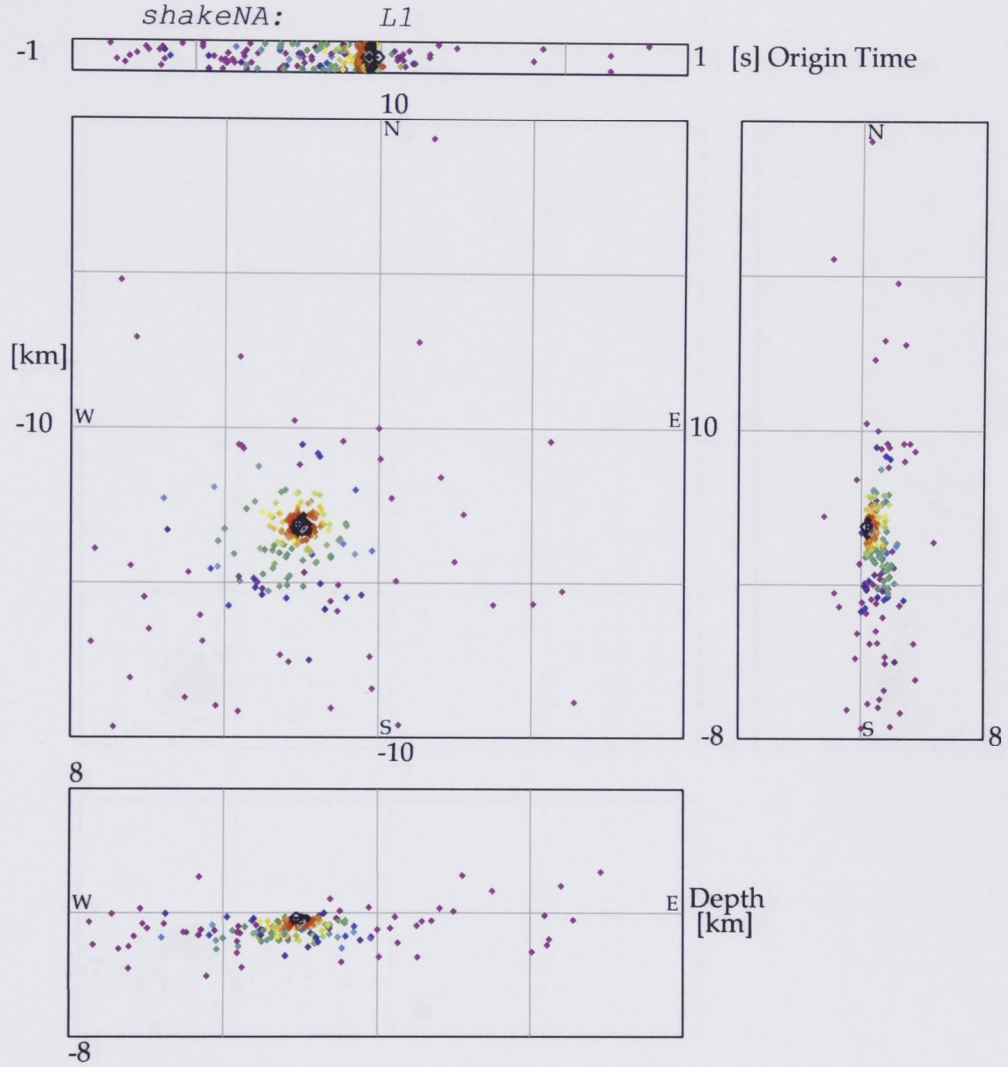

Fig. C-42: Illustration of the neighbourhood algorithm progression towards convergence for Event 8402180015F in the 4-D parameter space. The horizontal search area is 20 x 20 km. The centre of the plot is the starting search point and is given by the coordinate -4.265°S and 152.190°E. Each circle, irrespective of colour, denotes the tested epicenters. Note the spread of the purple circles. These are tested epicenters with high misfits. The area of strong clustering marked by the coloured circles gives the best location estimate. If they appear, the black circles have the least misfit.

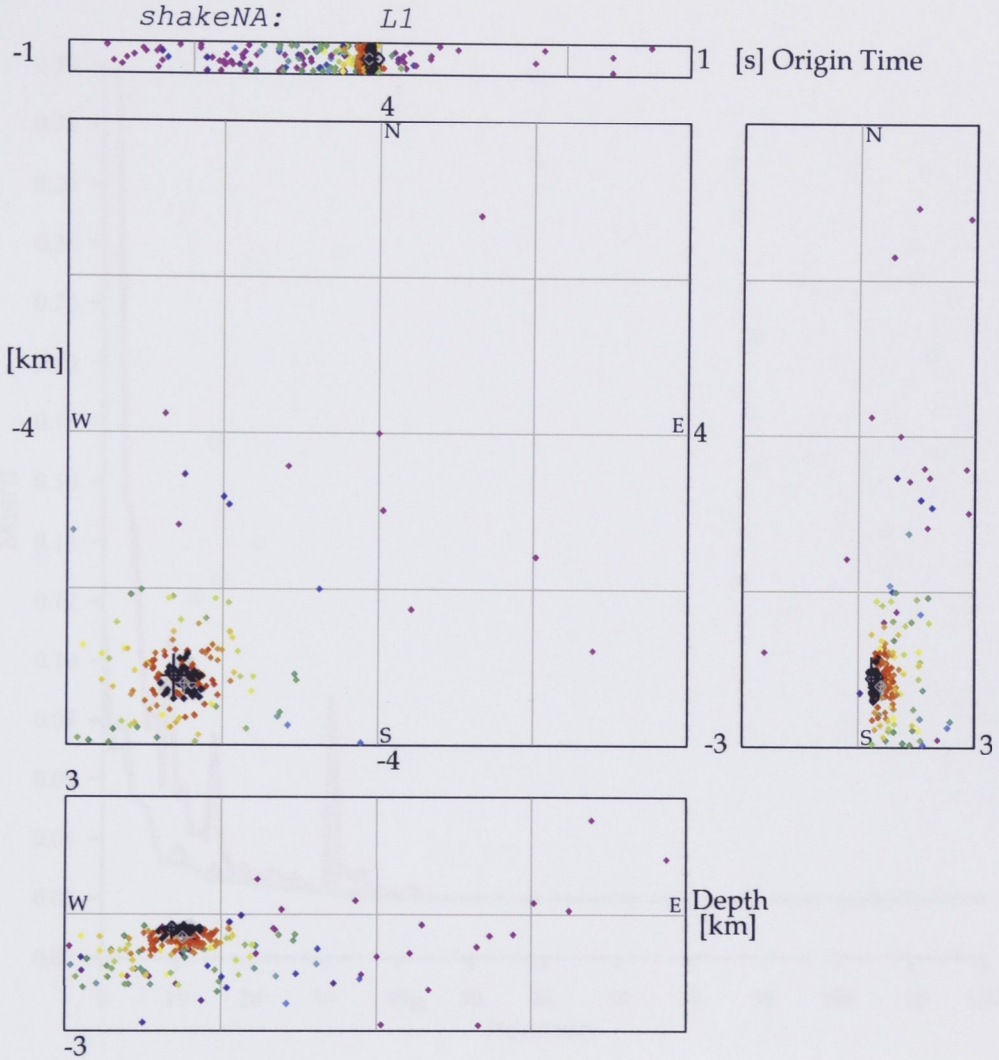

Fig. C-43: Illustration of the neighbourhood algorithm progression towards convergence for Event 8402180015F in the 4-D parameter space. The horizontal search area is 8 x 8 km. The centre of the plot is the starting search point and is given by the coordinate -4.265°S and 152.190°E. Each circle, irrespective of colour, denotes the tested epicenters. Note the spread of the purple circles. These are tested epicenters with high misfits. The area of strong clustering marked by the coloured circles gives the best location estimate. If they appear, the black circles have the least misfit.

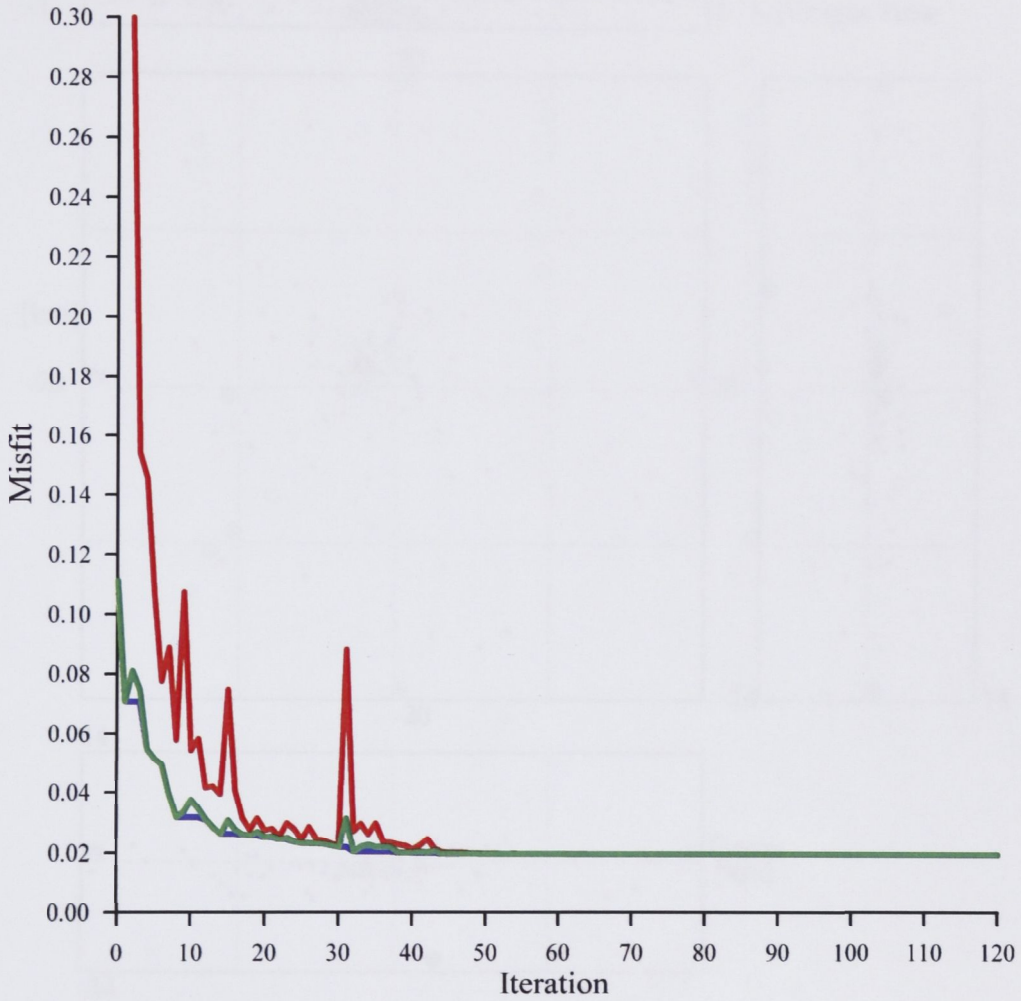

Fig. C-44: Plot of the misfit measure for Event 8402180015F. The blue line is for the lowest misfit in the model, red is the average misfit across all models and green is the current misfit. In this example the misfit convergences fully at about iteration 45.

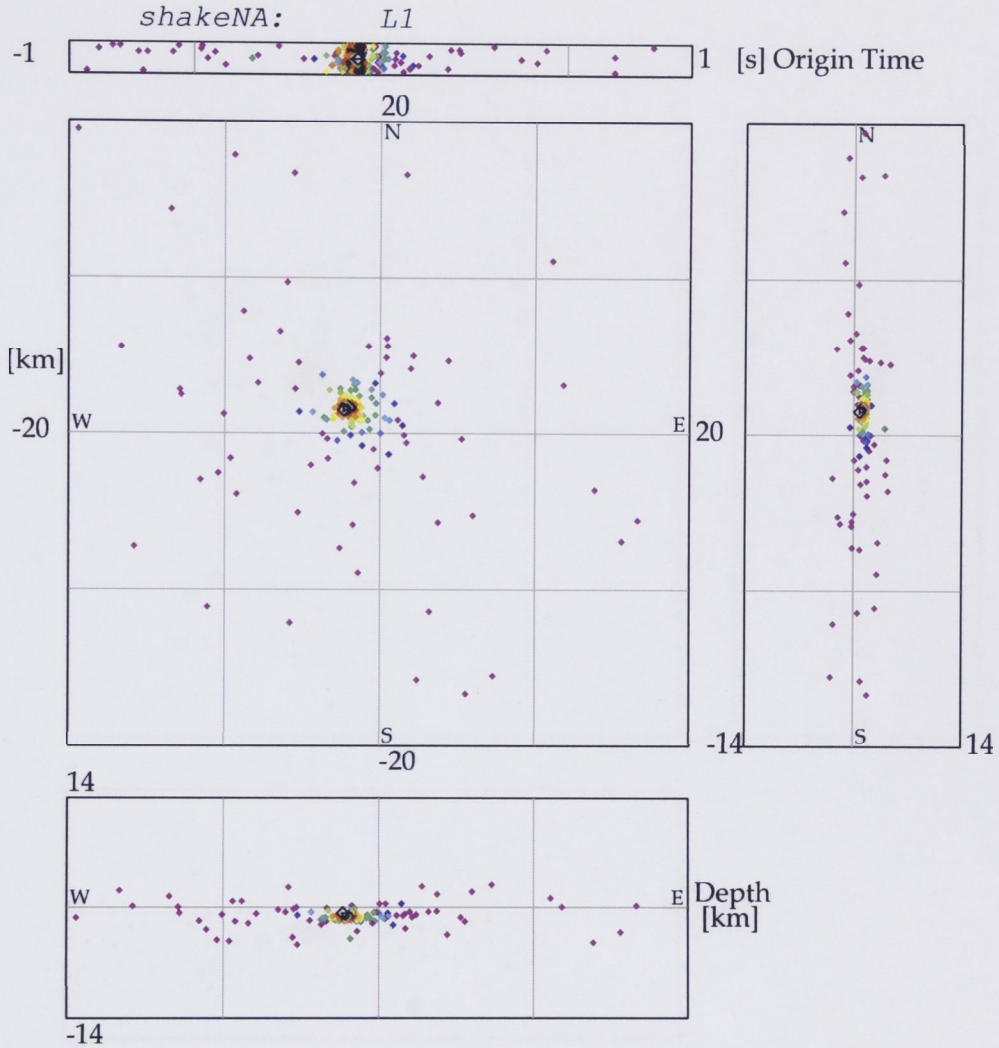

Fig. C-51: Illustration of the neighbourhood algorithm progression towards convergence for Event 8405040100F in the 4-D parameter space. The horizontal search area is 40 x 40 km. The centre of the plot is the starting search point and is given by the coordinate -4.265°S and 152.190°E. Each circle, irrespective of colour, denotes the tested epicenters. Note the spread of the purple circles. These are tested epicenters with high misfits. The area of strong clustering marked by the coloured circles gives the best location estimate. If they appear, the black circles have the least misfit.

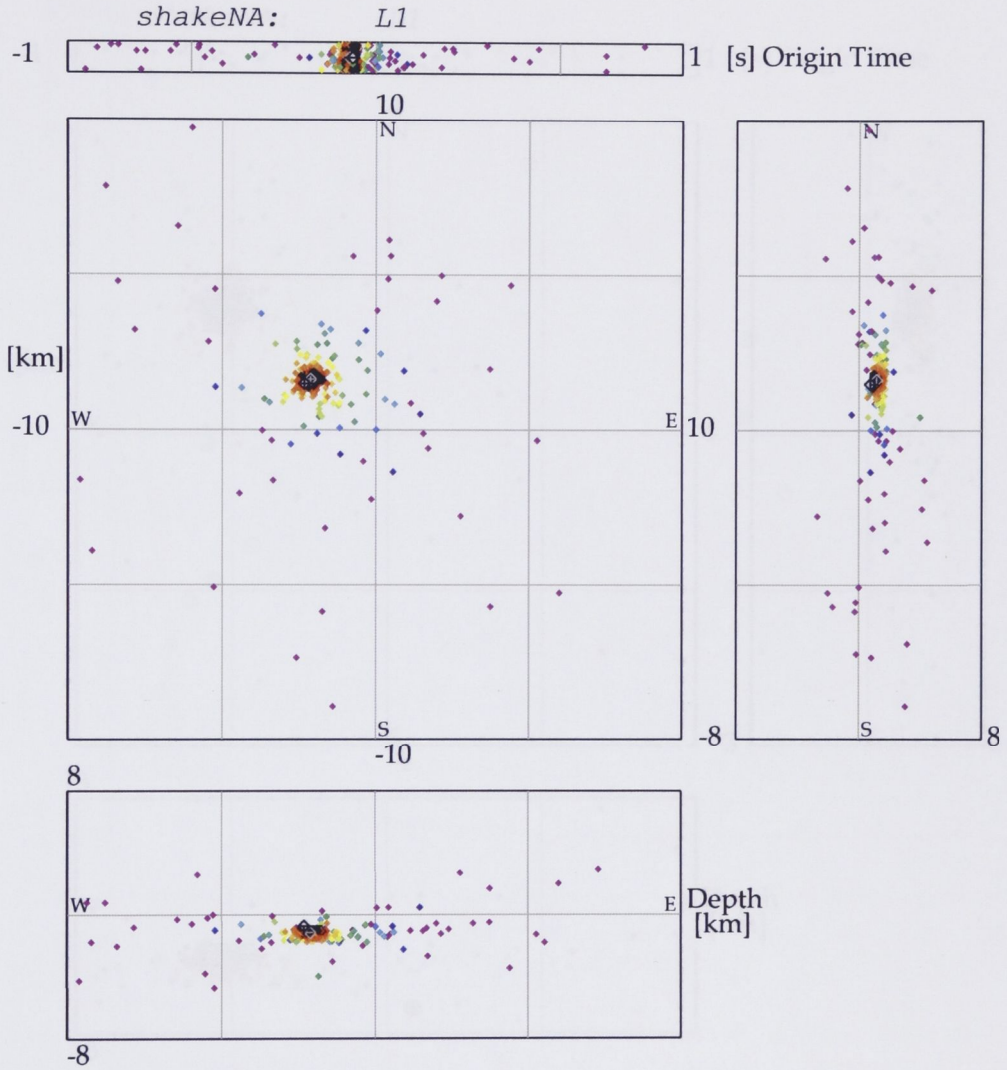

Fig. C-52: Illustration of the neighbourhood algorithm progression towards convergence for Event 8405040100F in the 4-D parameter space. The horizontal search area is 20 x 20 km. The centre of the plot is the starting search point and is given by the coordinate -4.265°S and 152.190°E. Each circle, irrespective of colour, denotes the tested epicenters. Note the spread of the purple circles. These are tested epicenters with high misfits. The area of strong clustering marked by the coloured circles gives the best location estimate. If they appear, the black circles have the least misfit.

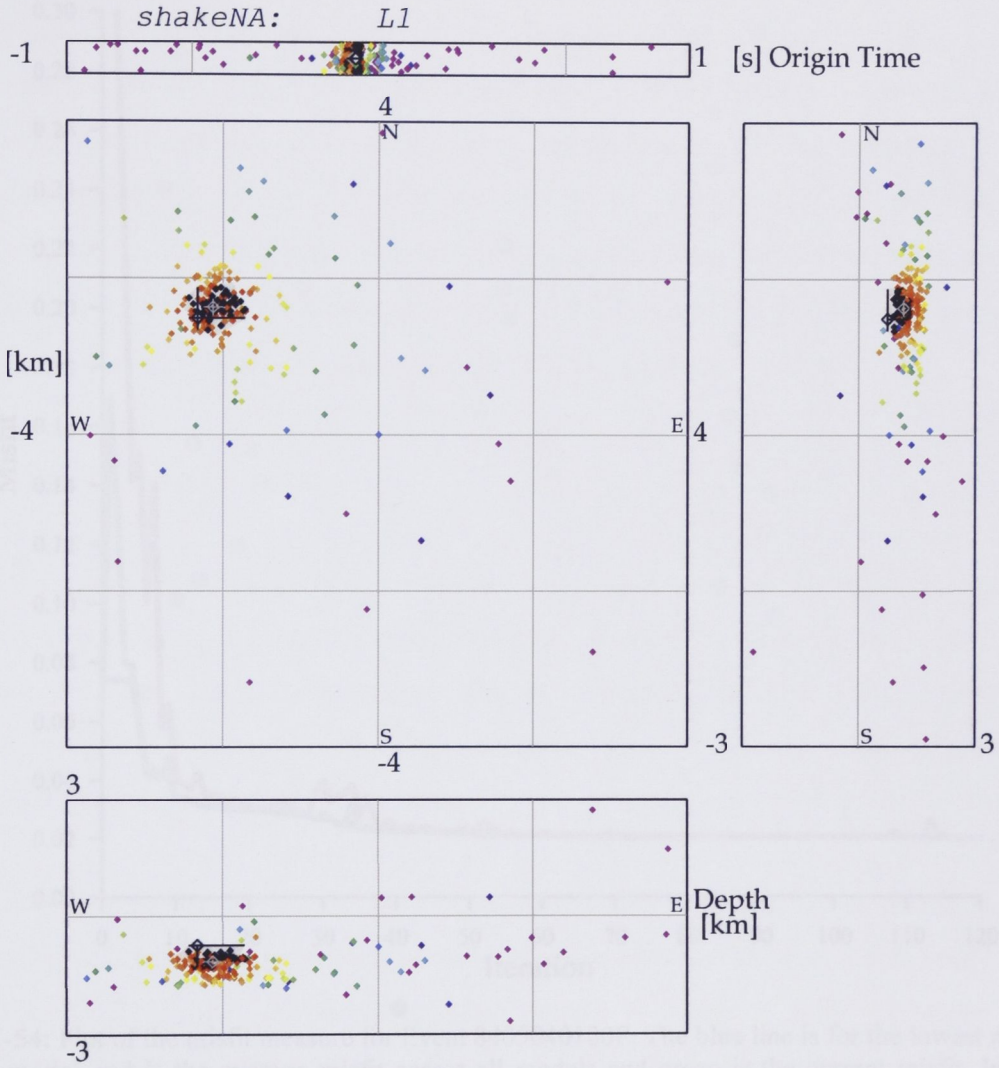

Fig. C-53: Illustration of the neighbourhood algorithm progression towards convergence for Event 8405040100F in the 4-D parameter space. The horizontal search area is 8 x 8 km. The centre of the plot is the starting search point and is given by the coordinate -4.265°S and 152.190°E. Each circle, irrespective of colour, denotes the tested epicenters. Note the spread of the purple circles. These are tested epicenters with high misfits. The area of strong clustering marked by the coloured circles gives the best location estimate. If they appear, the black circles have the least misfit.

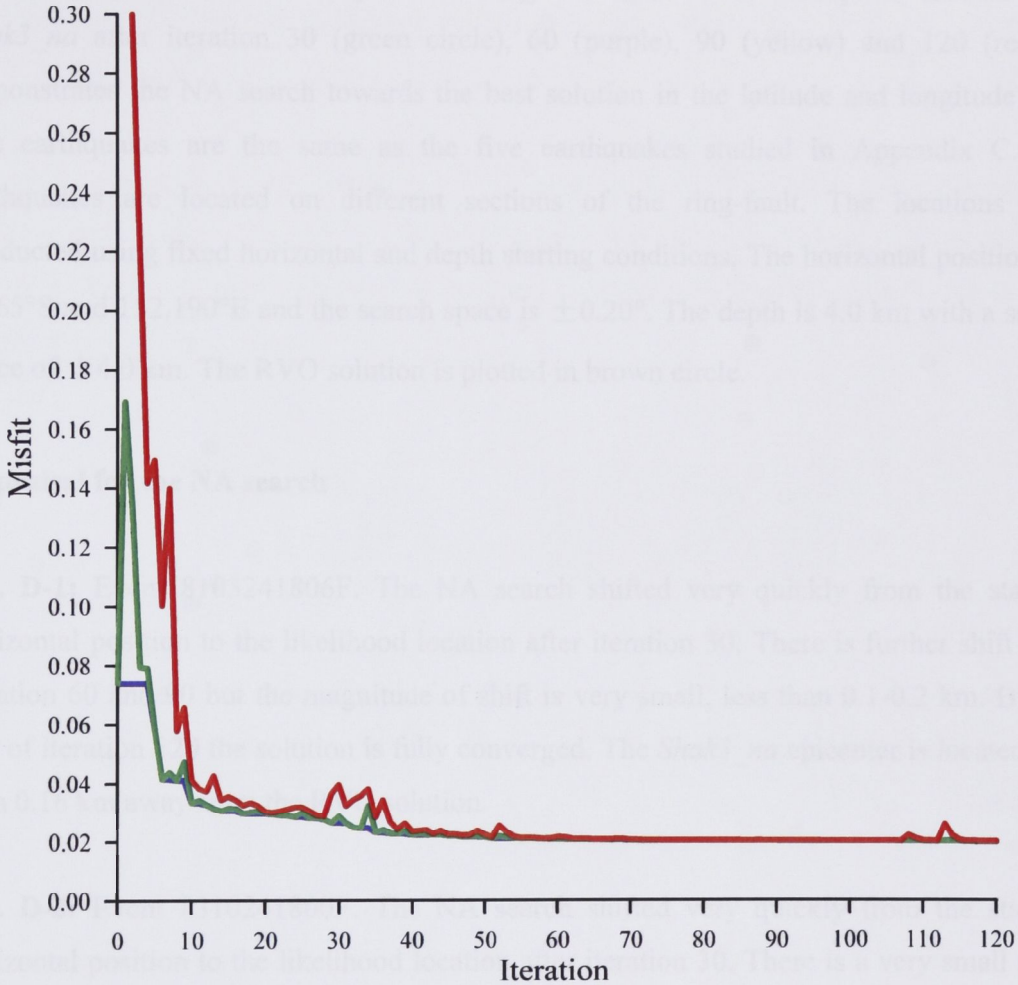

Fig. C-54: Plot of the misfit measure for Event 8405040100F. The blue line is for the lowest misfit in the model, red is the average misfit across all models and green is the current misfit. In this example the misfit convergences fully at about iteration 54.

APPENDIX D – NA Search

Appendix D has five plots showing the shift of an earthquake located with *Shak3_na* after iteration 30 (green circle), 60 (purple), 90 (yellow) and 120 (red). It demonstrates the NA search towards the best solution in the latitude and longitude axis. The earthquakes are the same as the five earthquakes studied in Appendix C. The earthquakes are located on different sections of the ring-fault. The locations were conducted using fixed horizontal and depth starting conditions. The horizontal position is -4.265°S and 152.190°E and the search space is ±0.20°. The depth is 4.0 km with a search space of ±4.0 km. The RVO solution is plotted in brown circle.

Appraisal for the NA search

Fig. D-1: Event 8103241806F. The NA search shifted very quickly from the starting horizontal position to the likelihood location after iteration 30. There is further shift after iteration 60 and 90 but the magnitude of shift is very small, less than 0.1-0.2 km. By the end of iteration 120 the solution is fully converged. The *Shak3_na* epicenter is located less than 0.16 km away from the RVO solution.

Fig. D-2: Event 8310241800F. The NA search shifted very quickly from the starting horizontal position to the likelihood location after iteration 30. There is a very small shift, less than 0.1 km, after iteration 60. After that the solution is fully converged. The *Shak3_na* epicenter is located less than 0.12 km from the RVO solution.

Fig. D-3: Event 8312282101F. The NA search for this earthquake is far more complicated. After iteration 30 the earthquake is located well outside the ring-fault and about 1.5 km from the RVO solution. The search moves closer to the RVO solution after iterations 60, 90 and 120, with the amount of shift reduced each time. The least shift is gained between iterations 90 and 120. By the end of iteration 120 the epicenter is about 0.25 km from the RVO epicenter. According to the misfit measure (Appendix C) the misfit converges more slowly than that for the two previous earthquakes. The misfit seems to have fully

converged at about iteration 115 but the NA search has not converged. The locations after iterations 90 and 120 are separated by about 0.2 km.

Fig. D-4: Event 8402180015F. The pattern of the NA search for this earthquake is similar to the two previous earthquakes. The search shifts very quickly to the likelihood location after iteration 30. The search remains within less than 0.1 km after iterations 60, 90 and 120. The final *Shak3_na* epicenter is about 0.18 km from the RVO epicenter.

Fig. D-5: Event 8405040100F. The NA search shifts very quickly to the likelihood location after iteration 30 just like the last and the two earlier earthquakes. After that the search is maintained within 0.1 km of the final solution. The final epicenter is about 0.35 km from the RVO epicenter.

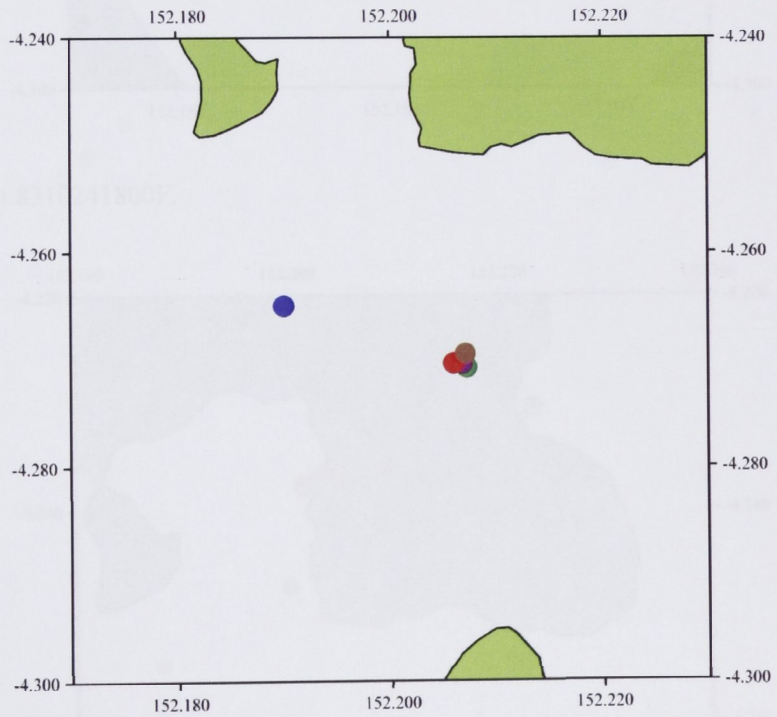

Fig. D-1: Event 8103241806F. The blue circle is the starting point. The others are the re-calculated positions after iteration 30 (green circle), 60 (purple), 90 (yellow) and 120 (red). The RVO epicenter is shown by the brown circle. The same figure caption information applies for the rest of the figures.

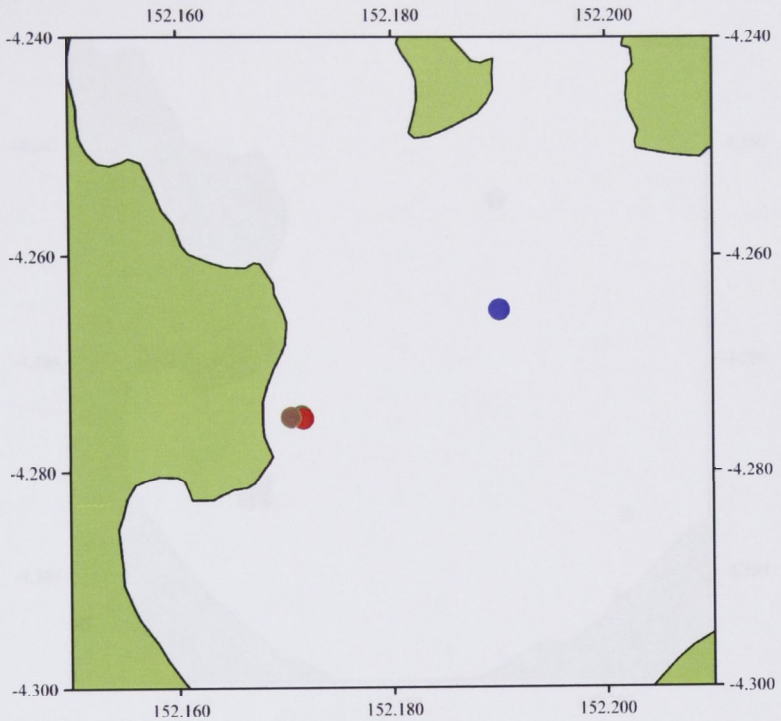

Fig. D-2: Event 8310241800F.

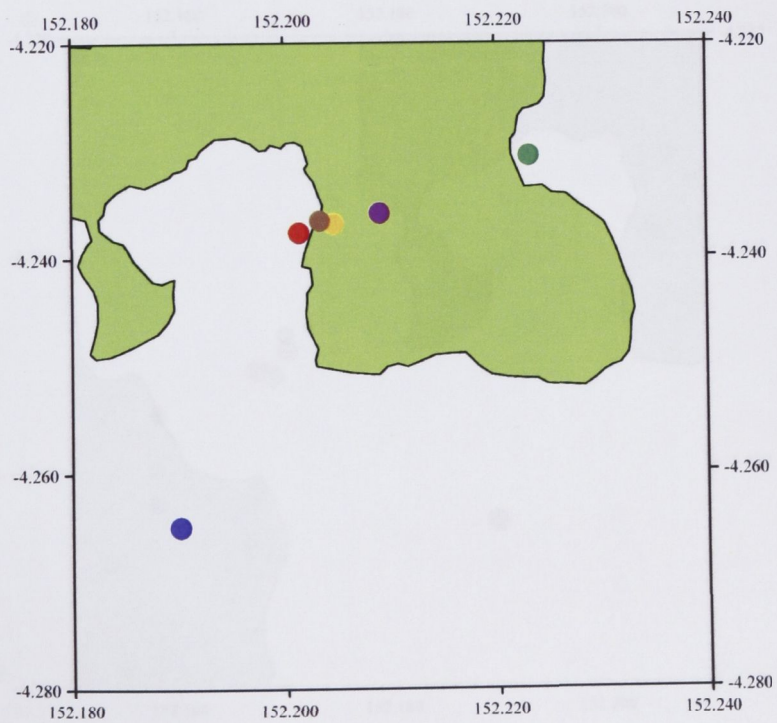

Fig. D-3: Event 88312282101F.

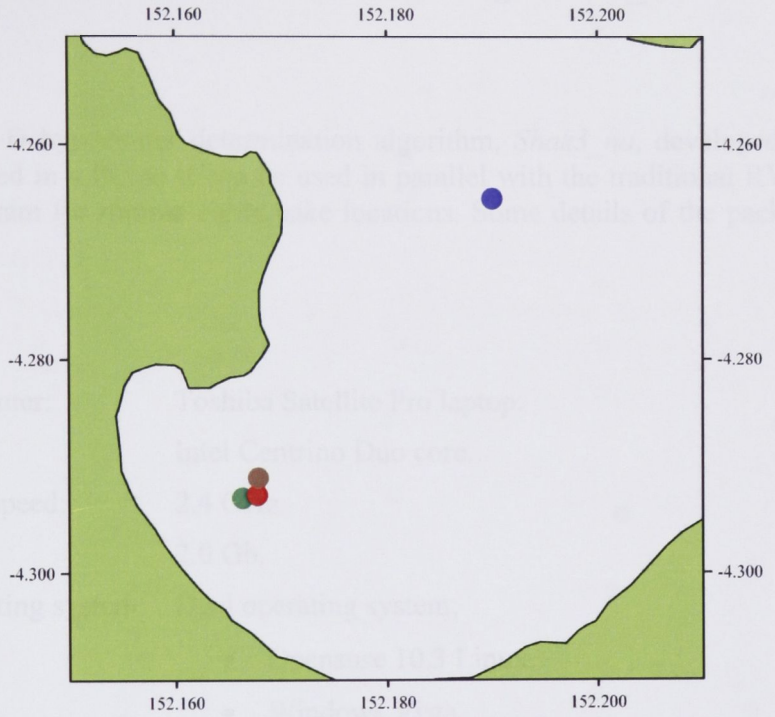

Fig. D-4: Event 8402180015F.

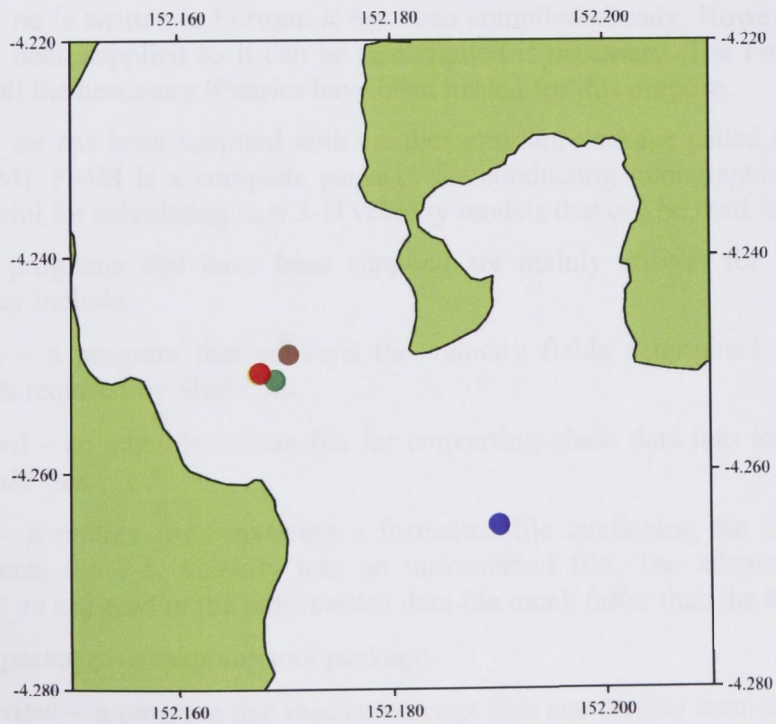

Fig. D-5: Event 8405040100F.

APPENDIX E – Porting *Shak3_na*

Introduction

The 3-D hypocenter determination algorithm, *Shak3_na*, developed in this study has been ported in a PC so it can be used in parallel with the traditional RVO earthquake location program for routine earthquake locations. Some details of the package are given below.

The PC

Computer:	Toshiba Satellite Pro laptop.
CPU:	Intel Centrino Duo core.
CPU speed:	2.4 GHz.
RAM:	2.0 Gb.
Operating system:	Dual operating system;

- Opensuse 10.3 Linux.
- Windows Vista.

The Program package

Shak3_na is written in Fortran. It has been compiled already. However, the source code has also been supplied so it can be re-compiled if necessary. The Fortran compiler *gfortran* and all the necessary libraries have been loaded for this purpose.

Shak3_na has been supplied with another program package called Fast Marching Method (FMM). FMM is a complete package for conducting tomographic studies. This package is useful for calculating new 3-D velocity models that can be used with *Shak3_na*.

Other programs that have been supplied are mainly utilities for use with both programs. They include:

- fm2na – a program that converts the velocity fields determined by FMM into formats required by *Shak3_na*.
- pha2evd – an editable fortran file for converting phase data into formats required by *Shak3_na*.
- t-unf – a routine for converting a formatted file containing the time fields that represents the 3-D velocity into an unformatted file. The advantage of this is *Shak3_na* can read in the unformatted data file much faster than the formatted file.
- GMT package – a mapping tool package.
- Ghostview – a program that reads postscript files and display them as images.
- nadens – a program that converts one of the key *Shak3_na* output files into postscript format so it can be read by the ghostview.

Conclusion

The main purpose for porting the above package is to enable RVO to conduct routine 3-D earthquake locations alongside the normal 1-D earthquake locations. The package provides the tool for RVO to review the 3-D velocity model if it becomes necessary. For example if there is omission or addition of stations to the network, or there is improved data, or both, then it is essential to use this information to generate a new 3-D velocity model.

Acknowledgements

The configuration of this package benefitted greatly from the encouragement of Prof Brian Kennett and technical assistance from Juerg Hauser (PhD student) and Dr Paul Davidson, the RSES IT Manager.